Looking for new physics in the $B_s^0 \to J/\psi\phi$ decay

Adam Edward Barton

· *Department of Physics* ·

This thesis is submitted for the degree of Doctor of Philosophy.

· *September 2013* ·

et suppositio nil ponit in esse

latin - and a supposition puts nothing in being

In the beginning the Universe was created. This has made a lot of people very angry and has been widely regarded as a bad move.

-Douglas Adams

Acknowledgements

I would like to offer my thanks to the following:

- The Science and Technology Facilities Council (STFC) for providing the funding for my research and Long Term Attachment (LTA) at CERN and the UK and European taxpayer for their contributions to the scientific research of the future.
- My Supervisor Roger Jones and my shadow supervisor Vato Kartvelishvili, for their continued help, and support.
- The Staff of Lancaster University physics department for giving me the studentship despite the fact I forgot the semi-leptonic decay I worked on during my master's project in the interview.
- My Technical Supervisor Maria Smizanska for her constant guidance, tutelage and leadership.
- To the STFC UK liaison office for organising my accommodation for the duration of the LTA.
- James Catmore for co-convening the ATLAS B-physics group, writing many of the B-physics tools, providing tutorials and patiently assisting with the debugging of code.
- James Walder for providing tutorials and help.
- Alastair Dewhurst and Louise Oakes for sharing their experience and tools for this analysis.

- To my other colleagues in the analysis Tatjana Jovin, Pavel Reznicek, Jochen Schieck and Claudio Heller

- To the B-physics trigger team for diligently ensuring our data was collected

- My family for supporting me.

Abstract

The CP violating phase ϕ_s is measured in decays of $B_s^0 \to J/\psi\phi$. This measurement uses 4.9 fb^{-1} of data from the ATLAS detector at the LHC at CERN. This data consists of the 2011 run of pp collisions at $\sqrt{s} = 7$ TeV. This measurement provides a means of potentially falsifying the standard model, which is known to provide insufficient levels of CP violation to account for the observable universe. This thesis includes material that has been publicly available in papers and ATLAS CONF notes, but provides greater detail. The measurement uses the proper decay time and angular distributions of the decay to measure key theoretical parameters of the flavour physics involved. The measurements in this thesis complement and compete with the measurements taken by various experiments around the world. This thesis contains details for both flavour tagged and untagged measurements. The tagged results are:

$\phi_s = 0.12 \pm 0.25$ (stat.) ± 0.11 (syst.) rad

$\Delta\Gamma_s = 0.053 \pm 0.021$ (stat.) ± 0.009 (syst.) ps^{-1}

$\Gamma_s = 0.677 \pm 0.007$ (stats.) ± 0.003 (sys.) ps^{-1}

Contents

List of Figures

List of Tables

Chapter 1

Introduction

While one can never be certain at which point in history important ideas were first conceived our history books first speak of the philosophers of ancient Greece who asked the questions we now identify as metaphysics and physics, "What is there?" and "What is it like?". Many centuries later when such questions have been categorised into academic fields it appears that high energy particle physics may be the final tool left in experimental physics for addressing the fundamental questions of matter and perhaps existence. Deeper study is left to mathematical theory and conceptual ontology.

The so called *Standard Model* is the current culmination of our understanding of basic building blocks of matter which has changed little[1] since the 1970s due to immense difficulty that has been had in finding deviations from its predictions using man made high energy experiments. While frustrating for the physicists engaged with improving theory further this indicates how robust the current model is.

There is a missing aspect, which is known due to the wider study of cosmology and astrophysics, that is the large dominance of matter in the universe. Andrei Sakharov first described the necessary physical requirements for a matter excess to occur [1]. Naïve particle physics would suggest a perfect symmetry between matter and antimatter, however that view was falsified in 1964 with the discovery of

[1] With perhaps the exception of the neutrino mass

asymmetries in kaon decays [2]. These differences were an example of the breakdown of symmetry under the combined application of charge conjugation and parity operations. This is dubbed CP violation. CP violation is now an accepted part of the standard model [3] but still fails to explain the magnitude of the disparity between matter and antimatter in the universe. This observation provides a strong motivation for investigating unexamined sources of asymmetry in hopes of falsifying the standard model predictions and explaining the observed universe.

This thesis describes my contribution to testing the CP violation in the Standard Model, specifically the CP violation that occurs in a B_s meson decay. Other quantities of interest to physics are also measured in the process.

Starting just at the beginning of the LHC operation, this work initially involved testing the performance properties relevant for B-decays by measuring physics quantities, such as mass and lifetime of B-mesons. that then becomes part of a high precision measurement of CP violation. This thesis will mostly focus on the latter making reference to the former when appropriate. The study of the $B_s^0 \to J/\psi\phi$ is of interest to particle physicists as it allows a measurement of the B_s mixing phase which is responsible for CP violation in this decay channel. This is described in more detail in chapter 4. Since the size of the CP violation allowed by the Standard Model when combined with current observations is small (of the order of 10^{-2}), any significant deviation should be found fairly easily and would be a clear indication of New Physics. Smaller deviations could also be identified in the future once more data has been amassed.

The $B_d^0 \to J/\psi K^{0*}$ is an analogous decay and was used to test the decay reconstruction using the ATLAS 2010 dataset. This was due to the higher production ratio of the B_d meson producing more $B_d^0 \to J/\psi K^{0*}$ decays.

The analysis presented in this thesis presents the extraction of the $B_s^0 \to J/\psi\phi$ decay from the ATLAS experiment's 2011 dataset at the LHC. The analysis is part of the ATLAS B-physics programme, which consists of measurement of production cross sections and production mechanisms of heavy flavoured hadrons, and of

studies of selected exclusive B-hadron decays. The measurement of the lifetimes are also an excellent probe of the performance of the ATLAS detector including the vertex reconstruction systems.

The first two chapters give a brief overview of the LHC collider and the ATLAS detector hardware. The third chapter gives a brief overview of the Standard Model, paying particular attention to the concepts surrounding CP violation and neutral B-meson mixing. The fifth chapter describes the computing and software infrastructure of the ATLAS detector and describes in detail the software used in the analysis. The author made significant contributions to the development and testing of the *Athena* algorithms used to select the relevant data from the ATLAS datasets. The author was also often responsible for using the algorithm with the Grid computing system in day to day operations.

The sixth chapter starts describing the initial steps of the analysis such as the candidate reconstruction and the determination of the selection cut. The author contributed significantly to the methods described here with the exception of the tagging method development. Chapter seven describes in detail the acceptance corrections which were implemented by the author. The eighth chapter provides description of the basic principles of maximum likelihood fitting and an in-depth description of the functions used in the statistical fitting in this analysis. While the author aided in minor developments and testing of the fit procedure, this version of the code was primarily implemented by the Munich group sometimes building on code written previously by physicists from the Lancaster group.

The ninth chapter details the estimation of the systematic errors. The author was responsible for the estimation of systematic error caused by the acceptance corrections and the general testing and improvement of the fit code. The rest of the systematic assessment was primarily done by the Munich group.

The tenth chapter presents the final results of the fitting procedures, discusses the limitations of the analysis and concludes the thesis.

Information about the preliminary fitting techniques are given in Appendix A.

The specifics about the ATLAS datasets and the good run lists used are given in Appendix B and additional consistency checks of the final angular fit are given in Appendix C.

Chapter 2

The Large Hadron Collider

The Large Hadron Collider (LHC) is a dual-beam proton synchrotron. It supersedes the Tevatron at Fermilab Chicago as the most powerful hadron collider in the world. It was approved for construction by CERN in 1994 and was completed in 2008. The first collisions occurred on the 30th March 2010 at beam energies of 3.5 TeV. Since then, the productivity of the machine has increased by several orders over the years that followed as the engineers better understood the machine and pushed the machine closer to its design performance. The LHC replaced the LEP (Large Electron-Positron Collider) accelerator which was contained inside a 27km circular tunnel under the Franco-Swiss border near Geneva and the French village of Saint-Genis-Pouilly. The existing accelerator chain (Linac/Booster/PS/SPS) is used for LHC injection but was modified to accommodate the various requirements of the LHC [4].

The proton beams are created by passing hydrogen through a magnetic field, ionising the gas into protons and electrons before being accelerated through the Linac and into the super proton synchrotron (SPS). In the LHC itself the beams are powered by using superconducting radio-frequency oscillators connected to the local power grid. The beam is manipulated into a circular path by 1232 superconducting dipole magnets and focused by approximately 392 quadruple magnets. In total, over 1,600 superconducting magnets are installed, with most weighing over 27 tonnes. Approximately 96 tonnes of liquid helium is needed

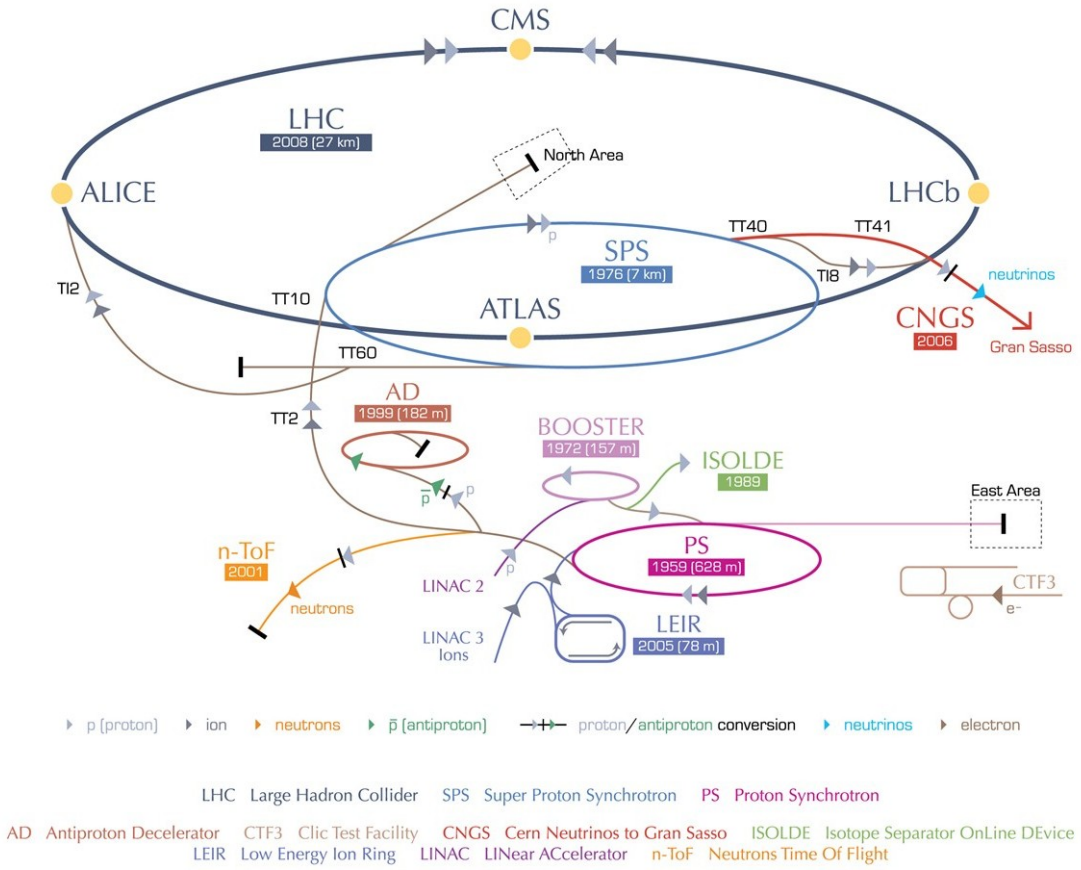

Figure 2.1: The LHC is the last ring (dark grey line) in a complex chain of particle accelerators. The smaller machines are used in a chain to help boost the particles to their final energies and provide beams to a whole set of smaller experiments.[7]

to keep the magnets, made of copper-clad niobium-titanium, at their operating temperature of 1.9 K (−271.25 °C), making the LHC the largest cryogenic facility in the world at liquid helium temperature [5]. Over 6000 corrector magnets are used to suppress undesired resonances [6]. The total power consumption of the LHC is 120 MW. When running at full power each beam will have a nominal energy of 7 TeV, providing a centre-of-mass energy of 14 TeV during a collision.

The input beam is provided by the pre-LHC complex of CERN accelerators, namely the 50 MeV linear accelerator, the 1.4 GeV Proton Synchrotron, the 26 GeV Proton Synchrotron and the 450 GeV Super proton Synchrotron (SPS). The beam is not a continuous stream of protons otherwise it would be distorted by the oscillating polarity of the electric fields used in the accelerator. Instead the beam consists of bunches 1 metre long. At collision points bunches pass through at most

every 25 ns. Like many factors, the exact rate of crossing can vary depending on the currently accepted safety limit. The luminosity of a collision is the number of particles passing through a unit area of the interaction region, per unit of time. If bunches containing n_1 and n_2 particles pass through one another with frequency f, the luminosity is given by:

$$L = f\frac{n_1 n_2}{4\pi\sigma_x\sigma_y} \tag{2.1}$$

where $\sigma_{x,y}$ are the profiles of the beam as a Gaussian distribution in the vertical and horizontal directions. The number of observed events of a given signal process P_0 with branching ratio B can be calculated by

$$N_{obs} = LT\sigma_{P0}B\epsilon_r \tag{2.2}$$

where L is the luminosity, T is the total time during which the collisions are occurring, σ_{P0} is the production cross section for the particle P_0 and ϵ_r is the reconstruction efficiency for the channel, which can only be determined from simulation. During a bunch crossing, it is likely that more than one collision will occur. These are called pile-up events and can be characterised by a Poisson distribution. The average number of collisions is thus:

$$< n >= \frac{L\sigma_{inelastic}}{f} \tag{2.3}$$

The number of pileup events per bunch crossing has grown significantly during the few years since the LHC has started taking data, see figure 2.2. The majority of processes involve low energy transfer and only low momentum hadrons. These are referred to as minimum bias events.

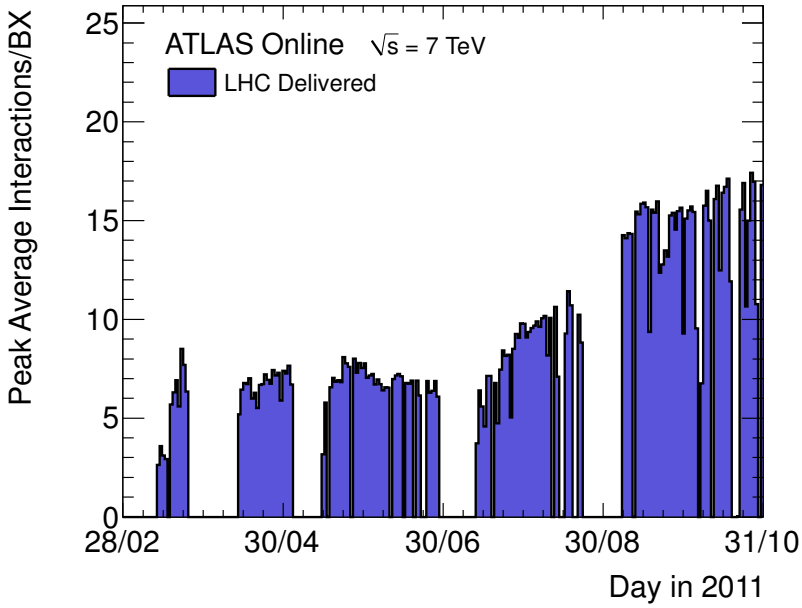

Figure 2.2: The mean number of interactions per bunch crossing at the peak of the fill for each day in 2011 for data used in physics analyses. The number of events per beam crossing is averaged over a short time period.

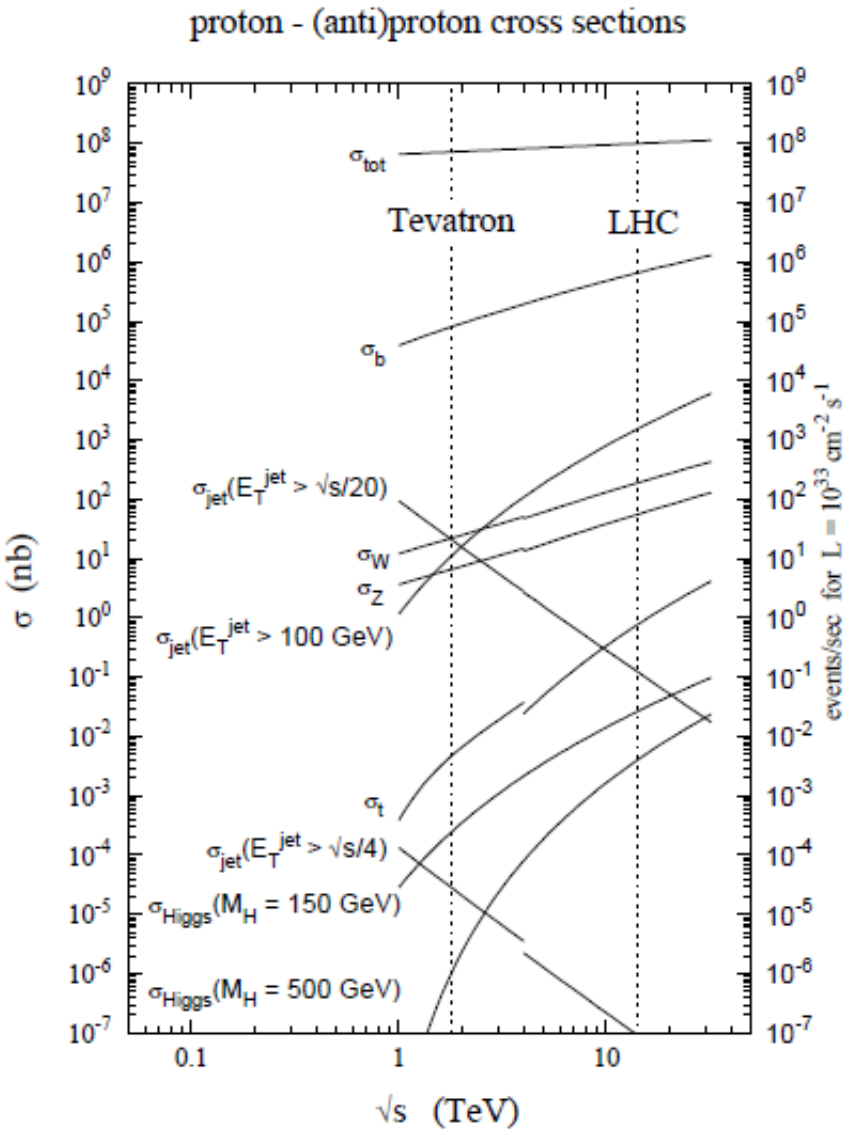

Figure 2.3: Prediction of the cross-section of the various physics processes in proton-proton collisions as a function of the centre-of-mass energy $\sqrt{s}$ [8]

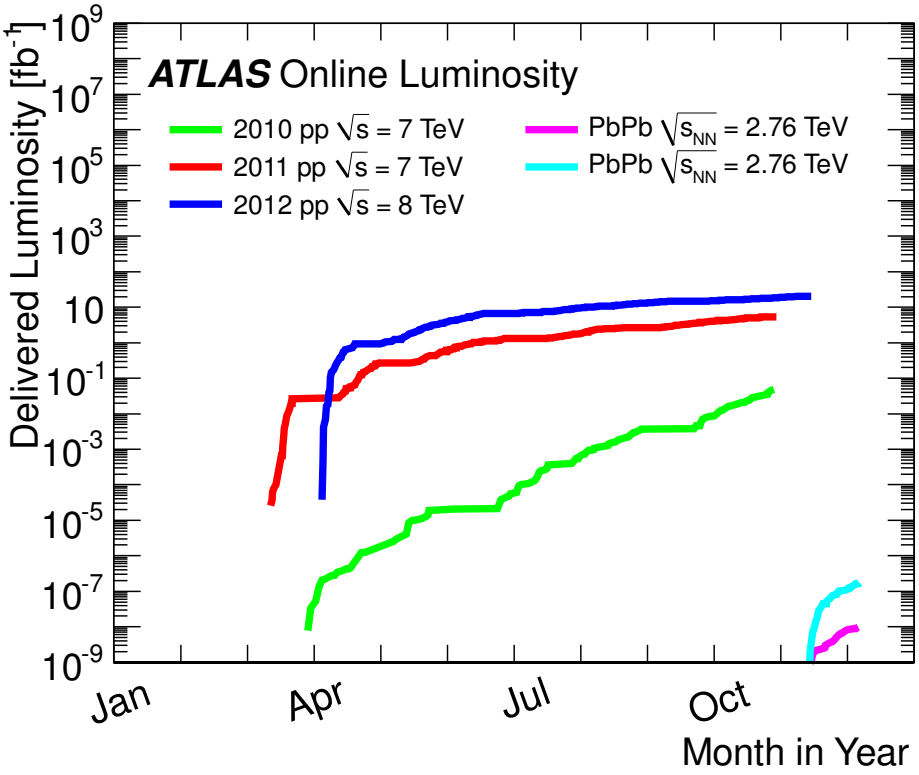

Figure 2.4: Delivered Luminosity versus time for 2010, 2011, 2012

Chapter 3

The ATLAS Detector

The ATLAS experiment is the largest of the LHC detectors and has the largest number of collaborators. It is the largest particle detector for a collider ever constructed, 45 metres long, 25 metres in diameter and weighs 7,000 tons. ATLAS is a general purpose detector and thus able to have its triggers set to many different physics signatures. The design requirements for the ATLAS detector are:

1. Efficient tracking, which allows full event reconstruction at low luminosity and identification of leptons, photons and heavy flavour jets at high luminosity.

2. High-precision muon momentum measurements using the muon spectrometer only at high luminosities.

3. Electromagnetic calorimetry for photon and electron identification and energy measurements, and hadronic calorimetry for jet and missing energy measurements.

4. The ability to trigger on both low p_T and high p_T particles, enabling selection of physics events with high efficiency.

5. Acceptance of high pseudo-rapidity values η and high azimuthal angle coverage ϕ (defined in section 3.1).

ATLAS is able to meet these requirements through a number of features: its *inner detector* which can produce high granularity tracking measurements;

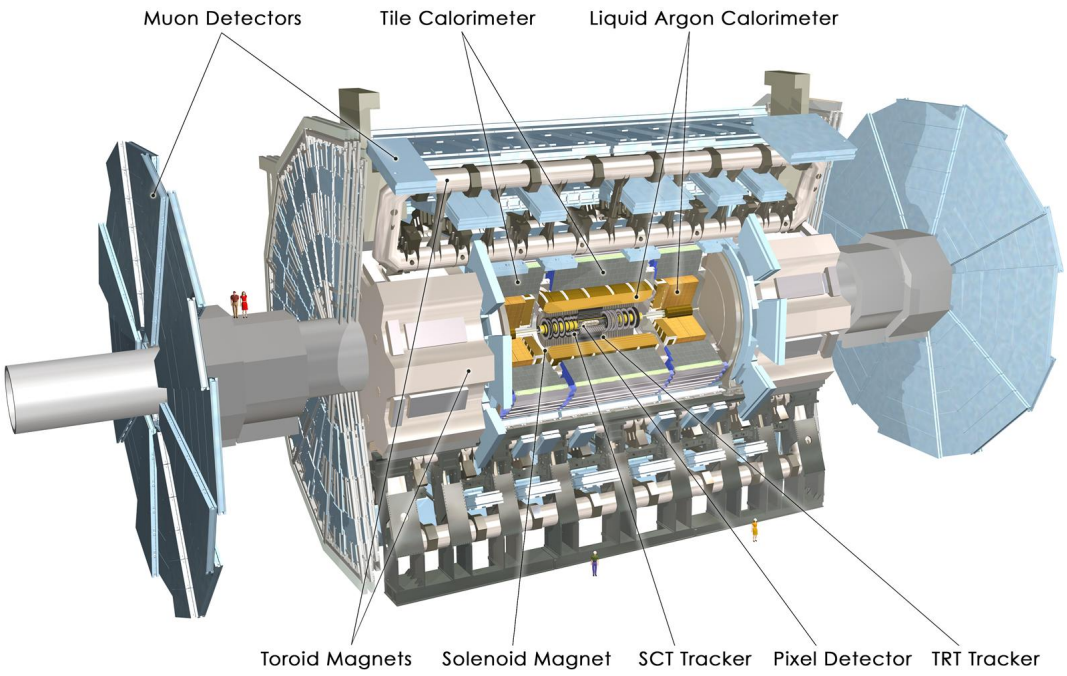

Figure 3.1: View of the ATLAS detector locating its main subsystems Figure provided by:[9]

electromagnetic and hadronic calorimeters with high granularity and excellent energy and position resolution; a full-coverage muon system that coupled with the 4 T field from the toroidal magnets allows for precise muon momentum measurements.

The detector also possesses a three-level highly selective and flexible fast trigger mechanism.

3.1 Nomenclature

The coordinate system and nomenclature used to describe the ATLAS detector and the particles emerging from the pp collisions are summarised here. The nominal interaction point is defined as the origin of the coordinate system, while the beam direction defines the z-axis and the $x - y$ plane is transverse to the beam direction. The x-axis is defined as a straight line from the interaction point to the centre of the LHC ring (positive closer to centre and negative further from the centre). The positive y-axis is defined as pointing up (towards the sky) from the interaction point [10]. The azimuthal angle ϕ is measured around the beam axis and the polar

angle θ is measured around the beam axis. The pseudo-rapidity η is given by

$$\eta = -\ln \tan \frac{\theta}{2}.$$

The beam (z-axis) is therefore at $\eta = \pm\infty$ and $\eta = 0$ is perpendicular to the beam.

While less often used, rapidity is defined as:

$$y = \frac{1}{2} \ln \left(\frac{E + p_z}{E - p_z} \right).$$

The transverse momentum, p_T, is defined in the xy plane. The distance ΔR in the pseudo-rapidity-azimuthal angle space is defined as $\Delta R = \sqrt{\Delta\eta^2 + \Delta\phi^2}$.

A track in ATLAS is parametrised at the point of closest approach to the z-axis using five *perigee parameters*:

- q/p - charge over momentum
- ϕ_0 the azimuthal angles of the tangent to the track at the point of closest approach to the nominal beam axis $(x, y) = (0, 0)$
- d_0, the transverse impact parameter - the minimum distance from the track to the nominal beam axis in the x, y plane. The sign of d_0 is positive when $\phi - \phi_0 = \frac{\pi}{2} \mod (2\pi)$, where ϕ denotes the angle to the perigee position in the x-y plane (visible in figure 3.2).
- z_0, the z-coordinate of the track at the point of closest approach to the beam axis.
- θ_0, the slope of the track in the rz plane.

Some of these parameters can be visualised in figure 3.2 where $\vec{p}$ is the total momentum of the track, $\vec{p_T}$ is the transverse momentum of the track.

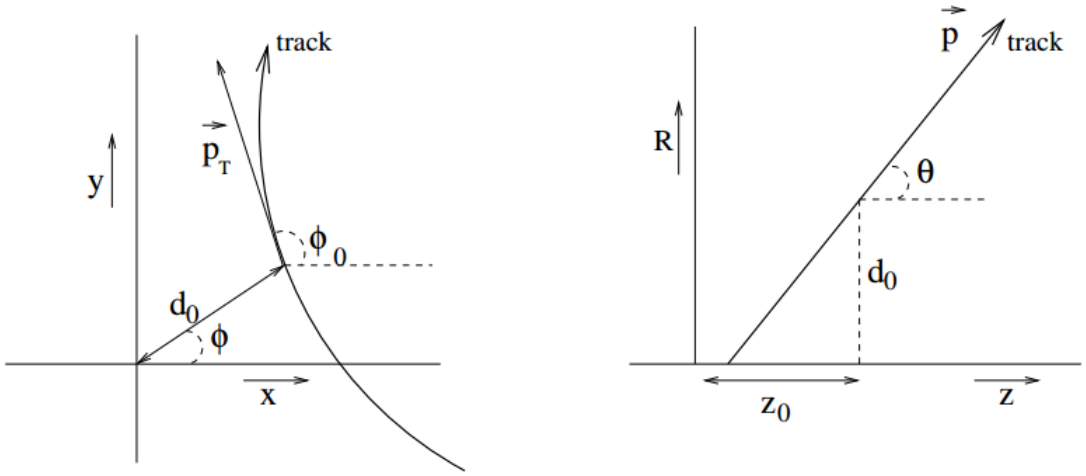

Figure 3.2: The perigee parametrisation used at ATLAS

3.2 Magnet System

Magnetic fields provide the opportunity for detectors to measure the momentum of charged particles. There are two magnetic systems in the ATLAS detector, the toroids and the central solenoid which are both operated at superconducting temperatures.

The central solenoid is cylindrical and contains the inner detector providing a central field of 2 T in the core of the inner detector, with a peak field of 2.6 T at the surface of the magnet. The outer and inner bore radii are 1.32 m and 1.22 m respectively and its length is 5.3 m. The total mass of the central solenoid assembly is 5.7 tonnes, and draws a current of 7.6 kA. Cooling is provided by liquid helium at 4.5 K [11].

The central solenoid is positioned away from the calorimetry to prevent material interfering with the particle tracks. This is aided by placing the central solenoid and the electromagnetic calorimeter into the same cryostat.

The toroid magnet system, which produces the field for the muon spectrometer, is comprised of a barrel toroid and end cap toroids. The barrel toroid consists of eight “race-track” coils which are arranged around the outside of the calorimetry in a “torus” assembly. Each coil has a length of 25.3 m and a width of 5.4 m. The total mass of the assembly is 830 tonnes and supplies a peak field of 3.9 T whilst

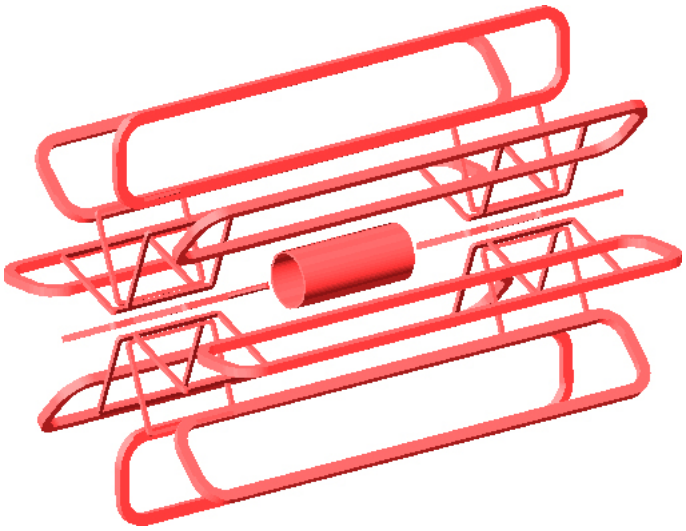

Figure 3.3: The toroid magnet system of ATLAS

drawing a current of 20.5 kA [11].

The two end-cap toroids are positioned beyond the forward hadronic calorimetry within the barrel toroid assembly. They produce a peak field of 4.1 T from a current of 20 kA, have a mass of 239 tonnes each and a radius of 5.4 m [11].

3.3 Inner Detector

The inner detector provides the most precise tracking information for making the high-quality measurements of momenta and locating primary and immediate secondary decay vertices. The inner detector is located within the central solenoid with a length of 7 m and a radius of 56 cm [12].

High precision measurements require the detection elements to be granular and very close to the interaction point. To accomplish this two semi-conducting pixel detectors and silicon micro-strips are used. This technology is expensive so to reduce cost these are strictly limited to regions of the highest track density. The key resolutions and efficiencies of the total inner detector system can be found in tables 3.2 and 3.3. The results shown for here for $H \rightarrow \gamma\gamma$ events are based on tracks reconstructed from the underlying event and do not make use of the measurement of the photon direction in the electromagnetic calorimeter. The primary vertex in $t\bar{t}$ events has always a rather large multiplicity and includes a number of high-p_T

tracks, resulting in a narrower and more Gaussian distribution than for $H \to \gamma\gamma$ events.

The **pixel detection** elements provide extremely fine granularity tracking close to the interaction point. It provides a very high granularity and high-precision set of measurements as close to the interaction point as possible. The system consists of three layers in the barrel module of the detector and four disks in the end-cap modules and has 80 million detector elements, each 50 μm in the $r\phi$ direction and the 400 μm in the z plane. The intrinsic resolution in the barrel are 10 μm in the $r\phi$ plane and 115 μm in z plane. For the end-caps the resolution is 10 μm $(r - \phi)$ and 115 μm (R). The maximal radius of the barrel layer is $\sim$ 12 cm and of the forward disk is $\sim$ 23 cm. However the most important layer to facilitate secondary vertex reconstruction is the layer closest to the beam pipe. This layer is $\sim$ 5 cm from the beam axis.

The **semi conductor tracker** (SCT) is a strip detector consisting of four barrel layers and nine forward wheels. The SCT system is designed to produce four precise measurements per track in the intermediate radial range and to contribute to the momentum, impact parameter and vertex position measurement. The four points are assured by eight silicon strip layers grouped into pairs with small angle (40 mrad) stereo strips to measure both coordinates. The strips are $\sim$ 6.4 cm long with typical distance between them 80 μm in the barrel; in the end-cap the strips are running radially but at similar average distance. In the barrel the inner most layers are at a radius of $\sim$ 30 cm, while the outer most at $\sim$ 51 cm. For the forward wheels the radius range is from $\sim$ 28 cm to $\sim$ 56 cm.

The **transition radiation tracker** (TRT) provides large numbers of hits (typically $\sim$ 36) per track using 4 mm diameter straw tubes, with length covering the pseudo-rapidity region $|\eta| < 2.0$. The TRT only provides $r - \phi$ information, reaching an intrinsic resolution of 130 μm per "straw". In the end-cap region the straws are arranged radially in wheels. The TRT detector is located at radii from $\sim$ 55 cm to 110 cm. TRT provides tracking information and electron identification

System	Position	Area (m^2)	Resolution $\sigma(\mu m)$	Channels (10^6)	η coverage ($\pm$)
Pixels	B layer	0.2	$r\phi = 12, z = 66$	16	2.5
	2 barrel layers	1.4	$r\phi = 12, z = 66$	81	1.7
	4 end-cap disks	0.7	$r\phi = 12, z = 77$	43	1.7-2.5
SCT	4 barrel layers	34.4	$r\phi = 16, z = 580$	3.2	1.4
	9 end-cap wheels	26.7	$r\phi = 16, z = 580$	3.0	1.4-2.5
TRT	Axial barrel straws		170 (per straw)	0.1	0.7
	Radial end-cap straws		170 (per straw)	0.32	0.7-2.5

Table 3.1: This table gives summary data on the sub-systems that make up the inner detector.

Track Parameter	$0.25 < \|\eta\| < 0.5$		$1.50 < \|\eta\| < 1.75$	
	$\sigma_X(\infty)$	p_X(GeV)	$\sigma_X(\infty)$	p_X(GeV)
Inverse transverse moment. (q/p_T)	0.34 TeV^{-1}	44	0.41 TeV^{-1}	80
Azimuthal angle (ϕ)	70 μ rad	39	92 μ rad	49
Polar angle ($\cot\theta$)	0.7×10^{-3}	5.0	1.2×10^{-3}	10
Transverse impact param. (d_0)	10μm	14	12μm	20
Longitudinal impact param. ($z_0 \sin\theta$)	91μm	2.3	71μm	3.7

Table 3.2: Extracted track-parameter resolutions. The momentum and angular resolutions are shown for muons, whereas the impact-parameter resolutions are shown for pions. The values are shown for two both the barrel and end-cap pseudorapidity regions. [13]

using the transition radius in the xenon-based gas mixture of the straw tubes. The use of these detectors in tandem provides very robust pattern recognition and high precision in both $r - \phi$ and z coordinates. Although the TRT has a lower precision per point than the two silicon detectors the longer measured track length assures significant contribution to the momentum measurement.

Event type	x-y resolution (μ m)	z resolution (μ m)	Reconstruction efficiency (%)	Selection efficiency (%)
$t\bar{t}$	11	40	100	99
$H \to \gamma\gamma$	14	66	96	79

Table 3.3: Primary Vertex resolutions (RMS) with beam constraints in the absence of pile-up. Also shown is the reconstruction and selection efficiency in the presence of pile-up at a luminosity of 10^{33} cm^{-2}s^{-1}. Only vertices reconstructed within $\pm 300\mu$m of the true vertex position in z are counted as passing reconstruction [13].

3.4 Calorimetry

Calorimeters measure the energy of a wide range of particles including electrons, photons, hadrons and jets. It is used in analyses to measure missing energy and low momentum muons, i.e. ones that cannot reach the muon detectors on the outside of ATLAS. The pseudo-rapidity coverage of the ATLAS calorimetry is $|\eta| < 4.9$ [14].

The ATLAS detector uses both an electromagnetic calorimeter and a hadronic calorimeter. Electromagnetic calorimeters usually terminate tracks of photons and electrons while hadronic calorimeters terminate tracks from isolated hadrons and jets.

The electromagnetic calorimeter comprises of lead/liquid argon detector electrodes and absorber plates. The barrel provides coverage in the pseudo-rapidity region $|\eta| < 1.475$. The length of each half-barrel is 3.2 m and the inner and outer radii are 2.8 m and 4 m respectively [14]. It is in two pieces with a 6 mm gap at z = 0. The barrel electromagnetic calorimeter shares the same cryostat with the central solenoid. The end-cap electromagnetic calorimeters are in two discs, the inner disc covering $2.5 < |\eta| < 3.2$ and the outer wheel covering $1.375 < |\eta| < 2.5$.

The hadronic calorimeter uses liquid argon technology for higher pseudo-rapidities. This area would be subjected to the most radiation so this design is chosen since it is intrinsically radiation hard. Plastic scintillators are used for areas expected to have less radiation ($|\eta| < 1.7$).

Data from the calorimeter is not used in my thesis except as a means for identifying low-p_T non-triggering muon tracks and providing information for the tagging.

3.5 Muon Detectors

The ATLAS muon detector system is especially important in this analysis as it also provides ATLAS with a trigger for selecting events containing high energy muons

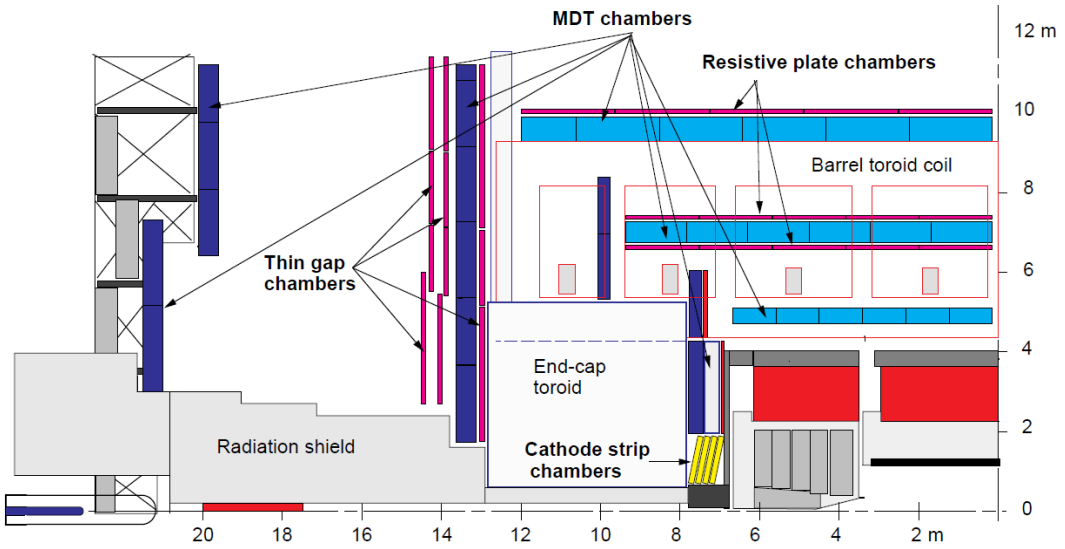

Figure 3.4: A view of a section of the muon spectrometer in the rz projection. Taken from [15]

such as in the decay $B_s^0 \to J/\psi\phi$. The muon momentum determination is based on the deflection of the tracks in the superconducting air-core toroid magnetic field and measured by separate muon chambers devoted for triggers and high-precision tracking.The barrel toroid provides the magnetic field for the range $|\eta| < 1.0$ and the end-caps cover the range $1.4 < |\eta| < 2.7$, while the region $1.0 < |\eta| < 1.4$ is covered by fields from the barrel and end-cap toroids. In the barrel region, the tracks are measured using chambers arranged in three cylindrical layers around the beam axis, while in the transition and end-cap regions, the chambers are installed in planes perpendicular to the beam in three layers. The technologies used in the detection elements differ depending on pseudo-rapidity and whether they are to be used for tracking or trigger decisions. Throughout most of the pseudo-rapidity range the detection elements used for tracking are muon drift tubes. For high η and close to the interaction point, highly granular cathode strip chambers are used. The trigger system, which covers the region $|\eta| < 2.4$, also uses two types of detector elements - resistive plate chambers in the barrel and thin gap chambers in the end-caps. These elements are covered in more detail in [15].

The layout of the muon system is detailed in diagrams in figures 3.4 to 3.6. The design provides almost full coverage catching most particles crossing the detector

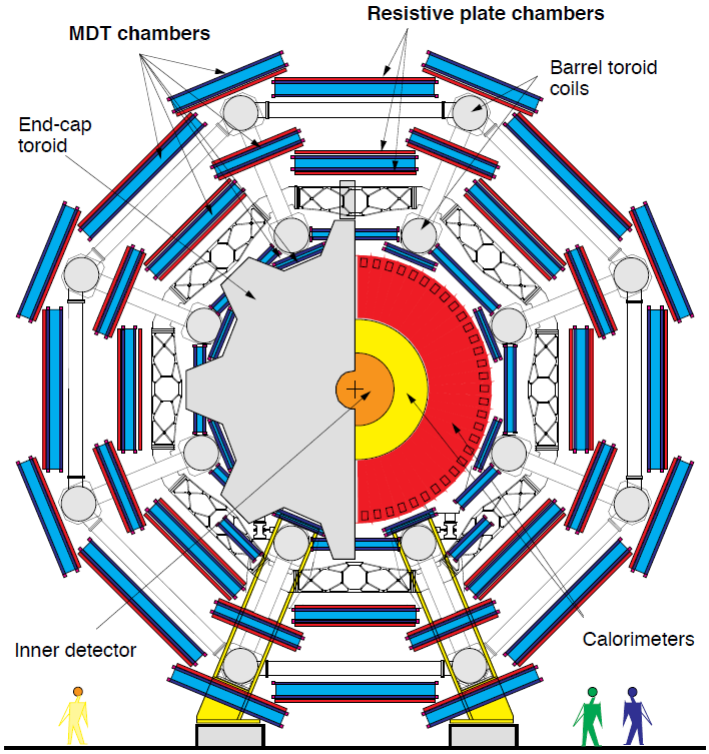

Figure 3.5: A transverse view of the spectrometer (xy plane). Taken from [15]

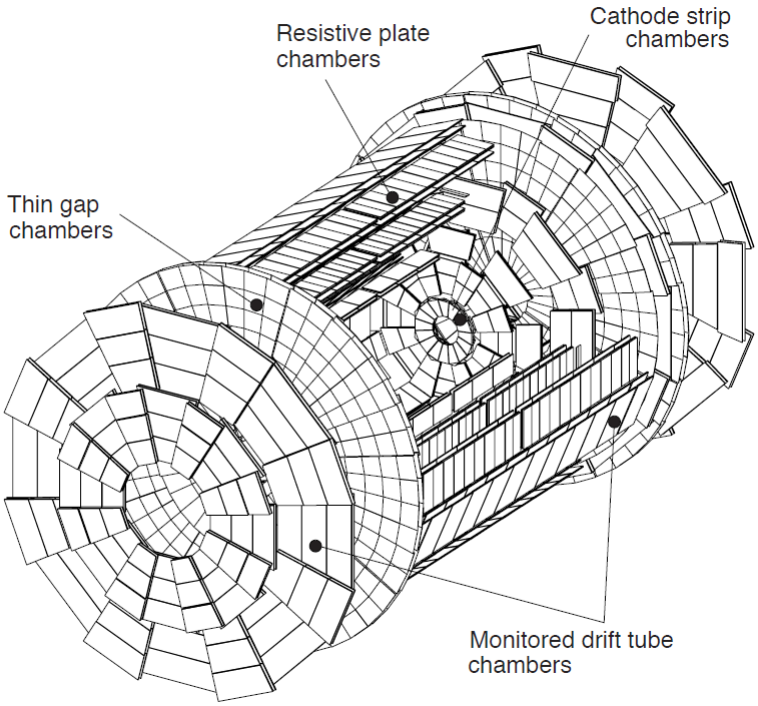

Figure 3.6: View of the muon spectrometer [15]

from the interaction point in three muon detector stations. The barrel chambers are arranged in three concentric cylinders with radii from 5 m to 10 m and the end-caps are in four disks at distances ranging from 7 m to 25 m from the interaction point. In the central $r\phi$ plane at $\eta = 0$ there is a gap to make room for cables from and to the inner detector, calorimetry and central solenoid.

3.6 Triggers

The ATLAS trigger system is required to reduce the collision rate of up to 40 MHz down to a few hundred Hz on average. Therefore it has to achieve approximately a 10^5 rejection factor while retaining as many of the interesting events as possible. An example of the composition of the triggered events in run 180636 from 2011 can be seen in figure 3.7. The trigger system has a three level structure: *Level 1* (L1), *Level 2* (L2) and *Event Filter* (EF), each level takes events passing the previous level and applies further criteria for selection. The L1 trigger is hardware based, L2 and the event filter are referred to as the *High Level Trigger* (HLT) that filters events using the ATLAS software framework. The data from all the detector subsystems is first written to the pipeline memory, at a rate peaking at 1 GHz. The pipeline memory circuit is located on the detector element read-out circuitry and inaccessible during data taking, as it must also operate in the high radiation environment of the LHC. Each subsystem has a customised design of pipeline memory associated with it, lacking uniformity across the detector. The data from the calorimetry and the muon chambers are then scanned by the level 1 trigger. This makes an initial selection based on reduced-granularity information from these two sub-detectors. High-p_T muons are identified through the use of the trigger muon chambers alone without using the precise muon tracking chambers. The full calorimeter is used, but with less granularity. The signatures that can activate ATLAS triggers are:

- muons of a sufficiently high p_T;

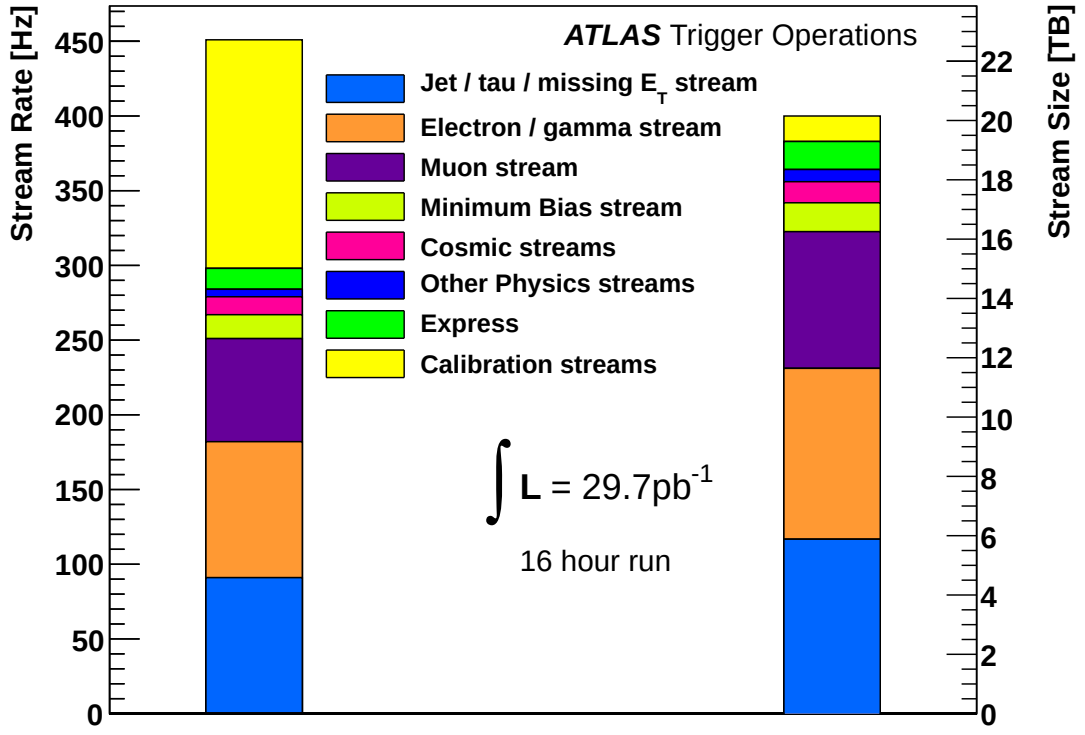

Figure 3.7: Data stream rates and sizes, separated into physics and calibration data for a given ATLAS run. This illustrates the ATLAS data composition in terms of number of taken events and size of the data in the data pipes and on tape. [16]

- electrons, photons and jets of sufficiently high p_T;
- missing transverse energies of sufficient magnitude.

The L1 triggers are implemented as custom electronics located inside the detector. These have programmable thresholds that are set according to the current luminosity conditions and the physics requirements decided for that particular run. Events passing the thresholds are then written to the read-out buffers which are also located within the detector and can contain up to 1700 events at one time. The L1 trigger should accept events at a rate of 75 kHz [17] but with safety factors this is closer to 40 kHz. The L1 trigger must have as short a latency as possible; the target is $2.0\mu s$ with a $0.5\mu s$ contingency [11]. This trigger must identify a bunch crossing, resolving the short time between them ($\sim$ 25 ns), which is also of the same order as the amount of time for muons to arrive at the muon trigger chambers from the interaction point.

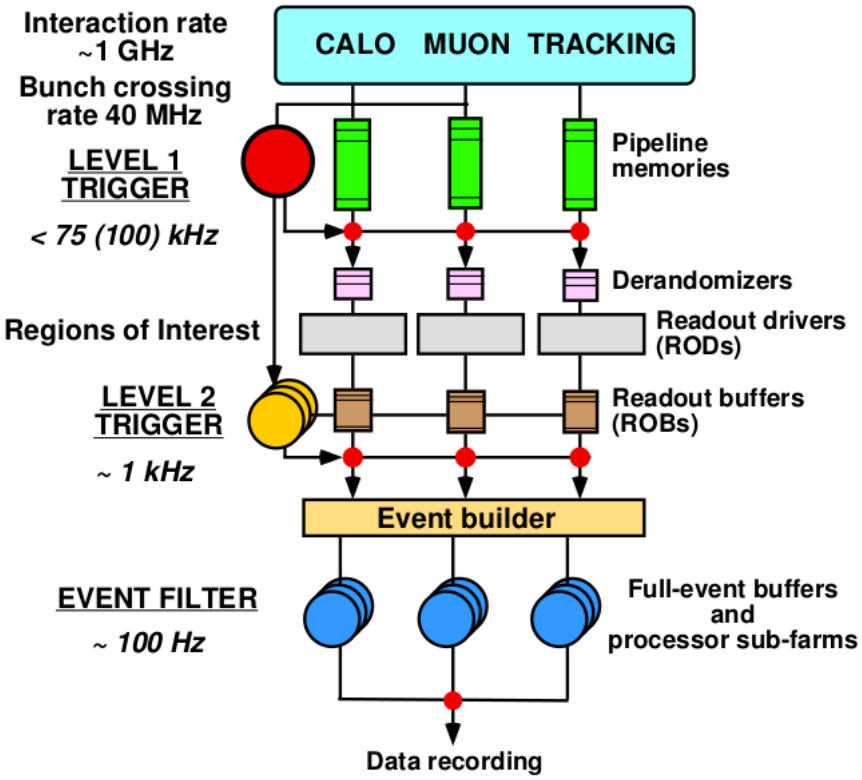

Figure 3.8: Diagram of the trigger system, taken from [11]

The L2 trigger scans the accepted events in the read out buffer, reading data from all subsystems at full granularity. The latency of the L2 trigger is reduced by only looking at regions of interest and is the lowest level of the high level trigger. To further improve latency the software is run on a processor farm close to the detector in an adjacent cavern. The L2 software verifies the decision from L1 and then makes additional rejections through additional or better calculated physical quantities and matching muon and calorimeter hits with inner detector tracks, requiring some inner detector track reconstruction. The average L2 processing time is 40 ms and the accepted event rate is reduced to 2 kHz at this stage. L2 processing nodes are standard computers connected to the central L2 switch through a set of switches. The actual data throughput per processing unit is small enough so that they can share switches. Inside a processing unit multiple threads are used to process events concurrently. Each thread handles one event at a time; when event data is accessed a thread sends out the request and then sleeps until all the data arrives; during this time another event is processed.

While L2 selection algorithms are optimised for timing performance, the event filter uses offline-like analysis tools for further event filtering. The EF algorithms needs several seconds to process, utilising complex pattern recognition algorithms and calibrations developed for offline processing, which allows additional event rejection. The output rate is 200 Hz. The high level trigger menu consists of around 700 types of different algorithms and their configurations (called L1-L2-EF trigger chains). The limited data storage means the trigger bandwidth must be appropriately assigned to the various ATLAS physics groups. Some of the chains must be reserved for calibrations and efficiency measurements. They consist of either dedicated supporting trigger algorithms or by reusing physics-oriented algorithms with looser criteria in the selection, or by having chains configured in the passthrough mode where the event will be recorded regardless of the trigger decision. To avoid consuming too much of the bandwidth this way, these calibration triggers are limited by prescaling - only accepting every n-th event that passes the criteria. Prescaling and passthrough recording can be applied on any of the three trigger levels. Prescaling often had to be introduced as the LHC increased its luminosity during the data taking in the first years of operation.

3.7 B-Physics Triggers

ATLAS can write to permanent storage 200 events per second. The amount dedicated to recording events of interest to the B-Physics group can vary but has typically been 20 events per second. The B-physics program is focused on the decay channels that can be clearly distinguished by the ATLAS trigger system. The $b\bar{b}$ events are of relatively low p_T compared to other processes studied at ATLAS. B-hadron decays have daughter tracks of a few GeV, leaving calorimetry information inappropriate for the analysis as it would be dominated by background. Triggering on hadron or electron final states would therefore only be possible at very low luminosities at which the LHC will not run for the majority of operation. The ATLAS B-physics group is thus dependent on muonic final states; in B-decays

these typically come from a $J/\psi \to \mu^+\mu^-$ intermediate decay. The B-trigger system is composed of algorithms searching for the following:

- **Single or two muon events** of various p_T thresholds. These events are common and thus must be prescaled heavily at high luminosities. These serve as control and calibration triggers as they are the least complicated and inefficient at selecting interesting events.

- **Di-muon vertex** This is the main type of trigger for ATLAS B-physics. Instead of just requiring two muons it requires that they appear to originate from a common vertex thus eliminating much of the background.

- **Multi Di-muon vertex** triggers are devoted to finding muon and J/ψ or multi-J/ψ events.

- $B \to \mu^+\mu^- X$ **reconstruction** triggers used for semileptonic rare B-hadron decays $B \to \mu^+\mu^- X$, include a search for particles like K^{*0} or ϕ combined with the di-muon vertex.

- $J/\psi \to e^+e^-$ triggers can only be used at low luminosities because of the high background of this decay.

- $D_s \to \phi\pi + \mu$ triggers are also only usable at low luminosities.

A requirement of two muon candidates with certain p_T thresholds and originating in a common vertex is one of the most important commonly used triggers in the B-physics programme at ATLAS. There are four types of these triggers currently in use. They are tuned for different luminosity levels by imposing different requirements on muon identification.

The topological di-muon trigger is the basic algorithm for the nominal luminosities. At L1 this requires two muon signatures. L2 confirms the two muons using the precision chambers, producing corresponding muon spectrometer tracks using an algorithm called *muFast*. The *IDSCAN* algorithm is then used to reconstruct inner detector tracks within the muon L1 regions of interest; the inner detector

and muon spectrometer tracks are then combined using the *muComb* algorithm [13]. Since the majority of muons coming from $b\bar{b}$ events produce relatively low p_T muons the inner detector contributes the most to the precision of combined muons. The L2 also fits the two muon tracks to a common vertex using an algorithm based on the Kalman filter. If the quality of the vertex is too poor or the invariant mass of the di-muon is outside a preselected mass window then the event is rejected. The event filter level repeats the analysis at L2 but using similar tools used in offline analysis for greater precision. Requirements at L1 and L2 combined with the material of the calorimetry blocking low p_T muons mean that the majority of muons selected have greater than 4 GeV momentum transfer.

These topological di-muon algorithms exist in several configurations. The most basic variable is the p_T threshold of the muon track, which is necessarily connected to the decision preprogrammed in the L1 hardware. For instance, in 2010 the only thresholds used at L1 were 4 GeV and 6 GeV, which could then be used in combination at higher levels. The next most common parameter to use is the selected di-muon invariant mass window. The B-physics group utilises the following windows; these intervals are chosen to account for the mass resolution of the L2 trigger processor:

- (2.5 - 4.3) GeV: for J/ψ events.
- (8.0 - 12.0) GeV: for Υ events
- (4.0 - 8.5) GeV: for rare $B^0_{s,d} \to \mu^+\mu^-$ decays
- (1.5 - 14.0) GeV: A window covering the whole B-physics region to include non-resonant semileptonic rare B-decays, $B \to \mu^+\mu^- X$

The $B^0_s \to J/\psi\phi$ analysis is reliant on the Di-muon triggers designed for J/ψ events; single muon triggers can also contribute, but to a lesser extent.

Chapter 4

Theory

4.1 The Standard Model

At the end of the 19th Century the atom was thought to be a solid object made up of negatively charged areas embedded in a positively charged sphere. This idea was eventually rejected due to the results of Ernest Rutherford's analysis of the scattering angles of α particles fired at a thin gold foil; the atom must have a nucleus several order of magnitude smaller than its total size [18]. Since then discoveries about the structure of the atom have revealed its fundamental particles and further particles that are never assembled into atoms. The theory describing these forms of matter and the forces governing them is called the *Standard Model*[1] [19]. While this model has a variety of problems there are only a few completely conclusive empirical finding that is incompatible with it - such as the discovery of neutrino masses.

The elementary particles making up the Standard Model include fermions (defined as a particle with a half-odd spin), which are further divided into the two categories: quark and leptons. Fermions have been found to come in at least three generations and appear to increase mass with each generation. Leptons have integer electric charge and the electric charge of quarks is fractional (in terms of 1 or 2 thirds). These fermions are summarised in table 4.1. Interactions between

[1] of particle physics - not cosmology or of the sun

Particle	Charge	I	mass/c^2	II	mass/c^2	III	mass/c^2
Lepton	-1	e	0.511 MeV	μ	105.658 MeV	τ	1776.84 MeV
	0	ν_e	< 2.25 eV	ν_μ	< 0.19 eV	ν_τ	< 18.2 eV
Quarks	+2/3	u	1.5-3.3 MeV	c	$1.27^{+0.07}_{-11}$ GeV	t	171.3 ± 1.63 GeV
	-1/3	d	3.5-6.0 MeV	s	105^{+25}_{-35} MeV	b	$4.2^{+0.27}_{-0.07}$ GeV

Table 4.1: Properties of fermions [20]

fermions are mediated by bosons, particles that can be thought to carry force and possess an integer spin. The forces of the Standard Model include the strong, weak and electromagnetic forces. The gravitational force is not included in the model.

4.1.1 Quarks and leptons

The fundamental fermions are spin-1/2 particles, each has an antiparticle of equal mass and lifetime but opposite electric charge. Paul Dirac predicted the existence of antimatter in 1931 as an interpretation of the negative energy solutions to the relativistic relation between energy, momentum and the mass of a particle. The 20$^{\text{th}}$ Century saw the prediction and observation of almost all of the fundamental particles of the Standard Model, a notable exception being the Higgs boson. The search for and subsequent discovery of the Higgs boson was one of the main goals of the LHC at CERN and a crucial test of the Standard Model.

Normal matter is only made up of the lightest fermion generation. This is mainly due to the fact the higher generations are too short lived to survive as components of matter. The electron was first discovered in 1896 by J.J. Thompson in cathode ray experiments [21], which demonstrated amongst other things that the atom was not indivisible.

Leptons have been observed as existing as free moving independent objects, however quarks appear to only exist in bound states in conventional circumstances. This is accounted for in the Standard Model by the notion of colour charges, which are acted on by the strong force. Quarks possess this attribute but leptons do not. The strong force binds quarks in hadron states; baryons contain three quarks and mesons contain two. Both types combine quarks in a way that the hadron has

integer electric charge and neutral colour charge.

The first generation quarks are called up and down, which make up the constituents of neutrons and protons. Other hadrons can be formed from combinations of the heavier quarks but as mentioned these decay in a length of time on the order of a picosecond; the results of the decay are usually lighter stable states. Hadrons containing top quarks have not been observed as the top quark lifetime is too short to form a hadron.

Strange particles that make up the second generation were first detected in cloud chamber tracks of cosmic rays in 1946, with the decay of the neutral kaon ($\bar{s}d$ or $s\bar{d}$) into two charged pions ($u\bar{d}$, $\bar{u}d$) [22]. The "strangeness" of these particles came from them being produced and decaying in greatly different time scales. This behaviour was accommodated by introducing a new quantum number; the strange particles were observed as being produced in pairs so if the pair had opposite "strangeness" (S=+1, S=-1) then this quantum number is conserved.

As more hadrons were discovered, it seemed implausible that there were so many independent elementary particles. Physicists sought to identify unifying patterns such as those presented by Mendeleev in the periodic table. In 1961, Murray Gell-Mann suggested the Eight-Fold way which places the known hadrons into octets according to their charge and strangeness quantum numbers [23]. This was later explained by the suggestion that they were composed of lighter elementary particles which he called quarks.

Charmonium, the $c\bar{c}$ resonance, was discovered in e^+e^- in 1974 at both SLAC [24] and BNL [25], which brought the quark model into good agreement with the experimental lepton sector. At the time only the first two generations of particles were known but that symmetry was broken after the discovery of the τ lepton. Quarks of the third generation were predicted by Kobayashi and Maskawa [26]. This was experimentally confirmed in 1977 when Fermilab observed a *bottomonium* state [27]. Naturally the existence of the *top* quark, up-type partner to the b quark was entirely expected, but not discovered until 1995 at Fermilab [28]. It took so

Force	Name	Mass	Spin	Coupling Strength
Strong	gluons	0	1	0.01 to 1
Weak	$W^{\pm}$	80 GeV/c^2	1	10^{-5} GeV^{-2}
	Z^0	91 GeV/c^2	1	
EM	photon	0	1	1/137

Table 4.2: The fundamental forces in the Standard Model

long because the top quark has a significantly higher mass than any of the other quarks.

There is no evidence thus far of a fourth generation. Some models predict further generations and they are not completely excluded since there are existing uncertainties in the CKM matrix.

4.1.2 Forces

The fundamental forces in the Standard Model describe the interactions of the fermions by the exchange of mediators called bosons. These are summarised in table 4.2.

Electromagnetic (EM) interactions bind electrons with nuclei in atoms and molecules, and are responsible for intermolecular forces. The mediator boson of the electromagnetic force is the photon, the massless particle that interacts with all electrically charged particles. Interactions of this type are described in the Quantum ElectroDynamics (QED) theory which is a gauge invariant field theory with symmetry group U(1). The coupling strength of the EM force is given by the constant α in terms of the electric charge e and Planck's constant $\hbar$:

$$\alpha = \frac{e^2}{4\pi\hbar c} \tag{4.1}$$

The classical EM potential between elementary charges at distance r (the Coulomb potential) is:

$$V_{em} = -\frac{\alpha}{r}$$

This demonstrates that the range of the electromagnetic force is infinite but

decreases rapidly with distance.

The Strong force allows bonding of neutrons and protons in the atomic nucleus and quarks within general hadrons. Gluons, the massless bosons mediate this force. Gluons only act on *colour*[2] charge like photons only act on electromagnetic charge. Quarks carry one of three possible colour charges, while antiquarks carry one of three possible anticolours. A stable hadron is formed if an object of a composite colour charge of zero (or *white*) can be formed, such as a meson of a quark and anti quark ($q_i\bar{q_i}$) or a baryon of three quarks ($q_r q_b q_g$). An important difference between QED and QCD is that gluons themselves carry colour charge, whereas photons are not charged. Gluons carry one colour and one anticolour, and as they act on colour charge they can interact between themselves. With three colour charges and three anti colours, it would be expected that there could be 3^2 gluons, but one is a colourless singlet state, so there are eight interacting gluons. Quark confinement is the phenomenon that occurs when an attempt is made to separate two quarks; there comes a point when it would take less energy to form a new $q\bar{q}$ than to resist the pulling which occurs.

Both quarks and leptons undergo weak interactions. This interaction is three orders of magnitude smaller than the electromagnetic interaction making them very rare compared to electromagnetic and strong interactions. Weak interactions occur with neutrinos and can also cause flavour changes between quarks which cannot happen with strong interactions. Weak interactions are mediated by $W^{\pm}$ and Z^0 bosons. Electroweak theory unifies the weak and electromagnetic forces as first suggested in the 1960s by Glashow, Weinberg and Salam.

4.1.3 Conservation Laws and Symmetries

The Standard Model along with many other physical models are built on symmetries, which are invariant under certain transformations. The **parity** operator, P, transforms a wave function in the following manner.

[2]nothing to do with visible colour

$$P\psi(\mathbf{r}) = \psi(-\mathbf{r}) \tag{4.2}$$

where $\mathbf{r}$ is the spatial position vector. Applying this operator a second time returns the function to its original state. Thus $P^2 = 1$ and it has the eigenvalues $P = \pm 1$. **Parity invariance** was considered to be a fundamental law until Lee and Yang found that there was no evidence that weak interactions conserved parity. Weak interactions were then tested by C. S. Wu using Cobalt 60 nuclei [29]. This was done by aligning the spins of the nuclei with a magnetic field, and the direction of the emitted electron was measured. They showed the majority of electrons were emitted opposite to the direction of the spin of the nuclei and therefore demonstrated parity violation in the weak interaction. The violation is most evident in neutrino physics where it is observed that all neutrinos are left handed and all antineutrinos are right handed.

Charge conjugation is an operator that reverses the electric charge and magnetic moment of a particle. Classical electrodynamics is invariant under this operation. In terms of quantum mechanics this operator also changes the sign of all internal quantum numbers, such as lepton number and strangeness, converting it to those of the antiparticle.

$$C|p\rangle = |\bar{p}\rangle. \tag{4.3}$$

As in the case of the neutrino this operator would fail in creating an antineutrino as it would not flip the handedness of the particle; on its own it would create an empirical impossibility. This demonstrates that nature is not always invariant under the C transformation.

To rectify this case the operators were combined into a CP transformation (**Charge Parity**) which would successfully convert a neutrino into an antineutrino. This seemed to fix the violations that occurred with the C and P operators individually.

Charge Parity time (CPT) theorem states that under the operation of time reversal, parity and charge conjugation there is an exact symmetry for any interaction. This is a fundamental principle in quantum field theory. Violation of this symmetry would invalidate most theories and models in mainstream physics.

4.2 CP Violation

Of the many discrete symmetries observed in particles physics, the three essential for defining CP violation are charge conjugation (C), parity transformation (P) and time reversal (T).

Combining C and P transformations gives the CP symmetry which describes a particle changing to its anti-particle state and the parity transformation. If CP was not violated particles physics would proceed identically for matter and antimatter. Most phenomena are symmetric separately under C and P transformations, which is why the consideration of the combined symmetry was not considered until violations of the individual symmetries were found during study of the weak interaction. The weak interaction was found to violate C and P symmetries separately, so theorists proposed that the combined CP transformation must be a fundamental symmetry. However, this was found to be violated in the decay of neutral kaons in 1964 [2] and more recently in B decays.

CP violation is accommodated in the Standard Model through a complex phase in the Cabibbo-Kobayashi-Maskawa (CKM) matrix. The CKM matrix relates the flavour eigenstates to the mass eigenstates. This in part describes the processes by which flavour changing weak decays occur. Provided no additional generations of quark are discovered, the matrix is believed to be unitary. It is defined as:

$$\begin{pmatrix} d' \\ s' \\ b' \end{pmatrix} = \begin{bmatrix} |V_{ud}| & |V_{us}| & |V_{ub}| \\ |V_{cd}| & |V_{cs}| & |V_{cb}| \\ |V_{td}| & |V_{ts}| & |V_{tb}| \end{bmatrix} \begin{pmatrix} d \\ s \\ b \end{pmatrix} \tag{4.4}$$

where q' are the flavour eigenstates and q are the mass eigenstates. The

probability of a transition from a q_1 to q_2 is porportional to $\mid V_{q_1 q_2} \mid^2$. One of the standard parametrisations of the CKM matrix shows the mixing angles and CP-violating phase:

$$\begin{bmatrix} 1 & 0 & 0 \\ 0 & c_{23} & s_{23} \\ 0 & -s_{23} & c_{23} \end{bmatrix} \begin{bmatrix} c_{13} & 0 & s_{13}e^{-i\delta_{13}} \\ 0 & 1 & 0 \\ -s_{13}e^{i\delta_{13}} & 0 & c_{13} \end{bmatrix} \begin{bmatrix} c_{12} & s_{12} & 0 \\ -s_{12} & c_{12} & 0 \\ 0 & 0 & 1 \end{bmatrix} \tag{4.5}$$

$$= \begin{bmatrix} c_{12}c_{13} & s_{12}c_{13} & s_{13}e^{-i\delta_{13}} \\ -s_{12}c_{23} - c_{12}s_{23}s_{13}e^{i\delta_{13}} & c_{12}c_{23} - s_{12}s_{23}s_{13}e^{i\delta_{13}} & s_{23}c_{13} \\ s_{12}s_{23} - c_{12}c_{23}s_{13}e^{i\delta_{13}} & -c_{12}s_{23} - s_{12}c_{23}s_{13}e^{i\delta_{13}} & c_{23}c_{13} \end{bmatrix} \tag{4.6}$$

$s_{ij} = \sin\theta_{ij}$, $C_{ij} = \cos\theta_{ij}$ and δ is the KM phase responsible for all CP violation in flavour changing processes in the established Standard Model.

Another useful parameterisation of the CKM matrix is the Wolfenstein variant. It is known from experiment $s_{13} \ll s_{23} \ll s_{12} \ll 1$. Using this information the mixing angles and CP violating phase can be described as:

$$s_{12} = \lambda \tag{4.7}$$

$$s_{23} = A\lambda^2 \tag{4.8}$$

$$s_{13}e^{i\delta} = A\lambda^3(\rho + i\eta) \tag{4.9}$$

The CKM matrix can then be written as:

$$V_{CKM} = \begin{bmatrix} 1 - \lambda^2/2 & \lambda & A\lambda^3(\rho - i\eta) \\ -\lambda & 1 - \lambda^2/2 & A\lambda^2 \\ A\lambda^3(1 - \rho - i\eta) & -A\lambda^2 & 1 \end{bmatrix} + \mathcal{O}(\lambda^4) \tag{4.10}$$

This leads to twelve equations, which can be separated into six normalisation relations and six orthogonality relations. The six orthogonality relations can be

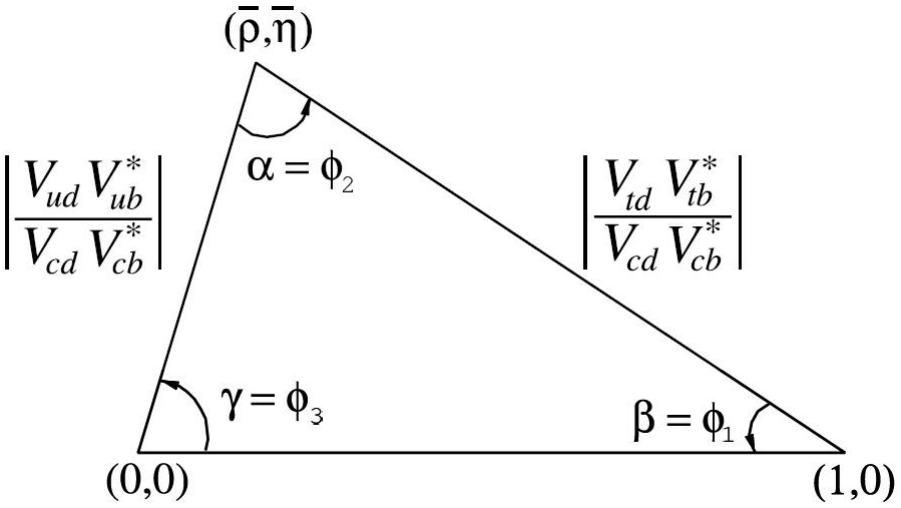

Figure 4.1: Figure showing the first CKM triangle

represented geometrically as six triangles in the complex plane. Each of these unitary triangles has the same area related to the size of the CP violation phase. Four of these triangles have one side suppressed relative to the other by $\mathcal{O}(\lambda^2)$ or $\mathcal{O}(\lambda^4)$. The remaining two triangles have all their sides of $\mathcal{O}(\lambda^3)$. The two orthogonal relations left are:

$$V_{ud}V_{ub}^* + V_{cd}V_{cb}^* + V_{td}V_{tb}^* = 0 \tag{4.11}$$

$$V_{ud}^*V_{td} + V_{us}^*V_{ts} + V_{ub}^*V_{tb} = 0 \tag{4.12}$$

In this parametrisation to $\mathcal{O}(\lambda^3)$ these two equations agree to leading order. These lead to triangles that are often referred to as the unitary triangles of the CKM matrix (see figures 4.1 and 4.2). The CP violating phase ϕ_s is found in this triangle due to the relation $\phi_s = 2\beta_s$. The LHC is expected to have the experimental accuracy to distinguish between these equations and next-to-leading order terms will have to be taken into account.

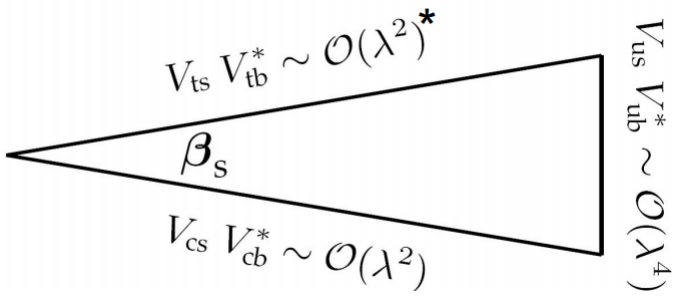

Figure 4.2: Figure showing the second CKM triangle

4.3 Neutral B_s mixing

Neutral B_s mixing refers to the oscillation between $B_s \leftrightarrow \bar{B}_s$ resulting from flavour non-conservation in weak decays and can be seen in figure 4.3. We see that mixing occurs in a single loop and it is a flavour changing neutral current process making it dependent on the mass of both fermions and the Yukawa couplings.

B_s mixing can be presented in quantum mechanical notation [30], describing a superposition of B_s and $\bar{B}_s$ states.

The time evolution of the $B_s \leftrightarrow \bar{B}_s$ system is described by the time dependent Schrodinger equation:

$$i\hbar\frac{\partial}{\partial t}\Psi = \mathbf{H}\Psi \tag{4.13}$$

The complex Hamiltonian can be expressed as a sum of two hermitian matrices.

$$\boldsymbol{M} = \begin{pmatrix} M_{11} & M_{12} \\ M_{12}^* & M_{22} \end{pmatrix}, \boldsymbol{\Gamma} = \begin{pmatrix} \Gamma_{11} & \Gamma_{12} \\ \Gamma_{12}^* & \Gamma_{22} \end{pmatrix} \tag{4.14}$$

The Hamiltonian can be simplified if either CP or CPT is conserved. Assuming CPT conservation then $M_{11} = M_{22} = M$. When limited to the Standard Model M_{12} and Γ_{12} are determined to leading order precision by box diagrams. In the B_s system these eigenstates are defined as B_L and B_H for the light and heavy state respectively.

$$|B_L\rangle = p|B_S\rangle + q|\bar{B}_S\rangle \tag{4.15}$$

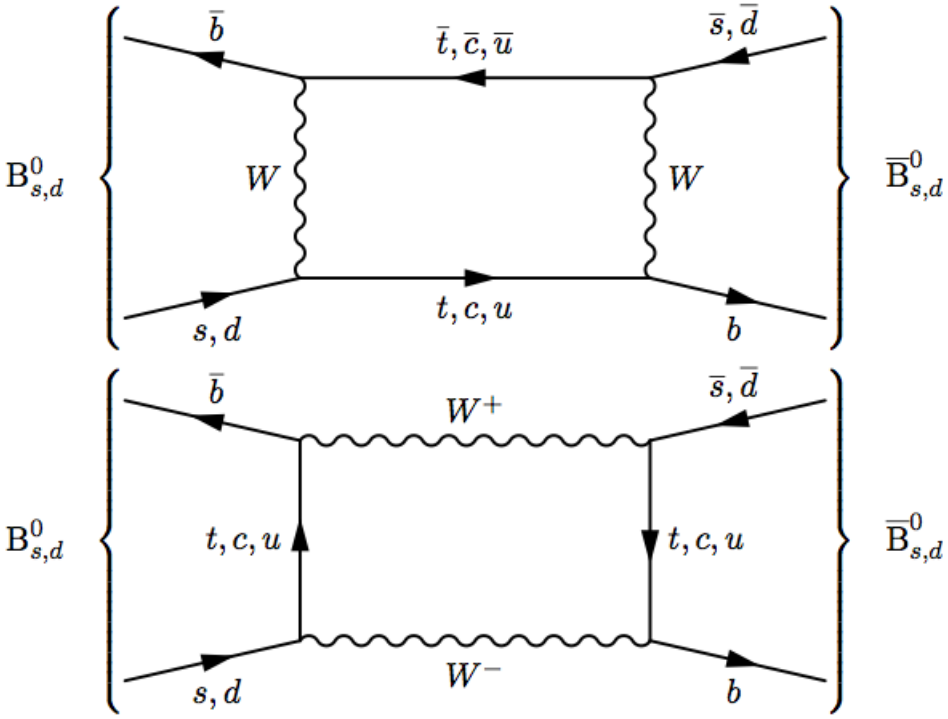

Figure 4.3: Box diagrams showing B_S mixing

$$|B_H\rangle = p|B_S\rangle - q|\bar{B_S}\rangle \tag{4.16}$$

which is normalised to $|p|^2 + |q|^2 = 1$, with eigenvalues:

$$M_L - \frac{i}{2}\Gamma_L = M - \frac{i}{2}\Gamma + \frac{q}{p}\left(M_{12} - \frac{i}{2}\Gamma_{12}\right) M_H - \frac{i}{2}\Gamma_H = M - \frac{i}{2}\Gamma - \frac{q}{p}\left(M_{12} - \frac{i}{2}\Gamma_{12}\right) \tag{4.17}$$

where

$$\frac{q}{p} = \pm\sqrt{\frac{M^*_{12} - \frac{i}{2}\Gamma^*_{12}}{M_{12} - \frac{i}{2}\Gamma_{12}}} = \sqrt{\frac{H_{21}}{H_{12}}} \tag{4.18}$$

The ambiguous sign depends on whether the heavy or light eigenstate is chosen. The real and imaginary parts of the eigenvalue $\omega_{L,H}$ corresponding to $|M_{L,H}\rangle$ represent their masses and decay width. The differences between the eigenstates are:

$$\Delta m_s \equiv m_H - m_L = \mathbf{Re}(\omega_H - \omega_L) \tag{4.19}$$

$$\Delta\Gamma_s \equiv \Gamma_L - \Gamma_H = -2\mathbf{Im}(\omega_H - \omega_L) \tag{4.20}$$

Here Δm is positive by definition, but the sign of $\Delta\Gamma$ is unrestricted in principle. The Standard Model predicts this to be positive and was confirmed by LHCb in [31]. For this reason it is often defined as $\Delta\Gamma = \Gamma_L - \Gamma_H$.

4.4 Time evolution

The mass eigenstates have a simple exponential evolution in proper time t:

$$|B_L(t) = e^{-i(M_L - \frac{i}{2}\Gamma_L)t}|B_L(0)\rangle, \tag{4.21}$$

$$|B_H(t) = e^{-i(M_H - \frac{i}{2}\Gamma_H)t}|B_H(0)\rangle. \tag{4.22}$$

The phase factor has no effect on measurable quantities, so for our approximation it can be discarded. The time evolution of pure B_s and $\bar{B_s}$ can be calculated by solving equation 4.16 for B_s or $\bar{B_s}$ and then using the time evolution equations. The result is:

$$|B_s(t) = g_+(t)|B_s(0)\rangle + \frac{q}{p}g_-(t)|\bar{B}_s(0)\rangle \tag{4.23}$$

$$|\bar{B}_s(t) = g_+(t)|\bar{B}_s(0)\rangle + \frac{q}{p}g_-(t)|B_s(0)\rangle \tag{4.24}$$

where:

$$g_\pm = \frac{1}{2}e^{-\frac{\Gamma t}{2}}e^{-iMt}\left(\cosh(\frac{\Delta\Gamma_s}{2}t) \pm \cos(\Delta M_s t)\right) \tag{4.25}$$

The amplitudes for B mesons can be defined in the following way:

$$A_f = \langle f|H|B_s(0)\rangle, \qquad \bar{A}_f = \langle f|H|\bar{B}_s(0)\rangle \tag{4.26}$$

$$A_{\bar{f}} = \langle \bar{f}|H|B_s(0)\rangle, \qquad \bar{A}_{\bar{f}} = \langle \bar{f}|H|\bar{B}_s(0)\rangle \tag{4.27}$$

where f or $\bar{f}$ are the final state. The ratio of the amplitudes can be defined as:

$$\rho = \frac{A_f}{\bar{A}_f} = \frac{1}{\bar{\rho}} \tag{4.28}$$

The amplitude can therefore be written:

$$A_{B_s(t)\to f} = g_+(t)A_f + \frac{q}{p}g_-(t)\bar{A}_f \tag{4.29}$$

$$A_{\bar{B}_s(t)\to f} = g_+(t)\bar{A}_f + \frac{q}{p}g_-(t)A_f \tag{4.30}$$

The time-dependent decay rate $\Gamma(B_s(t) \to f)$ of an initially tagged B_s into some final state f is defined as

$$\Gamma(B_s(t) \to f) = \frac{1}{N_B}\frac{dN(B_s(t) \to f)}{dt} \tag{4.31}$$

where $B_s(t)$ represents a meson at proper time t tagged as a B_s at $t = 0$, $dN(B_s(t) \to f)$ denotes the number of decays of $B_s(t)$ into the final state f occurring within the time interval $[t, t + dt]$, N_B is the total number of B_s's produced at time $t = 0$.

The branching ratios are calculated by taking the modulus squared of the amplitudes [32].

$$\begin{aligned}\Gamma(B_s(t) \to f) =& N_f e^{-\Gamma t}[(|A_f|^2 + |\frac{q}{p}\bar{A}_f|^2)\cosh\frac{\Delta\Gamma_s t}{2} + (|A_f|^2 - |\frac{q}{p}\bar{A}_f|^2)\cos\Delta M_s t \\ &+ 2\mathcal{R}(\frac{q}{p}A_f^*\bar{A}_f)\sinh\frac{\Delta\Gamma_s t}{2} - 2\mathcal{J}(\frac{q}{p}A_f^*\bar{A}_f)\sin\Delta M_s t]\end{aligned} \tag{4.32}$$

$$\Gamma(\bar{B}_s(t) \to f) = N_f e^{-\Gamma t}[(|A_f|^2 + |\frac{q}{p}\bar{A}_f|^2)\cosh\frac{\Delta\Gamma_s t}{2} - (|A_f|^2 - |\frac{q}{p}\bar{A}_f|^2)\cos\Delta M_s t$$

$$+ 2\mathcal{R}(\frac{q}{p}A_f^*\bar{A}_f)\sinh\frac{\Delta\Gamma_s t}{2} - 2\mathcal{J}(\frac{q}{p}A_f^*\bar{A}_f)\sin\Delta M_s t] \tag{4.33}$$

N_f is a time independent normalisation factor.

4.5 CP violation in the $B_s^0 \to J/\psi\phi$ decay

If the final state (f) is a CP eigenstate, $CP|f\rangle = \pm|f\rangle$, then direct CP violating or CP violating through mixing has occurred has occurred ($A_{CP}^{dir} \neq 0$ or $A_{CP}^{mix} \neq 0$ where A is the relevant amplitude).

- A non-vanishing direct amplitude (A_{CP}^{dir}) implies $|A_f| \neq |\bar{A}_f|$, meaning direct CP violation.
- A_{CP}^{mix} measures mixing-induced CP violation in the interference of $B_s \to f$ and $\bar{B}_s \to f$.
- A third quantity, $A_{\Delta\Gamma}$, plays a role if $\Delta\Gamma$ is sizable.

The sum of the square of each asymmetry should reach unity $|A_{CP}^{dir}|^2 + |A_{CP}^{mix}|^2 + |A_{\Delta\Gamma}|^2 = 1$.

Since both resulting particles in $B_s^0 \to J/\psi\phi$ are onia particles, both B_s and $\bar{B}_s$ mesons decay to the identical state. This allows CP violation to occur through interference between the mixing and the decay amplitudes.

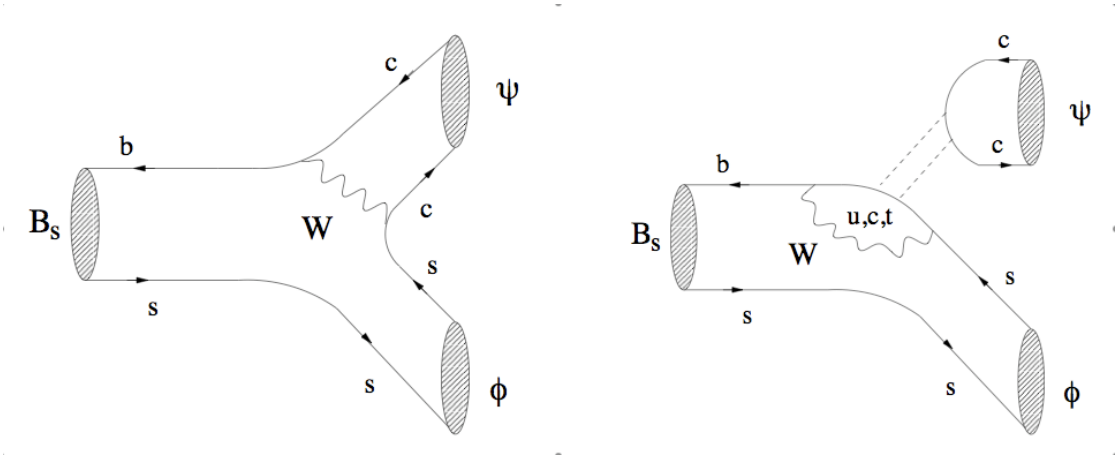

Figure 4.4: Tree (left) and penguin (right) diagrams showing the $B_s \to J/\psi\phi$ decay.

As seen in figure 4.4 the process proceeds via the quark transition $\bar{b} \to \bar{c}c\bar{s}$. There are two contributing weak phases from tree (t_f) and penguin processes (p_f^q). The total decay amplitude must therefore be a function of both effects:

$$A_f = (V_{cb}^* V_{cs}) t_f + \sum_{q=u,c,t} (V_{qb}^* V_{qs}) p_f^q \tag{4.34}$$

when f is substituted with the appropriate eigenstate and q the appropriate quark.

CP violation in interference between the mixing and the decay amplitudes can be observed using the asymmetry of the neutral meson decays into final CP eigenstates f_{CP} [33]:

$$A_{f_{CP}}(t) \equiv \frac{d\Gamma/dt[\bar{B}_s^0(t) \to f_{CP}] - d\Gamma/dt[B_s^0(t) \to f_{CP}]}{d\Gamma/dt[\bar{B}_s^0(t) \to f_{CP}] + d\Gamma/dt[B_s^0(t) \to f_{CP}]} \tag{4.35}$$

or

$$A_f(t) = -\frac{A_{CP}^{mix} \sin(\Delta M t)}{\cosh(\Delta\Gamma t/2) + A_{\Delta\Gamma} \sinh(\Delta\Gamma t/2)} \tag{4.36}$$

where for the $B_s^0 \to J/\psi\phi$ decay $A_{CP}^{mix}(B_s^0 \to J/\psi\phi\ )_{CP\pm} = \pm \sin\phi_s, A_{\Delta\Gamma} = \mp \cos\phi_s$. Where $\phi_s = 2\beta_s$.

The final state mesons are both vector mesons. As these do not have a well-defined orbital angular momentum, $V_1 V_2$ cannot be a CP eigenstate. Thus since both B_s and $\bar{B}_s$ decay to the same final state one cannot extract a CP phase cleanly, since the magnitudes are diluted by opposite CP components. However, this can be overcome by using an angular analysis. By examining the decay products of J/ψ and ϕ, one can measure the various helicity components of the final state. Since each helicity state corresponds to a state of well-defined CP, an angular analysis allows one to use $B_s^0 \to J/\psi\phi$ to obtain the CP phases cleanly.

4.6 The Helicity and Transversity formalisms and angular analysis

When considering the states of the J/ψ and ϕ resulting from the B_s or $\bar{B}_s$ decay in the rest frame of the B_s meson, the possible orbital angular momenta L can exist in one of three states: $L = \{0, 1, 2\}$. Thus the CP eigenvalues of the final state are:

$$\mathrm{CP}(J/\psi) \cdot \mathrm{CP}(\phi) \cdot (-1)^L = +1, -1, +1 \tag{4.37}$$

The final state is thus an admixture of two CP-even states ($L = 0, 2$) and a single CP-odd state ($L = 1$). The polarisation and the resulting angular distributions for daughter particles depend on whether these three states are mixed.

To describe this system mathematically one can choose between a variety of mathematical formalisms known as bases:

- The *partial wave basis* can express the total amplitudes as functions characterised by using the relative orbital angular momentum $L = \{0, 1, 2\}$ as a basis to distinguish three orthogonal states, but this basis is less convenient for an angular analysis in a relativistic environment.

- In the **helicity basis**, the spins of stable particles are projected on the momentum direction of the resonant vector mesons and decay amplitudes are decomposed in terms of helicity amplitudes. $(0, +1, -1$ e.g. $A_0, A_{+1}, A_{-1})$

- In the **transversity basis**, the spin of one daughter particle is projected onto the normal of the other daughter's decay plane and the decay amplitudes are decomposed using three independent linear polarisation states (amplitudes) of the vector mesons. The polarisation vectors are either longitudinal (denoted by 0 e.g. A_0) or transverse to the direction of motion of the vector mesons, where polarisation vectors are either parallel (denoted by $\parallel$ e.g. $A_\parallel$) or perpendicular (labelled by $\perp$ e.g. $(A_\perp)$) to each other.

Since the partial wave basis is not appropriate for this analysis this will not be described further. Both the transversity basis and the helicity basis will be described and investigated. While the transversity basis is used by previous publications, the helicity basis has been recommended by Gronau and Rosner (2008) as they state it provides a weaker dependence on the angular acceptance [34].

The spin of the mother B particle (which is a pseudo-scalar meson) is 0, thus the spin projection of the final state on the decay axis in the B rest frame is zero, and the daughter particles must have the same helicity. In the case of the $B_s^0 \to J/\psi\phi$ both daughter particles are spin 1 and the helicity h can take values $-1, 0$ or 1. Therefore the three possible spin combinations are $(+1,+1), (0,0), (-1,-1)$. One amplitude is associated to each case (A_{+1}, A_0, A_{-1}). These helicity amplitudes correspond to the helicity eigenstate and the helicity basis.

However, A_{-1} and A_{+1} are not eigenstates of parity and thus not CP eigenstates. In the transversity basis the amplitudes $(A_L, A_\parallel, A_\perp)$ correspond directly to the CP eigenstates and are related to the helicity amplitudes in the following way:

- The CP-even longitudinal amplitude: $A_L = A_0$
- The CP-even transverse amplitude: $A_\parallel = \frac{A_{+1}+A_{-1}}{\sqrt{2}}$
- The CP-odd transverse amplitude: $A_\perp = \frac{A_{+1}-A_{-1}}{\sqrt{2}}$

This provides a more direct method of calculating the $\sin 2\beta_s$ and makes deriving the time dependent relation easier.

The definition of helicity angles are shown in figure 4.5a. The figure consists of three different parts, each of which show particles in different inertial frames. The rest frame of the B_s is in the centre, the other frames are the centre of mass frames for the two kaons or two muons respective of which pair they contain. The helicity axis is defined in the direction of the dilepton in the B_s rest system. θ_K is the angle of the K^+ with the negative axis in the dimeson rest frame. The angle θ_l is the angle of the μ^+ with the positive helicity axis in the dilepton frame. The angle between the decay planes of the dimeson and the dileption is ϕ_{hel}, sometimes

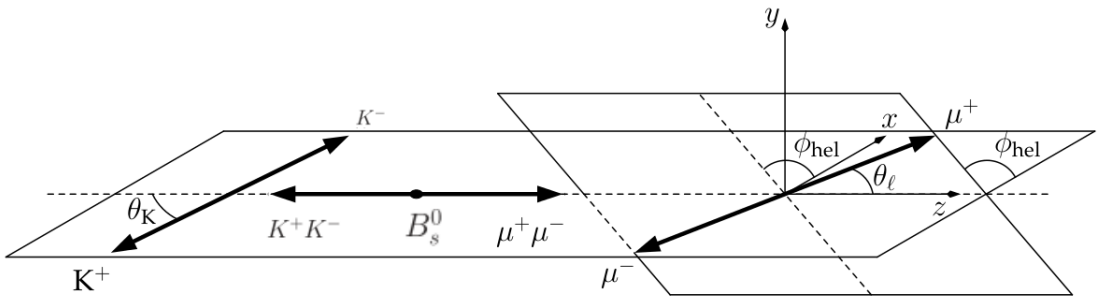

(a) A diagram showing the helicity angular definition

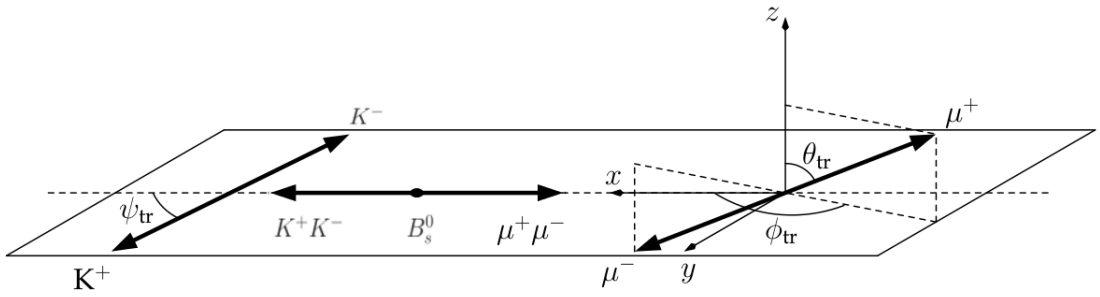

(b) A diagram showing the transversity angular definition

Figure 4.5: Diagrams showing the helicity and transversity angular definitions for the $B_s^0 \to J/\psi\phi$ decay. Based on LHCb diagrams.

written as χ; it is measured from the K^- side of the dimeson plane to the μ^+ side of the dileption plane. The polar angle ranges between 0 and π and the range of ϕ_{hel} is between $-\pi$ and $+\pi$.

The definition of transversity angles is shown in figure 4.5b. The polar angle of K^+ is defined as in the helicity frame (θ_K) however it is often denoted by ψ_T when describing the transversity basis. The remaining two angles, θ_T and ϕ_T, are spherical coordinates in the dileption rest frame. A right-handed coordinate system is defined by fixing the x-axis in the direction of the B_s momentum and its y-axis in the dimeson plane. The y-axis is chosen such that K^+ has a positive momentum in the positive y direction. The polar angle in the dilepton coordinate system θ_T runs between 0 and π and the azimuthal angle ϕ_T runs between $-\pi$ and $+\pi$, like ϕ_{hel}.

Experiments prefer, for convenience, to define the amplitudes using the transversity basis as these amplitudes (as mentioned) directly correspond to the different CP-states. The angles measured can be related thanks to the set of relations in

equation 4.38 [34]. Where possible this thesis will provide results and methodology for both angles. However the transversity angles are selected for the final results.

$$\begin{aligned} \sin\psi_T &= +\sin\theta_K \\ \sin\theta_T\cos\phi_T &= +\cos\theta_l \\ \sin\theta_T\sin\phi_T &= +\sin\theta_l\cos\phi_{hel} \\ \cos\theta_T &= +\sin\theta_l\sin\phi_{hel} \end{aligned} \tag{4.38}$$

Gronau and Rosner provide the time dependent functions using both sets of angles [34]:

$$\begin{aligned} \frac{d^4\Gamma\left[B_s(\bar{B}_s)\to(\ell^+\ell^-)_{J/\psi}(K^+K^-)_\phi\right]}{d\cos\theta_T d\phi_T d\cos\psi dt} \propto \frac{9}{32\pi}\{&[|A_0|^2 f_1(\vec{\rho_T}) + |A_\parallel|^2 f_2(\vec{\rho_T})]\mathcal{T}_+ \\ &+ |A_\perp|^2 f_3(\vec{\rho_T})\mathcal{T}_- + |A_\parallel||A_\perp| f_4(\vec{\rho_T})\mathcal{U} \\ &+ |A_0||A_\parallel|\cos(\delta_\parallel) f_5(\vec{\rho_T})\mathcal{T}_+ + |A_0||A_\perp| f_6(\vec{\rho_T})\mathcal{V}\} \end{aligned} \tag{4.39}$$

Here $A_i \equiv A_i(t=0)$, while dependence on time is given by the four functions:

$$\mathcal{T}_\pm \equiv e^{-\Gamma t}[\cosh(\Delta\Gamma t/2) \mp \cos(2\beta_s)\sinh(\Delta\Gamma t/2) \mp \eta\sin(2\beta_s)\sin(\Delta m_s t)] \tag{4.40}$$

$$\begin{aligned} \mathcal{U} \equiv& e^{-\Gamma t}[\eta\sin(\delta_\perp-\delta_\parallel)\cos(\Delta m_s t) - \eta\cos(\delta_\perp-\delta_\parallel)\cos(2\beta_s)\sin(\Delta m_s t) \\ &+ \cos(\delta_\perp-\delta_\parallel)\sin(2\beta_s)\sinh(\Delta\Gamma t/2)] \end{aligned} \tag{4.41}$$

$$\mathcal{V} \equiv e^{-\Gamma t}[\eta\sin(\delta_\perp)\cos(\Delta m_s t) - \eta\cos(\delta_\perp)\cos(2\beta_s)\sin(\Delta m_s t) + \cos(\delta_\perp)\sin(2\beta_s)\sinh(\Delta\Gamma t/2)] \tag{4.42}$$

where relative strong phases are defined by:

$$\delta_{\parallel} \equiv \arg(A_{\parallel}(0)A_0^*(0)), \delta_{\perp} \equiv \arg(A_{\perp}(0)A_0^*(0)) \tag{4.43}$$

There is a discrete two-fold ambiguity here as the $\cos\delta_{\parallel}$ term in the decay distribution and the time-dependent functions $\mathcal{T}_p m, \mathcal{U}, \mathcal{V}$ are invariant under the simultaneous substitutions:

$$2\beta_s \to \pi - 2\beta_s, \quad \Delta\Gamma \to -\Delta\Gamma, \quad \delta_{\parallel} \to -\delta_{\parallel}, \quad \delta_{\perp} \to \pi - \delta_{\perp}$$

Without flavour tagging information there is another invariance under:

$$\beta_s \to -\beta_s, \quad \delta_{\parallel} \to -\delta_{\parallel}, \quad \delta_{\perp} \to \pi - \delta_{\perp},$$

this leads to a fourfold ambiguity. The first ambiguity has been resolved by a separate measurement by LHCb [31] in which the interference between the S-wave and P-wave amplitudes is measured in the region around the resonant ϕ; this found $\Delta\Gamma_s > 0$ which can be easily incorporated into the fit by limiting the value of $\Delta\Gamma_s$. The second ambiguity can be resolved by adding tagging information. A tagged analysis has been done by LHCb [35] prior to the ATLAS untagged analysis. This information can resolve the ambiguity in an untagged fit by introducing a Gaussian constraint of $\delta_{\perp} = (2.95 \pm 0.39)$ rad.

4.7 S-Wave Contributions and the final PDF

The previous sections describes the primary contributions from the orbital P-wave amplitudes. However, in the vicinity of the $\phi(1020)$ mass, the K^+K^- can have contributions from other partial waves such as those from the decays of a non-resonant $B_s \to J/\psi K^+K^-$ and $B_s \to J/\psi f_0(K^+K^-)$. The BaBar experiment showed that in these decays the S-wave and P-wave contributions dominate in the mass range above threshold up to 1.1 GeV [36][37]. This requires an additional

amplitude to be added to our description and additional angular terms, details of which are found in [38].

Combining the time dependent amplitudes and the additional S-wave terms gives the terms $\mathcal{O}^{(k)}(t)$ shown in table 4.3:

k	Time dependent functions $\mathcal{O}^{(k)}(t)$
1	$\frac{1}{2}\|A_0(0)\|^2 \left[(1+\cos\phi_s\ )e^{-\Gamma_{\rm L}^{(s)}t} + (1-\cos\phi_s\ )e^{-\Gamma_{\rm H}^{(s)}t} \pm 2e^{-\Gamma_s t}\sin(\Delta m_s t)\sin\phi_s\right]$
2	$\frac{1}{2}\|A_\parallel(0)\|^2 \left[(1+\cos\phi_s\ )e^{-\Gamma_{\rm L}^{(s)}t} + (1-\cos\phi_s\ )e^{-\Gamma_{\rm H}^{(s)}t} \pm 2e^{-\Gamma_s t}\sin(\Delta m_s t)\sin\phi_s\right]$
3	$\frac{1}{2}\|A_\perp(0)\|^2 \left[(1-\cos\phi_s\ )e^{-\Gamma_{\rm L}^{(s)}t} + (1+\cos\phi_s\ )e^{-\Gamma_{\rm H}^{(s)}t} \mp 2e^{-\Gamma_s t}\sin(\Delta m_s t)\sin\phi_s\right]$
4	$\frac{1}{2}\|A_0(0)\|\|A_\parallel(0)\|\cos\delta_{\parallel}$ $\left[(1+\cos\phi_s\ )e^{-\Gamma_{\rm L}^{(s)}t} + (1-\cos\phi_s\ )e^{-\Gamma_{\rm H}^{(s)}t} \pm 2e^{-\Gamma_s t}\sin(\Delta m_s t)\sin\phi_s\right]$
5	$\|A_\parallel(0)\|\|A_\perp(0)\|[\frac{1}{2}\left(e^{-\Gamma_{\rm H}^{(s)}t} - e^{-\Gamma_{\rm L}^{(s)}t}\right)\cos(\delta_\perp-\delta_\parallel)\sin\phi_s$ $\pm e^{-\Gamma_s t}(\sin(\delta_\perp-\delta_\parallel)\cos(\Delta m_s t) - \cos(\delta_\perp-\delta_\parallel)\cos\phi_s\sin(\Delta m_s t))\ ]$
6	$\|A_0(0)\|\|A_\perp(0)\|[\frac{1}{2}\left(e^{-\Gamma_{\rm H}^{(s)}t} - e^{-\Gamma_{\rm L}^{(s)}t}\right)\cos\delta_\perp\sin\phi_s$ $\pm e^{-\Gamma_s t}(\sin\delta_\perp\cos(\Delta m_s t) - \cos\delta_\perp\cos\phi_s\sin(\Delta m_s t))]$
7	$\frac{1}{2}\|A_S(0)\|^2 \left[(1-\cos\phi_s\ )e^{-\Gamma_{\rm L}^{(s)}t} + (1+\cos\phi_s\ )e^{-\Gamma_{\rm H}^{(s)}t} \mp 2e^{-\Gamma_s t}\sin(\Delta m_s t)\sin\phi_s\right]$
8	$\|A_S(0)\|\|A_\parallel(0)\|[\frac{1}{2}\left(e^{-\Gamma_{\rm H}^{(s)}t} - e^{-\Gamma_{\rm L}^{(s)}t}\right)\sin(\delta_\parallel-\delta_S)\sin\phi_s$ $\pm e^{-\Gamma_s t}(\cos(\delta_\perp-\delta_s)\cos(\Delta m_s t) - \sin(\delta_\perp-\delta_s)\cos\phi_s\sin(\Delta m_s t))]$
9	$\frac{1}{2}\|A_S(0)\|\|A_\perp(0)\|\sin(\delta_\perp-\delta_S)$ $\left[(1-\cos\phi_s\ )e^{-\Gamma_{\rm L}^{(s)}t} + (1+\cos\phi_s\ )e^{-\Gamma_{\rm H}^{(s)}t} \mp 2e^{-\Gamma_s t}\sin(\Delta m_s t)\sin\phi_s\right]$
10	$\|A_0(0)\|\|A_S(0)\|[\frac{1}{2}\sin(\delta_S)\sin\phi_s\ \left(e^{-\Gamma_{\rm H}^{(s)}t} - e^{-\Gamma_{\rm L}^{(s)}t}\right)$ $\pm e^{-\Gamma_s t}(\cos\delta_s\cos(\Delta m_s t) + \sin\delta_s\cos\phi_s\sin(\Delta m_s t))]$

Table 4.3: A table showing the final time dependent amplitudes for the $B_s^0 \to J/\psi\phi$ including S-wave contributions

To complete the pdf each k term should be combined with one of the angular functions and the adjacent coefficient in table 4.4.

Thus the full differential decay can be described using the helicity angles:

$$\frac{d^4\Gamma}{dt\ d\Omega} = \sum_{k=1}^{10} \mathcal{O}^{(k)}(t)\mathcal{C}^{(k)}g^{(k)}(\theta_l, \theta_K, \phi_{hel}) \tag{4.44}$$

or the transversity angles:

$$\frac{d^4\Gamma}{dt\ d\Omega} = \sum_{k=1}^{10} \mathcal{O}^{(k)}(t)\mathcal{C}^{(k)}g^{(k)}(\theta_T, \theta_K, \phi_T) \tag{4.45}$$

		Angles	
k	Coef ($\mathcal{C}^{(k)}$)	Helicity ($g^{(k)}(\theta_l, \theta_K, \phi_{hel})$)	Transversity ($g^{(k)}(\theta_T, \theta_K, \phi_T)$)
1	2	$\cos^2\theta_K \sin^2\theta_l$	$\cos^2\psi_T(1-\sin^2\theta_T\cos^2\phi_T)$
2	1	$\sin^2\theta_K(1-\sin^2\theta_l\cos^2\phi_{hel})$	$\sin^2\psi_T(1-\sin^2\theta_T\sin^2\phi_T)$
3	1	$\sin^2\theta_K(1-\sin^2\theta_l\sin^2\phi_{hel})$	$\sin^2\psi_T\sin^2\theta_T$
4	$\frac{1}{\sqrt{2}}$	$\sin 2\theta_K \sin 2\theta_l \cos\phi_{hel}$	$\sin 2\psi_T \sin^2\theta_T \sin 2\phi_T$
5	1	$\sin^2\theta_K \sin^2\theta_l \sin 2\phi_{hel}$	$\sin^2\psi_T \sin 2\theta_T \sin\phi_T$
6	$\frac{1}{2}\sqrt{2}$	$\sin 2\theta_K \sin 2\theta_l \sin\phi_{hel}$	$\sin 2\psi_T \sin 2\theta_T \cos\psi_T$
7	$\frac{2}{3}$	$\sin^2\theta_l$	$1-\sin^2\theta_T\cos^2\phi_T$
8	$\frac{1}{3}\sqrt{6}$	$\sin\theta_K \sin 2\theta_l \cos\phi_{hel}$	$\sin\psi_T \sin^2\theta_T \sin 2\phi_T$
9	$\frac{1}{3}\sqrt{6}$	$\sin\theta_K \sin 2\theta_l \sin\phi_{hel}$	$\sin\psi_T \sin 2\theta_T \cos\phi_T$
10	$\frac{4}{3}\sqrt{3}$	$\cos\theta_K \sin^2\theta_l$	$\cos\psi_T(1-\sin^2\theta_T\cos^2\phi_T)$

Table 4.4: A table showing the angular functions for both the helicity basis and transversity basis

4.8 Physics Beyond the Standard Model

There is a consensus amongst theorists that ϕ_s is sensitive to many new physics models including supersymetry [39, 40, 41]. These could make significant contributions, producing a ϕ_s with a large magnitude. In the decay amplitude new physics (NP) can lead to polarisation-dependent mixing-induced CP asymmetries in $B_s^0 \to J/\psi\phi$ [40].

NP contributions are already quite constrained due to Δm_s measurements, however few currently have enough information to predict a single value for ϕ_s and theoretical progress is required in order to advance [42].

As such, this measurement in isolation cannot conclusively confirm the absence of new physics or determine the successor to the Standard Model. However, an accurate result that does not conform to the Standard Model would provide strong motivation for the presence of new physics. The current predictions for key physical parameters can be found in table 4.5.

Observable	SM prediction	References
Δm_s (ps^{-1})	17.3 ± 2.6	[33]
$\Delta\Gamma_s$ (ps^{-1})	0.087 ± 0.021	[33]
ϕ_s (rad)	-0.036 ± 0.002	[43]

Table 4.5: A table showing the predictions of the Standard Model for various key physical parameters [42]

In the context of model-independent analyses, the NP contributions can be parametrised in the form of two complex quantities Δ_q and Λ_q [44, 45]. These are general terms for the two generations of B meson so $q = d, s$.

$$M_{12}^q = M_{12}^{q,\mathrm{SM}} |\Delta_q| e^{i\phi_q^\Delta} \tag{4.46}$$

$$\Gamma_{12}^q = \Gamma_{12}^{q,\mathrm{SM}} |\Lambda_q| e^{i\phi_q^\Lambda} \tag{4.47}$$

This provides four real degrees of freedom. The observables which depend on these parameters are the mass and decay width differences and flavour-specific CP-asymmetries. They can be expressed in terms of the SM predictions and NP parameters as:

$$\Delta m_q = (\Delta m_q)_{\mathrm{SM}} |\Delta_q| \tag{4.48}$$

$$\Delta\Gamma_q = (\Delta\Gamma_q)_{\mathrm{SM}} |\Lambda_q| \frac{\cos(\phi_{12}^{q,\mathrm{SM}} + \phi_q^\Delta - \phi_q^\Lambda)}{\cos\phi_{12}^{q,\mathrm{SM}}} \tag{4.49}$$

$$a_{sl}^q = (a_{sl}^q)_{\mathrm{SM}} \frac{|\Lambda_q|}{|\Delta_q|} \frac{\sin(\phi_{12}^{q,\mathrm{SM}} + \phi_q^\Delta - \phi_q^\Lambda)}{\sin\phi_{12}^{q,\mathrm{SM}}} \tag{4.50}$$

up to corrections suppressed by tiny $(\Gamma_{12}^q/M_{12}^q)^2$. The last two expressions depend only on the difference $(\phi_q\Delta - \phi_q^\Lambda)$. The values of Δm_q have been precisely measured, giving constraints for $|\Delta_q|$, which are limited by the knowledge of hadronic matrix elements [42]. Equation 4.49 indicates that NP can only decrease $\Delta\Gamma_s$ since $\cos(\phi_{12}^{s,\mathrm{SM}})$ is maximal with respect to the Standard Model.

Chapter 5

ATLAS Software and Computing

5.1 Introduction

The software and computing infrastructure at the LHC experiments is necessarily vast in scale, in order to deal with the sheer volume and complexity of the data produced and the number of geographically dispersed collaborators. In the initial two years of data taking at the LHC the computing infrastructure was well prepared for the data produced, even though the online luminosity increased by a factor of a thousand times.

The roles of the computing infrastructure include:

- Monitoring the running of the collider and detectors
- Implementation of the trigger algorithms at the online data acquisition level
- Reconstructing the recorded RAW data at the Tier 0 data processing site into smaller formats (ESD and AOD)
- Sending the ESD and AOD files to computing sites across world using "the Grid" system
- Running ATLAS offline software restructuring the data into other formats or running analysis code
- Sending the resulting files to the physicist for local analysis

- Running simulation programs for producing Monte Carlo data
- Reconstructing the original data after software revisions

5.2 The Grid

The Worldwide LHC Computing Grid, abbreviated as WLCG, or just the LHC Computing Grid (LCG) before 2006, is an international collaborative project that consists of computer network infrastructure connecting over 170 computer centres in 36 countries (as of 2012). As of 2012, data from over 300 trillion LHC proton-proton collisions have been analysed at a rate of 25 petabytes per year. The size of the Grid currently is some 200,000 processing cores and 150 petabytes of disk space.

The sites are organised into three tiers. **Tier 0** is stationed at CERN and recently has been expanded to Budapest, Hungary. It is specially for reconstructing RAW data recorded by ATLAS. Due to the continuous data acquisition from normal operation of the LHC and the lack of redundancy (there are no back up tier 0 sites) the operation of this tier has the highest priority to prevent the permanent data loss that could occur if there was sufficient back log.

The rest of the sites on the Grid are split into separate groups referred to as **clouds** for management purposes. The clouds typically dividing according to the nation the sites are in. However, there are exceptions such as the Tokyo, Japan site which is in the French Cloud. Each cloud has a single **tier 1** site, a large data site that receives the data from tier 0 via fast network connections. The main role of the **tier 1** sites is to store and distribute this data, and also to run important central production tasks such as reprocessing and simulation "jobs".

Tier 2 sites account for the remaining WLCG. They primarily perform individual user analysis activities and do the bulk of the simulation.

ATLAS' data resources are organised on the Grid in the following way:

- **Datasets** are collections of files stored together on one or multiple sites. These are labelled with a string conforming to naming CERN conventions

(the exact details of which differ over time)

e.g. *data11_7TeV.00186729.physics_Egamma.merge.r2713_p705_p809_p811*

- **Dataset Containers** are logical objects that contain one or many datasets. One dataset can exist in multiple containers and a container can contain datasets from multiple sites. Data containers primarily exist for user convenience as any given task could require hundreds of datasets. These are distinguished from a dataset by requiring their string to have a forward slash (/) as the final character

  e.g. *data12_8TeV.periodB10.physics_Muons.grp14_v01_p1284/*

- **Physics Containers** are technically no different to dataset containers but are created by the production systems and contain data approved for analysis.

Writing files to Grid storage is a complex task. Whilst the Grid middleware returns the standard output and error streams of a job, and any other small files of the user's choosing to a directory on the user interface machine (the "output sandbox"), large files containing physics data must be stored on the Grid itself, so that they are available to other users. This would generally be beyond the skills of a non-Grid expert.

DQ2 is a series of tools written to provide a simple way for users to access the data resources on the Grid. The software is written in python and hides much of the complexity the Grid requires. For instance, entering the command *dq2-get data12_8TeV.periodB10.physics_Muons.PhysCont.grp14_v01_p128/* queries the dataset container given, identifies the datasets therein, locates the sites that store the datasets, downloads the datasets from any local sites to the current directory. If they are not available at local sites, remote sites are then accessed. It then validates the files after transfer is complete reporting any errors to the user. Other commands are also available for querying the contents of a dataset or manipulating your own datasets and data containers.

The **PanDA** Production ANd Distributed Analysis system has been developed

by ATLAS since summer 2005 to meet ATLAS requirements for a data-driven workload management system for production and distributed analysis processing capable of operating at the LHC data processing scale. While this system is used extensively by Grid managers, the average physics analyst will invoke PanDA systems to submit tasks or "jobs" to the Grid and monitor their status. There are numerous methods of submitting tasks to the Grid, however the two most prevalent at time of writing are the **PanDA client package** and **Ganga**. When submitting a job to the Grid the user will provide an input dataset or data container (if applicable) and an output data container name that will be created to contain the resulting output. The client will then query the input container to identify the sites that have the data and then submit jobs to the sites with the shortest job queues. Once a job is complete the output file is stored at the site and added to the output data container and can then be downloaded by users.

5.3 Types of Data

To ensure that the sheer quantity of data is analysed efficiently within available computing resources, variable data formats have been developed to provide the adequate level of information for various tasks:

- **RAW Data** are events as output by the ATLAS event Filter - the final level of the high level tracker. The expected size per event is 1.6 MB. Events arrive in "byte-stream" format, reflecting the format in which data are delivered from the detector rather than an object-orientated representation. Each file will contain events belonging to a single run and should not exceed 2 GB, but the events are not ordered consecutively by design.

- **Event Summary Data (ESD)** refers to event data written as the output of the data reconstruction process. ESD is usually 500 kB per event and is intended to make RAW data unnecessary for most physics applications other than re-reconstruction. ESD is written in an object-oriented representation

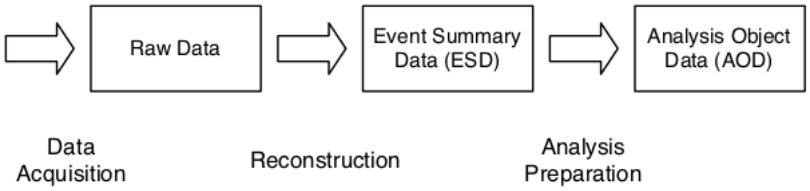

Figure 5.1: The reconstruction processing pipeline showing the primary data format employed by *Athena*. Taken from [46]

and stored in POOL ROOT format.

- **Analysis Object Data (AOD)** is a reduced event representation, derived from ESD and suitable for physics analysis. It contains physics objects and other elements of interest in most analyses but less than ESD. The size is about 100 kB per event. Like ESD it is written in an object-oriented representation and stored in POOL ROOT format.

- **Derived Analysis Object Data (DAOD)** are non-standard files derived from AODs that have been transformed for a more specific task such as filtering out unnecessary events and data stores. It could also have additional object stores not written in a standard AOD.

- **ntuples or ROOT files** are files containing root data TTrees that are commonly used at the final or intermediate level of physics analysis. Since the contents is not standardised it can exist in any size.

5.4 The Athena Framework

The *Athena* framework is an object-oriented framework written in C++ and python for physics data-processing applications. It provides a range of services and tools that facilitate the access, management and analysis of ATLAS data. The design of the framework has been guided by a number of principles [46]. The data reading and algorithms should be separate systems or classes. Classes which contain physics data (such as Tracks and Vertices) are independent of the algorithms

that use them. The classes defining tracks are separated from the track finding algorithms. These recommendations exist to reduce complexity that can arise from code dependencies i.e. it is not necessary to link to the entire reconstruction library to use a reconstructed track. The main components of *Athena* are as follows:

- **Application Manager** is the master class which drives and co-ordinates the entire data process scheme. There is one instance of the Application Manager (it is a global variable singleton).

- **Algorithms** are the basic data processing class; all algorithms must inherit from an Algorithm base class which enforce the use of three methods: *initalize*, which runs once at the start of job and is typically responsible for initialising tools, objects, histograms and output files; *execute*, which is run once per event and should process each event as appropriately using the tools prepared in *initialize*. Since there is no way to know how many events will be run over in a single process it is important not to store too much data and to clean up memory leaks in the execute method. The *finalize* method is run once at the end as the application closes down and should clean up the tools, flush any output buffers to disk and close file handles. Algorithms can be run in any chain or sequence as defined in the python based job options. Algorithms can pass data to each other by using the transient stores provided by the *Athena* framework but should otherwise be self contained.

- **Tools** are similar to algorithms in that they process data and can write to the transient stores, but they do not inherit from a common base class to be more flexible as they could be required to run multiple times per event. As such each tool can have a unique interface and must be carefully employed in an algorithm.

A number of built-in features in the *Athena* framework allow for:

- **Python driven Job Options** allow users to pass variables to algorithms at run time. Python is also used as a driving mechanism activating the

appropriate *Athena* library (usually written as C++) at the appropriate time.

- The **messaging service** provides a series of macros for printing messages to the screen or log. This is preferable to the standard C++ libraries as it standardises the output and amends information about the current algorithm and the priority of the message. The system also allows the level of verbosity to be altered during run time and provides a mechanism for enforcing error handling guidelines.

- *Athena* provides **performance monitoring** by default giving information on CPU and memory usage. This aids developers in optimising their code and identifies problems.

- **StoreGate** is the name given to the service that manages the transient data store. This allows the various modular algorithms to pass data to each other such as accessing the data read from the input file or passes data objects from one algorithm to another. It also provides the advantage of automating much of the memory clean up.

- **Persistency Services** manage the transfer of data between StoreGate and permanent files such as AOD and ESDs. The format used is referred to as POOL [47].

5.5 Event Generation Software

Simulated physics events are an essential tool for many types of particle physics analysis and was useful for planning analyses before the LHC was completed. In the case of the LHC these simulations model the initial proton-proton collisions, the production of elementary quarks, gluons and gauge bosons from the collision, the hadronisation that follows and the decay of these hadrons into the longer lived particles that travel to the detector. The data produced by these simulations are essentially lists of particles with their properties, positions, a record of their parent

and daughter particles; this format is called HepMC. The accuracy to which they simulate known physical processes varies depending on design and configuration but they cannot recreate every aspect of physical subtlety with complete accuracy. As such, many different generators exist optimised for different purposes.

The production and decay of sub-nuclear particles involves many inherently random processes. The resulting particles are randomly determined depending on the amplitudes or branching ratio information available to the generator. Outside particle physics, "Monte Carlo methods" are a broad class of computation algorithms that rely on random sampling to solve problems. Inside particle physics, **Monte Carlo** collectively refers to all simulated data or generators.

As mentioned there is a wide range of event generators. The common ones used by the LHC are *Pythia*[1] [48], and *Herwig*[2] [49] which handle the simulation of the initial partonic collision described by perturbative QCD. Some of the specialised packages include *Photos* [50] for QED radiative corrections, *Tauola* [51] for τ-lepton decays, *EvtGen* [52] for B-meson decays and and *Hijing* [53] for heavy ion collisions. In some cases more than one generator may be used, one for the initial hard process and another to decay the resulting particles in a less naïve manner. This is fully compatible with *Athena*, and HepMC data can be kept transiently in StoreGate or permanently in a POOL file.

ATLAS B-physics studies generally use *Pythia* as the main event generator and sometimes *EvtGen* to decay the B-mesons. In this analysis we only use *Pythia* that does not include the spin-physics and time-dependent effects mentioned in the chapter 4. When this additional physics is required we implement a rejection sampling method over the decays generated by *Pythia* utilising the probability density function derived in chapter 4. Initially the FORTRAN based *Pythia 6* is used but this was later superseded by the C++ based *Pythia 8*.

[1] named after the prophetic Oracle of Delphi

[2] Monte Carlo package for simulating Hadron Emission Radiation with Interfering Gluons

5.5.1 PythiaB

Unfortunately only 1% of proton-proton collisions result in the production of a b or $\bar{b}$ quark, and of those quarks an even smaller fraction become B_s mesons. Given our interest lies exclusively with such events this makes *Pythia* inefficient for our purposes from the perspective of CPU time. Altering the branching ratios inside *Pythia* would boost the proportion of B_s mesons, however this would have side effects altering other aspects of the decays.

To combat this ATLAS developed the *PythiaB* [54] algorithm. This utilises *repeated hadronisation* cloning generated b-quarks a user-defined number of times and hadronising each one as if an independent event. The b quark can be forced to decay into the channel of interest while the opposite $\bar{b}$ quark is left to decay according to the usual decay tables. In this way the efficiency of the generation is increased considerably. *PythiaB* also provides an additional mechanism for selected specific decay channels. By means of filtering code, events that lack the presence of the required, chains can be rejected, prompting *Pythia* to regenerate a decay.

$$\sigma_B = \frac{\sigma_{hard} N_{signal}}{N_{hard} N_{loop}} \tag{5.1}$$

Equation 5.1 shows the resulting process cross section (σ_B). N_{hard} is the number of produced hard processes, N_{signal} is the number of accepted B-signal events and N_{loop} is the number of repeat hadronisation loops (number of cloned quarks). The number must be multiplied by the cross-section of any forced decays and by a factor of two to reflect the fact the other quark is allowed to freely decay.

To ensure that the rehadronisation process is not contaminating the sample with too many duplications, the software calculates the **cloning factor**. This is the number of accepted signal events per set of hadronisation loops. A figure close to one indicates there is minimal duplication of hard processes in the final sample. A lower cloning factor indicates that it is generating more hard processes than those reaching the selected sample and so more repeated hadronisation should be used. This process is illustrated in figure 5.2.

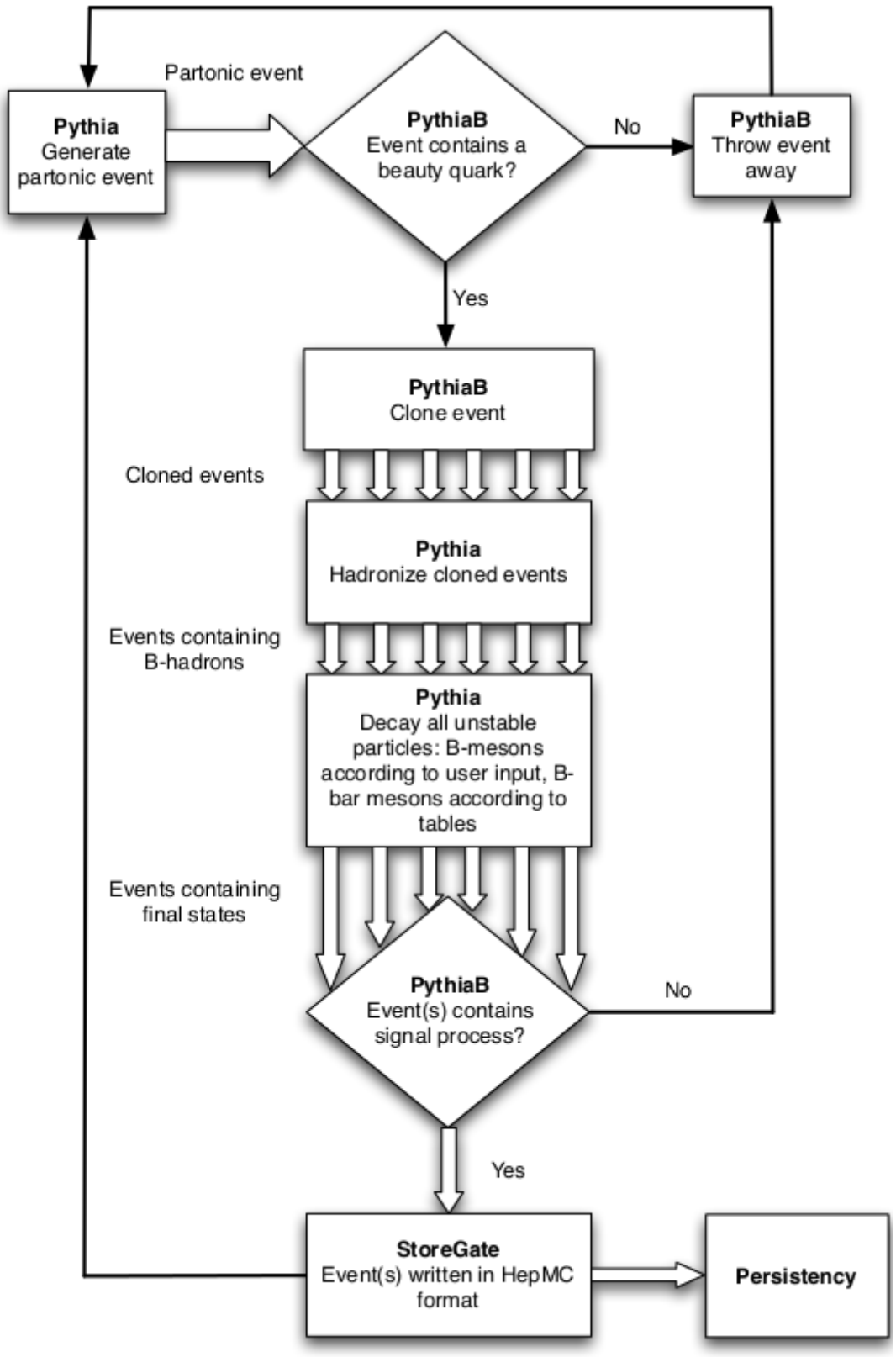

Figure 5.2: Data flow for the PythiaB algorithm. Taken from [55]

5.5.2 Rejection sampling

Rejection sampling is a basic pseudo-random number sampling technique used to manipulate a randomly generated distribution. It is also commonly called the acceptance-rejection method or "accept-reject algorithm". By rejecting events where a pseudo-random number exceeds the probability density function of the physics you wish to simulate, a homogeneous sample can be shaped according to the CP-violating physics. Since *Pythia* does not simulate the CP violation, this technique is used when generating signal requiring the presence of CP violation. If a sample does not require the additional physics (such as samples used in acceptance maps) this technique is disabled to save CPU time.

Below is pseudo C++ illustrating how the algorithm is implemented:

```
// BsJpsiPhi_PDF calculates the value of the pdf for this events
double prob1 = BsJpsiPhi_PDF();
//Bstau is the proper lifetime for this individual Bs-meson
//Bstau0 is the nominal proper lifetime for a Bs-meson generated by pythia
double prob2 = exp(Bstau / Bstau0) * Bstau0;
double rand = Rdmengine->flat() * prob_norm;
//rand is a flatly generated random number scaled to a set normalisation
if (rand < (prob1 * prob2)){
    return true;// The event is accepted into the sample
}else{
    return false;// The event is rejected from the sample
}
```

5.6 Simulation, Digitisation and Pile-up

The output from an event generator can be useful for many tasks. It is however completely ignorant of detector effects so the output will not resemble what is observed by the detector. To account for this, a detector simulation software tool can be applied and will be described in this section. Detector simulation involves

reading the particles from the HepMC store file and modelling their passage through the detector. It must account for a wide range of processes but also reflect the geometry of the physical machine. Since each detector has a different geometry and is made of different materials the software must be adapted by ATLAS.

The package used by ATLAS is based on a simulation suite called Geant4[3]. The software provides the tools needed for tracking particles through the detector material and magnetic fields, creating new events from interactions with the materials and for simulating the reactions of active detector components to the particles. These are based on a library of Monte Carlo algorithms for a wide range of physics processes including electromagnetic and hadronic interactions and the decay of particles in flight. The ATLAS implementation takes the required simulation tools and establishes the detector geometry and composition from the main *Athena* geometry service (**GeoModel** [56]). The simulation accounts for particles with energies as low as 10 electronvolts, which is the ionisation potential of the active gases for many of the detector tubes, and for energies as high as a few Tera-electronvolts, to account for the muons that deposit all their energy in the calorimeters. The tracking detectors require a particularly detailed simulation to account for track reconstruction efficiencies and momentum accuracy. The geometry of the magnetic field must be well-understood to gain insight into the moment measuring and muon identification capacity of the detector. When complete the simulator outputs its results as an SDO (Simulation Data Object) file.

The next step is to take these effects and simulate the activation of the active components producing the electronic signal that lead to particle detection ("hits"). This part of the process is known as **digitisation**. The effects of pile-up[4] can also be simulated at this stage. The output of this process is identical to output recorded by the real detector when taking data, meaning that all subsequent steps can use software identical to that used on real data taking. This is not only convenient but

[3]French for 'giant'

[4]The hits from other interactions not related to the physics event. This often increases with high instantaneous luminosities.

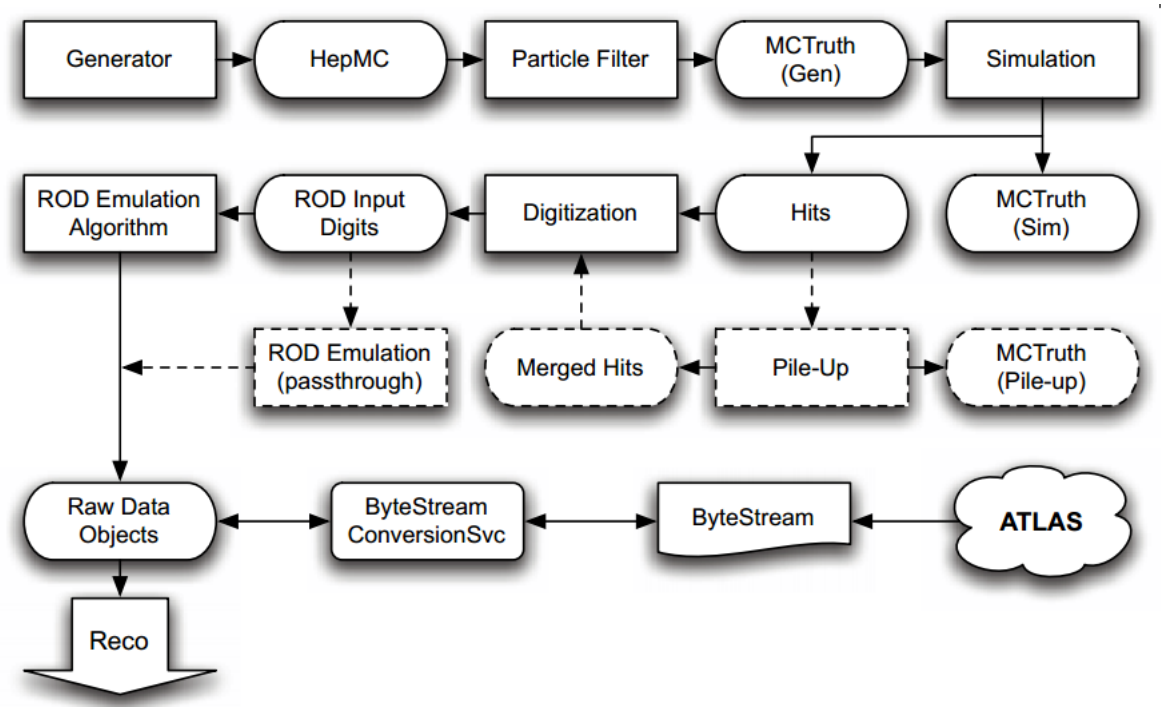

Figure 5.3: The ATLAS data chain from both event generation and real data collection. Taken from [46]

can help in identifying software bugs. This process is illustrated in figure 5.3.

5.7 Reconstruction Software

Reconstruction is the process by which pattern recognition software inspects the digital hits from the detector (or in the case of Monte Carlo from the digitisation process) and attempts to deduce the physical event that produced it. In the example of the tracking system it associates the activity to a possible track. This is essential to provide the physicist with the concepts he or she is familiar with (such as particle tracks or jets). This involves different algorithms taking data from all the detector subsystems from the inner detector to the muon chambers. For instance, the inner detector hits are matched up with hits in the muon chambers or clusters in the calorimeters and use all the information to produce a hypothesis track that is most effective at accounting for the hits. This is called *combined reconstruction*. Some particle identification can be done on this stage for photon, electrons, muons and τs. This study and B-physics at ATLAS are generally most

dependent on the inner and muon detectors. Sometimes the calorimetry is used to aid flavour tagging.

The output of the reconstruction software can be Event Summary Data files (ESDs) or Analysis Object Data files (AODs) or both. They both contain persistent C++ data objects representing the abstractions made by the reconstruction software i.e. the track, vertices and energy clusters. For instance a track is defined by the various parameters described in section 3.1.

A **vertex** is a common point of origin for a number of tracks and is stored in the ESD format with the position, the associated covariance matrix and the information about the fitter which created it, such as the quality of fit measures. Vertices are calculated at both the reconstruction level and later at analysis level. The reconstruction procedure is tasked with identifying possible primary vertices from which the entire event originated. There are a variety of methods for identifying these and involve attempting to fit various tracks to a vertex, this will produce a variety of candidates for the primary vertex. The primary vertex with the highest $\sum p_T^2$ is usually given priority by *Athena*. During physics analysis the quality of a vertex fit can be used to determine which tracks originated from the same decay. This is a number associated with the vertex describing the likelihood that the tracks truly converge to that vertex.

A vital feature when reconstructing generated events is to propagate the original HepMC information, also known as the *truth*. This allows the software to associate the reconstructed objects with the original object produced by the generator at later stages. This is immensely useful to an analyst allowing him or her to see the smearing caused by the detector resolution or estimate the efficiency at which the detector and software are operating.

5.8 Analysis Software

The B-physics group at ATLAS has developed a series of tools for performing much of the analytical tasks common in the B-physics analysis that are beyond

the reconstruction tasks. These include tools for:

- Unique pairs or triplets of a collection of tracks for vertexing
- Filtering out pairs that are not of opposite charge
- Calculating the invariant mass of a set of tracks
- Fitting the tracks to a vertex
- Calculating the properties of the vertex fit in relation to the primary vertices (e.g. the proper decay time)
- Obtaining the Monte Carlo particle corresponding to a given track, or providing the closest match where no direct association exists.

Chapter 6

$B_s^0 \to J/\psi\phi$ Analysis

6.1 Candidate Reconstruction

After the reconstruction process creating the objects described in chapter 5.7 the reconstruction of candidates for the particles relevant to this analysis can be started. This is produced by the *Bd2JpsiKstar* or the *Bd2JpsiKstarPerEvent* which the author worked on. It should be noted that both algorithms are equivalent but output the data in different formats. This was necessary to account for the evolution of *BPhysicsTools* packages and even though the algorithm is named after the $B_d^0 \to J/\psi K^{0*}$ decay it is also for the $B_s^0 \to J/\psi\phi$ decay.

The algorithm proceeds in the following manner:

- The *JpsiFinder* tool is run to identify J/ψ particles that pass specifications set by the B-Physics and muon groups (see table 6.2). These candidates are fitted to a vertex; in doing so the track parameters are modified to point to that vertex (the tracks are refitted). If no J/ψ are found the algorithm moves onto the next event. The vertexing software used is the *VKalVrt* package [57].

- Each J/ψ muon pair contains at least one *combined* muon and both pass the Muon Combined Performance (MCP) group recommended selection criteria:

  - Requires a B-layer hit when expected

  - The sum of pixel hits and pixel dead sensors to be no less than two.
  - The sum of SCT hits and dead sensors to be no less than six.
  - No more that one pixel of SCT hole.
  - If $|\eta(\mu)| < 1.9$, it requires at least six TRT hits + outliers where the outliers are less than 90% of the sum
  - If $|\eta(\mu)| \geq 1.9$, require the number of outliers to be less than 90% of the sum of TRT outliers + hits, if the sum is at least six.

- The reconstructed primary vertices are retrieved and valid ones selected. If there are no valid primary vertices the event is skipped.

- Any J/ψ found by the *JpsiFinder* tool are retrieved. For each J/ψ candidate each primary vertex is refitted to exclude any tracks used in the construction of the J/ψ . The properties of each J/ψ with respect to each primary vertex are calculated and stored (e.g. the proper decay time).

- The reconstructed muon and inner detector tracks are retrieved and those that pass selection cuts in table 6.1 are selected.

- Any tracks used in the construction of the accepted J/ψ are deselected.

- Inner detector tracks are arranged in pairs; any pair with the same polarity of charge are rejected.

- Each J/ψ is then paired with each oppositely charged pair to form a quadruplet of tracks. The mass of the particles that produced the quadruplet is calculated using the PDG masses [58] of the three decay channels $B_s \to J/\psi(\mu^+\mu^-)\phi(K^+K^-)$, $B_d \to J/\psi(\mu^+\mu^-)K^{0*}(K^+\pi^-)$ and $\bar{B}_d \to J/\psi(\mu^+\mu^-)\bar{K^{0*}}(K^-\pi^+)$. The $\bar{B}_s^0$ does not need separate consideration because of the mass symmetry of the final state tracks. Any candidate that has a mass not within the specified window is not considered further.

- The mass of the particle resulting from the two hadronic tracks is calculated using the PDG masses for the hypothesis $\phi \to K^+K^-$, $K^{0*} \to K^-\pi^-$ and $\bar{K^{0*}} \to \pi^-K^+$. Then any that fall outside the specified mass windows are not considered further. The values used can be found in table 6.3.

- If the data being used is Monte Carlo, then the truth information is accessed and matched to the tracks as appropriate. Those matching certain decay chains are identified and the provenance of the tracks is identified.

- Each quadruplet of tracks is then fitted to a common vertex. The tracks are refitted to this vertex and associated with this candidate. In a small minority of cases this process fails the candidate is not considered further. During this procedure the mass of the J/ψ is constrained to the PDG world average. This constraint improves the B_s mass resolution and partly recovers the effect of the systematic J/ψ mass shift (described in section 6.3.1).

- For each quadruplet of tracks each selected primary vertex is recalculated removing any of the quadruplet that may have been used constructing the vertex.

- The properties of each candidate in relation to each primary vertex are calculated and stored appropriately as a B_s, B_d or $\bar{B_d}$ candidate. A single quadruplet can pass multiple hypotheses.

- If a tagging algorithm is present, it is then run to gather the necessary information, but details for this are beyond the scope of this thesis.

- The trigger decisions associated with an event that passes selection are stored.

While additional cuts and selections are made at a later stage, the ones mentioned above help reduce CPU and disk usage but eliminate the most unlikely candidates early.

Track p_T	> 800 MeV
number of hits on the B-layer	> 0
number of hits on the pixel detector + number of dead pixels	> 1
number of hits B layer and pixel detector	> 1
number of hits in the SCT + number of dead SCT	> 3

Table 6.1: The cuts applied to each track during candidate reconstruction. NOTE: Additional cuts are made later in the process and can supersede these cuts

MuAndMu (Take tracks identified as muons)	true
assumeDiMuons (uses PDG values for muon masses)	true
Di-muon mass windows	(2700 to 3600) MeV
Quality of Vertex cut (χ^2)	50
oppChargesOnly (takes opposite charged tracks)	true
sameChargesOnly (take same charged tracks)	false
allChargeCombinations (take any combination of charged tracks)	false
allMuons (includes all muons not combined)	true
atLeastOneComb (requires one combined muon)	false

Table 6.2: A table showing the configuration of the *JpsiFinder* package. NOTE: Additional cuts are made later in the process and can supersede these cuts

Mass of the B_s meson	4600 - 5900 MeV
Mass of the ϕ meson	850 - 1190 MeV
Quality of the 4 track vertex fit	$\frac{\chi^2}{NDF} < 15$

Table 6.3: Cuts applied to the reconstruction of the candidates in the *Bd2JpsiKstar* algorithm. NOTE: Additional cuts are made later in the process and cut supersede these cuts

6.2 Calculation of proper decay time

The proper decay time is an essential component of any time-dependent analysis. The proper decay time τ is defined as:

$$\tau = \frac{L}{\beta\gamma c}$$

where L is the distance between the primary vertex and the fitted B-vertex, $\beta\gamma$ is the Lorentz factor of the B meson and c is the speed of light in vacuum. To attain a more accurate measurement from using the measured parameters, the mass can be incorporated with a more accurate value:

$$\tau_{B_s^0} = \frac{L_{xy} M_{\mathrm{PDG}(B_s^0)}}{c \cdot p_T(B_s^0)}$$

where $p_T(B_s^0)$ is the reconstructed transverse momentum of the B_s^0 candidate, $M_{\mathrm{PDG}(B_s^0)} = 5366.3 \pm 0.6$ MeV [20], L_{xy} is the transverse distance between the primary and B_s^0 vertex.

$$L_{xy} = |\Delta r_{xy}| \cdot \cos\theta_{XY}$$

Since the reconstruction algorithm can identify many different candidates for the primary vertex in an event (see figure 6.2), one must be selected in order to calculate τ. There are two common methods for deciding the best primary vertex to choose. One method is to choose the one with the highest $\sum p_T^2$ of the constituent tracks. The other is to select the vertex that gives the minimal impact parameter d_0 for the B_s^0 meson. The d_0 parameter is the distance between the point of closest approach of the B_s^0 trajectory and primary vertex as defined in the x, y plane (see figure 6.1). The minimal d_0 method is chosen however in 97% of cases in the 2011 dataset. The two methods choose the same vertex and changing the selection produces no significant difference to any results.

As mentioned, the primary vertices are refitted removing the tracks used in the

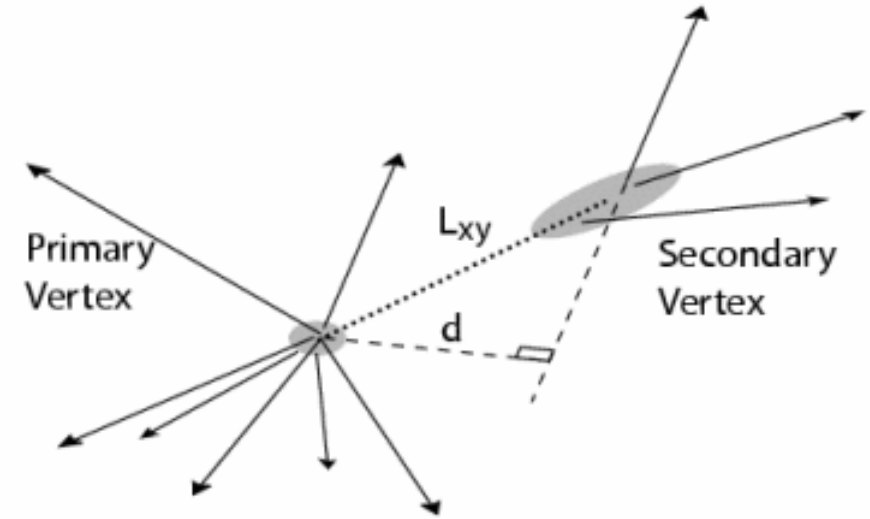

Figure 6.1: A diagram showing the relation between the primary and secondary vertex

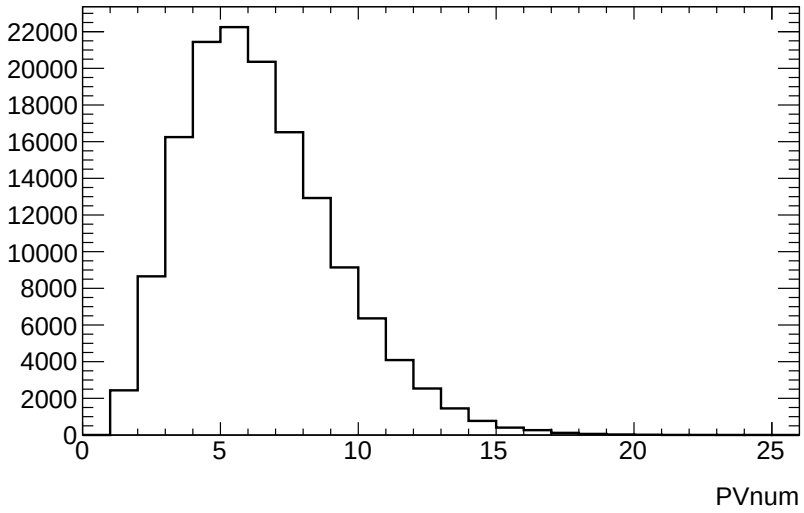

Figure 6.2: A plot showing the number of primary vertices found in the selected B_s^0 events from the ATLAS 2011 dataset

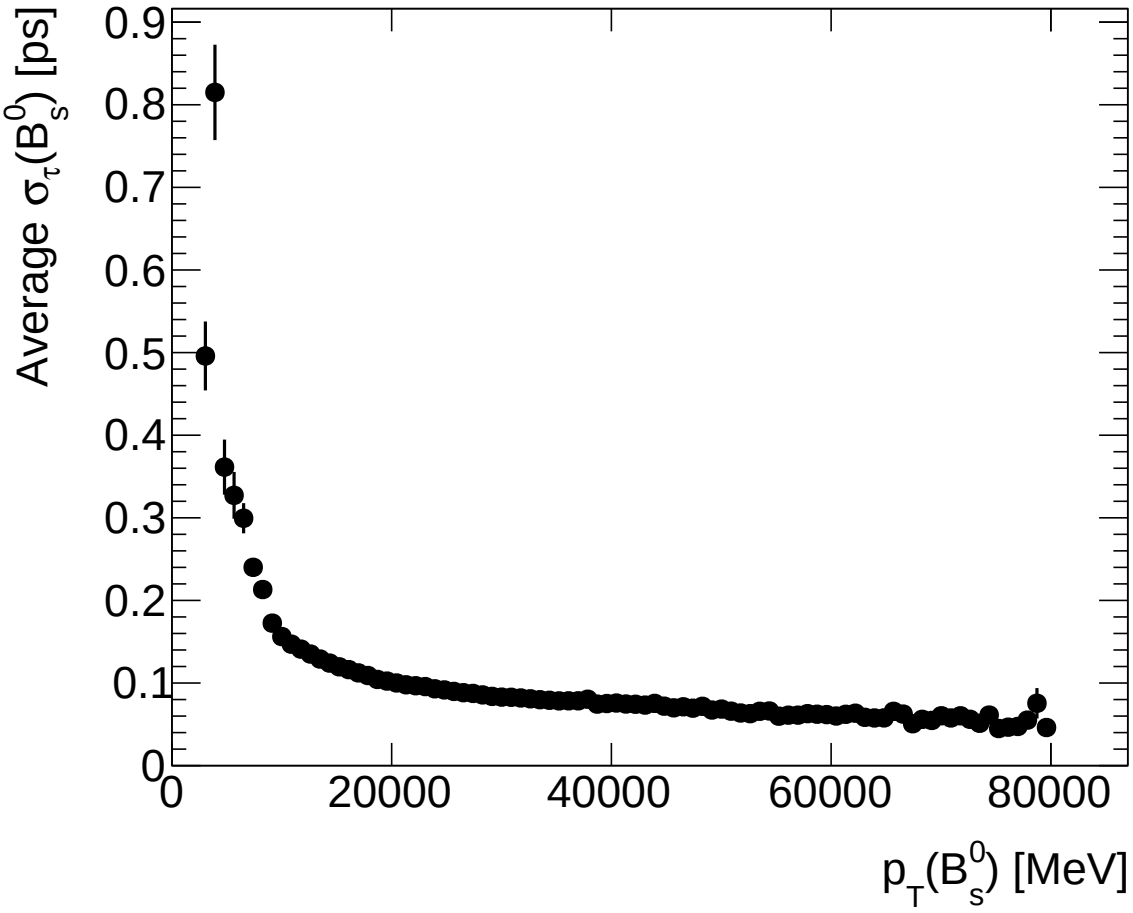

Figure 6.3: A plot showing the average proper decay time uncertainty of candidates with varying p_T

B_s meson candidate; this prevents possible bias in the L_{xy}. Approximately 80% of candidates did not share a track with the primary vertex, 3% of candidates share one to three tracks and 15% of candidates shared all their tracks with the primary vertex.

Each proper decay time is calculated with an associated uncertainty. This is calculated using the covariance matrix of the tracks quadruplet vertex fit. This value is known to be correlated with the p_T of the tracks; higher energy tracks offer better vertex and lifetime resolution as can be seen in figure 6.3.

6.3 Further Selections

A piece of software written by the author is employed to make further selections and any additional calculations necessary before placing the data in a final root file to be stored before maximum likelihood fitting. This applies the final selection cuts described later. If more than one candidate in any event passes all the cuts, the candidate with the best vertex fit quality is selected. The appropriate ATLAS good run list is also applied; this eliminates events that may have been recorded while important equipment was not in a fully functional state and so were potentially mismeasured.

6.3.1 J/ψ Selection

The J/ψ are found by fitting oppositely charged muon tracks to a vertex; a cut is applied to only include those with a quality of vertex of $\frac{\chi^2}{NDOF} < 10$ (see figure 6.4). This loose vertex quality cut is just to exclude the worst $\mu^+\mu^-$ combinations. This cut is highly correlated with the cut on the quality of the B_s vertex, so is almost superseded by that cut later on. The invariant mass of the J/ψ candidates is calculated using the refitted tracks (ID track parameters in the fitted J/ψ vertex) of the muon-candidates. In order to account for variations in the track measurement precision and subsequently the mass resolution as a function of the pseudorapidity of the muon tracks, the J/ψ candidates were divided into three samples and different mass windows are opened for each of them:

- **Both muons in barrel region (BB)**, where barrel region is defined by requiring the muon track $|\eta < 1.05|$. Only J/ψ with invariant mass inside window of $2959 < m_{\mu^+\mu^-} < 3229$ MeV are considered further.

- **One muon in the barrel and second in endcap region (EB)** where the barrel region is defined as $|\eta < 1.05|$ and the endcap $|\eta > 1.05|$. Only J/ψ with invariant mass inside window of $2913 < m_{\mu^+\mu^-} < 3273$ MeV are considered further.

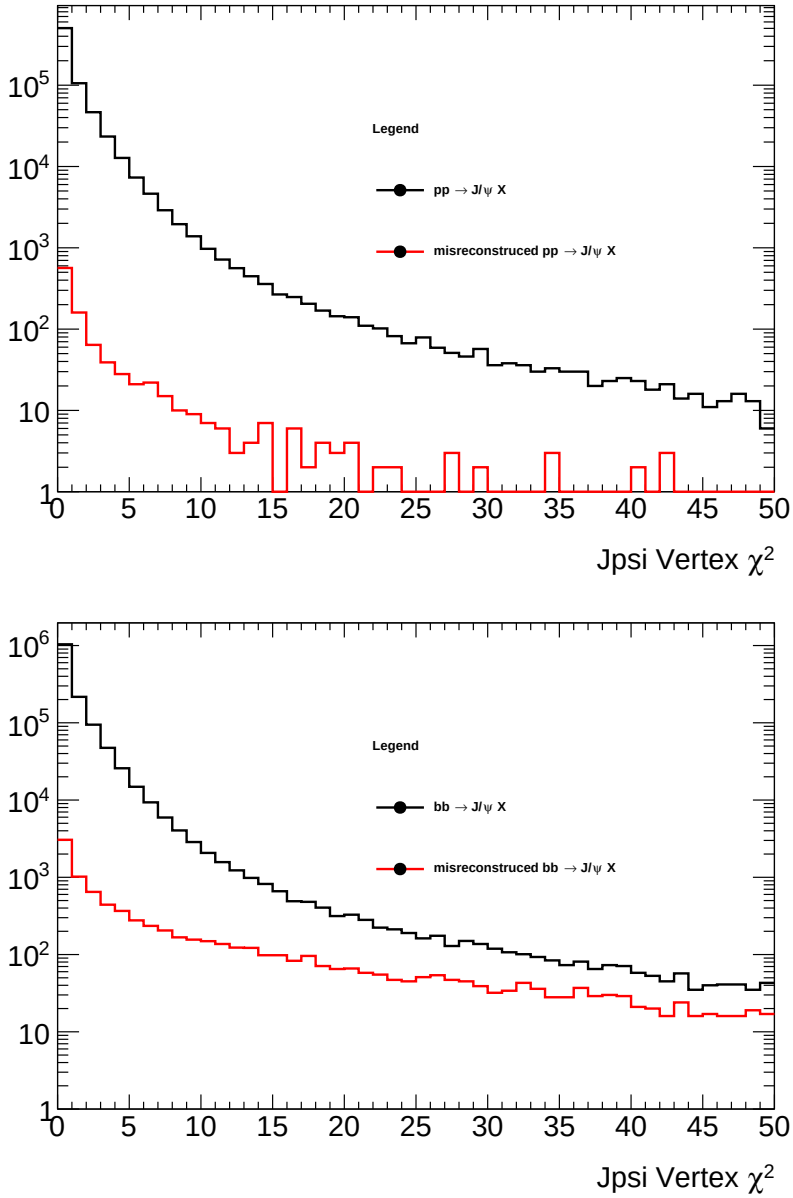

Figure 6.4: Plots showing the quality of the J/ψ vertex quality for Monte Carlo samples generated from $pp \to J/\psi\ X$ and $bb \to J/\psi\ X$. They demonstrate that a cut can exclude a significant amount of reconstructed J/ψ .

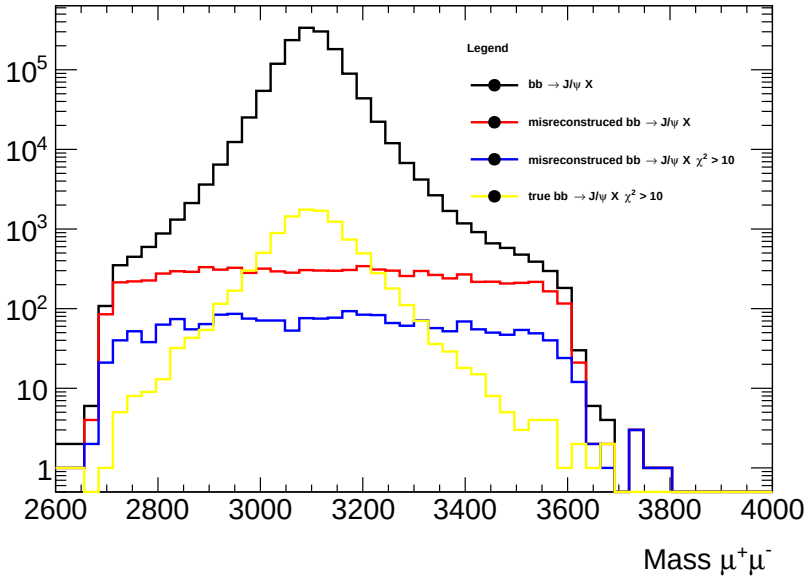

Figure 6.5: A plot showing the proportion of true and false candidates removed from the mass distribution by the chosen cut.

- **Both muons in endcap region (EE)** Only J/ψ with invariant mass inside window of $2852 < m_{\mu^+\mu^-} < 3332$ MeV are considered further.

The effect of these cuts can be see in figure 6.5.

The selection of the J/ψ mass windows is based on an unbinned, event by event error maximum likelihood fit of the J/ψ mass of the same η selection (see figure 6.6. See Appendix A). The mass windows are symmetric around the fitted mean value with a width retaining 99.8% of the extracted signal events. The fitted mean values are systematically shifted from the world average ($M_{PDG}(J/\psi\ ) = 3096.916 \pm 0.011$ MeV [20]) due to trigger p_T cuts and agree with the results of a detailed J/ψ analysis at the ATLAS detector [59].

6.3.2 Determining cuts with Monte Carlo

In order to justify the final cuts used and to understand the background composition of the final sample, simulations of the background components must be made and run through the same selections. *PythiaB* is used to generate a large sample of data with each event containing at least one b-quark pair decaying to a J/ψ with any other particle. The branching ratios that *Pythia* is configured to use are not

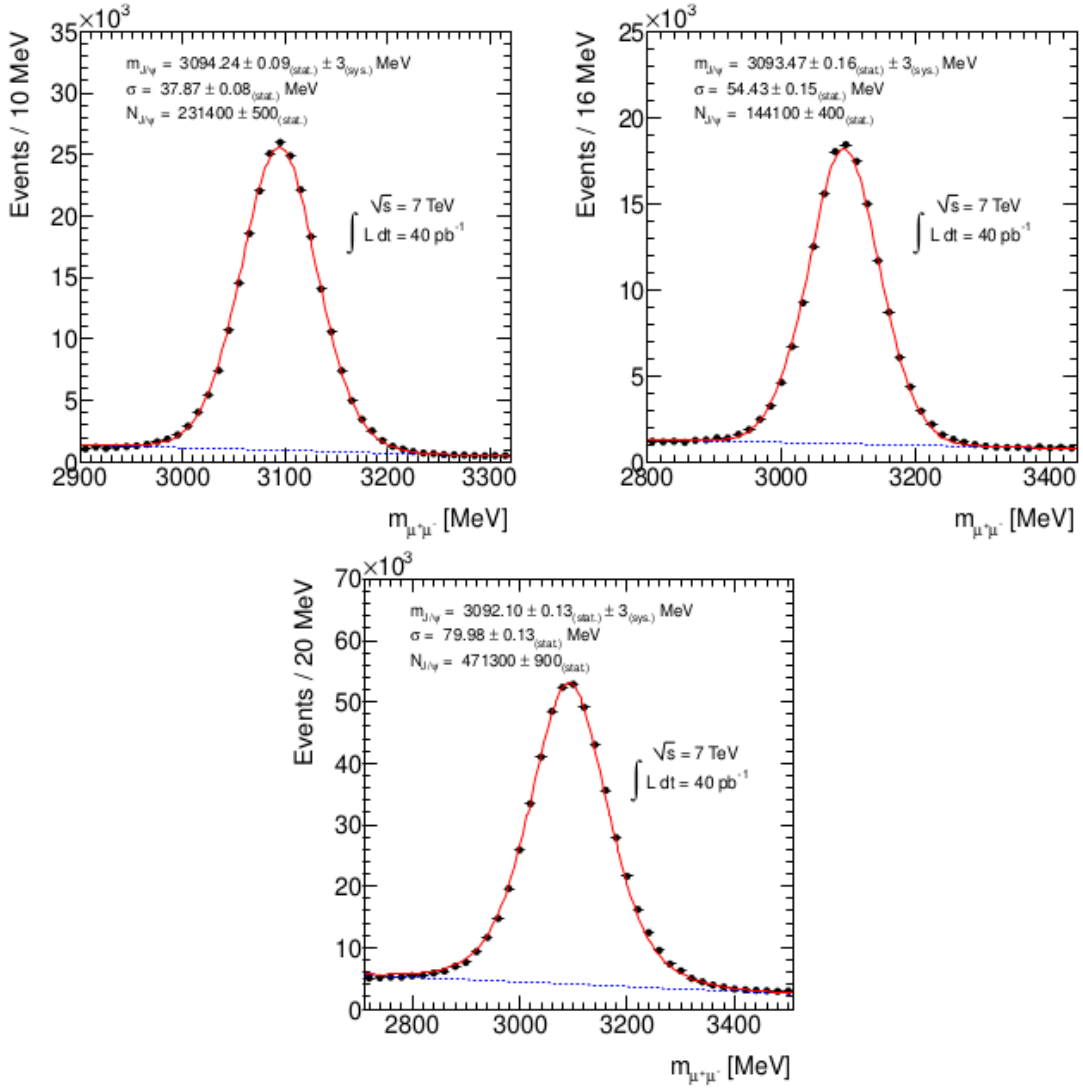

Figure 6.6: Di-muon invariant mass distributions for BB (top left), EB (top right) and EE (bottom) data samples accounting for different η of the muon tracks. The points are data and the solid red line represents the total of the fit to the data while the blue dashed lines show the background component of the fit. The signal model of the fit is a poly-Gaussian function, while the background is a linear function. Taken from Pavel Reznicek

Decay	Pythia	PDG (2012)
$B_s^0 \to J/\psi\phi$	0.00093	0.00109 ± 0.0028
$B_d^0 \to J/\psi\ K_0^*$	0.00132	0.00134 ± 0.00006
$B_d^0 \to J/\psi\ K\pi$	0.00029	0.0012 ± 0.0006
$B^+ \to J/\psi\ K\pi\pi$	0.00069	0.00081 ± 0.00013
$B_s^0 \to J/\psi\ KK$	0.0013	0.0014 estimated

Table 6.4: The branching rations of the exlcusive decays considered as measured by the PDG group and as set in the *Pythia* generator used. A correcting weighting is applied to the data accordingly.

regularly updated so the dedicated backgrounds are rescaled to match the latest PDG branching ratios (see table 6.4).

We initially apply a cut to the invariant mass of the B_s^0 candidate. This is to exclude the extremities of the mass spectrum while providing a sufficient amount of side-band and background to analyse.

Since there are a large number of hadronic tracks found by the inner detector (compared to the relatively few muons) the cut on the ϕ mass ($M_{K^+K^-}$) is essential to exclude much of the mis-reconstructed backgrounds and non-resonant decays. It also excludes a significant portion of combinatorial backgrounds. This can be seen in figure 6.7a. As can be seen in figure 6.7b a cut on the quality of the B_s vertex is very useful for excluding much of the combinatorial background, since such tracks are less likely to come from a similar vertex. A moderate cut to the transverse momentum of the hadronic tracks is also made to exclude further combinatorics.

Figure 6.7 shows the composition of the sample in terms of the parameters cut upons as each cut is applied. Figure 6.8 shows the final mass spectrum after all the cuts have been applied. The final cuts are described in table 6.5. The truth information of the selected "K" track can be found in table 6.6. The truth information of the particle that produced these tracks can be found in table 6.7. The truth information pertaining to the particle that produced this particle is in table 6.8. Table 6.9 contains the truth information about the parent of the selected "B_s".

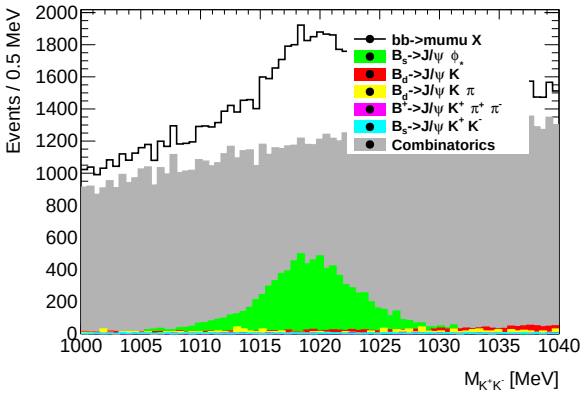

(a) A plot showing the composition of the ϕ mass spectrum after the J/ψ cuts were applied

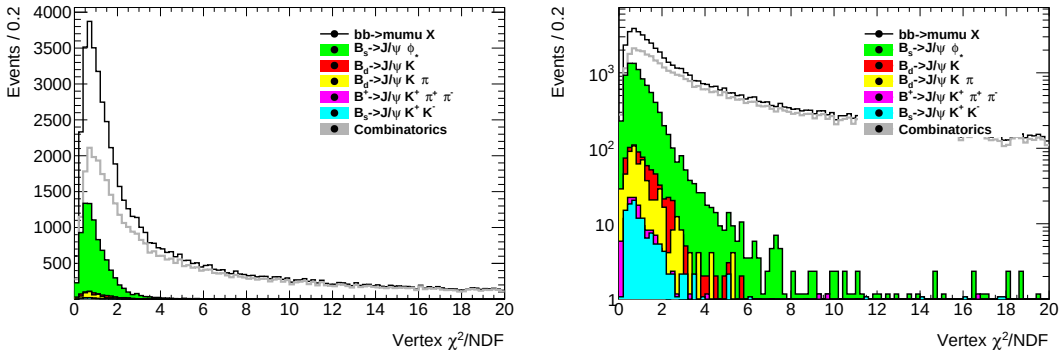

(b) Plots showing the composition of the $\frac{\chi^2}{NDF}$ spectrum and the J/ψ and ϕ mass cuts were applied. Left linear scale, right log scale.

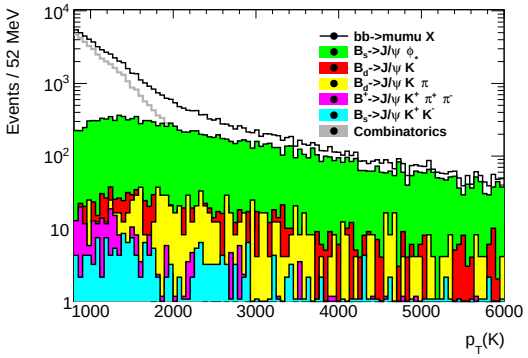

(c) A plot showing the composition p_T spectrum of the K meson after the J/ψ, ϕ mass and $\frac{\chi^2}{NDF}$ cuts were applied.

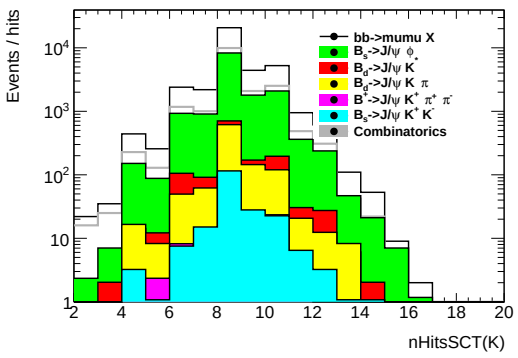

(d) A plot showing the composition of the SCT hit spectrum after the J/ψ , ϕ mass, $\frac{\chi^2}{NDF}$ and $p_T(K)$ cuts are applied

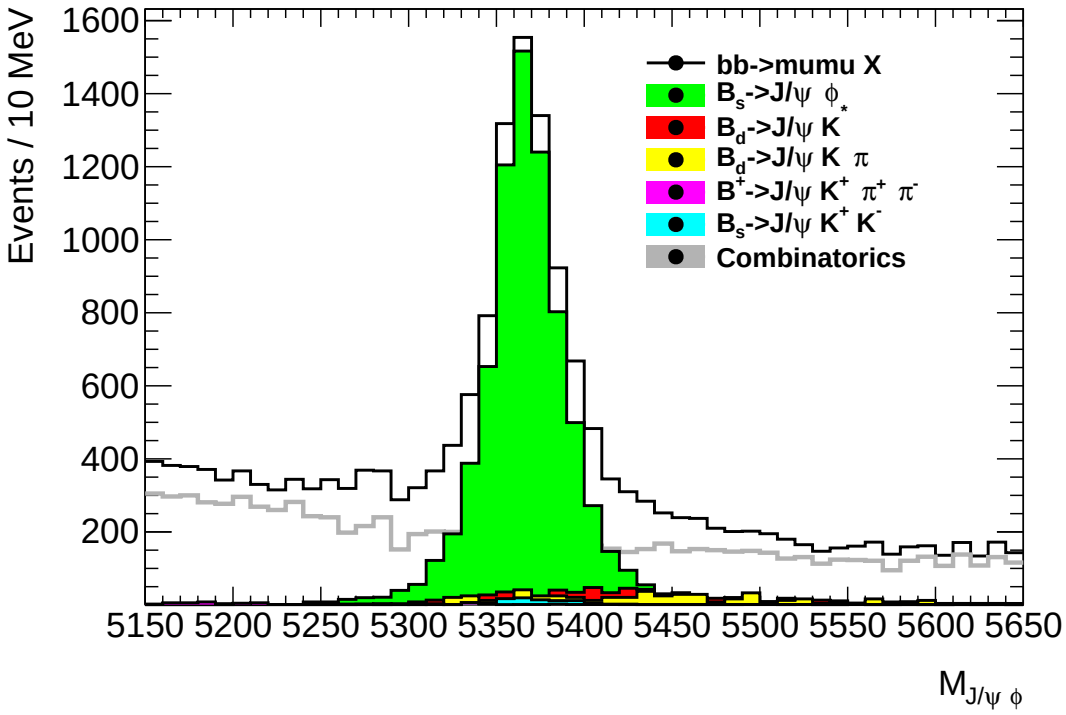

Figure 6.8: A plot showing the composition of the $B_s^0 \to J/\psi\phi$ mass spectrum after all cuts have been applied

Parameter	Final Cut
Muons	at least one combined muon
B_s^0 mass window	5150 to 5650 MeV
$p_T(K)$	> 1000 MeV
Quality of B_s vertex fit $\frac{\chi^2}{DOF}$	< 3.0
Number of SCT hits on all tracks	≥ 4
Mass window for the K^+K^-	1008 to 1030 MeV

Table 6.5: A table showing the final selection cuts

Composition of reconstructed and selected K track sample in Monte Carlo			
Parton	PDG Code	% in full mass window	% in signal region (3 sigma)
K^+	321	30.41%	40.59%
π	-211	24.15%	12.04%
K^-	-321	23.56%	37.01%
π^+	211	17.38%	8.45%
$\bar{p}$	-2212	1.28%	0.60%
p	2212	1.23%	0.55%
false track	0	1.11%	0.39%

Table 6.6: A table showing the truth information from the selected K inner detector tracks for the reconstructed $B_s^0 \to J/\psi\phi$ from a $bb \to J/\psi\ X$ sample after the full selection cuts have been made

Sources for the selected candidate K track			
Parton	PDG Code	% in full mass window	% in signal region (3 sigma)
ϕ	333	40.33%	69.70%
"string"	92	11.88%	5.15%
K^{0*}	313	6.54%	5.42%
K^{*+}	323	4.72%	2.16%
ρ^{+}	213	4.35%	2.08%
ρ^{0}	113	3.93%	1.95%
ω	223	3.83%	2.03%
K^{0}	10313	3.32%	0.79%
B^{+}	521	2.53%	1.12%
$K(1270)^{+}$	10323	2.53%	0.71%
B^{0}_{d}	511	2.22%	1.19%
η	221	1.61%	0.76%
combinatoric	0	1.11%	0.39%

Table 6.7: A table showing the truth information from the reconstructed $K^{+}K^{-}$ particle inner detector tracks for the reconstructed $B^{0}_{s} \rightarrow J/\psi\phi$ from a $bb \rightarrow J/\psi\ X$ sample after the full selection cuts have been made

Sources for the source of the selected candidate K track			
Parton	PDG Code	% in full mass window	% in signal region (3 sigma)
combinatoric	0	49.70%	22.36%
B^{0}_{s}	531	35.86%	67.52%
B^{0}_{d}	511	6.56%	4.66%
string	92	3.24%	2.09%
B^{0*}	513	0.66%	0.42%
B^{*}_{s}	-531	0.45%	0.86%
B^{*+}	523	0.31%	0.12%
B^{*}_{s}	533	0.27%	0.51%
D^{+}_{s}	-431	0.21%	0.12%
$K(1270)^{+}$	10323	0.20%	0.06%

Table 6.8: A table showing the truth information about the reconstructed $B^{0}_{s} \rightarrow J/\psi\phi$ from a $bb \rightarrow J/\psi\ X$ sample after the full selection cuts have been made

Source for the grandparent of the selected candidate K track.			
Parton	PDG Code	% in full mass window	% in signal region (3 sigma)
combinatorics	0	57.15%	26.90%
B^{0*}_{s}	533	20.11%	37.80%
string	92	16.55%	28.88%
B^{0*}	513	3.77%	2.75%

Table 6.9: A table showing the truth information about the parent of the reconstructed $B^{0}_{s} \rightarrow J/\psi\phi$ from a $bb \rightarrow J/\psi\ X$ sample after the full selection cuts have been made

6.4 Optimising the Trigger Strategy

The trigger strategy employed is applied online and must meet the requirements of all the B-physics group's analyses. For this particular analysis the most important factor relating to the trigger is the uncertainty it introduces into the ϕ_s determination; this is affected by both the number of events and the quality of the proper decay time measurement.

$$\sigma_{\phi_s} = \frac{1}{D \times \sqrt{N}} \tag{6.1}$$

where σ_{ϕ_s} is a relative estimate of the uncertainty of the ϕ_s measurement, N is the number of signal events in the sample and D is:

$$D = \exp(-0.5 \times (\bar{\sigma_\tau} \times \Delta m_s)^2) \tag{6.2}$$

where $\bar{\sigma_\tau}$ is the average uncertainty on the proper decay time of the sample and Δm_s is the mixing rate of the B_s^0 meson.

As demonstrated in figure 6.3, the higher the p_T of the B_s meson the lower the uncertainty on the proper decay time. This would suggest that increasing trigger thresholds will provide a richer sample provided the triggers are pre-scaled in a way to ensure the bandwidth is filled with events, as sacrificing total events would also harm accuracy. This is in contrast with the alternative strategy of simply pre-scaling the lower p_T triggers to keep within bandwidth limits which would not serve to improve the average proper decay time uncertainty.

6.5 Tagging

To make full use of the information on the B_s^0 states one can determine the state of the neutral B meson i.e. whether it is a B_s or $\bar{B_s}$ during its creation ($t = 0$), before it is given a chance to mix (neutral B mixing). This can be done by a variety of complex methods called flavour tagging. These methods come in two

categories: **same side tags** where the decay chain on the same side of the $b\bar{b}$ pair of the selected B-meson decay chain is analysed to find associated fragment tracks that could identify the flavour of the B-meson, and **opposite side tags** where the decay chain on the opposite side of the $b\bar{b}$ pair is analysed to find elements that could identify the flavour of the B-meson. Associated fragment tracks can also be used in opposite side tagging. In this section a brief overview of tagging will be presented but no technical details, as these are better addressed by dedicated theses and papers.

Opposite side tags rely on the quark of the $b\bar{b}$ pair that does not participate in the signal process. Sometimes this decay process is such that the original state of the quark can be determined. From this we can determine the state of the signal B-meson since it is necessarily the opposite of the quark in this decay chain. One method relies on the decay containing a semi-leptonic decay and since this is easily identified by the detector, the charge can be measured and used to infer the flavour of the b-quark. A positively charged lepton indicates a $\bar{b}$-quark and therefore a $\bar{B}$ (which contains a b-quark) meson on the signal side and vice-versa for negative muons.

Much of the time an opposite side semi-leptonic decay is not available, so a weighted sum of the charge of the tracks associated to the B-meson decay will also provide some statistical indicator for separation.

6.5.1 Common measures of tag quality

Tagging, since it is very probabilistic and prone to error, comes with a variety of methods for describing the quality of a given result. Generally these refer to the efficiency and the resulting purity of the sample. The efficiency is the fraction of events which received a tag decision (a right or wrong decision):

$$\epsilon_{\text{tag}} = \frac{N_r + N_w}{N_t} \tag{6.3}$$

where N_r and N_w are the number of correctly and incorrectly tagged events

respectively. N_t is the total number of events processed by the tagging algorithm.

The purity is given by the dilution factor:

$$D_{\text{tag}} = \frac{N_r - N_w}{N_r + N_w} = 1 - 2w_{\text{tag}} \tag{6.4}$$

where w_{tag} is the wrong tag fraction, that is, the number of incorrect tags as a fraction of the total number of tagged events, given by:

$$w_{\text{tag}} = \frac{N_w}{N_r + N_w}. \tag{6.5}$$

A better sample is that with a low wrong tag fraction and that with a purity close to 1. These can be combined into a metric called the tag quality or tag power and is given by:

$$Q_{\text{tag}} = \epsilon_{\text{tag}} D_{\text{tag}}^2 = \sum_i \epsilon_i D_i^2 \tag{6.6}$$

While not used directly in the analysis, it is useful when selecting the optimum tagging criteria and provides insight into the tagging method.

6.5.2 Tagging Method

The determination of the initial flavour of neutral B-mesons is inferred using information from the other B-meson that is typically produced from the other b quark - opposite side tagging. To study and calibrate this other-side tagging, the decay $B^{\pm} \to J/\psi K^{\pm}$ is used since the charge of the B-meson at production is provided by the kaon charge.

Candidates for $B^{\pm} \to J/\psi K^{\pm}$ decays are identified in the following way:

- using two oppositely-charged combined muons forming a good vertex using information supplied by the inner detector (STACO Muons).
- Each muon is a *combined* muon and passes the Muon Combined Performance (MCP) group recommended selection criteria as described here: Only the

inner detector measurements of the muon are used for the fitting after the following kinematic selection cuts:

- The transverse momentum of each muon should be $p_T > 4$ GeV
- The pseudo rapidity of the muon $|\eta| < 2.5$
- The χ^2 probability of the vertex fit ≥ 0.001
- The invariant mass be within $2.8 < m(\mu\mu) < 3.4$ GeV

An additional track is combined with the muon to be the J/ψ candidate and a mass-constrained (for the J/ψ) fit is performed. The kaon is required to have:

- $p_T(K) > 1$ GeV
- $|\eta(K)| < 2.5$ GeV
- Requiring a B-layer hit, if a hit in the B-layer would have been expected
- $\chi^2(B) \geq 0.001$
- A transverse decay length of $L_{xy} > 0.1$ cm is applied to remove the majority of the prompt component of the background.

To fit the invariant mass of the candidates that pass this criteria, a *RooFit*[1] [60] extended binned likelihood is used. Events are separated into five regions of B candidate rapidity and three mass regions. The mass regions are defined as a signal region around the fitted peak signal mass position $\mu \pm 2\sigma$ and the sidebands are $[\mu - 5\sigma, \mu - 3\sigma]$ and $[\mu + 3\sigma, \mu + 5\sigma]$ where μ and σ are the peak and widths of the Gaussian model of the B signal mass respectively. Individual binned extended likelihood fits are performed to the invariant mass distribution in each region of rapidity.

The background is modelled by an exponential to describe combinatorial background and a hyperbolic tangent function to parametrise the low-mass contribution from the misreconstructed or partially reconstructed B^+ decays. This component

[1] a framework extending the statistically fitting software available in ROOT

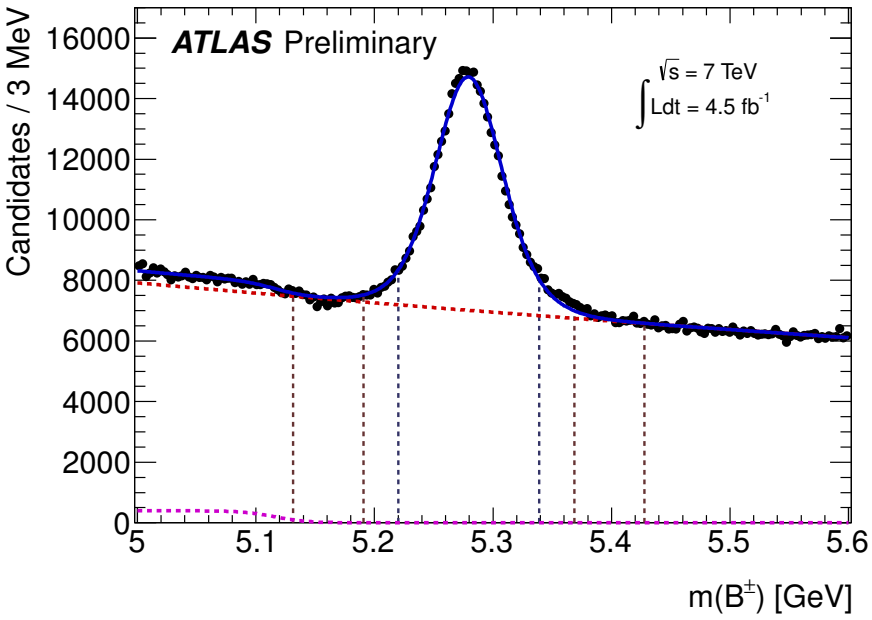

Figure 6.9: The invariant mass distribution for $B^{\pm} \to J/\psi K^{\pm}$. Included in this plot are all events passing the mentioned criteria. The red vertical dashed lines indicate the left and right sidebands while the blue vertical dashed lines indicate the signal region. Taken from [61]

makes negligible contribution to either the signal or sideband regions. Figure 6.9 shows the invariant mass distribution of B^{+} candidates for all rapidity regions overlaid with the fit results for the combined data.

Several methods of opposite-side flavour tagging are available, with differing efficiencies and discriminating powers. One method is to identify the charge of a muon through the semi-leptonic decay of the B meson which provides a strong power of separation. Problems arise however from the $b \to \mu$ transitions that are diluted through neutral B meson oscillations, as well as by cascade decays $b \to c \to \mu$ which can alter the sign of the muon relative to the one coming from direct semi-leptonic decays $b \to \mu$. This separation power of tag muons can be enhanced by considering a weighted sum of the charge of the tracks in a cone around the muon. If no muon is present, a weighted sum of the charge of tracks associated to the opposite side B meson decay will provide some separation.

An additional muon is searched for in the event, having originated near the original interaction point. Muons are separated into their reconstruction types,

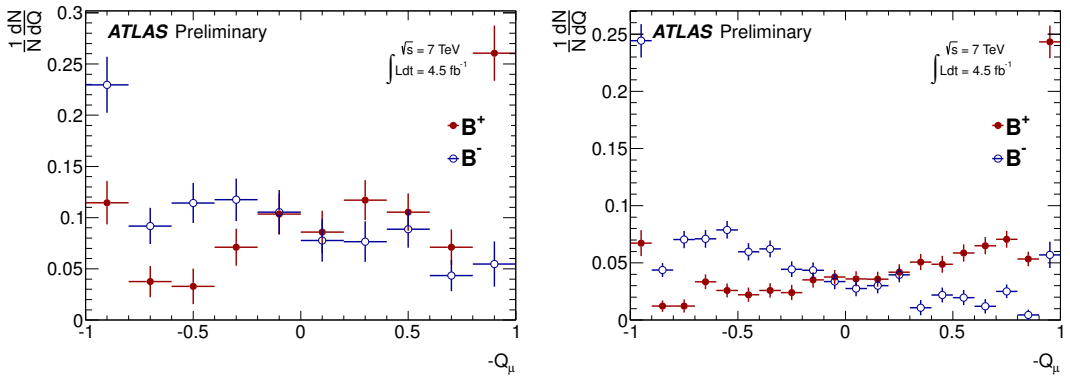

Figure 6.10: Muon cone charge distribution for $B^{\pm}$ signal candidates for *segment tagged* (left) and *combined* (right) muons. [61]

combined and *segment tagged*. When an event contains more than one additional muon, the one with the highest transverse momentum is chosen. A muon *cone charge* variable is constructed:

$$Q_{\mu} = \frac{\sum_{i}^{N_{\text{tracks}}} q^{i} \cdot (p_{T}^{i})^{k}}{\sum_{i}^{N_{\text{tracks}}} (p_{T}^{i})^{k}} \tag{6.7}$$

where the value of the parameter $k = 1.1$, which was tuned to optimise the tagging power, and the sum is performed over the reconstructed ID tracks within a cone of $\Delta R < 0.5$ around the muon momentum axis, with $p_T > 0.5$ GeV and $|\eta| < 2.5$. The value of parameter k is determined in the process of optimisation of the tagging performance. Tracks associated to the signal-side of the decay are excluded from the sum. Figure 6.10 shows the distribution of muon cone charge for candidates from $B^{\pm}$ signal decays for the different types of muons.

When extra muons are not found, a b-tagged jet [62] is searched for in the event, with tracks associated to the same primary vertex as the signal decay, excluding those tracks from the signal candidate. The jet is reconstructed using the anti-k_T algorithm with a cone size of 0.6. In the case of multiple jets, the jet with the highest value of the b-tag weight reference is used.

A *jet charge* is defined:

$$Q_{\text{jet}} = \frac{\sum_{i}^{N_{\text{tracks}}} q^{i} \cdot (p_{T}^{i})^{k}}{\sum_{i}^{N_{\text{tracks}}} (p_{T}^{i})^{k}} \tag{6.8}$$

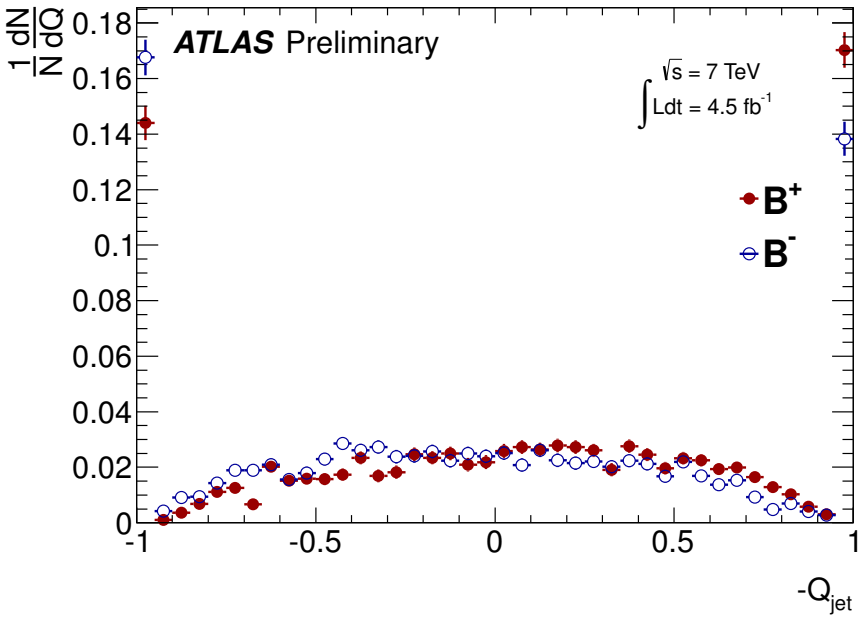

Figure 6.11: Jet-charge distribution for $B^{\pm}$ signal candidates [61]

where $k = 1.1$ and the sum is over the tracks associated to the jet, using methods described in [13]. Figure 6.11 shows the distribution of charges for the jet-charge from $B^{\pm}$ signal-side candidates.

Using the efficiency of an individual tagger as defined in equation 6.3, a probability that a specific event has a signal decay containing a $\bar{b}$ given the value of the discriminating variable $P(B|Q)$ is constructed from the calibration samples for each of the B^+ and B^- samples, defining $P(Q|B^+)$ and $P(Q|B^-)$ respectively. The probability to tag a signal event as a $\bar{b}$ is therefore

$$P(B|Q) = \frac{P(Q|B^+)}{P(Q|B^+) + P(Q|B^-)}$$

and

$$P(\bar{B}|Q) = 1 - P(B|Q)$$

For this system the tagging power is defined as $\epsilon D^2 = \sum_i \epsilon_i \cdot (2P_i(B|Q_i) - 1)^2$, summing over the bins of the probability distribution as a function of the charge variable. The effective dilution D is calculated from the tagging power and the efficiency. The combination of the tagging methods is applied according to the

Tagger	Efficiency [%]	Dilution [%]	Tagging Power [%]
Segment Tagged muon	1.08 ± 0.02	36.7 ± 0.7	0.15 ± 0.02
Combined muon	3.37 ± 0.04	50.6 ± 0.5	0.86 ± 0.04
Jet Charge	27.7 ± 0.1	12.68 ± 0.06	0.45 ± 0.03
Total	32.1 ± 0.1	21.3 ± 0.08	1.45 ± 0.05

Table 6.10: Summary of tagging performance for the different tagging methods used in the tagged fit. Only statistical uncertainty shown.

hierarchy of performance, in order of descending performance: *combined* muon cone charge, *segment tagged* muon cone charge, jet charge. The single best performing tagging measurement available in the given event is used. If no tagging method is available the probability value of 0.5 is assigned. A summary of the performance is given in table 6.10. Fits for the tag probability can be seen in figure 6.12.

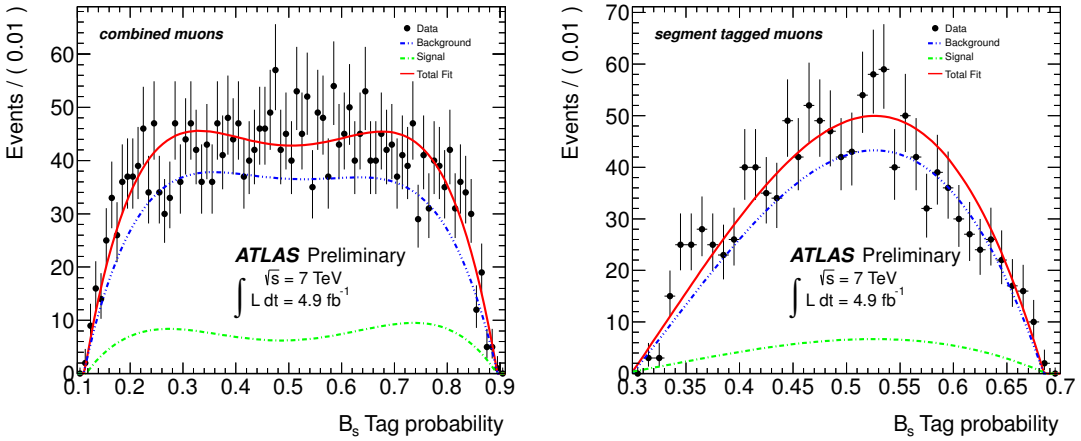

(a) The tag probability for tagging using combined muons.

(b) The tag probability for tagging using segment tagged muons.

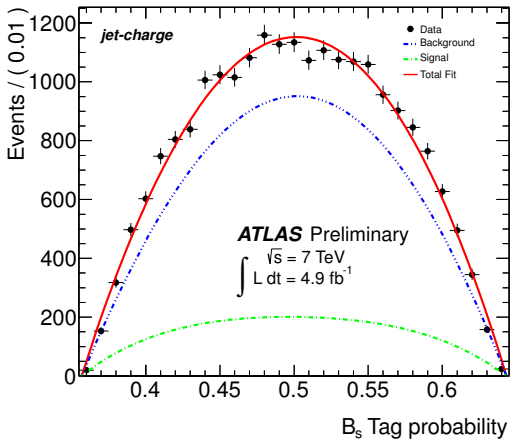

(c) The tag probability for tagging using jet-charge.

Figure 6.12: The tag probability for tagging using the applied methods. Black dots are data after removing spikes, blue is a fit to the sidebands, green to the signal and red is a sum of both fits. [61]

Chapter 7

Acceptance Corrections

It is essential to study if the acceptance of events such as this would distort the distributions and introduce systematic biases into the measurement. Such biases can usually be corrected by introducing factors into the likelihood fit.

Since this measurement is not reliant on crosssection information there is no need to account for absolute reconstruction efficiencies except when any are lifetime or angular dependent. The cuts applied must also be checked using Monte Carlo data to identify any biases introduced.

A large sample of $B_s^0 \rightarrow J/\psi\phi$ events are produced using *PythiaB* and the ATLAS simulation and reconstruction software via the official ATLAS production system. A selection of exaggerated cuts are applied and the average true proper decay time is calculated. Looking at table 7.1 one can identify that applying a mass cut on the reconstructed ϕ introduces a lifetime bias. However, the bias is so small that it is far smaller than the statistical error currently associated with measurements of real data and therefore not worth correcting at this time.

A small lifetime acceptance bias is identified using the tag and probe method in the muon triggers affecting the distribution of the muon transverse impact parameter d_0. This method examines offline reconstructed muons with muons selected by the trigger to identify biases (described in [63]). These measurements allow a correcting term to be introduced into the fit.

Simulations show that the di-muon trigger efficiency can be expressed as a

$B_s(\tau)$ set in PythiaB	1.534 ps^{-1}
No cuts applied	1.5333 ± 0.0004 ps^{-1}
$M_{KK} = 1019.45 \pm 11$ MeV	1.5318 ± 0.0004 ps^{-1}
$M_{KK} = 1019.45 \pm 5$ MeV	1.5228 ± 0.0005 ps^{-1}
$p_T(K) > 3000$ MeV	1.5332 ± 0.0007 ps^{-1}
$3050 < M_{J/\psi} < 3200$ MeV	1.5332 ± 0.0004 ps^{-1}
$\frac{\chi^2}{NDF}$ of $B_s < 3$	1.5330 ± 0.0004 ps^{-1}

Table 7.1: The average proper decay time for a variety of cuts from reconstructed $B_s^0 \to J/\psi\phi$ - we identify that the M_{KK} cut introduces a bias into the proper decay time measurement

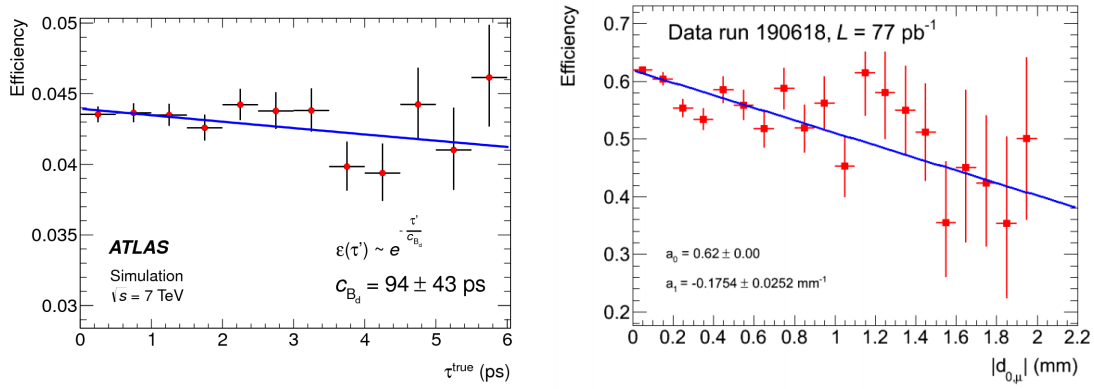

Figure 7.1: Plots showing tag-and-probe efficiency distributions found in the 2011 triggers. Taken from the work of Daniel Scherich and [63]

product of the single muon efficiencies (see figure 7.2). The efficiency correction is determined using a weighted MC sample by comparing the B_s^0 lifetime of an unbiased sample with the lifetime obtained after including the dependence of the trigger efficiency on the muon transverse impact parameter as measured from the data. The difference of the two lifetimes determines the value of ϵ ($\epsilon = 0.013 \pm 0.004$ ps). The uncertainty 0.004 ps, which reflects the precision of the tag-and-probe method, is used to assign a systematic uncertainty due to this time efficiency correction. The effeciency determined by the tag and probe can be seen in figure 7.1.

$$w = e^{-|t|/(\tau_{\text{sing}}+\epsilon)} / e^{-|t|/\tau_{\text{sing}}} \tag{7.1}$$

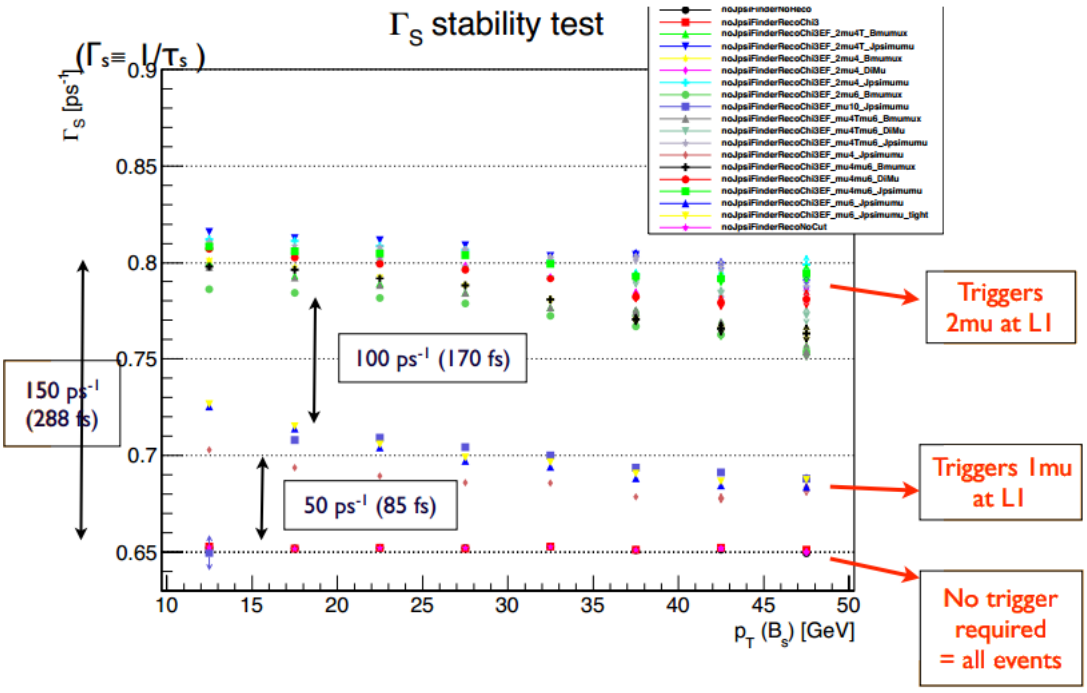

Figure 7.2: A plot demonstrating the effect of the trigger bias using Monte Carlo data. Note the size of the effect is larger in Monte Carlo compared to the real data because of a bug in the simulation software. It also remonstrates that there is no bias in the reconstruction process, only the trigger selection.

7.1 Angular Acceptance

The acceptance of the angles needed for the analysis are explored by using *PythiaB* to generate a large number of events using no additional physics considerations beyond those provided by *Pythia*. For each angle the resulting distribution is flat before any cuts are applied. Applying p_T cuts to any of the four end state tracks shapes the distributions in different ways. Applying cuts to the p_T of the muons shape the $\cos(\theta_l)$ of the helicity angles and both the $\cos(\theta_T)$ and ϕ_T angles in the transversity angles; this can be seen in figure 7.3a. Applying cuts only to the kaon track shapes apply minor shaping to the different angles; this can be seen in figure 7.3b. A "realistic" set of cuts are applied in figure 7.3c; when used in combination we see additional shaping in $\cos(\theta_l)$ of the helicity angles and both the $\cos(\theta_T)$ and ϕ_T angles in the transversity angles. These acceptance functions also depend on the p_T of the B_s meson; the shapes are less pronounced for B_s^0 mesons of higher p_T, and this can be scene in figure 7.4.

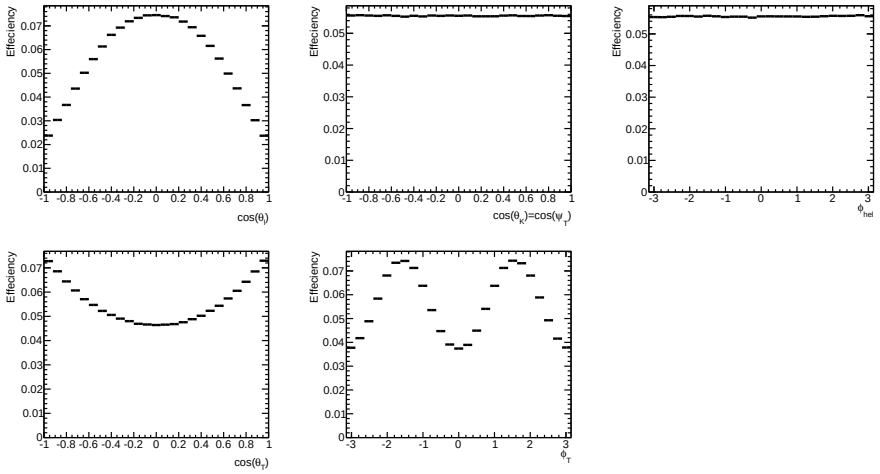

(a) Flatly generated $B_s^0 \to J/\psi\phi$ after applying a cut of 4 GeV to both muons

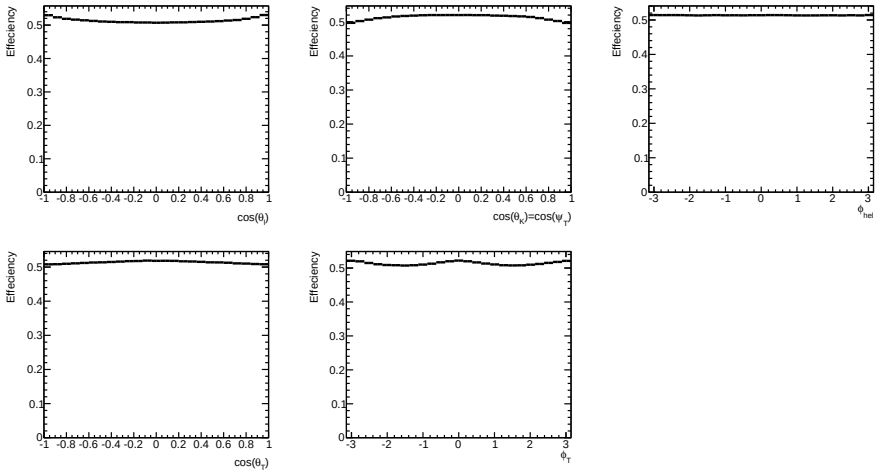

(b) Flatly generated $B_s^0 \to J/\psi\phi$ after applying a cut of 1 GeV to both kaons

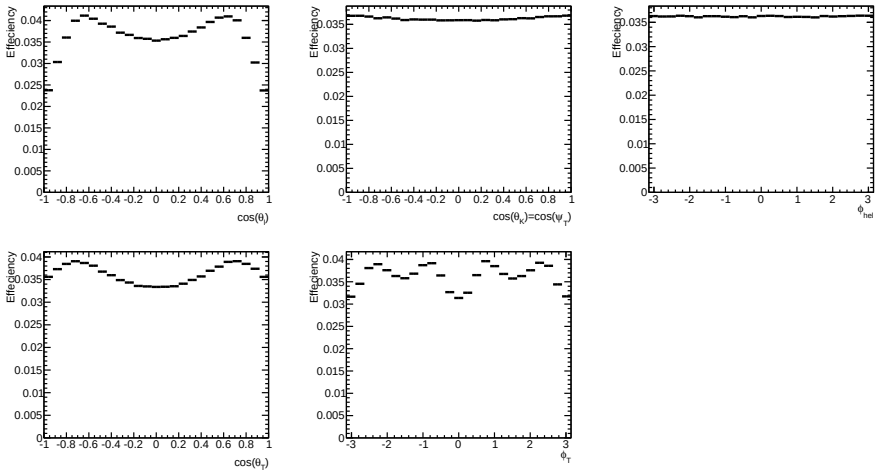

(c) Flatly generated $B_s^0 \to J/\psi\phi$ after applying a cut of 4 GeV to both muons and 1 GeV cut to both kaons

Figure 7.3: A series of plots to demonstrate how the acceptance functions of the angles react to cuts to the four end-state tracks

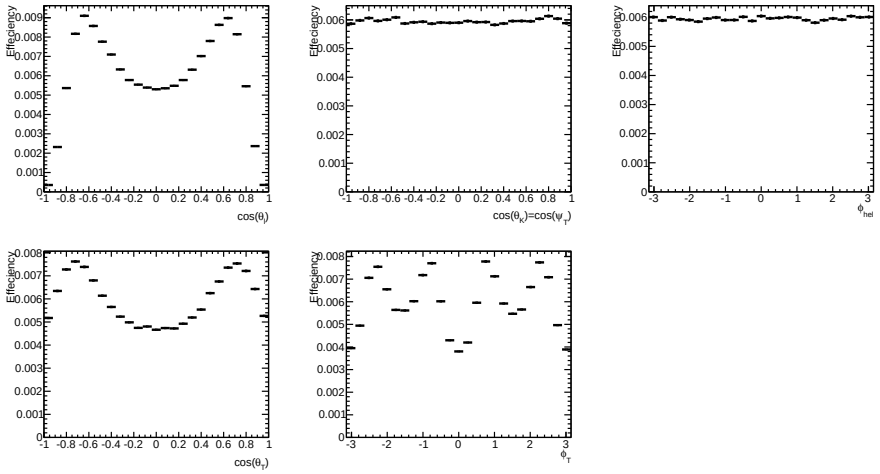

(a) Flatly generated $B_s^0 \to J/\psi\phi$ after applying a cut of 4 GeV to both muons and 1 GeV cut to both kaons and $p_T(B_s) < 14$ GeV

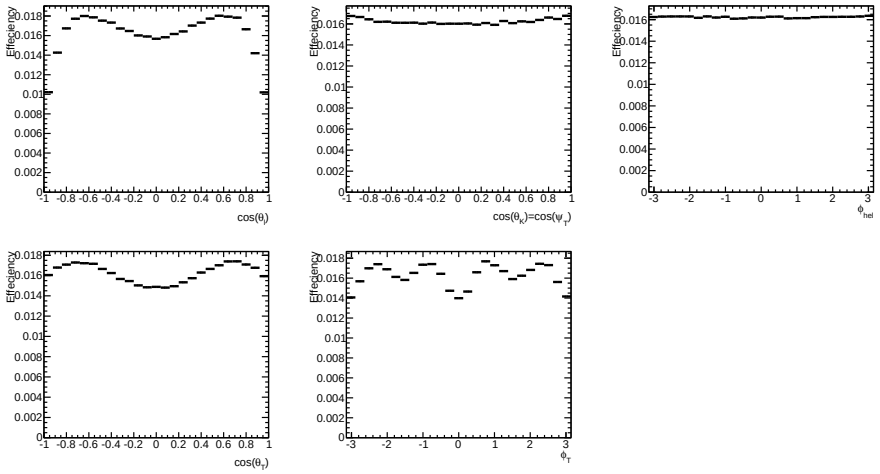

(b) Flatly generated $B_s^0 \to J/\psi\phi$ after applying a cut of 4 GeV to both muons and 1 GeV cut to both kaons and $14 < p_T(B_s) < 21$ GeV

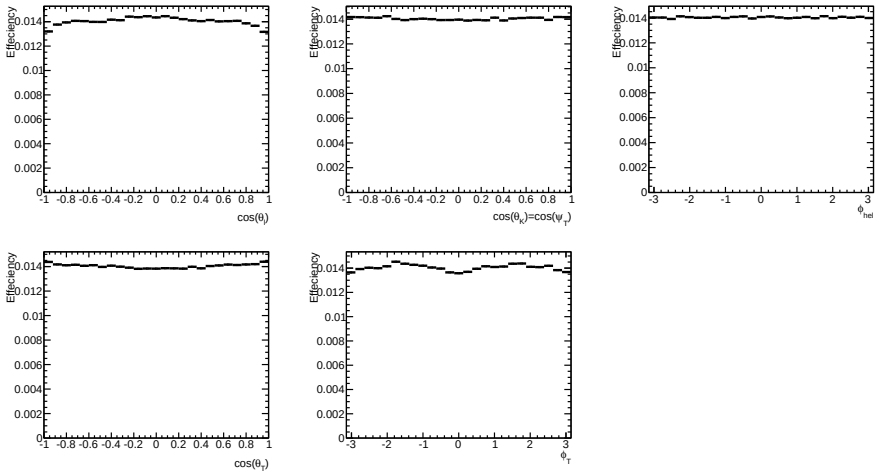

(c) Flatly generated $B_s^0 \to J/\psi\phi$ after applying a cut of 4 GeV to both muons and 1 GeV cut to both kaons and $p_T(B_s) > 21$ GeV

Figure 7.4: A series of plots to demonstrate how the acceptance functions of the angles react to cuts to the B_s meson.

As demonstrated, the primary influence on the acceptance is the p_T cut on the muons. No cut on the p_T of the muons is applied at the offline analysis but instead through the online triggers. Thus the acceptance actually used is a mixture of the trigger menus, including prescaling. Monte Carlo reconstruction simulates the various triggers used but not the prescaling used during data taking; to account for this *trigger weighting* is used to shape the distributions accordingly. This can be verified by comparing the weighted Monte Carlo with the real data sample. This is done by creating a binary map to attach a weight to various combinations of triggers; this weight is then introduced during the construction of the acceptance maps.

For trigger combination i the trigger weight map W_i is obtained by taking the ratio of events that appear in real data N_{data_i} and Monte Carlo N_{MC_i} from an uncut generated sample after the full offline selection cuts for the following collection of triggers (some triggers are in the same collection because they have almost identical effects):

1. EF_2mu4_Jpsimumu or EF_2mu4T_Jpsimumu
2. EF_mu4mu6_Jpsimumu or EF_mu4Tmu6_Jpsimumu
3. EF_mu4_Jpsimumu
4. EF_mu6_Jpsimumu or EF_mu6_Jpsimumu_tight
5. EF_mu10_Jpsimumu
6. EF_mu18_MG or EF_mu18_MG_medium

These trigger names are internal ATLAS strings for various trigger configurations. They can naïvely be thought of as applying a p_T cut to the muons in the event; the magnitude of the cut corresponds to the number following the "mu" in the string. For instance "2mu4" indicates both muons passed a 4 GeV p_T cut at the trigger level. While "mu4mu6" requires one muon to be have passed a 6 GeV p_T cut and

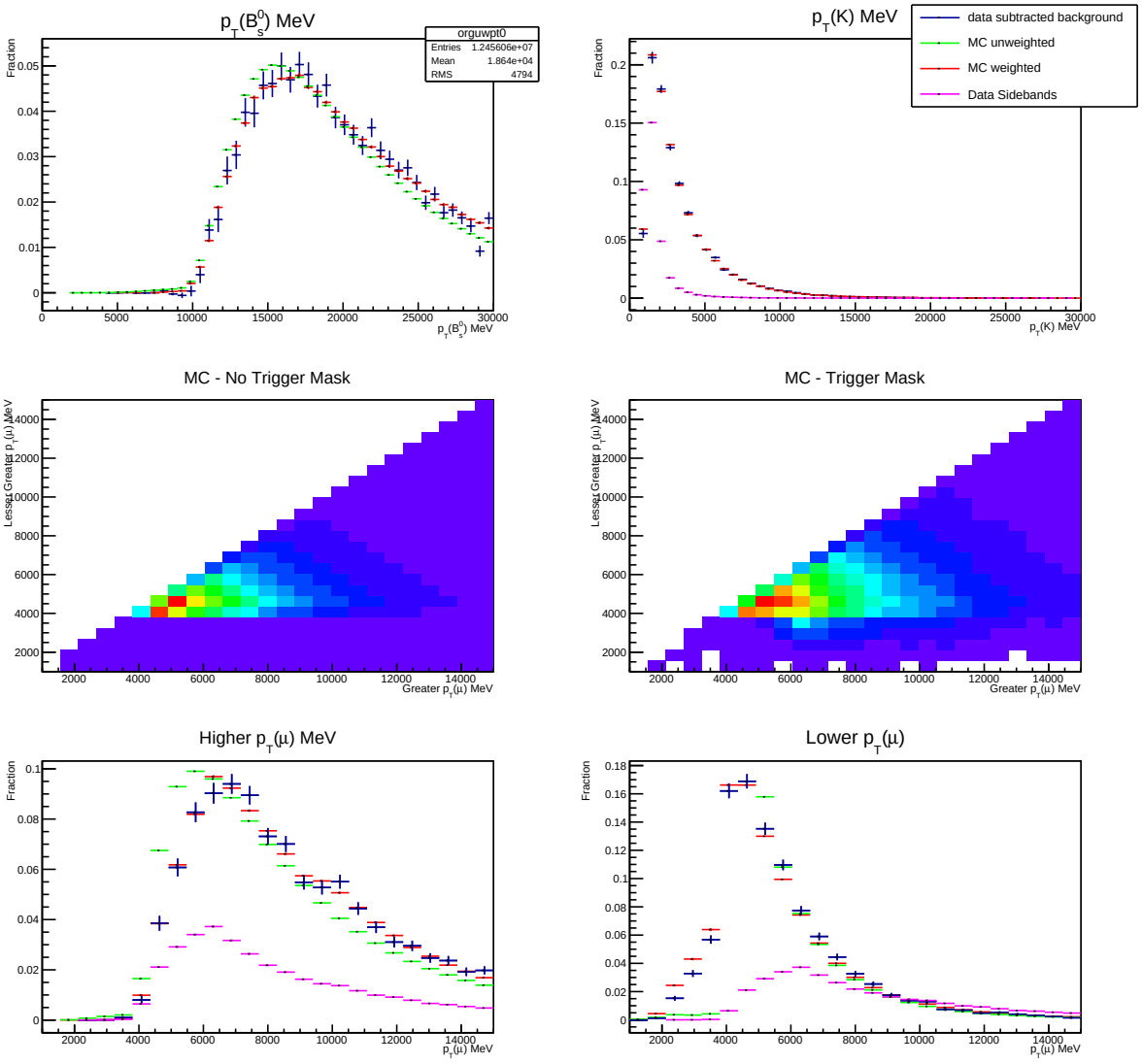

Figure 7.5: A series of plots comparing various parameters of the 2011 data sample with the combined Monte Carlo sample after applying trigger masks

the other to have passed a 4 GeV p_T cut. Further information on the triggers can be found in ATLAS documentation [64].

$$W_i = \frac{N_{data_i}}{N_{MC_i}} \tag{7.2}$$

If a given Monte Carlo event has passed one or more of the six combinations then the assigned weight to that trigger combination is the greatest of those weighting factors. While this method could be improved further, it does provide an adequate represention of the 2011 trigger menus, as can be seen in figure 7.5.

The acceptance map is built by combining signal events from two reconstructed

PythiaB generations with cuts placed on the muons of $p_T(\mu) > 1000$ MeV and $p_T(\mu) > 4000$ MeV; these are separated for efficiency sake. While most of the events accepted by triggers are above 4 GeV, those below are also sensitive to acceptance corrections and need a lot of data to account for the trigger prescaling. These samples are mixed by combining the trigger weight factor with an additional mixing factor. To calculate this factor f a function is used to count and weight all the events in both samples with a $p_T > 4$ GeV. This is calculated as:

$$A = \sum_{i=0}^{N_{\mu 1}} \begin{cases} W_i & \text{if } p_T > 4000\text{MeV} \\ 0, & \text{otherwise} \end{cases} \tag{7.3}$$

$$B = \sum_{j=0}^{N_{\mu 4}} \begin{cases} W_i & \text{if } p_T > 4000\text{MeV} \\ 0, & \text{otherwise} \end{cases} \tag{7.4}$$

$$f = \frac{A}{A+B} \tag{7.5}$$

where $N_{\mu 1}$ and $N_{\mu 4}$ are total number of signal events in the $p_T(\mu) > 1$ GeV and $p_T(\mu) > 4$ GeV respectively. A and B are the weighted count of the respective samples and W is a function returning the appropriate weight from the trigger map for the given event.

The acceptance maps are then populated with the samples as below:

$$M = \sum_{i=0}^{N_{\mu 1}} \begin{cases} W_i \times f & \text{if } p_T > 4000 \text{ MeV} \\ W_i, & \text{otherwise} \end{cases} + \sum_{j=0}^{N_{\mu 4}} \begin{cases} W_i \times f & \text{if } p_T > 4000 \text{ MeV} \\ W_i, & \text{otherwise} \end{cases} \tag{7.6}$$

where M is the 4 dimensional acceptance map where 3 dimensions are the chosen angular basis and the fourth is transverse momentum of the B_s^0.

It is observed that each angle is mostly symmetrical about zero and it is confirmed that there little diagonal correlation by looking at 2D dimensional plots (see figure 7.6). This fact is exploited to increase statistical precision by making

Bin number	$p_T(B_s^0)$ Boundary (MeV)
1	< 10000
2	10000 to 13000
3	13000 to 16000
4	16000 to 18000
5	18000 to 20000
6	> 20000

Table 7.2: A table showing the $p_T(B_s^0)$ boundaries chosen for the acceptance maps used in the publication [65]

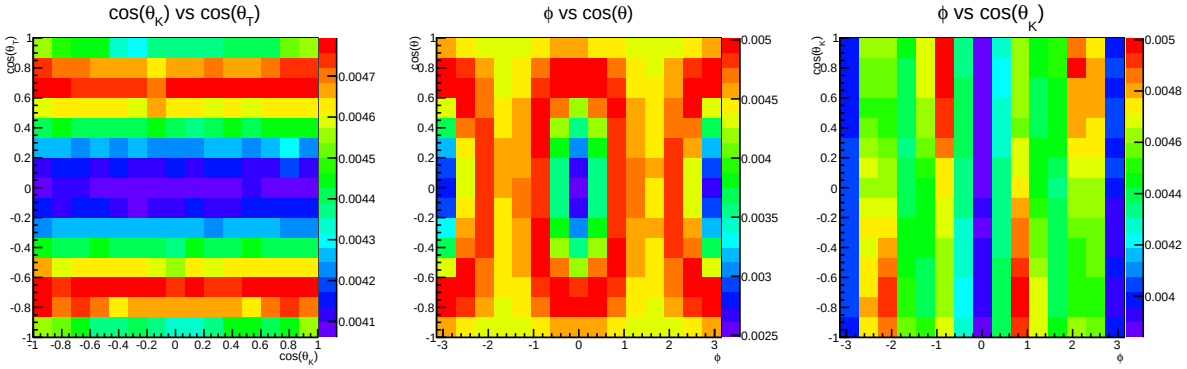

Figure 7.6: A figure showing the two dimensional projections in the transversity basis angles. Taken from fully reconstructed Monte Carlo signal

the acceptance maps take the absolute value of each angles.

The binning of the map is adjusted by hand to ensure the key shapes are described with adequate statistics at low $p_T(B_s^0)$. In the 2012 paper published by ATLAS [65] where the transversity angles are used, the binning used is 4, 1 and 7 equally distanced bins for $\cos\theta_T$, $\cos\theta_K$ and ϕ_T respectively. Six bins are chosen for $p_T(B_s^0)$; these are detailed in table 7.2.

Figure 7.7 isolates the acceptance effects produced by just the reconstruction process and shows it is of the order of 1%, negligible compared to effects introduced by the final track p_T cuts. This is included in the acceptance corrections already included in the acceptance method described above.

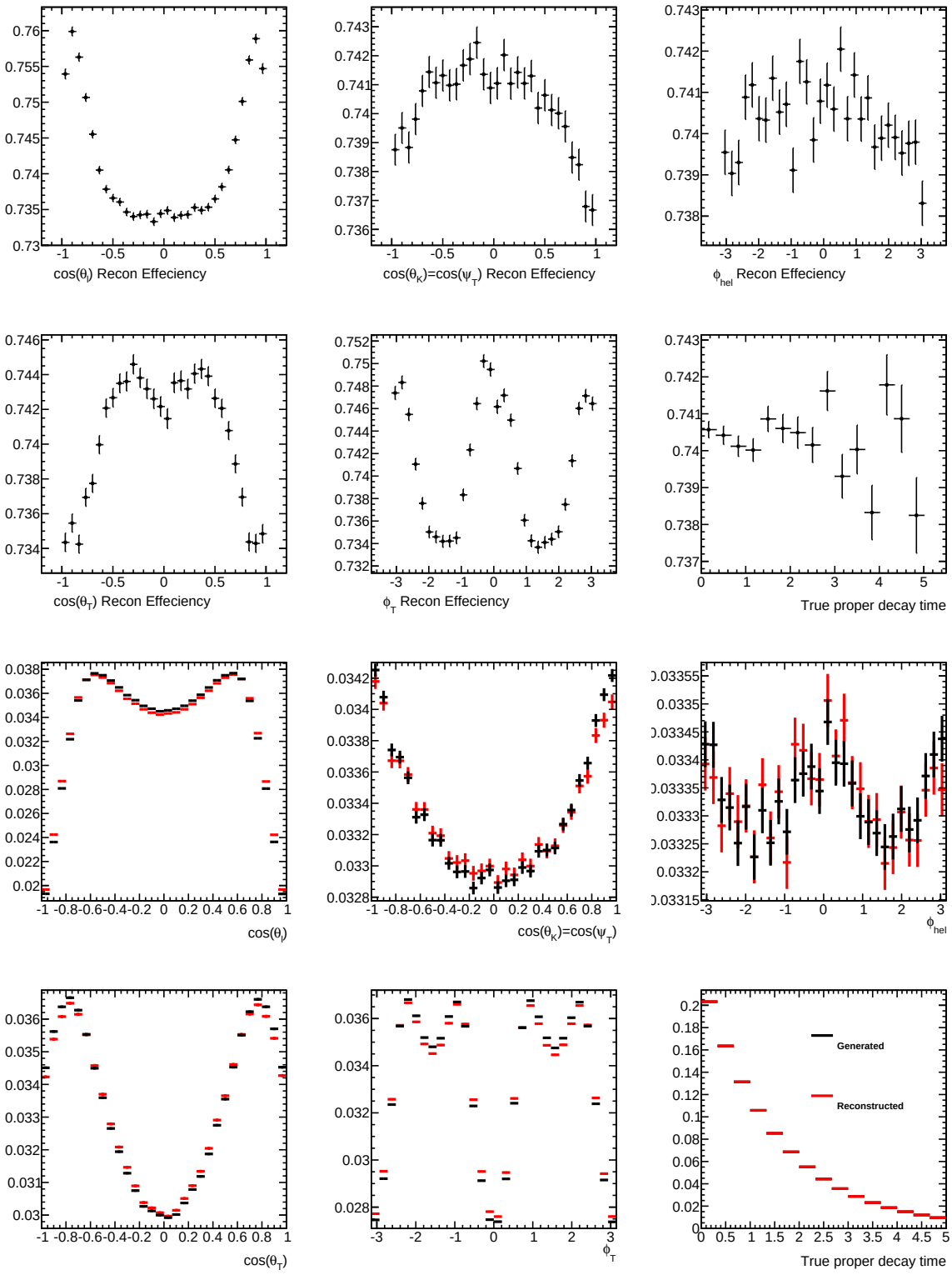

Figure 7.7: These plots illustrate the acceptance effect caused by the reconstruction; the top plots show the efficiency and the bottom plots show the normalised plots overlapped. The effects are negligible compared to the acceptance produced by the kinematic cuts

Chapter 8

Data Fitting

To extract the physical parameters a statistical method for hypothesis testing must be applied. One of the more rigorous methods is the **maximum likelihood** technique. The following chapter reviews the principles and properties of a maximum likelihood fit.

8.1 Maximum Likelihood

A hypothesis in the form of a probability density function (PDF) $f(x;\lambda)$ can be imposed on a sample of data where λ is a set of parameters. The task of the maximum likelihood fit is to extract the values of λ. This carries the assumption that the structure of the function f is valid for describing the data. A maximum likelihood function can incorporate each event in a sample individually or through a histogram collection of events. Considering events individually usually offers better precision for samples of a relatively small size. Once the sample has received sufficient size, rounding errors can become dominant, distorting the fit. We can say that the probability for the ith measurement to be in an interval $x_i + dx_i$ is given by $f(x_i;\lambda)dx_i$.

The probability that this describes all n measurements is given by:

$$P = \prod_{i=1}^{n} f(x_i;\lambda)dx_i \tag{8.1}$$

Again assuming the structure of the equation f is correct the parameters for λ should yield the highest value of P.

$$\mathcal{L} = \prod_{i=1}^{n} f(x_i; \lambda) \tag{8.2}$$

where $\mathcal{L}$ is the likelihood function. A maximum likelihood fit typically finds the set of the parameters λ where $\mathcal{L}$ is a maximum. Usually the negative value of the logarithm of the $\mathcal{L}$ is taken enabling the sum to be used instead of the product and a typical minimiser function (using the negative value renders the minima of the function the solution with the highest probability). For most purposes the function must be normalised by integrating the pdf over the whole applicable area.

$$\int_0^\infty \mathcal{L} dx = 1 \tag{8.3}$$

In high energy physics the typical minimiser is **Minuit** [66]. Minuit provides a variety of minimisation algorithms. This explores the parameter space of the likelihood function, identifies the minima and calculates the associated uncertainty of each parameter. Each parameter is typically given limits to provide a finite parameter space to explore in a reasonable time. It is also necessary to exclude unphysical areas that would introduce errors into the fit.

8.2 Development of the Likelihood Function

The probability density function for the signal is described in chapter 4, but since a lot of background is unavoidably included in the data sample this must be carefully accommodated to avoid contamination of the signal. As such the probability density function must account for:

- the time-dependent angular function of the signal; this must also account for lifetime convolution on a per-candidate error basis.
- the lifetime distributions of the $p\bar{p} \to J/\psi\ X$ and $b\bar{b} \to J/\psi\ X$ backgrounds,

accounting for lifetime convolution on a per-candidate error basis.

- the angular distributions of the background
- the mass distribution of the signal accounts for Gaussian convolution on a per-candidate estimate of the uncertainty
- the mass distribution of the general background
- a weighting term to account for the angular acceptance effect.
- the mass distribution of reconstructed exclusive decay chains contaminating the sample
- the angular distributions of the reconstructed exclusive decay chains contaminating the sample
- the fractions of the primary signal and the dedicated backgrounds

8.2.1 Background angles

To fit the background angular distributions these need to be understood empirically. Figure 8.1 demonstrates a p_T dependence on the angles but this is relatively minor and ignored in the current analysis. In figure 8.2 we can see there are no strong correlations between angles.

The following functions are empirically chosen to fit the transversity background angles and their parameters ($p_{X,bckY}$ where X denotes the angle selected and Y is an arbetary number) are allowed to float freely in the fit.

$$f(\cos\theta_T) = \frac{1 - p_{\theta_T,\mathrm{bck1}}\cos^2(\theta_T) + p_{\theta_T,\mathrm{bck2}}\cos^4(\theta_T)}{2 - 2p_{\theta_T,\mathrm{bck1}}/3 + 2p_{\theta_T,\mathrm{bck2}}/5} \tag{8.4}$$

$$f(\cos\psi_T) = \frac{1 - p_{\psi_T,\mathrm{bck1}}\cos^2(\psi_T)}{2 - 2p_{\psi_T,\mathrm{bck1}}/3} \tag{8.5}$$

$$f(\phi_T) = \frac{1 + p_{\phi_T,\mathrm{bck1}}\cos(2\phi_T + p_{\phi_T,\mathrm{bck0}})}{2\pi} \tag{8.6}$$

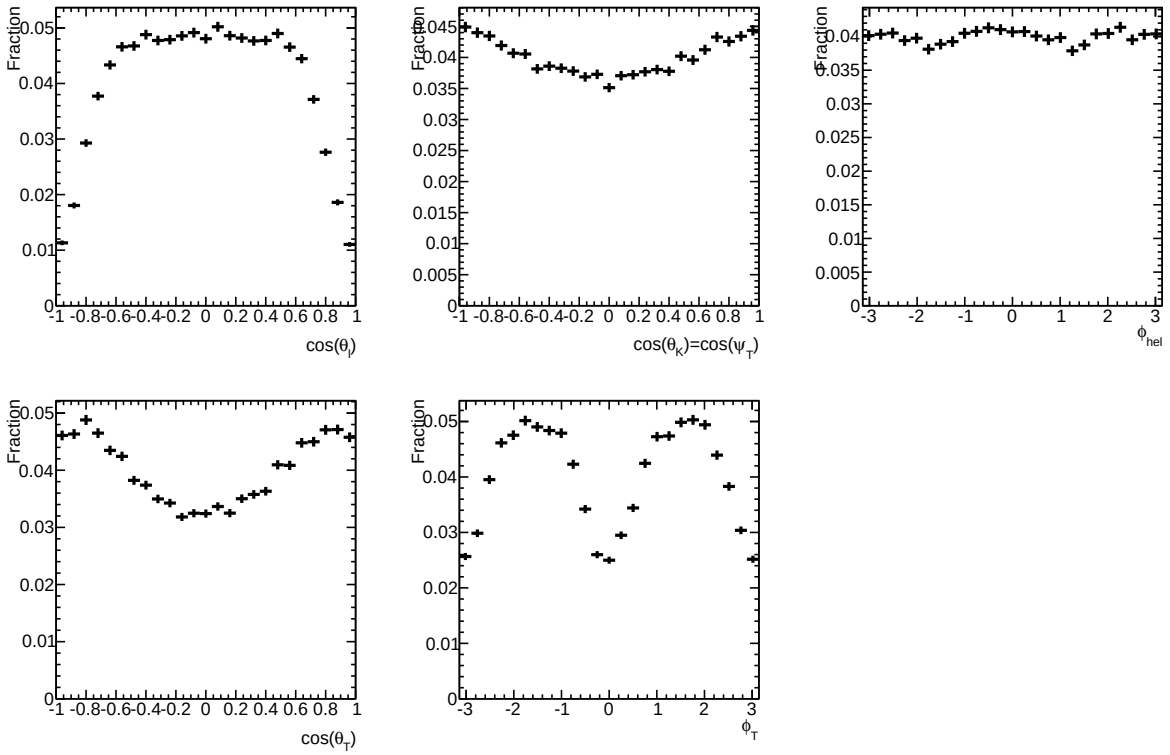

(a) A plot showing the angular distribution of the candidates in the mass side bands of the 2011 sample

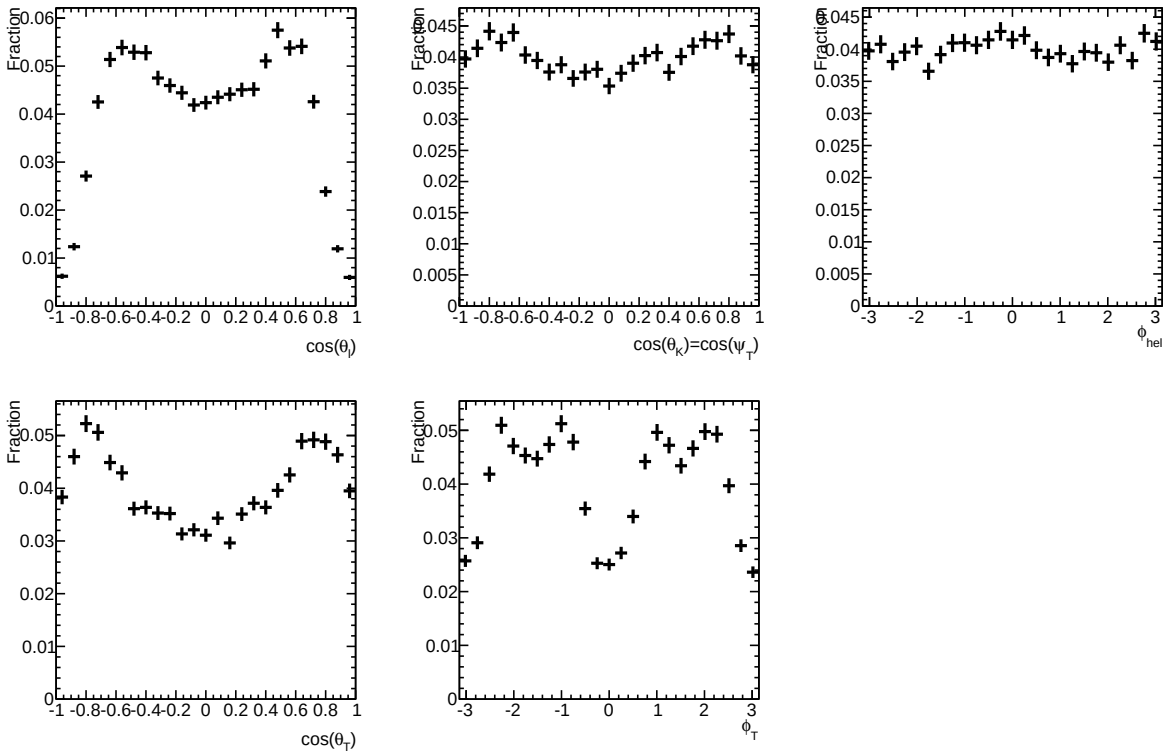

(b) A plot showing the angular distribution of the candidates in the mass side bands of the 2011 sample after a cut of $p_T < 14$ GeV on the B_s^0 meson

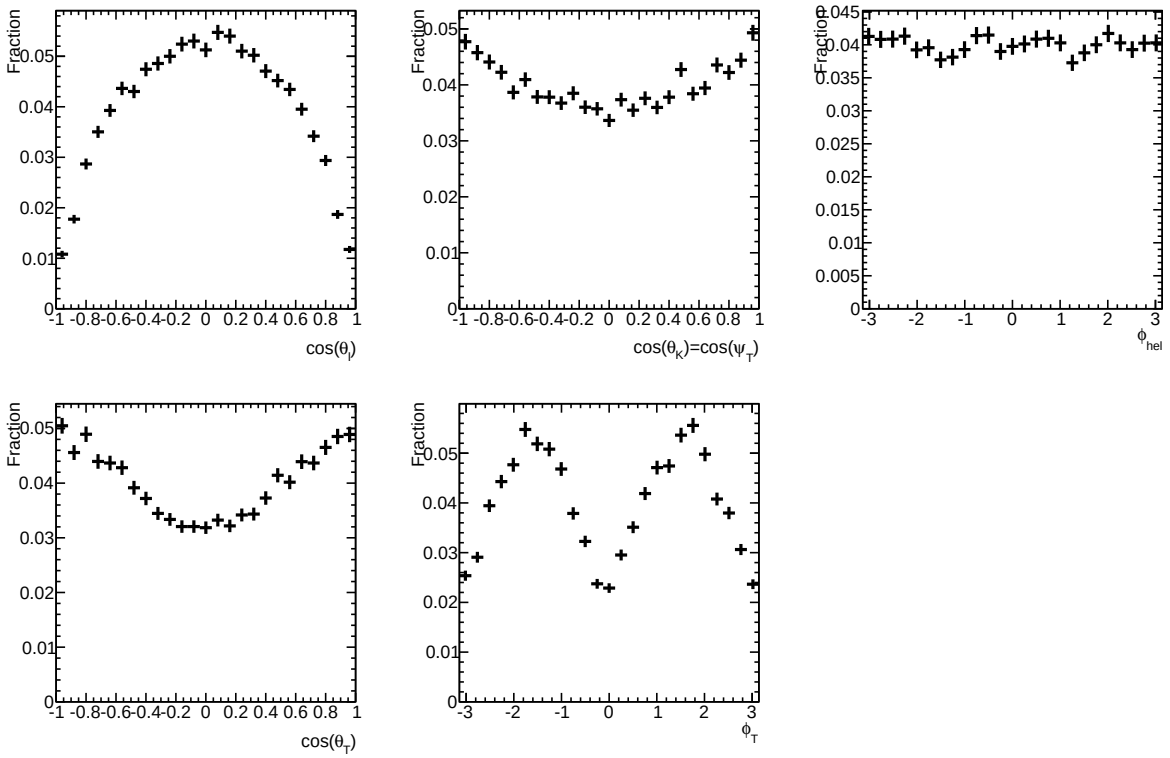

(c) A plot showing the angular distribution of the candidates in the mass side bands of the 2011 sample after a cut of $14 < p_T < 21$ GeV on the B_s^0 meson

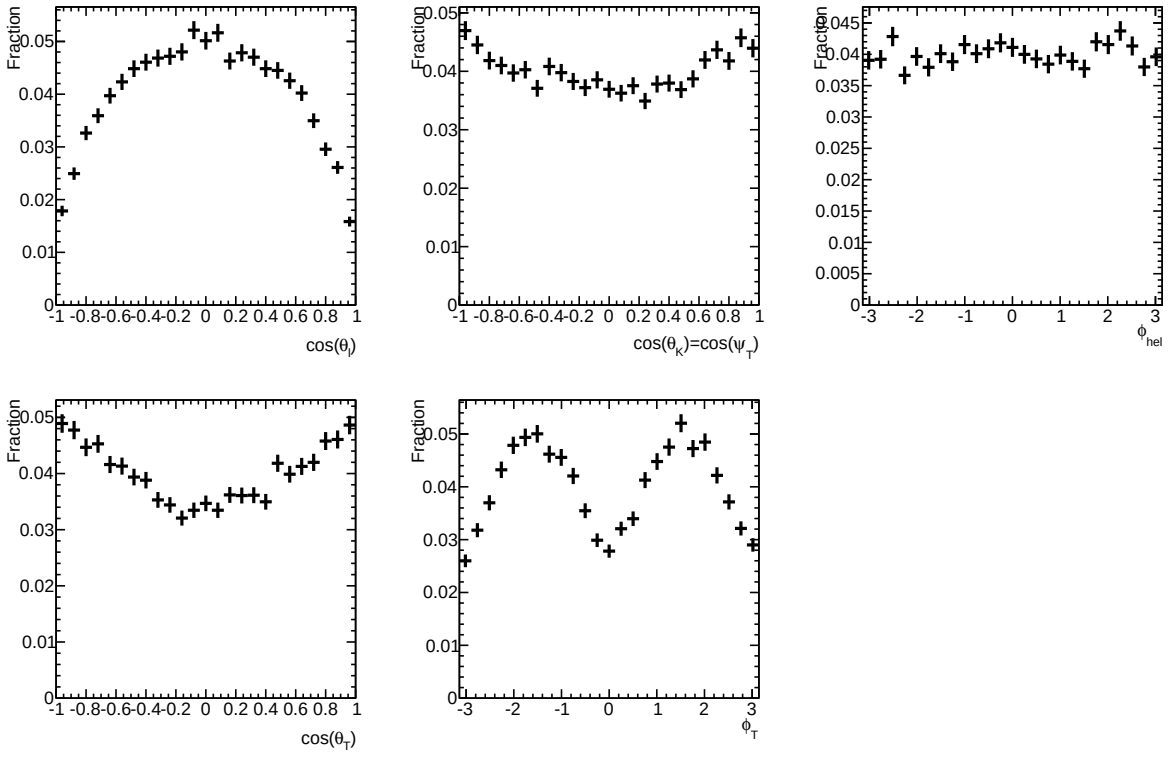

(d) A plot showing the angular distribution of the candidates in the mass side bands of the 2011 sample after a cut of $21 < p_T$ GeV on the B_s^0 meson

Figure 8.1: Plots showing the angular distribution of the candidates in the mass side bands of the 2011 sample. The cut on the mass spectrum is 5125 to 5280 and 5500 to 5625 MeV

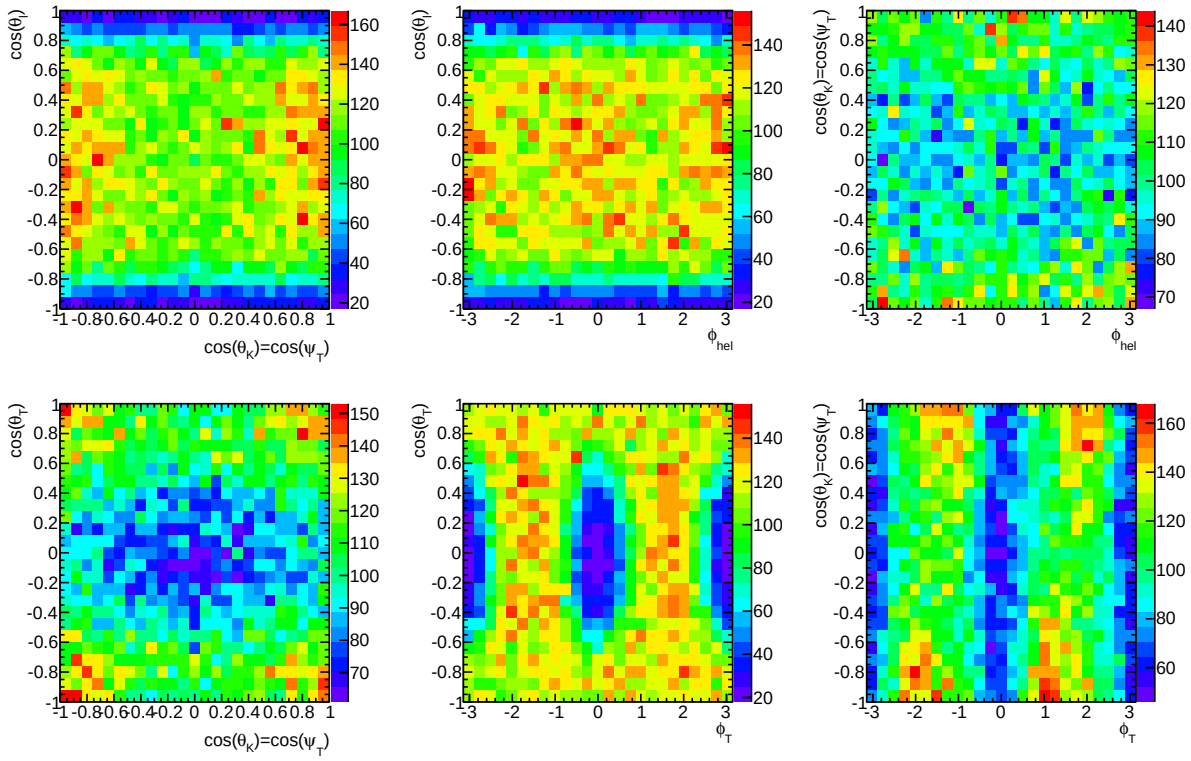

Figure 8.2: Plots showing the angles in the mass sidebands plotted against each other

8.2.2 The dedicated background angles

The exclusive decay $B_d^0 \to J/\psi K^{0*}$ contaminates our sample as demonstrated in figure 6.8. This decay has spin physics producing angular structure in a manner similar to the $B_s^0 \to J/\psi\phi$. To account for this background these events must be independently described. To achieve this the *Pythia* generator with an "*accept-reject*" algorithm described in section 5.5.2 is used to generate the signal according to the parameters in table 8.1. This generated sample is then subjected to the same selection cuts applied to the $B_s^0 \to J/\psi\phi$ signal, substituting the mass hypothesis where appropriate; the resulting distributions can be seen in figure 8.3. These are then fitted using the empirically determined functions below (equations 8.7 to 8.9); the parameters are extracted and entered in the main fit as fixed parameters (used below as $p_{X,Z}$ where X is angle being fitted and Z in an arbitrary number to distinguish parameters). The signal fraction is calculated using the Monte Carlo methods described in chapter 6.3.2 and also enters the main fit as a fixed parameter.

Parameter	Value
$\|A_0(0)\|^2$	0.587
$\|A_\parallel\|^2$	0.252
$\Delta\Gamma$	0.0
Γ_d	0.659
ΔM	0.507
ϕ_d	0
$\delta_\parallel$	2.87
$\delta_\perp$	3.02
Mass	5279.5 MeV

Table 8.1: A table containing the parameters used to generated the $B_d^0 \to J/\psi K^{0*}$ sample

$$f(\cos\theta_T) = \frac{p_{\theta_T,0} - p_{\theta_T,1}\cos^2(\theta_T) + p_{\theta_T,2}\cos^4(\theta_T)}{2 - 2p_{\theta_T,1}/3 + 2p_{\theta_T,2}/5} \tag{8.7}$$

$$f(\cos\psi_T) = \frac{p_{\psi_T,0} - p_{\psi_T,1}\cos(\psi_T) + p_{\psi_T,2}\cos^2(\psi_T) + p_{\psi_T,3}\cos^3(\psi_T) + p_{\psi_T,4}\cos^4(\psi_T)}{2 + 2p_{\psi_T,2}/3 + 2p_{\psi_T,4}/5} \tag{8.8}$$

$$f(\phi_T) = \frac{1 + p_{\varphi_T,1}\cos(2\phi + p_{\varphi_T,0}) + p_{\varphi_T,2}\cos^2(2\phi + p_{\varphi_T,0})}{(2 + p_{\varphi_T,2})\pi} \tag{8.9}$$

The exclusive decay $B_d^0 \to J/\psi\ K^+\pi^-$ also contaminates the sample; this decay has no natural angular structure and so can be described with a standard *Pythia* generator. The candidates are generated, simulated and mis-reconstructed with the appropriate mass hypothesis; this is then independently fitted and the appropriate parameters and fraction are fixed in the main fit. These angles can be seen in figure 8.4.

8.2.3 Mass and Lifetime Background Functions

From figures 8.5 and 8.6 we can see that the background mass spectrum can be adequately represented by a linear polynomial. The lifetime for the prompt (pp) background is represented by a delta function convoluted by a Gaussian distribution in the same per-candidate manner as the signal. Two positive exponentials and a negative exponential are used to model the rest of the background from $b\bar{b}$ sources. The two positive exponentials are to account for a small fraction of longer lived

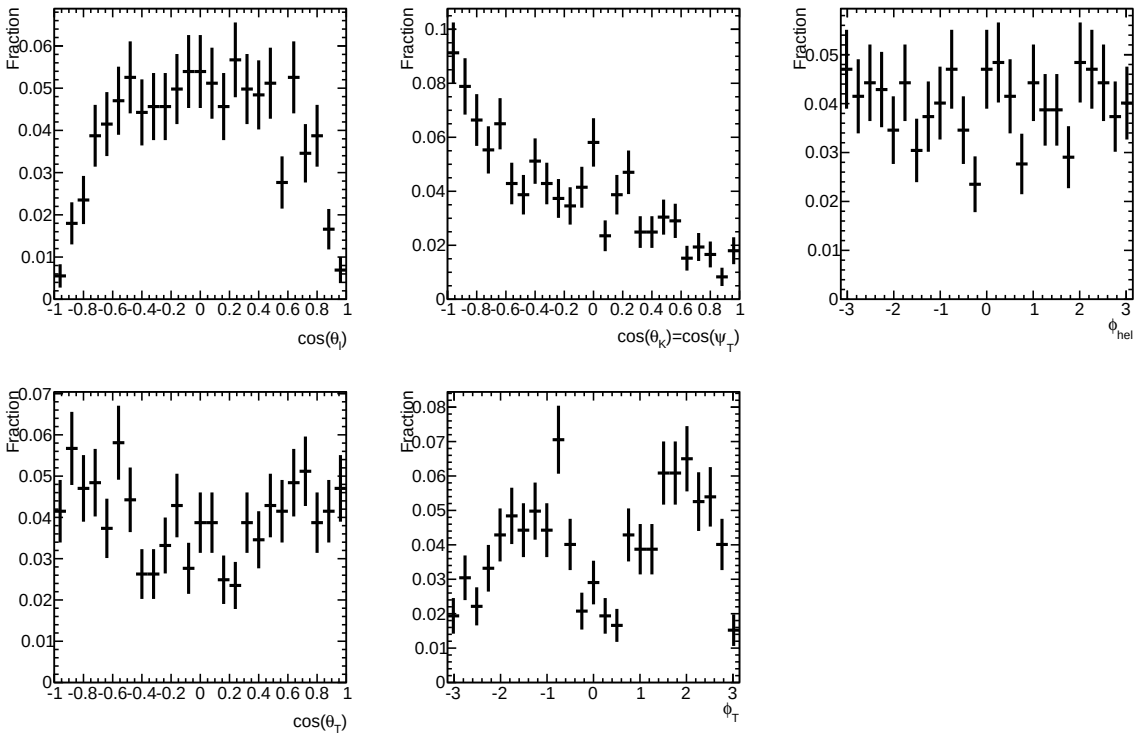

Figure 8.3: A plot showing the angle distributions of generated $B_d^0 \to J/\psi K^{0*}$ signal after going through the signal selection cuts

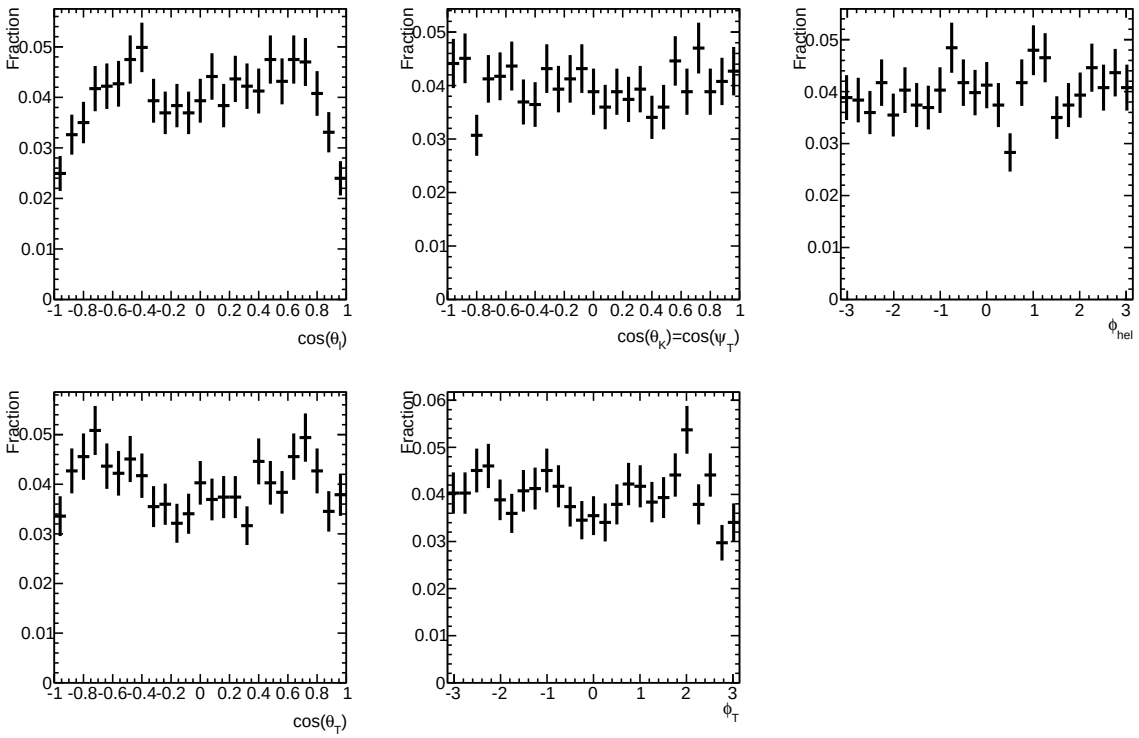

Figure 8.4: A plot showing the angle distributions of generated $B_d^0 \to J/\psi\ K^+\pi^-$ (non-resonant) signal after going through the signal selection cuts

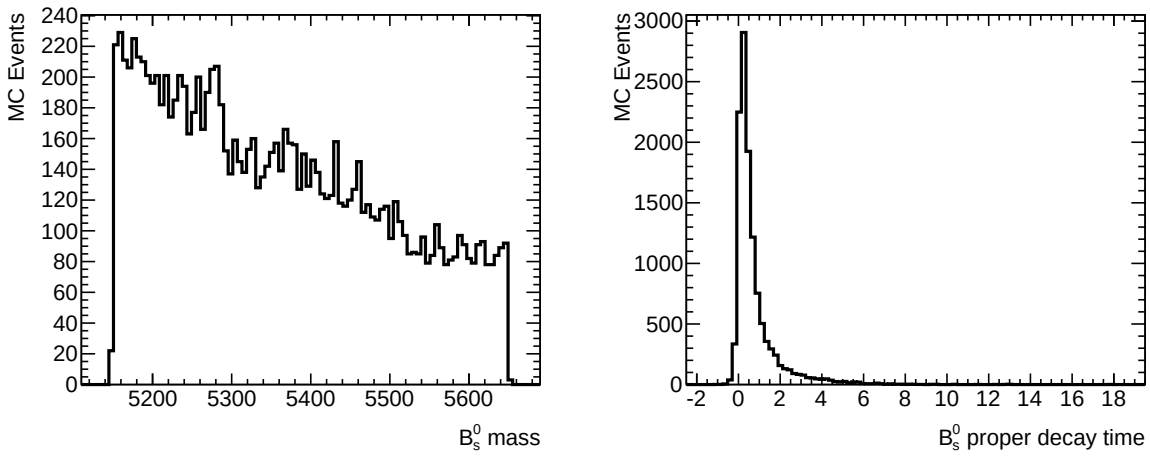

Figure 8.5: Plots showing the mass and proper decay time spectra of a generated $b\bar{b} \to J/\psi X$ sample after the usual selection cuts and true B_s^0 candidates removed

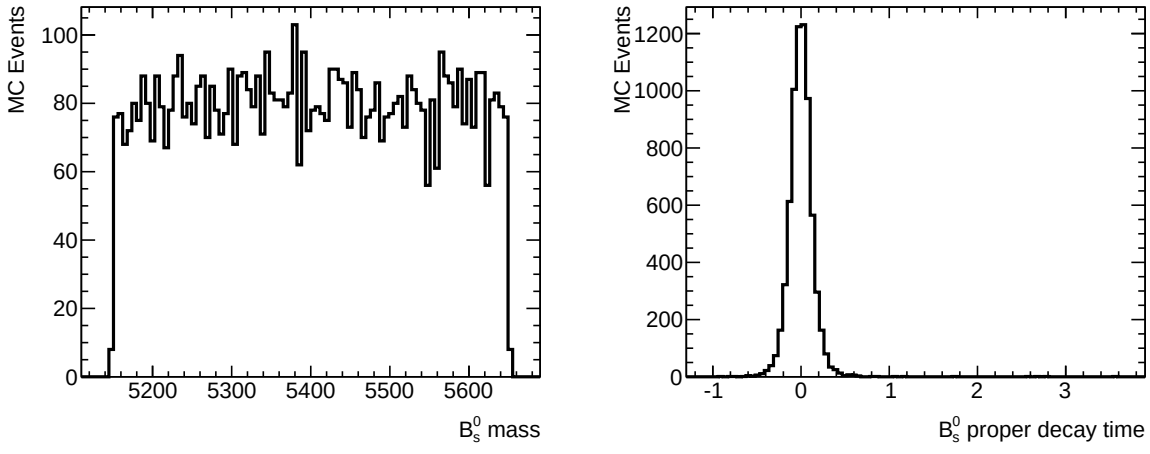

Figure 8.6: Plots showing the mass and proper decay time spectra of a generated $pp \to J/\psi X$ sample after the usual selection cuts

background such as real kaons. The negative exponentials take into account any events with poorly reconstructed lifetimes operating in a non-Gaussian manner.

$$P_{\tau\ \mathrm{Gaus}}(t_i) = \frac{\exp(-0.5 \times (\tau - \sigma_\tau)^2)}{\sqrt{2\pi}} \tag{8.10}$$

$$P_{\tau\mathrm{fast,slow,neg}}(t_i) = \exp\left(\frac{\sigma_\tau^2 - 2t_i\tau_{\mathrm{fast,slow,neg}}}{2\tau^2_{\mathrm{fast,slow,neg}}}\right) \times \frac{\mathrm{erfc}\left(\frac{\sigma_\tau - 2t_i\tau^2_{\mathrm{fast,slow,neg}}}{\sqrt{2}\sigma_\tau\tau_{\mathrm{fast,slow,neg}}}\right)}{2\tau_{\mathrm{fast,slow,neg}}} \tag{8.11}$$

$$\begin{aligned} P_b(t_i|\sigma_t) =& f_{\mathrm{prompt}}P_{\tau\ \mathrm{Gaus}}(t_i) + (1 - f_{\mathrm{prompt}})(f_{\mathrm{tails}}P_{\tau_{neg}}(t_i) + (1 - f_{\mathrm{tails}}) \\ & (f_{\mathrm{indirect}}P_{\tau\mathrm{slow}}(t_i) + (1 - f_{\mathrm{indirect}})P_{\tau\mathrm{fast}}(t_i))) \end{aligned} \tag{8.12}$$

where f_x terms are freely floating fractional parameters. In the following equation the proper decay time of the $B^0_d \to J/\psi K^{0*}$ is described; the uptime convolution terms for the decay are not included here for the sake of simplicity; they are correctly included in the final fit.

$$\begin{aligned} \mathcal{F}_{B^0}(t_i) = & \exp(-\tau\Gamma_{Bd}) + T_{\mathrm{mix}}A_{Bd}\exp(-\tau\Gamma_{Bd})\sin(\Delta m_d\tau)\cos(\Delta\Gamma_{Bd}) \\ & - T_{\mathrm{mix}}A_{Bd}\exp(-\tau\Gamma_{Bd})\cos(\Delta m_d\tau)\sin(\Delta\Gamma_{Bd}) \end{aligned} \tag{8.13}$$

where T_{mix} is a term that accounts for the charge flavour tagging information.

8.2.4 The time uncertainty PDFs

The event-by-event lifetime uncertainty distributions for signal and background differ significantly. These PDFs cannot be factorised out of the likelihood function and it is necessary to include PDFs describing the error distribution. Both the signal and background time error distributions can be described with Gamma functions:

$$P_{s,b}(\sigma_\tau) = \frac{(\sigma_\tau - c)^{a_{s,b}}e^{-(\sigma_\tau - c)/b_{s,b}}}{b^{a_{s,b}+1}_{s,b}\Gamma(a_{s,b}+1)} \tag{8.14}$$

where $a_{s,b}$ and $b_{s,b}$ are constants fitted from sidebands (denoted by b) and sideband subtracted signal (denoted by s) and fixed in the likelihood fit.

8.2.5 Signal PDF

For the purposes of the description it will be assumed the transversity angles are being used; the substitutions required to convert the likelihood equations to the helicity basis are trivial. The distribution for the decay time t and the transversity angles for $B_s^0 \to J/\psi(\mu^+\mu^-)\phi(K^+K^-)$ decays ignoring the detector effects can be given as described in equation 4.45 (see also table 4.3 and 4.4):

$$\frac{d^4\Gamma}{dt\ d\Omega} = \sum_{k=1}^{10} \mathcal{O}^{(k)}(t)\mathcal{C}^{(k)}g^{(k)}(\theta_T, \theta_K, \phi_T) \tag{4.45}$$

As mentioned in the theory chapter, $A_\perp(t)$ describes a CP-odd final-state configuration while both $A_0(t)$ and $A_\parallel(t)$ correspond to CP-even final-state configurations. A_s describes the contribution of CP-odd $B_s \to J/\psi K^+K^-(f_0)$, where the non-resonant KK or f_0 meson is a S-wave state; the amplitudes that correspond to these are given in lines $k = 7 - 10$ in tables 4.4 and 4.3. The likelihood does not take into account the invariant mass of the $\phi(KK)$. The equations are normalised such that the squares of the amplitudes sum to 1; $|A_\perp(0)|^2$ is determined by this constraint while the other three are left to float according to the likelihood. The definition of the angles $\theta_T, \theta_K, \phi_T$ are given in section 4.6.

To account for detector effects this needs to take into account lifetime resolution so each time element in table 4.3 is smeared by a Gaussian function; the smearing is done on an event-by-event basis where the width of the Gaussian is the proper decay time uncertainty multiplied by a scale factor to account for any mis-measurement of the errors. The reconstruction does not introduce any significant smearing in the distribution, and may be safely neglected, as shown in figure 8.7.

The $B_s^0 - \bar{B}_s^0$ oscillation frequency, Δm_s cannot be extracted easily from the $B_s^0 \to J/\psi\phi$ decay but can be measured through other methods. Attempts were made at earlier experiments such as ALEPH, DELPHI, OPAL and SLD but were only able to establish a limit. The Tevatron detectors and LHCb have been able to make measurements, as summarised in table 8.2. Δm_s is fixed to the CDF value of 17.77 ps^{-1} since this was the more precise measurement available at the start of

Experiment	Δm_s ps^{-1}
LHCb [67]	17.768 ± 0.023 (stat) ± 0.006 (syst)
CDF [68]	17.77 ± 0.10 (stat) ± 0.07 (syst)
D0 [69]	18.56 ± 0.87 (stat)
DELPHI [70]	> 8.5 (95% CL)
ALEPH [71]	> 10.9 (95% CL)
OPAL [72]	> 5.2 (95% CL)
SLD [73]	> 10.3 (95% CL)

Table 8.2: A table summarising the current measured values of Δm_s

the analysis.

The final signal likelihood for the untagged fit is:

$$\mathcal{F}_{\rm s}(m_i, t_i, \Omega_i) = P_{\rm s}(m_i|\sigma_{m_i}) \cdot P_{\rm s}(\sigma_{m_i}) \cdot P_{\rm s}(\Omega_i, t_i|\sigma_{t_i}) \cdot P_{\rm s}(\sigma_{t_i}) \cdot A(\Omega_i, p_{{\rm T}i}) \cdot P_{\rm s}(p_{{\rm T}i}) \tag{8.15}$$

The $P_s(m_i|\sigma_m)$ term accounts for the mass of the signal and is modelled as a single Gaussian function smeared with an event-by-event mass resolution σ_m, which is scaled using a factor to account for any mistakes in estimating the mass errors. The PDF is normalised over the range $5.15 < m_{B_s^0} < 5.65$ GeV. The term $P_s(\Omega_i, t_i|\sigma_{t_i})$ accounts for the signal PDF described in chapter 4 but incorporates the time resolution; this involves convoluting the proper decay time element with a Gaussian function. This is done numerically on an event-by-event basis where the width of the Gaussian is the proper decay time uncertainty σ_t, multiplied by an overall scale factor to account for mis-measurement.

The angular sculpting of the detector and kinematic cuts on the angular distributions are included in the likelihood function through $A(\Omega_i, p_{T_i})$. This is calculated using a four-dimensional binned acceptance method, applying an event-by-event efficiency according to the transversity angles in this case, although substituting the helicity angles would not change the structure of the likelihood. $P_s(\sigma_m)$ and $P_s(\sigma_{t_i})$ model the event-by-event uncertainties; these are beneficial as the distributions differ significantly between signal and background. These

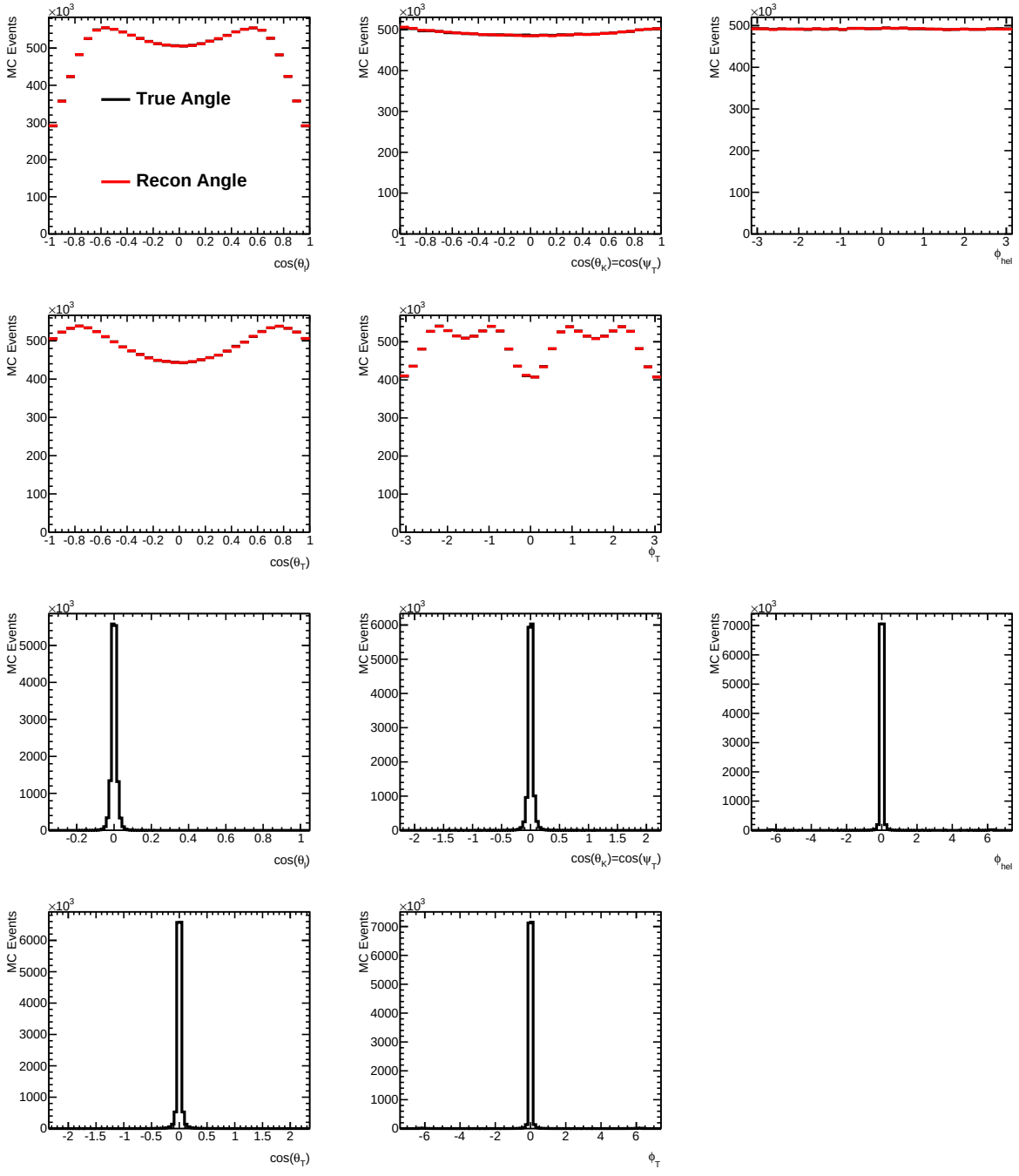

Figure 8.7: Plots overlapping the angular distributions using the "true" and reconstructed vectors (above), plots showing the difference between the true and reconstructed angular distributions (below).

are explained in more detail in section 8.2.4. Since $P_{s,b}(\sigma_{t_i})$ is dependent on the transverse momentum of the B_s meson, they were determined in six selected p_T bins. The same treatment is used for the $p_T(B_s^0)$ signal and background by introducing the term $P_s(p_{T_i})$ into the PDF. These are described using the same functions $P_s(p_{T_i})$ but with different values for the parameters; these are obtained from a fit to sideband and sideband subtracted signal p_T distributions.

8.2.6 Background PDF

The combined background PDF is as follows:

$$\begin{aligned} \mathcal{F}_{\rm bkg}(m_i, t_i, \Omega_i) &= P_{\rm b}(m_i) \cdot P_{\rm b}(\sigma_{m_i}) \cdot P_{\rm b}(t_i|\sigma_{t_i}) \\ &\cdot \quad P_{\rm b}(\theta_T) \cdot P_{\rm b}(\phi_T) \cdot P_{\rm b}(\psi_T) \cdot P_{\rm b}(\sigma_{t_i}) \cdot P_{\rm b}(p_{{\rm T}i}) \end{aligned} \tag{8.16}$$

$P_b(t_i|\sigma_{t_i})$ parametrises the proper decay time as a prompt peak modelled by a Gaussian, two positive lifetime exponentials and a negative lifetime exponential; these and the mass background ($P_b(m_i)$) are described in section 8.2.3. The uncertainty on this is treated in the same manner as the signal (per-event Gaussian). The angles $P_{\rm b}(\theta_T)$, $P_{\rm b}(\phi_T)$ and $P_{\rm b}(\psi_T)$ are described in section 8.2.1.

8.2.7 Final likelihood function

The final likelihood function for the untagged fit is:

$$\begin{aligned} \ln\ \mathcal{L} = \sum_{i=1}^{N} \{ & w_i \cdot \ln(f_{\rm s} \cdot \mathcal{F}_{\rm s}(m_i, t_i, \Omega_i) + f_{\rm s} \cdot f_{B^0} \cdot \mathcal{F}_{B^0}(m_i, t_i, \Omega_i) \\ & + (1 - f_{\rm s} \cdot (1 + f_{B^0})) \mathcal{F}_{\rm bkg}(m_i, t_i, \Omega_i)) \} + \ln P(\delta_\perp) \end{aligned}$$

The angular sculpting of the detector is included in the likelihood signal function and is described in more detail in chapter 7. In cases where the normalisation

cannot be calculated by analytical integrals then it is numerically integrated. N is the number of selected candidates, f_s is the fraction of signal candidates, f_{B^0} is the fraction of peaking B^0 meson background events calculated relative to the number of signal events, which is fixed in the likelihood fit. The mass m_i, the proper decay time t_i and the decay angles Ω_i are the values measured from the data for each event i. $\mathcal{F}_s$, $\mathcal{F}_{B^0}$ and F_{bkg} are the probability density functions (PDF) modelling the signal, the specific B^0 background and the other background distributions respectively. These are mentioned in more detail in the previous section. The term $P(\delta_\perp)$ is a constraint on the strong phase $\delta_\perp$; this is to constrain the parameter to a value measured by LHCb [74]; this is required to eliminate a symmetry that exists in the function in the absence of tagging.

The final likelihood for the tagged fit is similar to the untagged fit without the $\delta_\perp$ constraint:

$$\ln\ \mathcal{L} = \sum_{i=1}^{N}\{w_i \cdot \ln(f_{\text{s}} \cdot \mathcal{F}_{\text{s}}(m_i, t_i, \Omega_i) + f_{\text{s}} \cdot f_{B^0} \cdot \mathcal{F}_{B^0}(m_i, t_i, \Omega_i) + (1 - f_{\text{s}} \cdot (1 + f_{B^0}))\mathcal{F}_{\text{bkg}}(m_i, t_i, \Omega_i))\} \tag{8.17}$$

8.3 Testing the fitter with Monte Carlo signal

To test the maximum likelihood fitter, samples can be generated using the PDF established in chapter 4.7 and the software in chapter 5.5.1. The maximum likelihood fit is used to find the most probable parameters for the sample and these are compared to the parameters entered into the generator to see if they are consistent. One must note that the same PDF is used in generation and fitting, so the test demonstrates self-consistency and working infrastructure rather than a correct PDF. Tables 8.3 and 8.4 show fits of generated signal. Table 8.3 shows expected physics fit are consistent within 1σ with the generated value with

Parameter	Generated value	fitted value
$\|A_0(0)\|^2$	0.5241	0.5302 ± 0.0034
$\|A_{\|\|}(0)\|^2$	0.2313	0.2301 ± 0.0045
$\|A_S(0)\|^2$	0	0
Γ_s [ps^{-1}]	0.652	0.6522 ± 0.0044
$\Delta\Gamma$ [ps^{-1}]	0.075	0.073 ± 0.013
ΔM [$\hbar$s^{-1}]	17.77	17.77 - fixed
ϕ_s	-0.04	-0.0417 ± 0.0094
$\delta_{\|\|}$ [rad]	2.8	2.777 ± 0.033
$\delta_\perp$ [rad]	0.2	$6.457 \pm 0.026 - 2\pi = 0.174 \pm 0.026$

Table 8.3: A table demonstrating the constancy of a generated Monte Carlo sample using standard model parameters of 40000 events

Parameter	Generated value	fitted value
$\|A_0(0)\|^2$	0.5241	0.5240 ± 0.0024
$\|A_{\|\|}(0)\|^2$	0.2313	0.2323 ± 0.0029
$\|A_S(0)\|^2$	0	0
Γ_s [ps^{-1}]	0.652	0.6488 ± 0.0028
$\Delta\Gamma$ [ps^{-1}]	0.075	0.0887 ± 0.0085
ΔM [$\hbar$s^{-1}]	17.77	17.77
ϕ_s	0.39	0.3720 ± 0.0076
$\delta_{\|\|}$ [rad]	2.8	2.778 ± 0.024
$\delta_\perp$ [rad]	0.2	0.187 ± 0.018

Table 8.4: A table demonstrating the constancy of a generated Monte Carlo sample using new physics model parameters of 80000 events

the exception of one of the amplitudes. Table 8.4 uses increased statistics to demonstrate a fit to a new physics measurement, it shows greater deviation from the generated value but this is well within the statistical error posible at the time of the thesis. This will have to be investigated more thoroughly when higher precision measurements are being planned.

Figure 8.8 shows one dimensional projections of the angles and lifetimes for a small and a large value of ϕ_s. The difference is most apparent in the lifetime projection where a large ϕ_s produces a visible oscillation. Figure 8.9 shows projections for expected and unexpected values of the transversity amplitudes. The difference in this case is most apparent in the angular distributions as many distributions appear to be flipped.

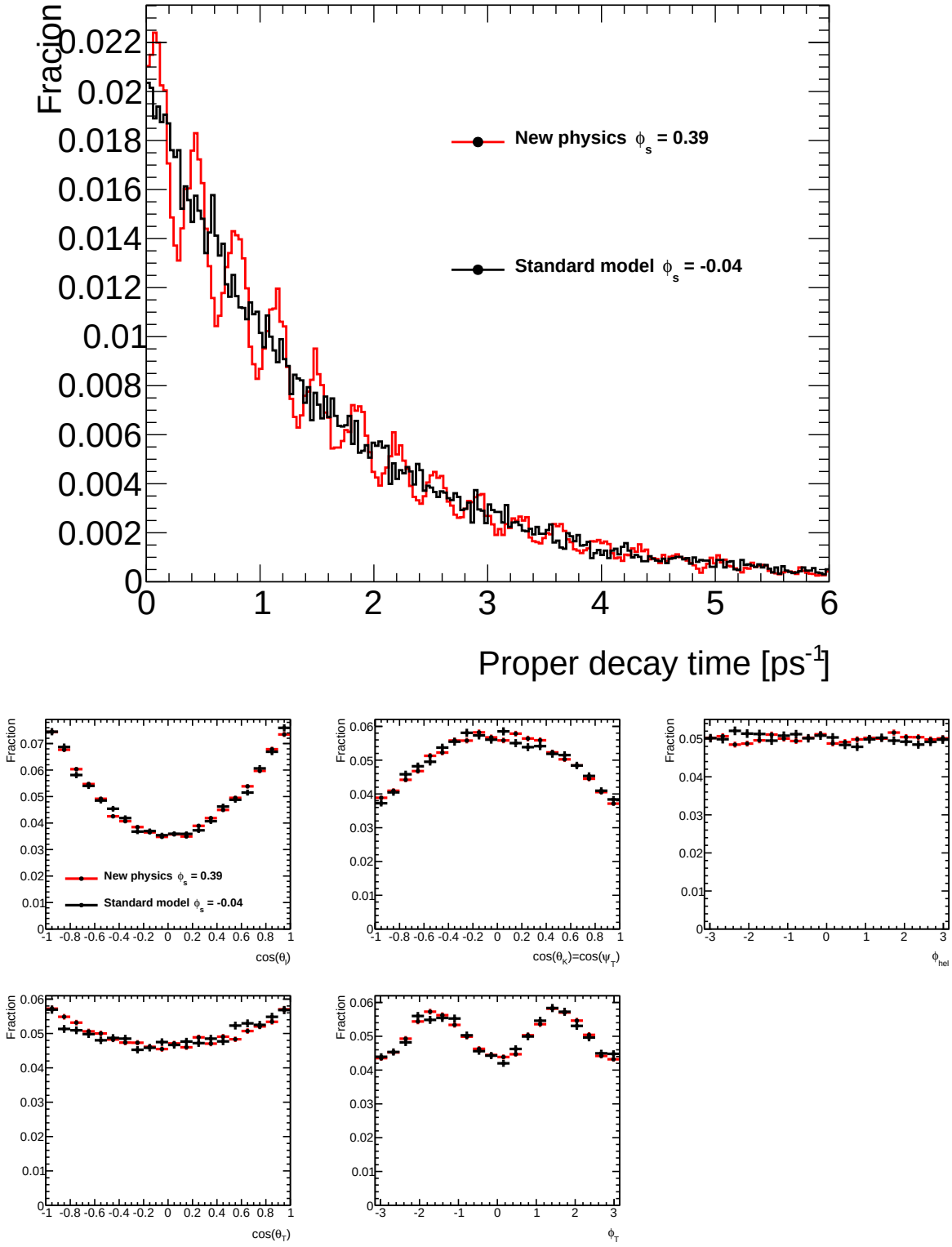

Figure 8.8: Comparing the proper decay time and angular distributions of models with low and high amounts of CP violation

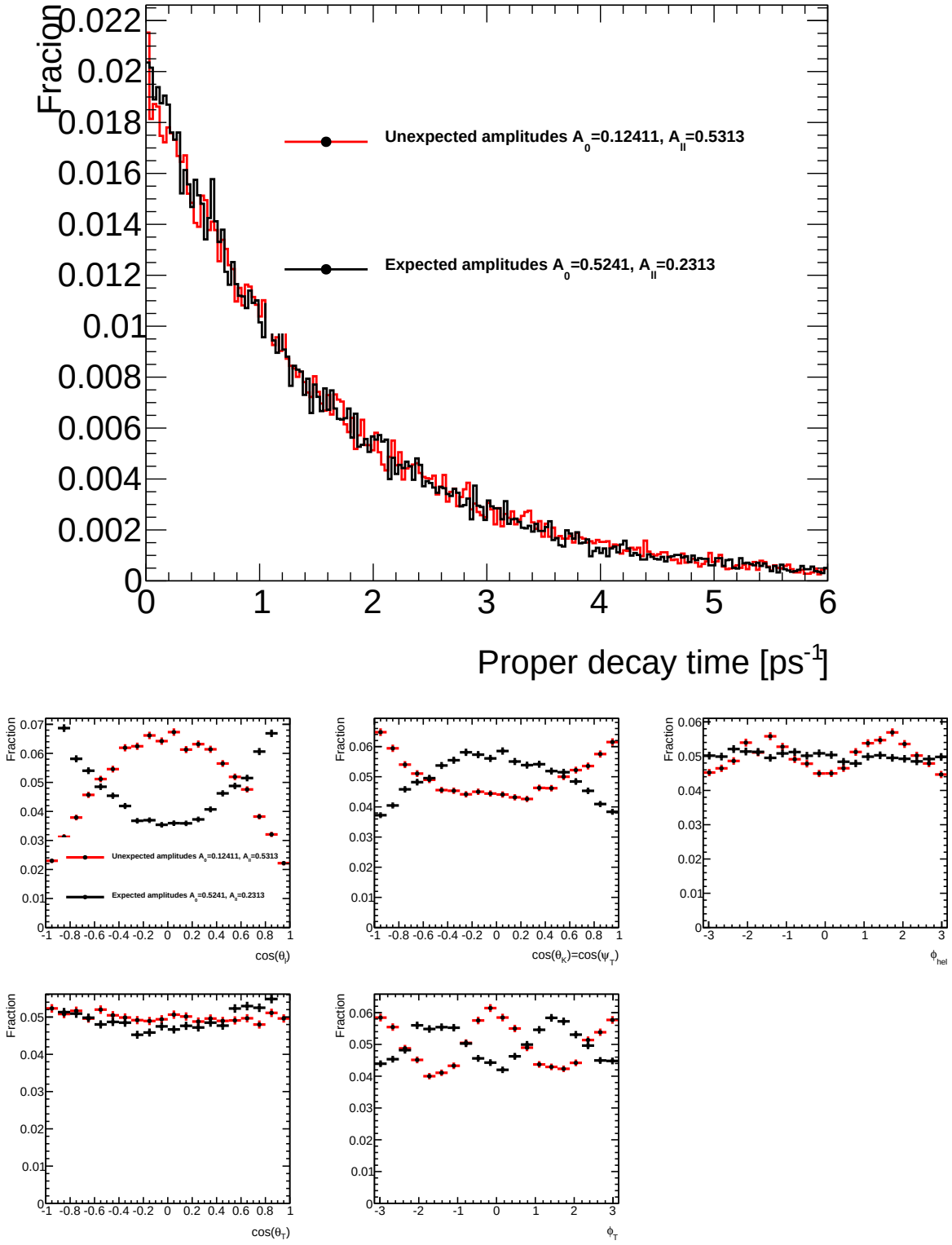

Figure 8.9: Comparing the proper decay time and angular distributions of models with different transversity amplitudes

Chapter 9

Systematics

Systematic uncertainties have to be assigned to the measurements to account for uncertainties that may arise from imperfections in the method applied that are not accounted for in the likelihood fit or statistical in nature. An overview of the systematic errors are below:

- **Inner Detector Alignment:** Misalignment of the inner detector can affect the impact parameter distribution with respect to the primary vertex. This effect can be estimated using events simulated with perfect and distorted ID geometries. The distorted geometry is emulated by moving detector components in the simulation model to match the observed small shifts in data in the impact parameter distribution with respect to the primary vertex as a function of η and ϕ. The mean value of this impact parameter distribution for a perfectly aligned detector is expected to be zero; in data a maximum deviation of 10μm is observed. The difference between the measurements using simulated events reconstructed with a perfect geometry compared to this given distorted geometry is used to assess the systematic uncertainty.

- **Fit Model:** To account for assumptions made in the fit model, variations of the model are tested in pseudo-experiments. A set of 1000 pseudo-experiments is generated for each variation considered and fitted. These include tests for the signal and background mass model, resolution model, background lifetime

and background angles model. These pseudo-experiments are then fitted with the default fit model used to obtain the main result. The systematic error quoted for each model variation is determined by taking the difference between the result from the fit using pseudo-experiment generated with the default model and the result using the pseudo-experiments produced with the altered model. The following variations of model parameters are considered to evaluate the systematic uncertainty:

  - The signal mass distribution is generated using a sum of two Gaussian functions. Their relative fractions and widths are determined from a likelihood fit to data. In the probability density function (PDF) for this fit, the mass of each candidate is modelled by two different Gaussians with widths equal to products of the scale factors multiplied by a per-candidate mass error.
  - The background mass is generated using an exponential distribution. The default fit uses a linear model for the mass of the background events.
  - Two different scale factors instead of one are used to generate the lifetime uncertainty.
  - The values used for the background lifetime are generated by sampling data from the mass sidebands. The default fit uses a set of functions to describe the background lifetime.
  - Pseudo-experiments are performed using two methods of generating the angles for background events. The default method uses a set of functions describing the background angles of data without taking correlations between the angles into account. In the alternative fit the background angles are generated using a three dimensional histogram of the sideband-data angles.

- **Angular Acceptance:** The angular acceptance is calculated from binned Monte Carlo data. This introduces an arbitrary choice of bin widths and cen-

tral values. To estimate the uncertainty the binning is shifted, the uncertainty assigned is the mean difference between the fitted parameters.

- **Trigger efficiency:** To correct for the trigger lifetime bias the events are reweighted using equation 7.1. The uncertainty determined with parameter ϵ is used to estimate the systematic uncertainty due to the time efficiency correction.

- B_d^0 **contribution:** Contamination from $B_d^0 \to J/\psi K^{0*}$ and $B_d^0 \to J/\psi K^+\pi^-$ events mis-reconstructed as $B_s^0 \to J/\psi\phi$ are accounted for in the default fit. This is done by introducing the fractions of these contributions as fixed parameters obtained using selection efficiencies in Monte Carlo simulation and decay probabilities from PDG [20]. To estimate the systematic uncertainty arising by the precision of these estimates the data is fitted with these fractions increased and decreased by 1σ of the uncertainty. The largest shift in the fitted parameters from the default case is taken as the systematic uncertainty for each parameter. This is by most accounts an over estimatation of the error.

9.1 Acceptances

During the data fit, the acceptance corrections are applied as described in chapter 7. The acceptance correction function corrects only the signal contribution to the probability density function since the background angles are fit according to empirically chosen functions that fit the background after they have been affected by acceptance. In addition, to the prior normalisation of the acceptances according to their p_T bin, the precise likelihood fit requires normalisation of the product $P_s(\Omega, t|\sigma_t) \cdot A(\Omega_i, p_{Ti})$ over the angular part (the time normalisation can be worked out analytically). Two numerical methods were tested: using a simple 3D histogram method with various binning or using ROOT-framework 3D function (TF3) integration. The comparison of the final fit results can be seen in figure 9.1.

Default pT bin boundaries	Stepped binning 1	Stepped binning 2
2000	2000	2000
10000	9000	11000
13000	12000	14000
16000	15000	17000
18000	17000	19000
20000	19000	21000

Table 9.1: A table showing the bin boundaries of the default acceptance maps and those used for systematic study

As described in chapter 7, the angular acceptance corrections are $p_T(B_s^0)$ dependent and are constructed in several $p_T(B_s^0)$ bins. The systematics arising from the acceptance construction is estimated by building the alternative acceptance correction function in different sets of the p_T bins, these values are seen in table 9.1. An additional systematic test was comparing the symmetrised angular acceptances with those where the symmetry was not used. The difference of the fit results for the several acceptances is shown in figure 9.2, demonstrating negligible systematics in both cases.

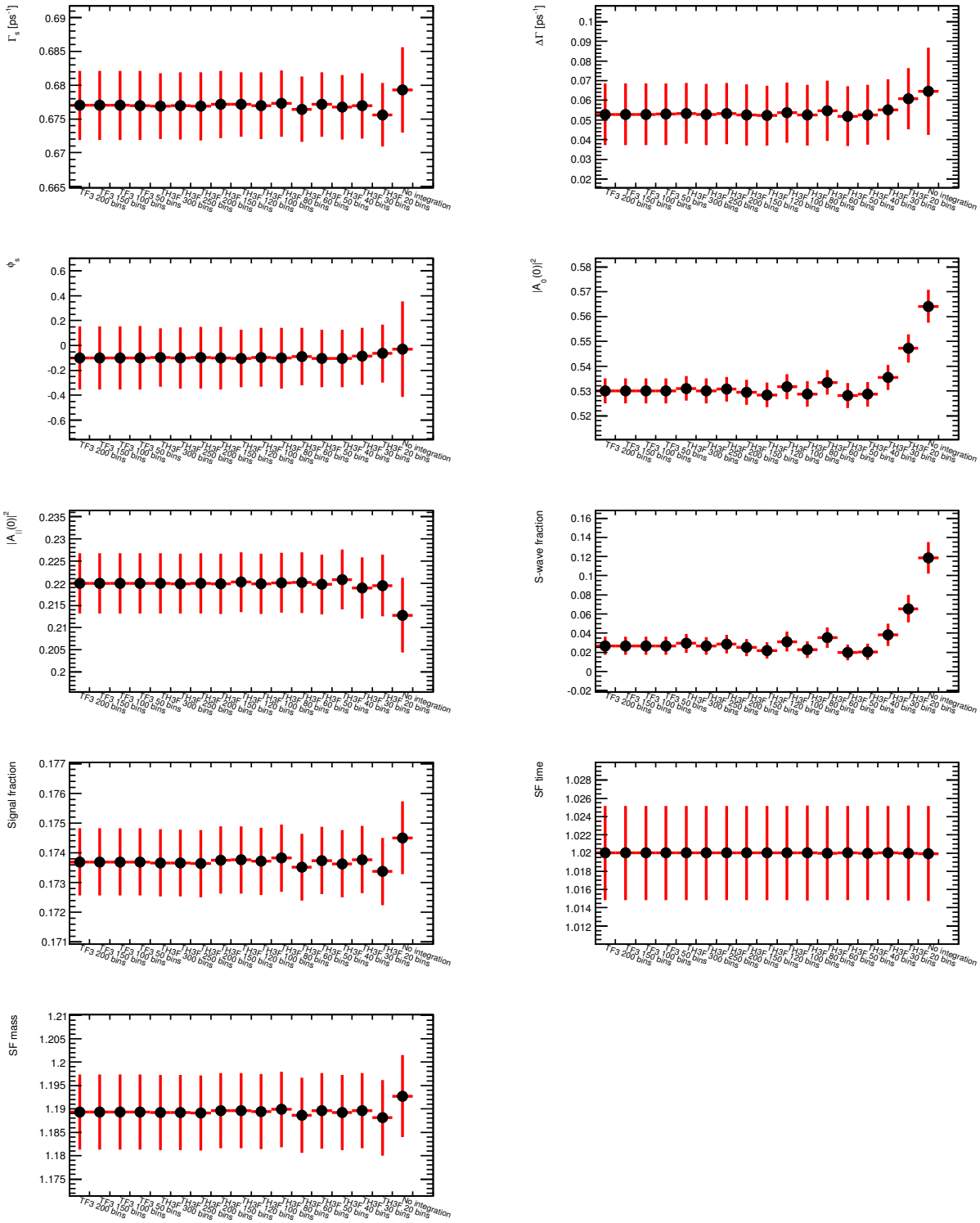

Figure 9.1: Stability of the main fit results using various integration techniques to normalise signal angular PDF corrected by the detector and selection acceptance. The last point shows bias of the fit results in case the $P_s(\Omega, t|\sigma_t)$ and $A(\Omega_i, p_{Ti})$ are normalised separately. Work done by Munich team [75].

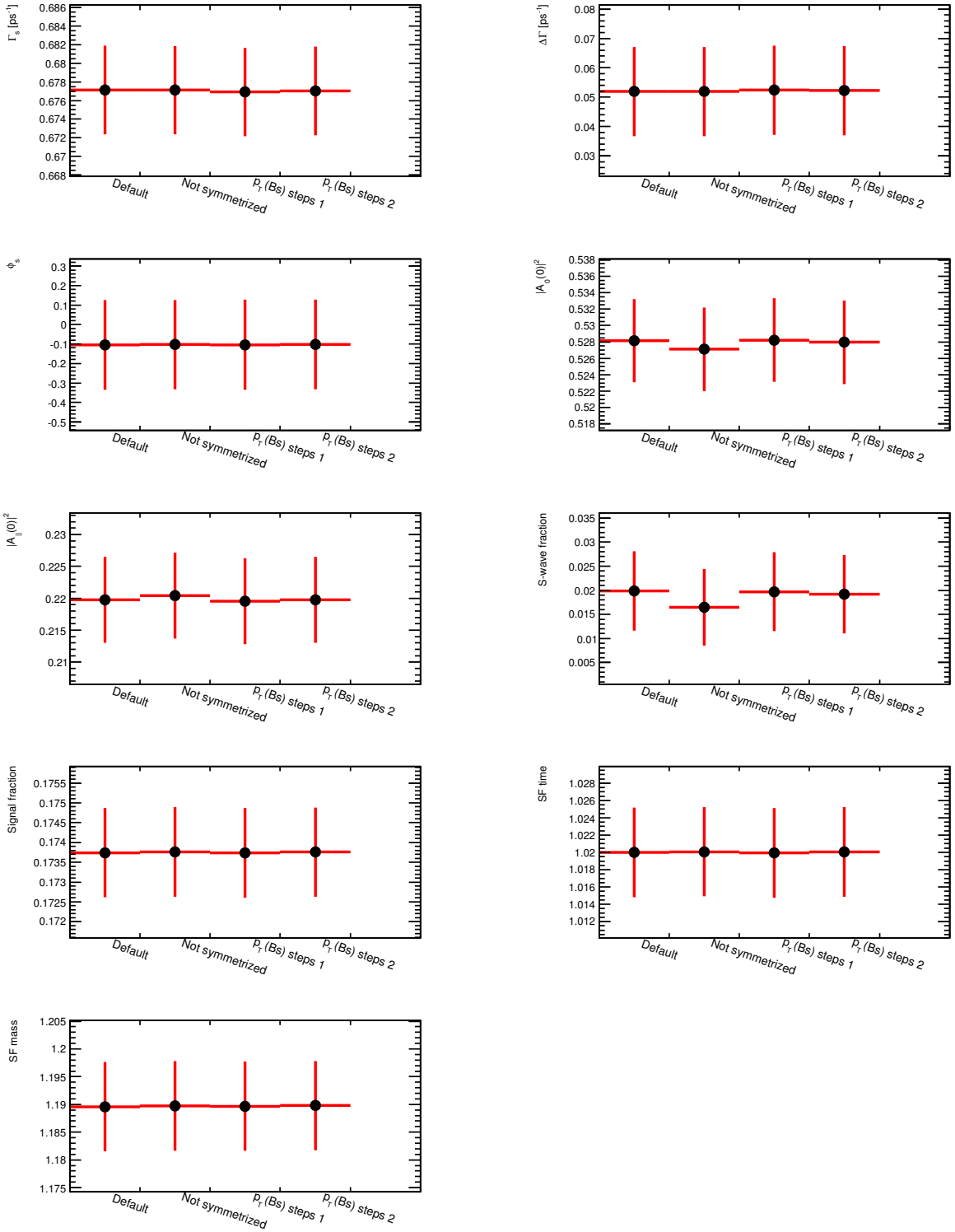

Figure 9.2: Stability of the main fit results for four different acceptance corrections.

9.2 Fit Procedure

In this section the details of the systematic uncertainties in the fit are given; most of this work was done by the Munich team of the ATLAS B-physics group and the author was not personally involved in it.

9.2.1 Pull Study of the Fit Procedure

To check the fit for biases the pull distributions of the measured parameters are investigated. This is done using 580 generated pseudo-experiments. The final fit functions are used and the results from the real data fit are taken as input values for the generation of the pseudo-experiments. Each is then fitted with the fit model and the pull distributions are then determined. The pull for each parameter is calculated as:

$$\frac{\text{fitted value} - \text{generated value}}{\text{fitted error}}$$

The pulls are compiled into histograms and these distributions are fitted with a Gaussian (seen in figure 9.3). The fit is demonstrated to be unbiased if the pull Gaussian has a mean around 0 and a sigma around 1. Due to the symmetries in the function such as $\pm\Delta\Gamma_s$ small deviations from the perfect scenario arise such as two peaks in the $\Delta\Gamma_s$ scan. The other plots are generally in agreement with an unbiased fit.

Systematics due to fit parameterisation

To estimate the size of the systematic uncertainties caused by the assumption made in the fit model, variations of the model are used to produce pseudo-experiments. Each of the pseudo-experiments is then fitted with the default fit model. The systematic error for each variation is the shift between the mean fit value of the 1000 pseudo-experiment events from the input value for the pseudo-experiment generation.

To deal with the ambiguities leading from $\Delta\Gamma_s$ being symmetric around zero, both solutions to the term are fitted with two symmetric Gaussians. The systematic error for each variation is taken as the shift of the mean of the fitted Gaussian from corresponding value resulting from the default fit on data. In this manner data-like sets with over 120000 events are generated for each model, an example of which can be seen in figure 9.4. This demonstrates agreement between the data-like generation and real data.

The following paragraphs describe the variations in the fit model and the results of each model for the parameters of interest are in figures 9.5 to 9.8. The individual uncertainties are summed in quadrature and presented in the final results table. To avoid redundancy only the results from the untagged systematic analysis are presented in detail.

Variation of signal mass model The default fit uses a single mass scale factor for the B_s^0 mass. The effect of this assumption is tested by generating pseudo-experiments with two different mass scale factors. Each pseudo-experiment is fitted with the default model to emulate the effect of choosing the wrong parametrisation. The parameters for the alternative model are obtained by fitting the two Gaussians and two mass error scale factors. Figure 9.5 shows the distributions of fit values of the 1000 pseudo-experiments for each parameter of interest.

Variation of background mass model The default fit uses a linear/first order polynomial model to fit the background mass shape. The systematic effect of this parametrisation is checked by generating pseudo-experiments with an exponential function and fitting with the default fitter. The parameter for the exponential function is obtained by fitting the data with the simple mass-lifetime fit with an exponential background mass function. Figure 9.6 shows the distributions of the fits of each parameter.

Variation of Signal Resolution Model The time resolution for signal events is modelled in the default fit by convoluting each lifetime exponential term with a single Gaussian distribution, making use of event-by-event errors scaled by a single

scale factor. The alternative model used in pseudo-experiments uses two Gaussians with two separate scale factors. The values for the alternative model are estimated from data. The results are in figure 9.7.

Variation of Background Lifetime Model Pseudo-experiments are generated with background lifetime histograms from side band data rather than according to the fit model to provide the systematic uncertainty for this component. Figure 9.8 shows the distributions of fit values for each of the key parameters.

Variation of Background Angle Model Background angle histograms from sideband data are generated as pseudo-experiments and are fitted with the default model to assess the systematic uncertainty with the choice of functions for the background angles used in the fit. To account for any correlations in the background angles, the θ_T is generated, then using this value ϕ_T is selected from one of four sideband data histograms of ϕ_T binned in terms of θ_T. Figure 9.9 shows the systematic uncertainty and shows the distributions of fit values for each parameter of interest.

The uncertainties discovered in this subsection are summed in quadrature and summarised in section 9.5.

Systematics due to $B_d^0 \to J/\psi K^{0*}$ reflection

To estimate the systematic uncertainty due to the background contribution of $B_d^0 \to J/\psi K^{0*}$ decays misreconstructed as $B_s^0 \to J/\psi\phi$, the fraction of the contribution is estimated using Monte Carlo generated as $B_d^0 \to J/\psi K^{0*}$ but reconstructed as $B_s^0 \to J/\psi\phi$ decays. This is used to estimate the relative selection and reconstruction efficiencies taking into account the relative production fractions obtained from the PDG [20]. The contamination is estimated to be $\sim 4\%$. To estimate the systematic error the fit is run neglecting the contributions from $B_d^0 \to J/\psi K^{0*}$ and then including it. More information including the parameters used for generation and the functions used can be found in subsection 8.2.2. The results are found in table 9.2.

Parameter	B_s + B_d	B_d down by 1σ	Difference	B_d up by 1σ	Difference
$\|A_0(0)\|^2$	0.528 ± 0.005	0.523 ± 0.005	0.004	0.532 ± 0.005	0.004
$\|A_\parallel(0)\|^2$	0.220 ± 0.007	0.220 ± 0.007	0.0002	0.220 ± 0.007	0.0003
$\Delta\Gamma$	0.054 ± 0.015	0.053 ± 0.015	0.0003	0.054 ± 0.015	0.0003
Γ_s	0.680 ± 0.005	0.681 ± 0.005	0.0002	0.680 ± 0.005	0.0004
$\|A_s(0)\|^2$	0.019 ± 0.008	0.020 ± 0.008	0.0007	0.018 ± 0.008	0.001
ϕ_s	-0.101 ± 0.206	-0.116 ± 0.213	0.015	-0.090 ± 0.202	0.011

Table 9.2: Fit parameter variations and resulting systematic uncertainty due to reflected $B_d^0 \to J/\psi K^{0*}$. Work done by Tatjana Jovin [76]

9.2.2 Systematics due to triggers

The systematic uncertainty caused by the trigger selection effects is determined by dividing selected data into many subsets according to the dominant triggers. The fit is then performed for each of them separately and compared with each other. The sample is split by the L1 trigger algorithm used; the topological triggers di-muon based J/ψ triggers are listed in table 9.3.

L1 di-muon based topological J/ψ triggers	L1 single muon TrigDiMuon Algorithm
EF_2mu4_Jpsimumu	EF_mu4_Jpsimumu
EF_2m4T_Jpsimumu	EF_mu6_Jpsimumu
EF_mu4mu6_Jpsimumu	EF_mu6_Jpsimumu_tight
EF_mu4Tmu6_Jpsimumu	EF_mu10_Jpsimumu

Table 9.3: The list of ATLAS triggers used in the final data selection for the fit. Consult documentation for detailed explanation [64].

The groups of triggers in table 9.3 account for 92% of the B_s events after the final selection cuts. The remaining events were triggered by single muon triggers and supporting calibration J/ψ triggers. To test the effect this might have contributed, the data is split into 4 subsamples, a sample containing all events that pass selection from all triggers, a sample just taking the topological triggers, a sample just taking the TrigDiMuon algorithm triggers and a sample of the remaining triggers accounting for 8% of the sample. These subsamples are then fit using the default fitter. The results show that the 8% subsample gives a much lower value of A_0, which could be accounted for by the different topology of the selected muons affecting the kinematic acceptance of the angular distributions (see figure 9.11). Acceptance corrections using these specific triggers were not

Parameter	Selected topology trigger	Full Sample	trigger systematic
$\|A_0(0)\|^2$	0.561 ± 0.006	0.536 ± 0.005	0.024
$\|A_\|\|(0)\|^2$	0.202 ± 0.013	0.215 ± 0.01	0.013
Γ_S	0.673 ± 0.008	0.662 ± 0.005	0.011
$\Delta\Gamma_s$	0.071 ± 0.024	0.071 ± 0.016	< 0.001
ϕ_S	-0.155± 0.337	-0.035± 0.258	0.120

Table 9.4: Systematics associated with the dimuon trigger selection

Parameter	Selected topology trigger	Full Sample	trigger systematic
$\|A_0(0)\|^2$	0.547 ± 0.008	0.536 ± 0.005	0.01
$\|A_\|\|(0)\|^2$	0.197 ± 0.016	0.215 ± 0.01	0.018
Γ_S	0.656 ± 0.008	0.662 ± 0.005	0.006
$\Delta\Gamma_s$	0.071 ± 0.024	0.071 ± 0.016	< 0.001
ϕ_S	-0.163± 0.36	-0.035± 0.258	0.128

Table 9.5: Systematics associated with the single muon trigger selection

applied and therefore not corrected; this could be investigated further in the future. However there would be a problem with low statistics leading to problems trying to gain accurate acceptance corrections. Comparing the acceptance of the two other samples indicates a general agreement (figure 9.10).

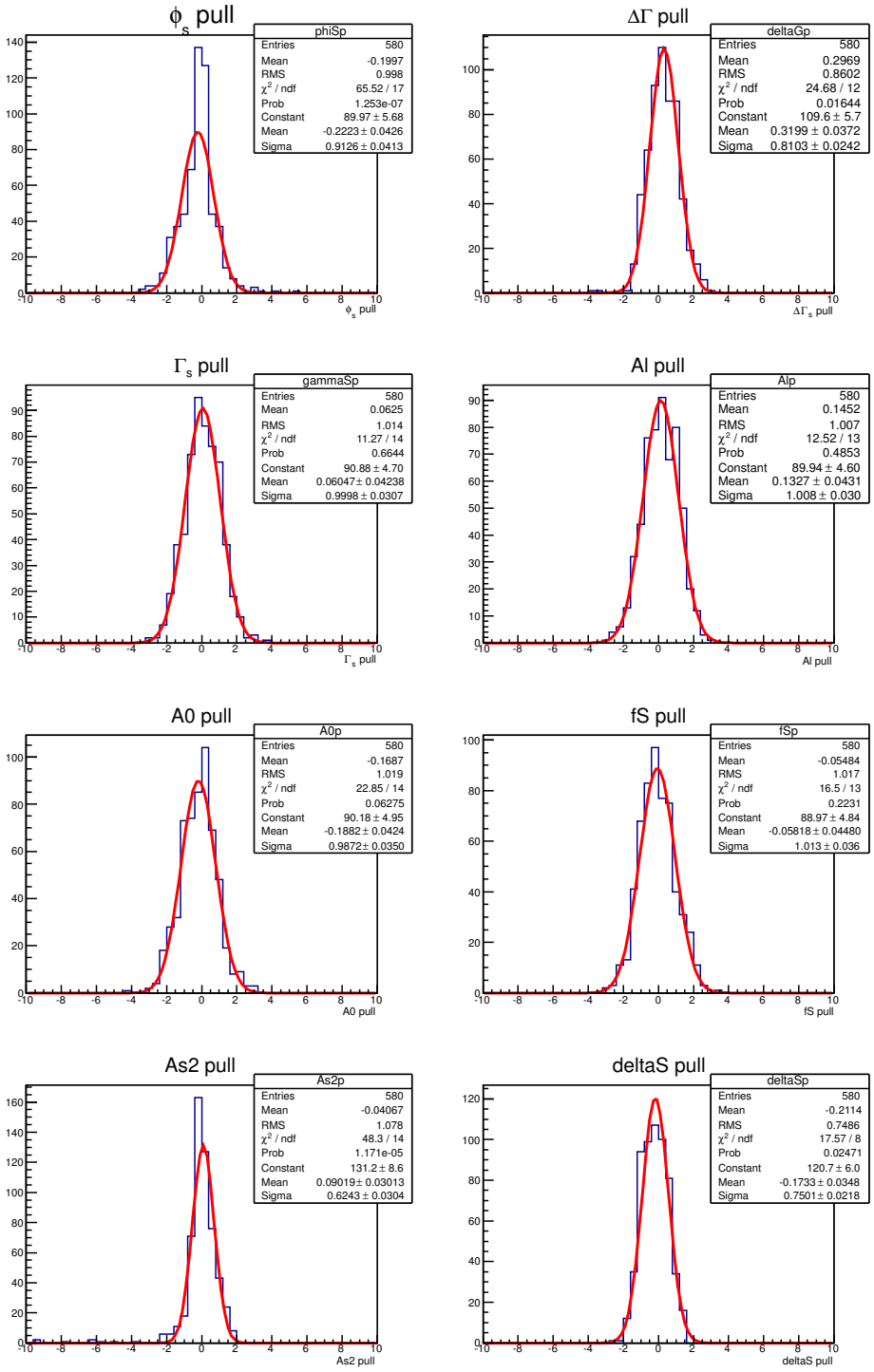

Figure 9.3: Pull distribution of 580 pseudo-experiments fitted with a Gaussian function. Provided by Munich Team [75].

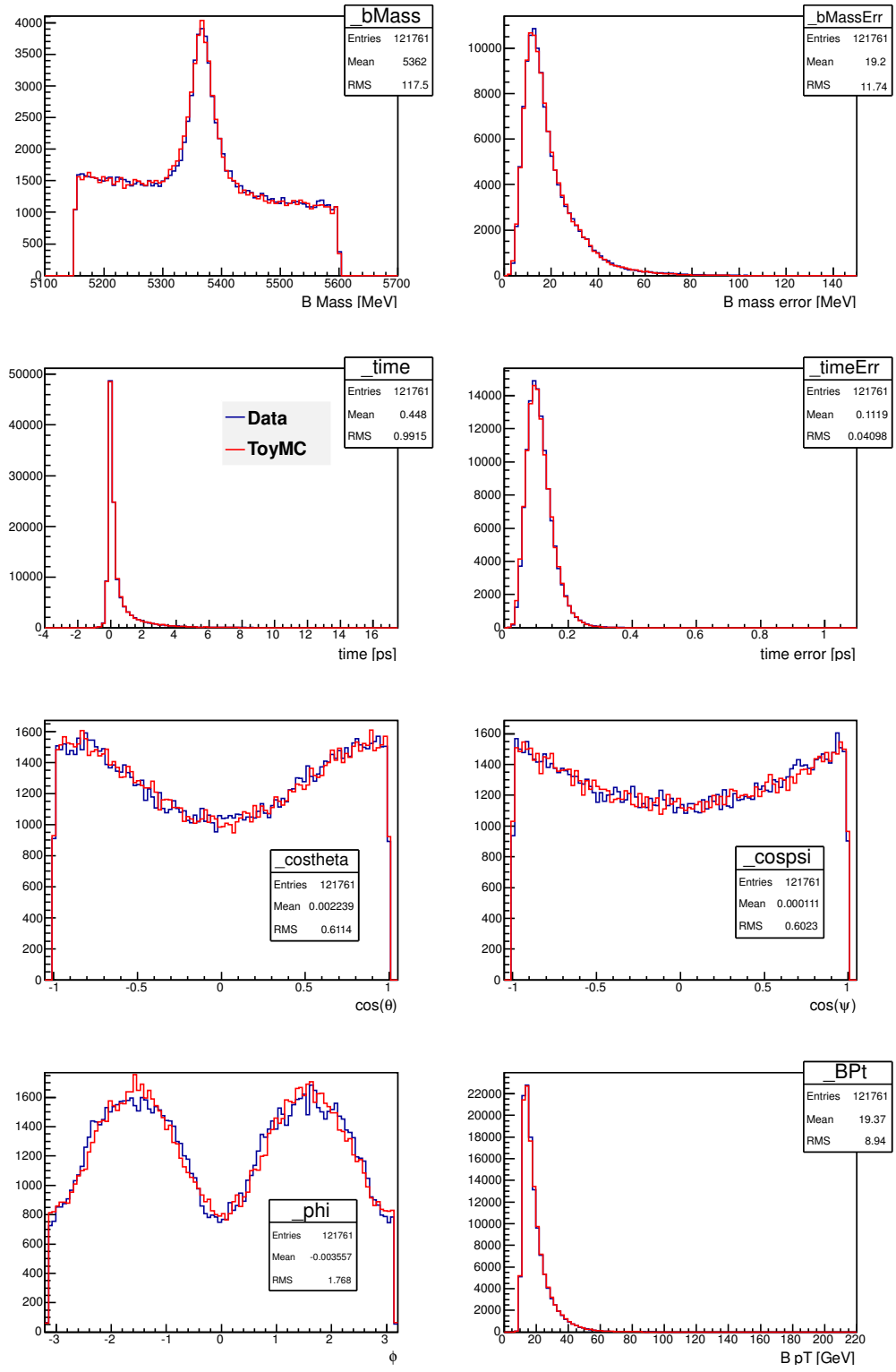

Figure 9.4: Distributions of event parameters for a toy Monte-Carlo pseudo-experiment (red) and the real data (blue). Made by Munich team [75].

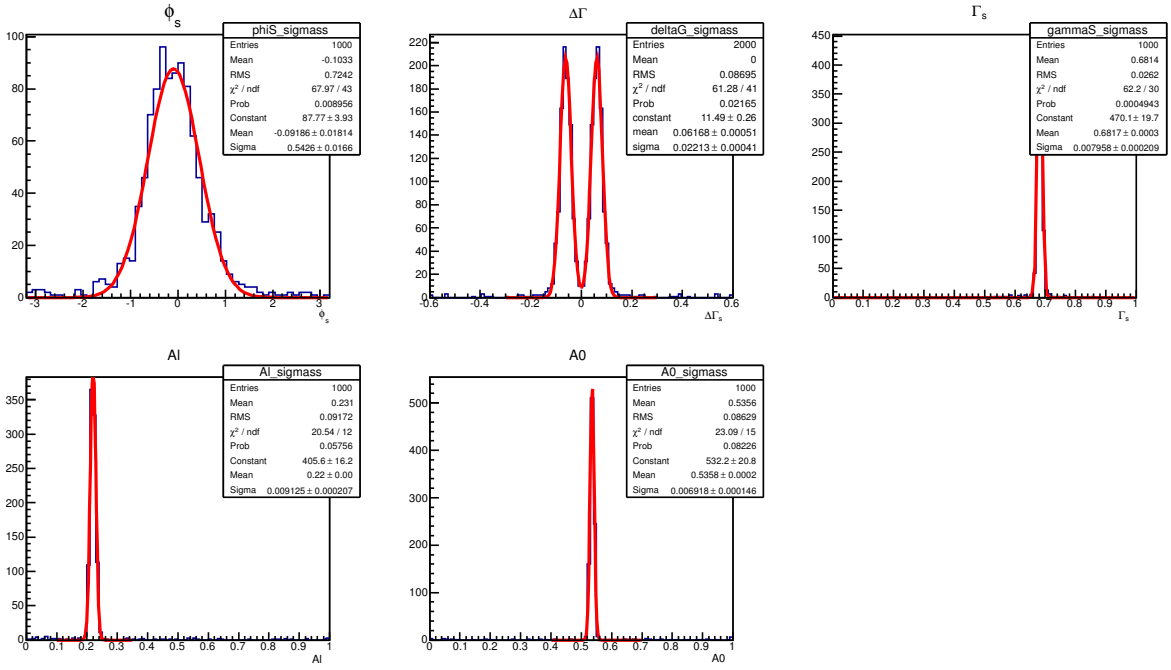

Figure 9.5: Distributions of fit values of the 1000 pseudo-experiments with signal mass model systematically altered. Work done by Munich team [75].

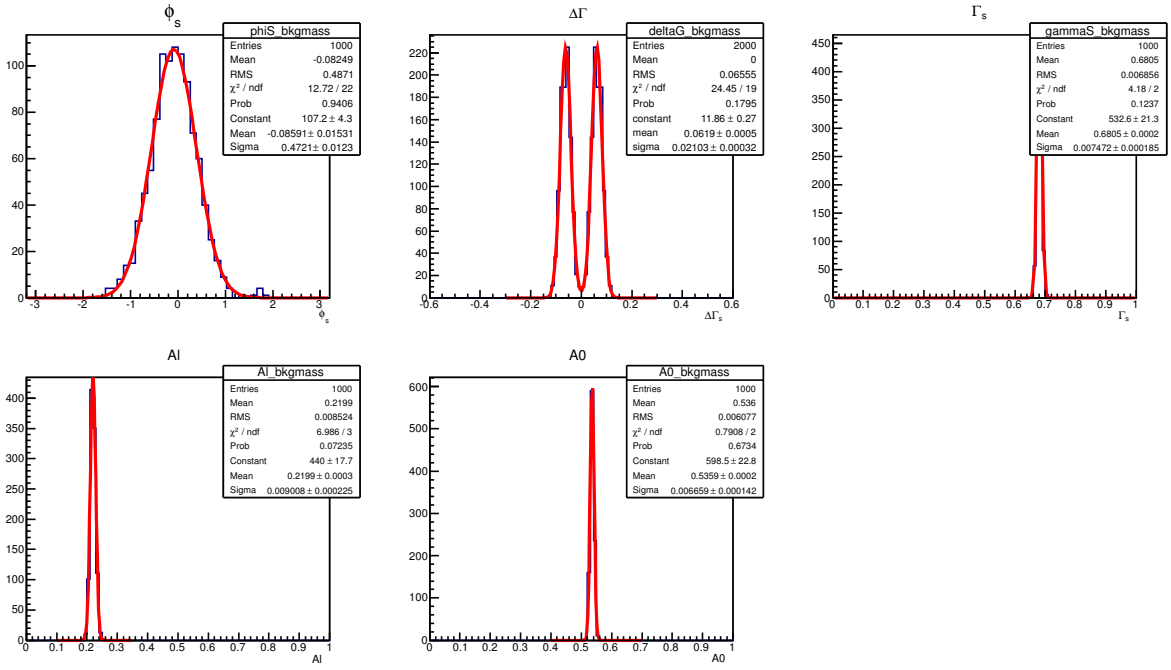

Figure 9.6: Distributions of fit values of the pseudo-experiments with background mass model systematically altered. Provided by Munich team [75].

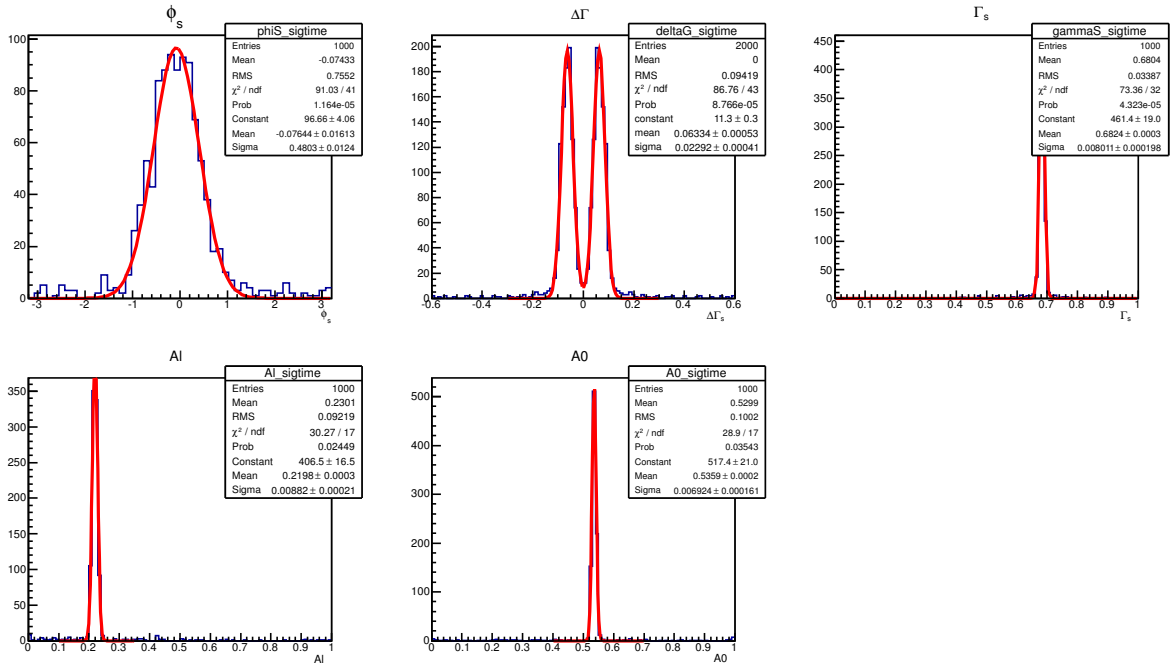

Figure 9.7: Distributions of fit values of the pseudo-experiments with signal resolution model systematically altered and shifts of mean fit value for pseudo-experiments with signal resolution model systematically altered from input values for pseudo-experiment generation. Provided by Munch group.

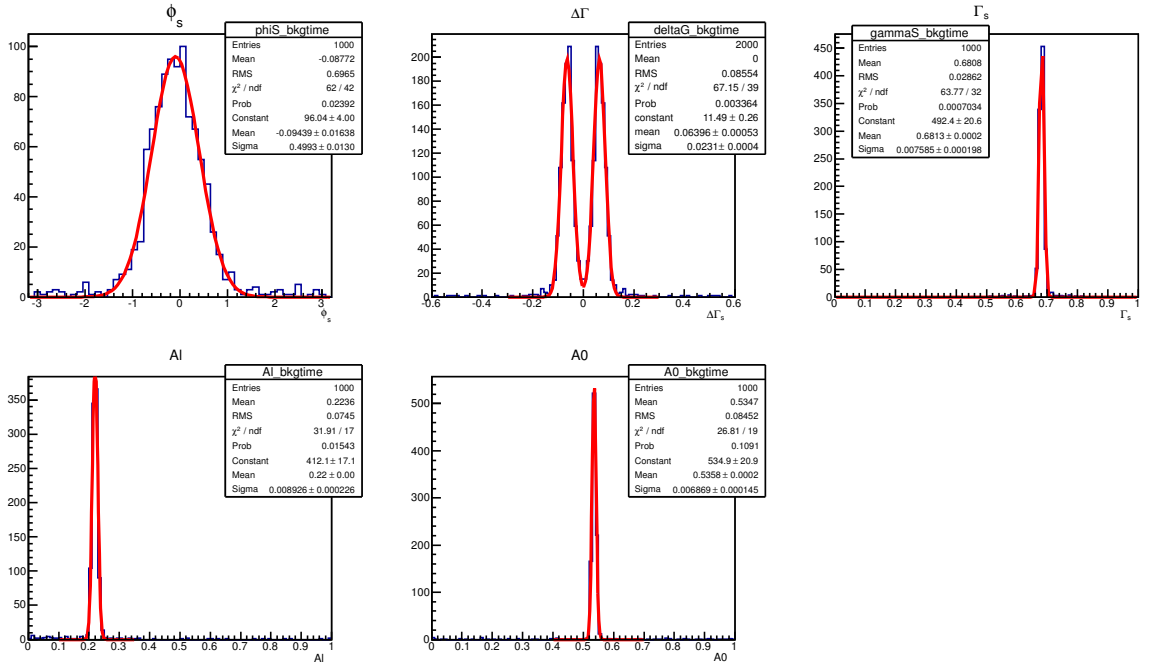

Figure 9.8: Distributions of fit values of the pseudo-experiments with background lifetime model systematically altered. Provided by Munich team [75].

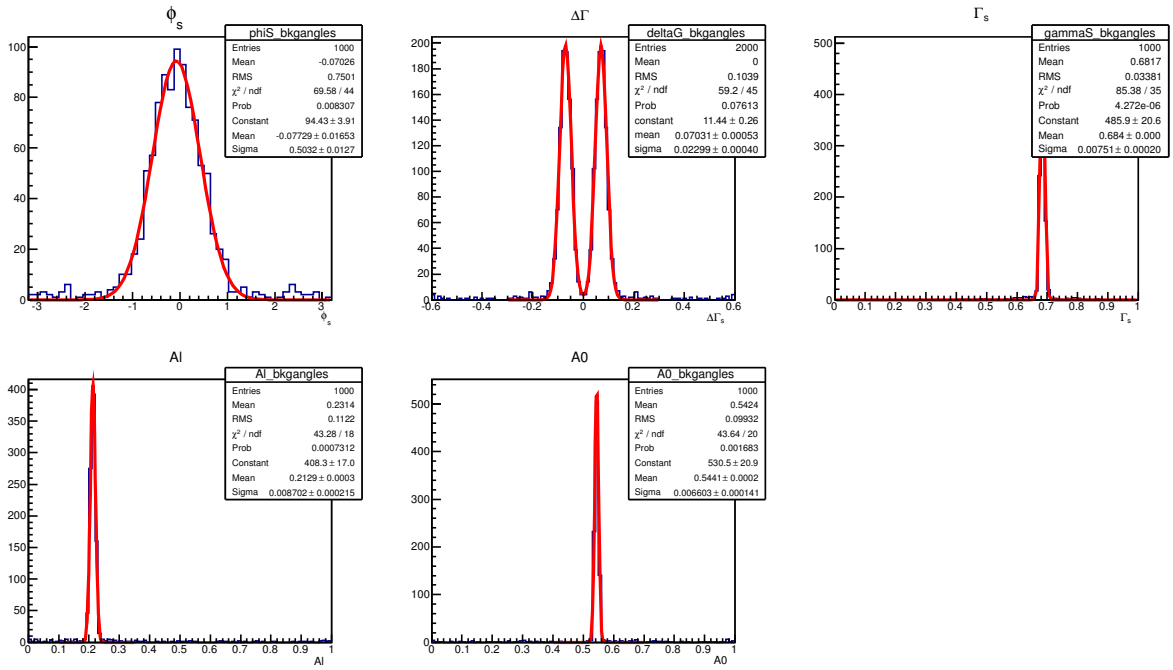

Figure 9.9: Distributions of fit values of the pseudo-experiments with background angle model systematically altered. Provided by Munich team [75].

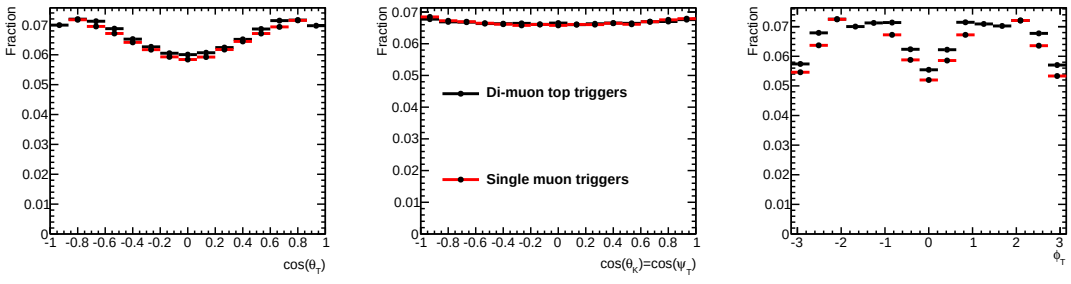

Figure 9.10: A plot showing the angular acceptance for the transversity angles for the different trigger sets considered for systematics.

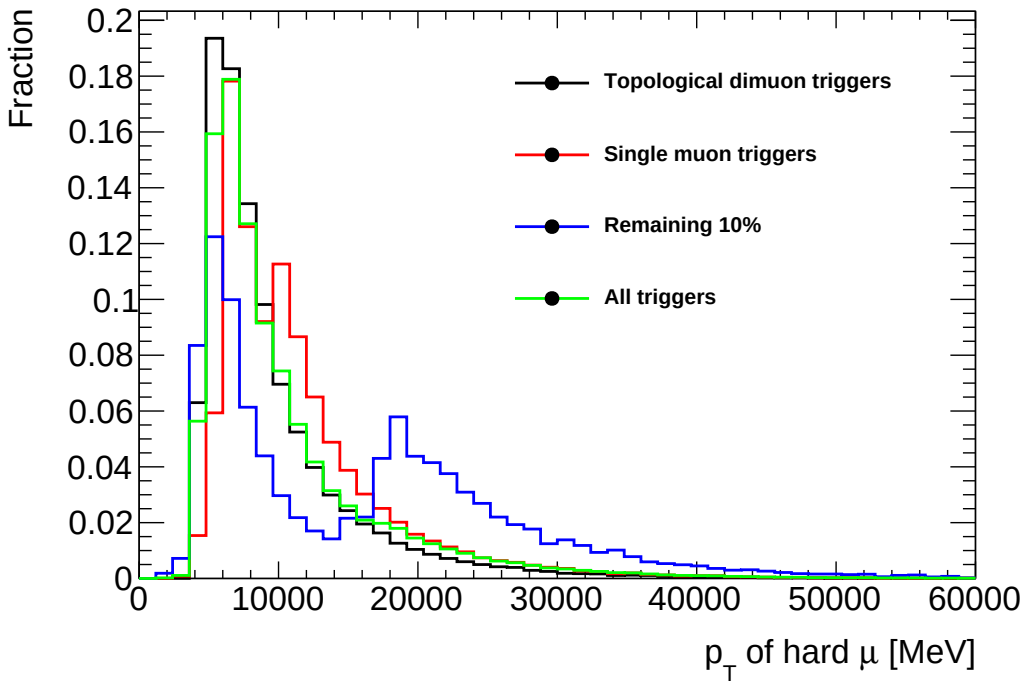

Figure 9.11: A plot showing the p_T distribution of the muon with the larger p_T with the different trigger sets considered in the systematics.

9.3 Systematics due to residual Inner Detector alignment effects

Knowing the exact position of the sensitive elements of the detector is crucial for the vertex measurements that the lifetime aspect of this measurement relies on. To estimate the impact on our measurements from misalignment effects, simulated events were studied. The most important aspect of the track measurements with regard to the lifetime is the transverse impact parameter d_0, so this parameter will be focused on. First the impact parameter d_0 is measured with respect to the primary vertex as a function of η and ϕ in a grid with 25×25 entries. The d_0-distribution is fitted for each η and ϕ with a Gaussian function. The results obtained reflects the offset and the mean value and is stored as a separate histogram. For the hypothetical perfectly aligned detector, the d_0 distribution is expected to be centred around zero and any observed offset reflects residual misalignment effects. The left 2D-histogram in figure 9.12 shows the mean value of the d_0 value obtained with data for bins in η and ϕ. The histogram was produced for data obtained during different data taking periods and significant changes between them are not observed; this is consistent with a stable Inner Detector during data taking.

The second step used is to take the histogram obtained to introduce the d_0-offset observed in data to simulated events. The track based alignment algorithm as used for the alignment of the ATLAS inner detector is used for this [77]. The simulated tracks used as an input to the algorithm are distorted using the information from the d_0 histogram created earlier. The d_0-value of each of the input tracks as a function of η and ϕ is forced to the value measured in the data and obtained from the histogram. The track based alignment algorithm automatically tweaks the detector geometry in order to minimise the residuals obtained from the d_0 distorted track. It is configured to only change the geometry of the pixel detector, the detector that dominates the d_0 measurement. All six degrees of freedom of each individual pixel sensor are aligned. The right plot in figure 9.12 shows the mean

value of the d_0 value obtained from simulated events after the alignment algorithm with d_0 distorted tracks is performed. The plot presenting the simulated events reproduces nicely the shape and size of the d_0 offset as observed in data. The overlap residual distribution, an independent measure for residual misalignment effects in the radial direction is obtained from both data and simulated events. The overlap residual distribution using simulated results nicely reproduces the behaviour observed in data. The procedure is described in more detail in [78].

Two different alignment geometry files are produced, one corresponding to the inner detector performance obtained with *Athena* release 16 processed data and one with release 17 processed data. The average d_0 offset obtained with release 17 data is reduced when compared with 16 data as would be expected with further alignment improvements.

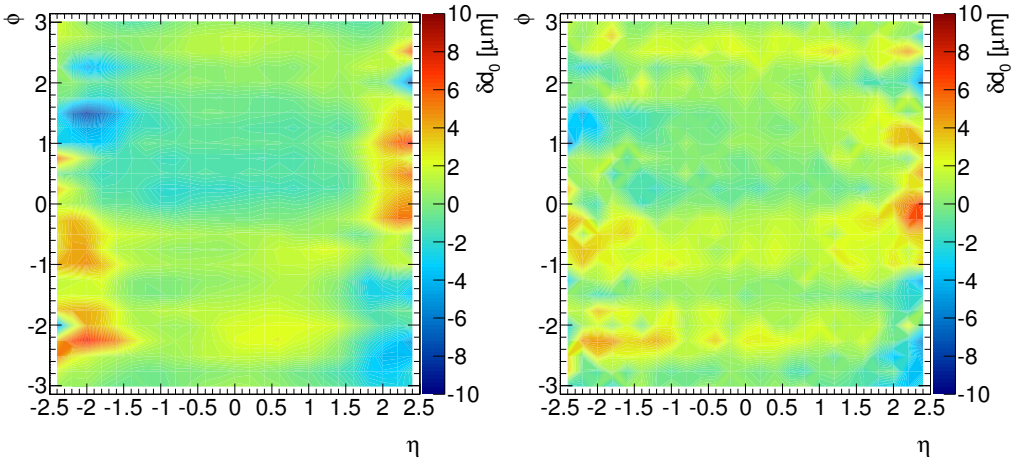

Figure 9.12: The two figures show the average d_0 offset as a function of η and ϕ measured with data reconstructed with release 17 (left) and from simulated events (right). The geometry used to reconstruct the simulated events is distorted using the information obtained from data. Work done by Munich team [75].

The uncertainty from residual misalignment effects is determined using the geometry files produced from the alignment algorithm. This geometry file is used to reconstruct simulated B_s events. The difference between the parameters determined with the unbinned maximum likelihood fit obtained with simulated events reconstructed with and without misaligned geometry is used to determine the systematic uncertainty. Some 7000 $B_s^0 \to J/\psi\phi$ signal events are reconstructed;

the same events at generator level are used to measure any residual misalignment effects affecting the reconstruction. The statistical uncertainties returned from the fit are strongly correlated. This is tested by repeating the measurement using 100 subsamples with events randomly chosen. The differences in the mean value of this distribution obtained from the 100 subsamples is consistent with the offset measured with the complete set of simulated events.

Parameter	Perfect Alignment	rel. 17 Alignment	Alignment Systematics
NSig	6951	6934	
τ_s	1.518 ± 0.0023	1.520 ± 0.023	0.002
$\Delta\Gamma_s$	0.1028 ± 0.0309	0.1024 ± 0.00	-0.003
Γ_s	0.6590 ± 0.0099	0.6577 ± 0.0100	-0.0012
ϕ_S	-0.61 ± 0.330	-0.58 ± 0.34	-0.03

Table 9.6: The main parameters obtained with the fit with perfect and misaligned geometry. The last column reflects the systematic uncertainty assigned to residual misalignment effects in data.

9.4 Systematics due to uncertainty in tagging

The systematic errors due to the uncertainty in tagging[1] are estimated by comparing the default fit with fits obtained using alternate tag probabilities. The tag probabilities are altered in two ways: they are varied coherently up and down the statistical uncertainty on each bin of the distribution and altered by varying the models of the parameterisation of the probability distributions from the central value. Additional uncertainties are included by varying the PDF terms accounting for differences between signal and background tag probabilities. Small differences between the kinematics of the signal decays B_s and $B^{\pm}$ mean that the difference in the opposite side tag response is estimated to be small compared to the other uncertainties and has not been considered as an additional systematic within the analysis.

[1]These are only applicable for the tagged fit

9.5 Summary of systematic uncertainties

The individual systematic uncertainties are summed in quadrature and presented in table 9.7 for the untagged fit and table 9.8 for the tagged fit to give the total contribution to the errors for each parameter due to sources of systematic uncertainty.

Systematic	ϕ_s (rad)	$\Delta\Gamma_s$ (ps^{-1})	Γ_s (ps^{-1})	$\lvert A_\parallel(0)\rvert^2$	$\lvert A_0(0)\rvert^2$	$\lvert A_s(0)\rvert^2$
ID alignment	0.04	< 0.001	0.001	< 0.001	< 0.001	< 0.01
Trigger efficiency	< 0.01	< 0.001	0.002	< 0.001	< 0.001	< 0.01
Signal mass model	0.02	0.002	< 0.001	< 0.001	< 0.001	< 0.01
Bkg mass model	0.03	0.001	< 0.001	0.001	< 0.001	< 0.01
Resolution model	0.05	< 0.001	0.001	< 0.001	< 0.001	< 0.01
Bkg lifetime model	0.02	0.002	< 0.001	< 0.001	< 0.001	< 0.01
Bkg angles model	0.05	0.007	0.003	0.007	0.008	0.02
B_d contribution	0.05	< 0.001	< 0.001	< 0.001	0.005	< 0.01
Total	0.10	0.008	0.004	0.007	0.009	0.02

Table 9.7: Summary of systematic uncertainties assigned to parameters of interest in the untagged fit

Systematic	ϕ_s (rad)	$\Delta\Gamma_s$ (ps^{-1})	Γ_s (ps^{-1})	$\lvert A_\parallel(0)\rvert^2$	$\lvert A_0(0)\rvert^2$	$\lvert A_S(0)\rvert^2$	$\delta_\perp$ (rad)	$\delta_\parallel$ (rad)	$\delta_\perp - \delta_S$ (rad)
ID alignment	$<10^{-2}$	$<10^{-3}$	$<10^{-3}$	$<10^{-3}$	$<10^{-3}$	-	$<10^{-2}$	$<10^{-2}$	-
Trigger efficiency	$<10^{-2}$	$<10^{-3}$	0.002	$<10^{-3}$	$<10^{-3}$	$< 10^{-3}$	$<10^{-2}$	$<10^{-2}$	$<10^{-2}$
B_d contribution	0.03	0.001	$<10^{-3}$	$<10^{-3}$	0.005	0.001	0.02	$<10^{-2}$	$<10^{-2}$
Tagging	0.10	0.001	$<10^{-3}$	$<10^{-3}$	$<10^{-3}$	0.002	0.05	$<10^{-2}$	$<10^{-2}$
Models:									
Default fit	$<10^{-2}$	0.002	$<10^{-3}$	0.003	0.002	0.006	0.07	0.01	0.01
Signal mass	$<10^{-2}$	0.001	$<10^{-3}$	$<10^{-3}$	0.001	$<10^{-3}$	0.03	0.04	0.01
Bkg mass	$<10^{-2}$	0.001	0.001	$<10^{-3}$	$<10^{-3}$	0.002	0.06	0.02	0.02
Resolution	0.02	$<10^{-3}$	0.001	0.001	$<10^{-3}$	0.002	0.04	0.02	0.01
Bkg time	0.01	0.001	$<10^{-3}$	0.001	$<10^{-3}$	0.002	0.01	0.02	0.02
Bkg angles	0.02	0.008	0.002	0.008	0.009	0.027	0.06	0.07	0.03
Total	0.11	0.009	0.003	0.009	0.011	0.028	0.13	0.09	0.04

Table 9.8: Summary of systematic uncertainties assigned to parameters of interest in the tagged fit

Chapter 10

Results

10.1 Results from other experiments

Similar analyses have been performed by other experiments at the LHC and Tevatron accelerators. Table 10.1 summarises their results. There have been measurements prior to these, however they were only able to set limits for the value of ϕ_s.

Variables	CDF [79]	D0 [74]	LHCb [80]
Number of events	6500	5598 ± 113	27617
ϕ_s [rad.]		-0.55 ± 0.38	$0.07 \pm 0.09 \pm 0.01$
Γ_s [ps$^-$1]	$0.654 \pm 0.011 \pm 0.005$	0.693 ± 0.018	$0.663 \pm 0.005 \pm 0.006$
$\Delta\Gamma_s$ [ps$^-$1]	$0.075 \pm 0.035 \pm 0.006$	0.163 ± 0.065	$0.100 \pm 0.016 \pm 0.003$
$\lvert A_0(0)^2 \rvert$	$0.524 \pm 0.013 \pm 0.015$	0.558 ± 0.019	$0.521 \pm 0.006 \pm 0.010$
$\lvert A_\parallel(0)^2 \rvert$	$0.231 \pm 0.014 \pm 0.015$	0.231 ± 0.030	$0.230 \pm 0.008 \pm 0.011$[1]
$\delta_\perp$ [rad.]	$2.95 \pm 0.64 \pm 0.07$		$3.07 \pm 0.22 \pm 0.07$

Table 10.1: A table giving the results from other experiments. Where two uncertainties are given the first is the statistical the second is the systematic.
[1] approximated from 1-$|A_0(0)^2| - |A_\perp(0)^2|$

10.2 ATLAS 2011 dataset untagged fit results

The initial ATLAS publication [65] used the 2011 ATLAS dataset and the methods and tools described in this thesis. The fit utilised the transversity angles. The results can be seen in table 10.2 and the correlations in table 10.3. The fitted

per-candidate error distributions can be seen in figure 10.1, the mass and lifetime fit projections in figure 10.2 and the fitted angular distribution projections in figure 10.3. The transversity amplitudes $|A_0(0)|$ and $|A_\parallel(0)|$ are consistent within one standard deviation with the measurements from other experiments. The measurement of $\Delta\Gamma_s$ is consistent within one standard deviation (when including systematic uncertainty). The ATLAS central point for this parameter is the lowest of those presented. In addition, Γ_s is consistent within one standard deviation to the other experiments listed and falls towards the centre of the other measurements. The comparisons for $\Delta\Gamma_s$ and Γ_s are better illustrated on figure 10.5. Even in the untagged case the uncertainty on these parameters are very similar to the LHCb result. The fit extracts 22690 ± 160 signal events from 131513 selected candidates.

Without flavour tagging information the uncertainty on the measurement of ϕ_s is not as competitive with measurements using a similar level of statistics, however it is consistent within one standard deviation with the standard model prediction and the measurements from other experiments. This comparison is better illustrated on figures 10.7. Figure 10.4 also shows the theoretical relation between the two parameters as a green band demonstrating the importance of correlations.

When considering both the statistical and systematic uncertainty, the $|A_s(0)|$ is consistent with zero. The parameter $\delta_\perp$ is also consistent within one standard deviation of the other measurements.

Figure 10.6 shows the mass spectrum of the sample after a proper decay time cut of > 0.3 ps which eliminates the majority of the direct J/ψ background ($pp \to J/\psi\ X$). This sub-sample is not used in the fit, however the plot helps to illustrate the relative proportion of the background sources.

The remaining parameters are either not available for comparison, not applicable to the scope of the analysis, or are not physical parameters. Such nuisance parameters arbitrarily result from the design of the detector and the analysis.

Parameter	Explanation	Fitted value ± stat ± sys
$\|A_0(0)\|^2$	Transversity Amplitude	0.5282 ± 0.0061 ± 0.009
$\|A_{\|\|}(0)\|^2$	Transversity Amplitude	0.2198 ± 0.0076 ± 0.007
$\Delta\Gamma_s$ [ps^{-1}]	$\Gamma_L - \Gamma_H$	0.0528 ± 0.0208 ± 0.008
Γ_s [ps^{-1}]	$\frac{\Gamma_L+\Gamma_H}{2}$	0.6772 ± 0.0072 ± 0.004
ΔM	ΔM_s B_s mixing [$\hbar s^{-1}$]	17.7700 (fixed)
ϕ_s	CP violation	0.2218 ± 0.4105 ± 0.1
$\delta_{\|\|}$ [rad]	Strong phases	3.1403 ± 0.0959
$\delta_\perp$ [rad]	Strong phases	2.8756 ± 0.3603
SF τ_{Bs}	B_s Lifetime ScaleFactor	1.0200 ± 0.0052
m_{Bs} [GeV]	B_s Mass	5.3668 ± 0.0002
SF m_{Bs}	B_s mass scale factor [GeV]	1.1896 ± 0.0087
τ_{tails} [ps]	τ for tails componant	0.1582 ± 0.0062
τ_{fast} [ps]	τ for fast componant	0.3358 ± 0.0063
τ_{slow} [ps]	τ for slow componant	1.5929 ± 0.0415
f_{prompt}	fraction of prompt time bkg	0.6329 ± 0.0050
f_{indirect}	fraction of indirect time bkg	0.1790 ± 0.0073
f_{tails}	fraction of tails time bkg	0.1223 ± 0.0079
f_{sig}	Signal fraction	0.1738 ± 0.0012
b	Mass bkg slope	-1.7579 ± 0.0419
$p^0_{\theta_T,\mathrm{bck}}$	bkg angles for generic background	0.0084 ± 0.0007
$p^1_{\theta_T,\mathrm{bck}}$	bkg angles for generic background	-0.0117 ± 0.0010
$p^2_{\theta_T,\mathrm{bck}}$	bkg angles for generic background	-0.0070 ± 0.0007
$p^0_{\psi_T,\mathrm{bck}}$	bkg angles for generic background	0.0219 ± 0.0029
$p^1_{\psi_T,\mathrm{bck}}$	bkg angles for generic background	-0.0050 ± 0.0007
$p^0_{\varphi_T,\mathrm{bck}}$	bkg angles for generic background	-3.1284 ± 0.0111
$p^1_{\varphi_T,\mathrm{bck}}$	bkg angles for generic background	0.3902 ± 0.0043
$\|A_S(0)\|^2$	S-wave Amplitude $\|A_s(0)\|^2$	0.0203 ± 0.0165 ± 0.02
δ_s [rad]	Strong phase	0.0285 ± 0.1339

Table 10.2: A table showing the fit results for the untagged fit on the 2011 ATLAS dataset

Correlations	$\lvert A_0(0)\rvert^2$	$\lvert A_{\lvert\rvert}(0)\rvert^2$	$\Delta\Gamma_s$	ΔM	ϕ_s	$\delta_{\lvert\rvert}$	$\delta_\perp$	SF τ_{Bs}	τ_{tails}	τ_{fast}	τ_{slow}
$\lvert A_0(0)\rvert^2$	1	-0.3	0.118	-0.064	-0.028	-0.009	-0.01	0	0.002	0	0
$\lvert A_{\lvert\rvert}(0)\rvert^2$	-0.3	1	0.109	-0.097	-0.043	0.032	0	-0.002	-0.002	0.005	-0.001
$\Delta\Gamma_s$	0.118	0.109	1	-0.599	-0.128	-0.002	-0.021	0	0	0.005	0
ΔM	-0.064	-0.097	-0.599	1	0.38	-0.006	-0.039	0.005	-0.003	0.03	0.001
ϕ_s	-0.028	-0.043	-0.128	0.38	1	-0.009	-0.152	0	-0.001	-0.002	0
$\delta_{\lvert\rvert}$	-0.009	0.032	-0.002	-0.006	-0.009	1	0.006	0	0	-0.001	0
$\delta_\perp$	-0.01	0	-0.021	-0.039	-0.152	0.006	1	0	0	-0.001	0
SF τ_{Bs}	0	-0.002	0	0.005	0	0	0	1	0	0.004	0.44
τ_{tails}	0.002	-0.002	0	-0.003	-0.001	0	0	0	1	-0.008	0
τ_{fast}	0	0.005	0.005	0.03	-0.002	-0.001	-0.001	0.004	-0.008	1	0.002
τ_{slow}	0	-0.001	0	0.001	0	0	0	0.44	0	0.002	1

Table 10.3: A table showing the correlation coefficient for the first twelve parameters for the untagged fit on the 2011 ATLAS dataset

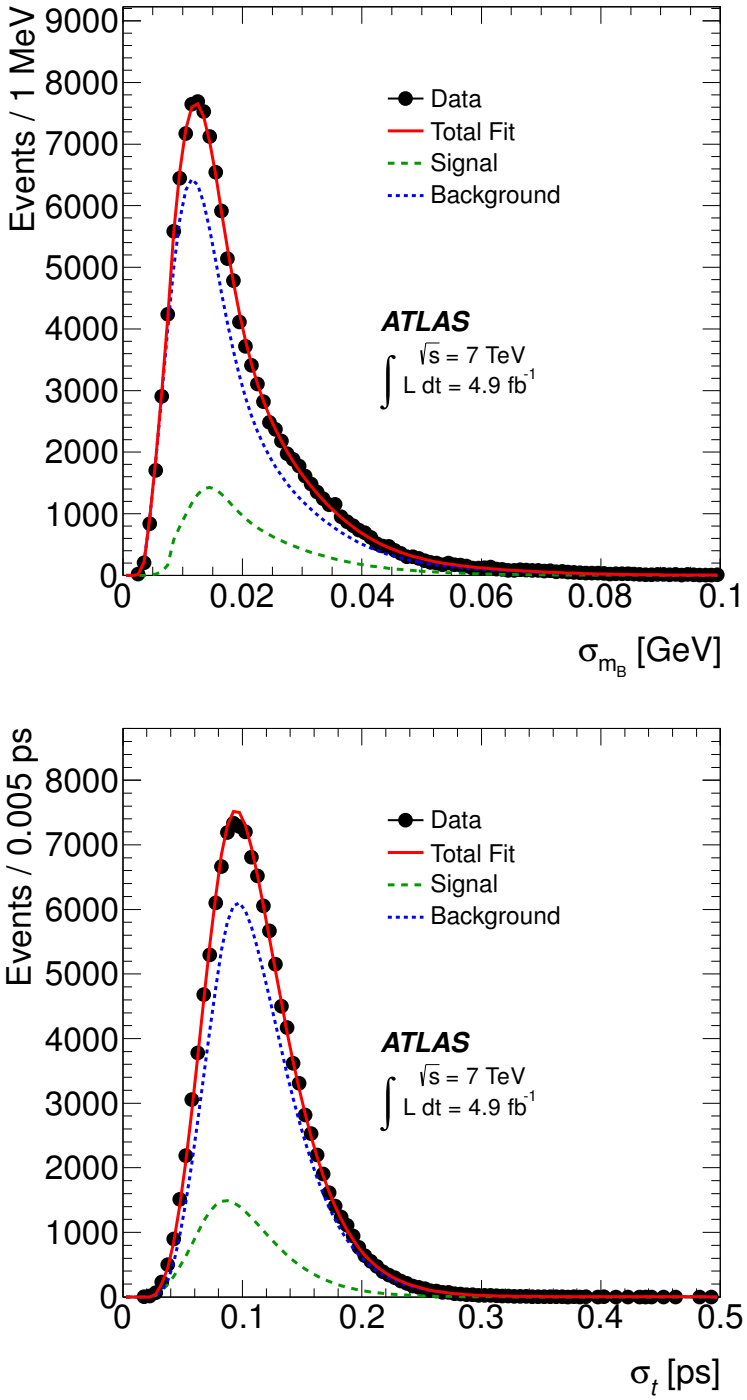

Figure 10.1: Plots showing the projections for the uncertainty of the B_s mass and B_s proper decay time for the ATLAS untagged fit using the 2011 dataset.

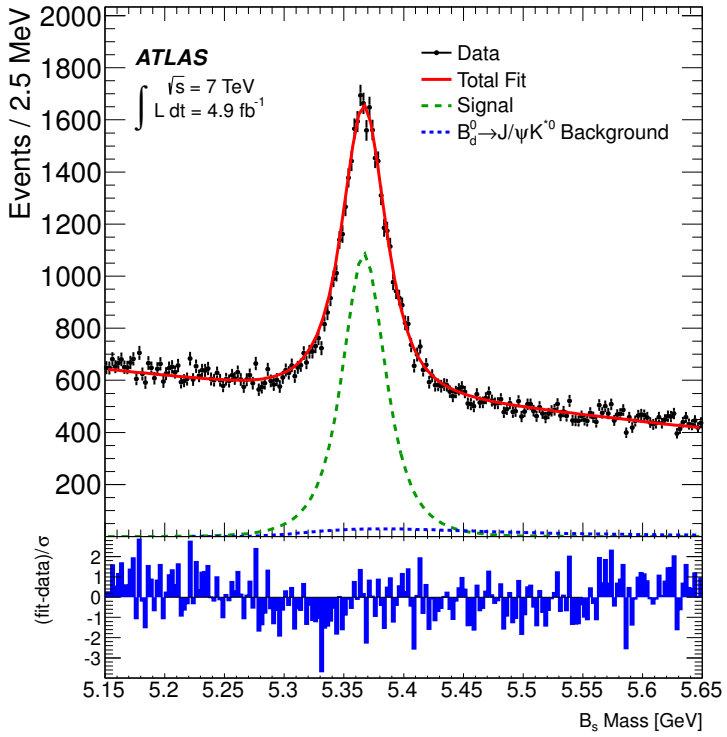

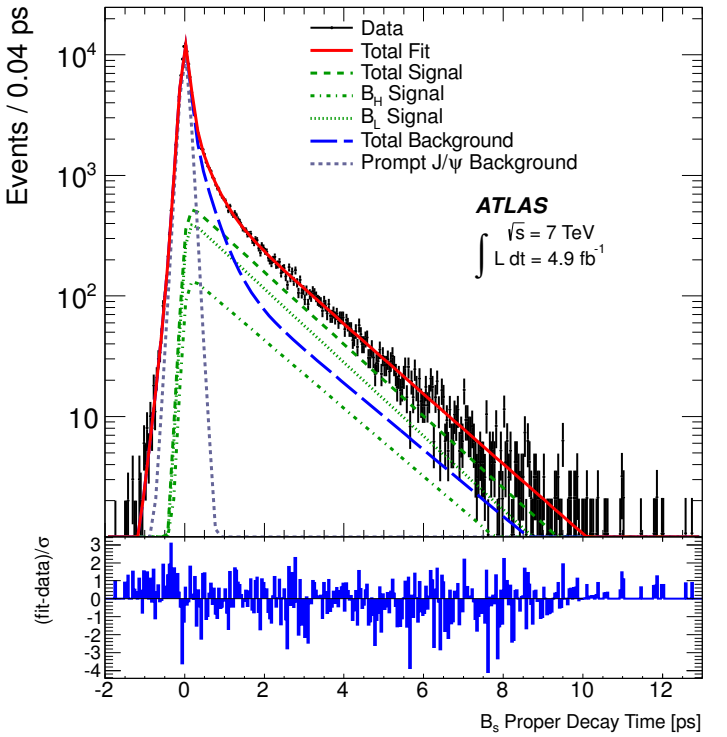

Figure 10.2: Plots showing the projections of B_s mass and B_s proper decay time of the ATLAS untagged fit using the 2011 dataset. The pull distribution at the bottom shows the difference between the data and fit value normalised to the data uncertainty.

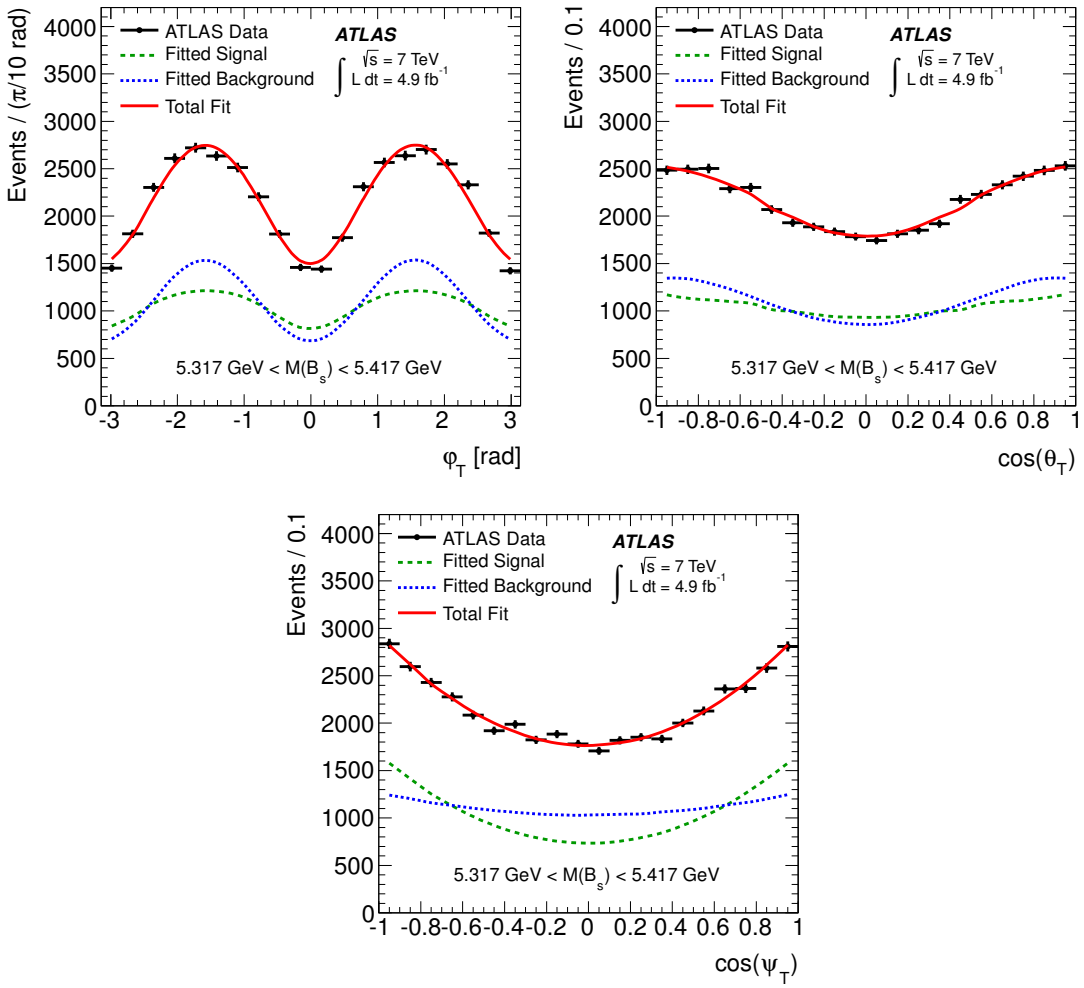

Figure 10.3: Plots showing the projections of the Tranversity angles for the ATLAS untagged fit using the 2011 dataset.

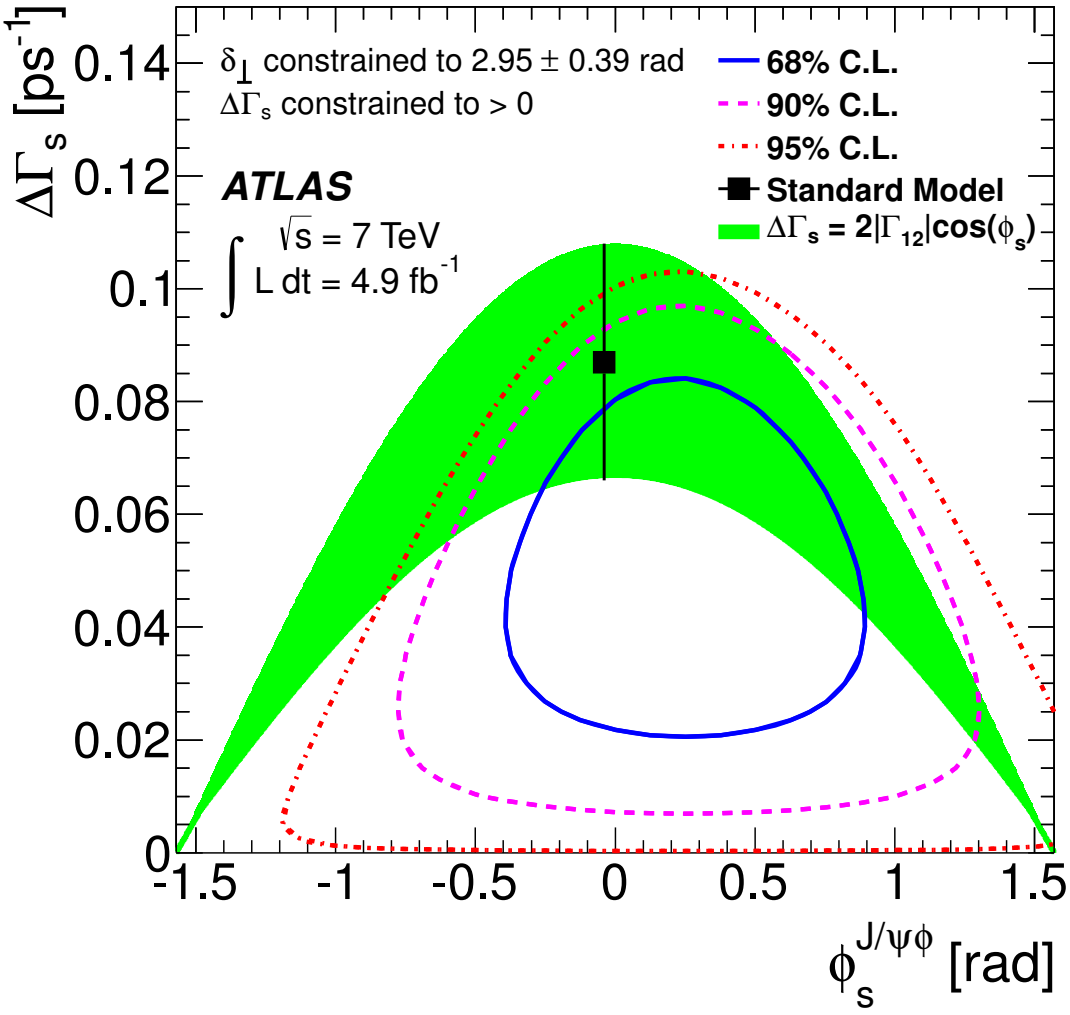

Figure 10.4: Likelihood contours in the ϕ_s - $\Delta\Gamma_s$ plane. Three contours show the 68%, 90% and 95% confidence intervals (statistical uncertainty only). The green band is the theoretical prediction of mixing-induced CP violation. The PDF contains a fourfold ambiguity. Three minima are excluded by applying the constraints from the LHCb measurements. Plot produced by the Munich team using the main fit [75].

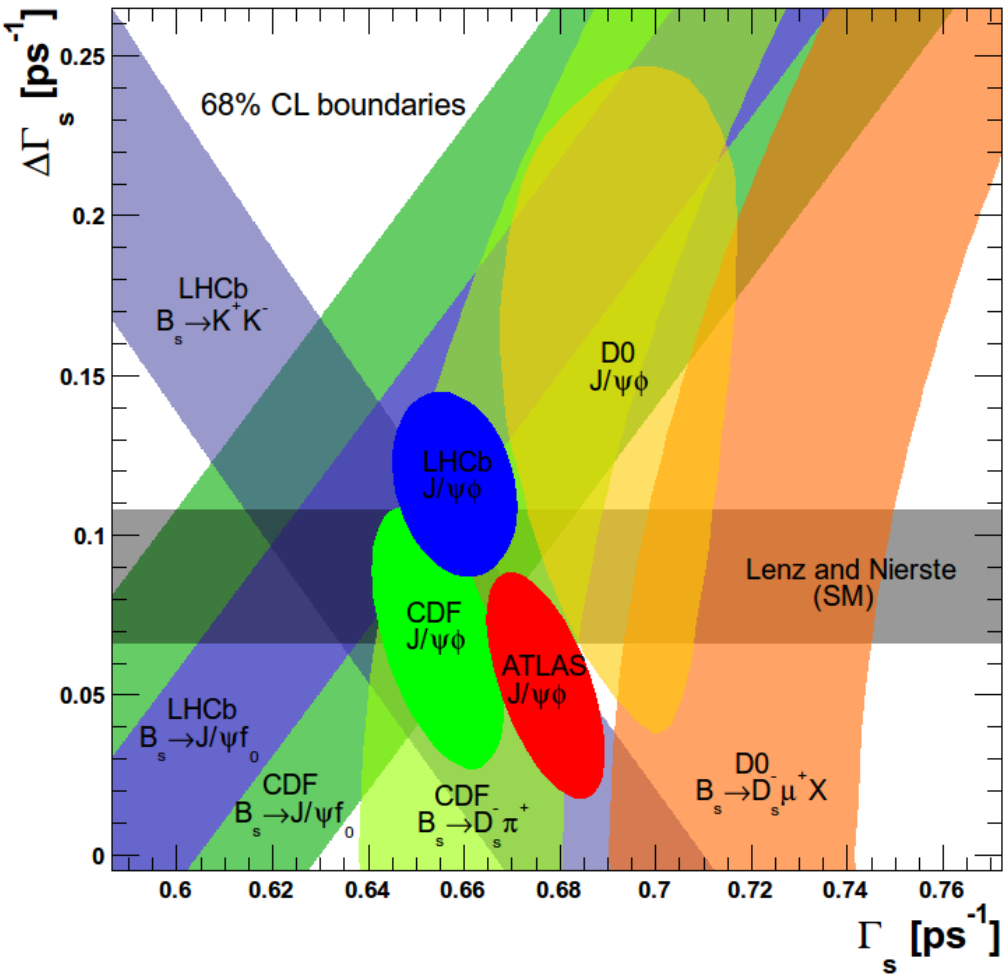

Figure 10.5: Likelihood contours in the $\Gamma_s - \Delta\Gamma_s$ plane comparing measurements from various experiments. The ATLAS contour is using the untagged fit with the 2011 dataset [65].

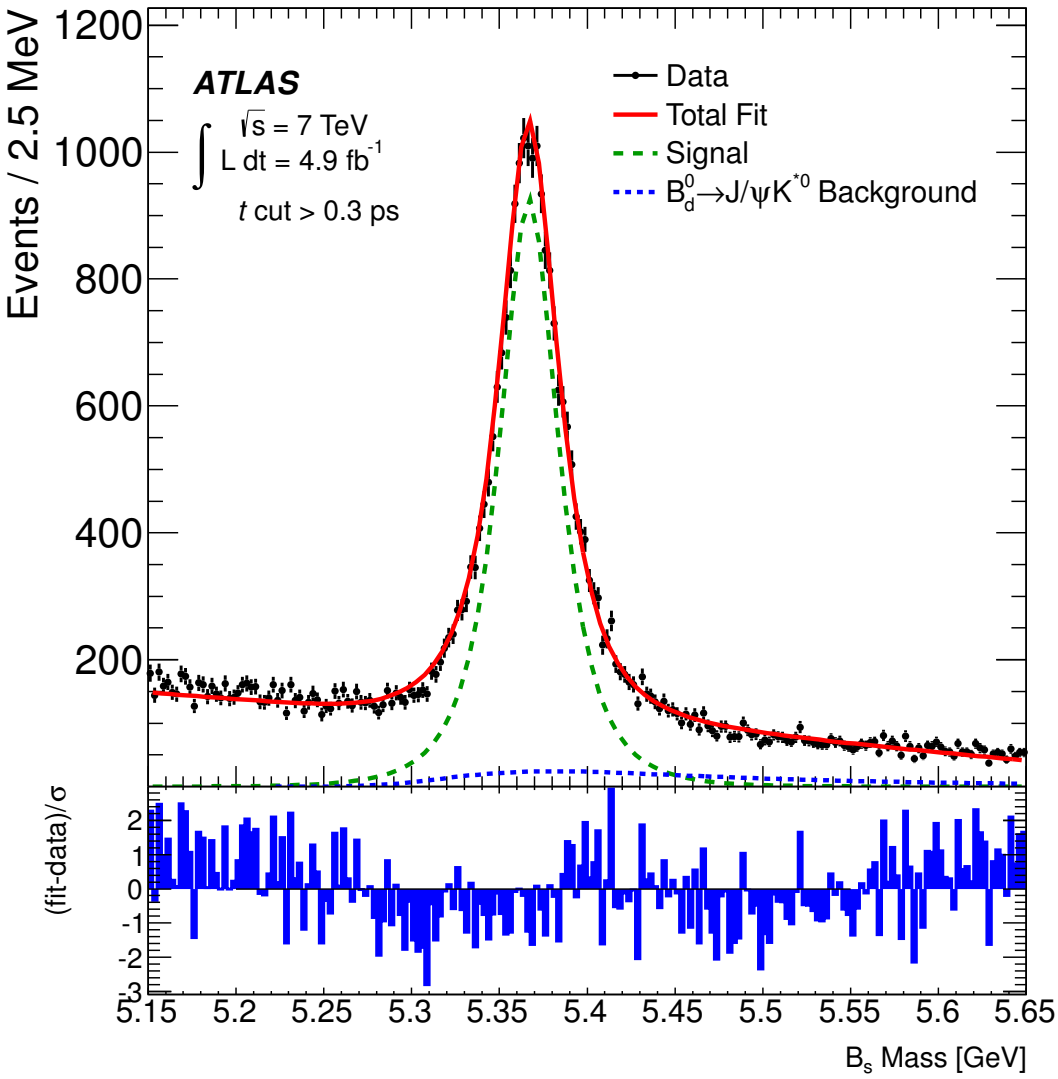

Figure 10.6: Plots showing the projections of B_s mass fit after a cut on the proper decay time. This cut is not used in the data fit, this plot is to illustrate the effect of the prompt J/ψ background $pp \to J/\psi$.

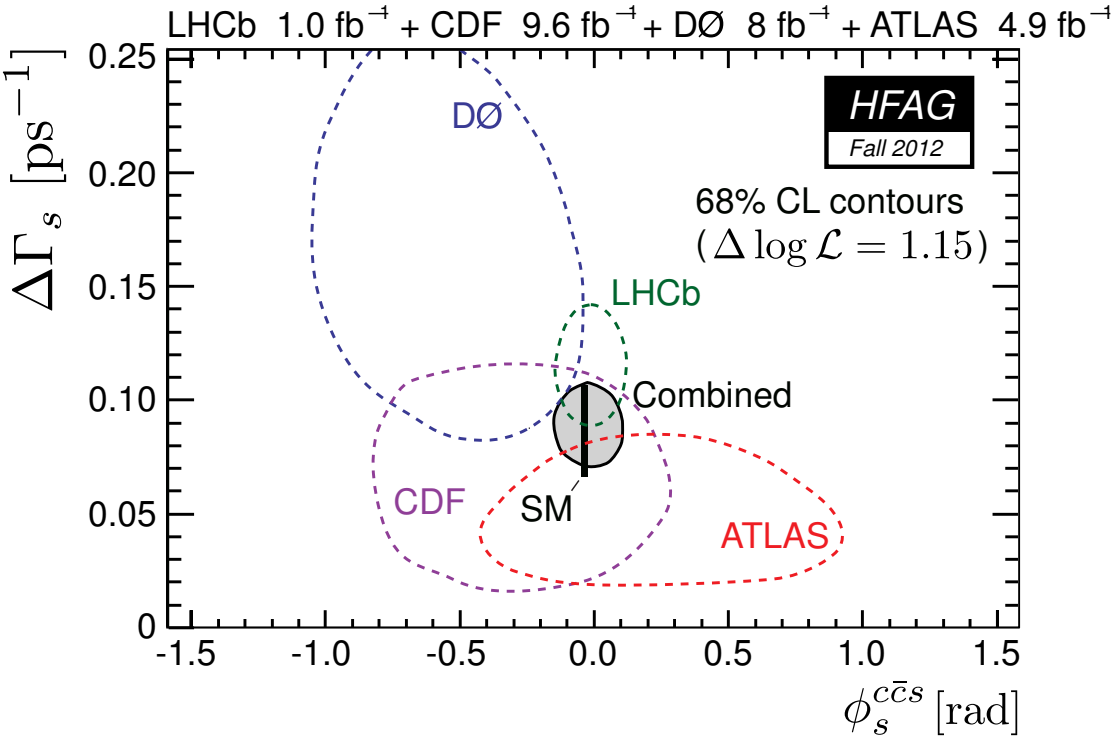

Figure 10.7: Likelihood contours in the ϕ_s - $\Delta\Gamma_s$ plane comparing measurements from various experiments. The ATLAS contour is using the untagged fit with the 2011 dataset.

10.3 ATLAS 2011 dataset tagged fit results

A second ATLAS result [61] was recently released using the same dataset (2011) and choice of angles but including tagging information. This extra information leads to lower uncertainty on key variables such as ϕ_s making it the second most precise measurement at time of writing. The improved contours are visible in figure 10.8. As seen in table 10.4 the addition of tagging information has not significantly changed the centre value or the magnitude of the uncertainty for the majority of the remaining parameters. The transversity amplitudes $|A_0(0)|$ and $|A_\parallel(0)|$ are still consistent within one standard deviation with the measurements from other experiments . The measurement of $\Delta\Gamma_s$ is still consistent with other experiments within one standard deviation. In addition, Γ_s is consistent within one standard deviation to the other experiments listed and falls towards the centre of the other measurements.

With the addition of tagging information the constraint on $\delta_\perp$ is no longer needed. Removing the constraint causes the result for this parameter to change significantly and is no longer consistent with previous measurements within one standard deviation. This result is public and ATLAS has no explanation for the large disagreement with other experiments at this time.

Table 10.5 contains correlations between key variables and figure 10.9 shows one dimensional likelihood scan for key parameters providing a visual means for assessing the stability of fit. This conflict should be investigated in future measurements. The plots show deep and consistent minima suggesting the fits are healthy and stable.

Parameter	Explanation	Fitted Value ± stat ± sys
$\|A_0(0)\|^2$	Transversity Amplitude	0.5287 ± 0.0059 ± 0.011
$\|A_{\|\|}(0)\|^2$	Transversity Amplitude	0.2201 ± 0.0075 ± 0.009
$\|A_S(0)\|^2$	Transversity Amplitude for S-wave	0.024 ± 0.014 ± 0.028
Γ_s [ps^{-1}]	$\frac{\Gamma_L+\Gamma_H}{2}$	0.6776 ± 0.0068 ± 0.003
$\Delta\Gamma_s$ [ps^{-1}]	$\Gamma_L - \Gamma_H$	0.053 ± 0.021 ± 0.009

ΔM [$\hbar$s^{-1}]	B Mixing rate	17.77
ϕ_s	CP violation	0.11 $\pm$ 0.25 $\pm$ 0.11
$\delta_{\|\|}$ [rad]	Strong phases	3.138 $\pm$ 0.095 $\pm$ 0.09
$\delta_\perp$ [rad]	Strong phases	3.89 $\pm$ 0.48 $\pm$ 0.13
$\delta_\perp - \delta_S$ [rad]	Strong phases	3.14 $\pm$ 0.11 $\pm$ 0.04
m_{Bs} [GeV]	B_s Mass	5.36681 $\pm$ 0.00016
SF m_{Bs}	B_s Mass Scale factor	1.1937 $\pm$ 0.0088
SF τ_{Bs}	B_s time Scale factor	1.0206 $\pm$ 0.0052
f_{sig}	signal fraction	0.1737 $\pm$ 0.0012
b	Background mass slope	-0.2206 $\pm$ 0.0052
f_{prompt}	fraction of prompt time bkg	0.6335 $\pm$ 0.0049
f_{indirect}	fraction of indirect time bkg	0.2002 $\pm$ 0.0079
f_{tails}	fraction of tails time bkg	0.0987 $\pm$ 0.0065
τ_{fast} [ps]	τ for fast componant	0.3349 $\pm$ 0.0063
τ_{slow} [ps]	τ for slow componant	1.590 $\pm$ 0.041
τ_{tails} [ps]	τ for tails componant	0.1588 $\pm$ 0.0062
$f_{\mathrm{Bd}\,K^*}$	fraction of $B_d \to J/\psi\ K^{0*}$ bkg	0.065
$f_{\mathrm{Bd}\,K\pi}$	fraction of $B_d \to J/\psi\ K\pi$ bkg	0.045
mpv$_{\mathrm{Bd}\,K^*}$ [GeV]	Mass dedicated $B_d \to J/\psi\ K^{0*}$	5.39178
$\sigma_{\mathrm{Bd}\,K^*}$ [GeV]	scale factor $B_d \to J/\psi\ K^{0*}$	0.048
τ_{BdBs} [ps]		1.5441
$p^0_{\theta_T,\mathrm{BdK^*}}$	bkg angles $B_d \to J/\psi\ K^{0*}$	0.0177904
$p^1_{\theta_T,\mathrm{BdK^*}}$	bkg angles $B_d \to J/\psi\ K^{0*}$	0.00101918
$p^2_{\theta_T,\mathrm{BdK^*}}$	bkg angles $B_d \to J/\psi\ K^{0*}$	0.00138518
$p^0_{\psi_T,\mathrm{BdK^*}}$	bkg angles $B_d \to J/\psi\ K^{0*}$	0.4856
$p^1_{\psi_T,\mathrm{BdK^*}}$	bkg angles $B_d \to J/\psi\ K^{0*}$	0.449817
$p^2_{\psi_T,\mathrm{BdK^*}}$	bkg angles $B_d \to J/\psi\ K^{0*}$	-0.0210129
$p^3_{\psi_T,\mathrm{BdK^*}}$	bkg angles $B_d \to J/\psi\ K^{0*}$	0.107954
$p^4_{\psi_T,\mathrm{BdK^*}}$	bkg angles $B_d \to J/\psi\ K^{0*}$	0.0444173

$p^0_{\varphi_T,\mathrm{BdK}^*}$	bkg angles $B_d \to J/\psi\ K^{0*}$	1.27078
$p^1_{\varphi_T,\mathrm{BdK}^*}$	bkg angles $B_d \to J/\psi\ K^{0*}$	0.193838
$p^2_{\varphi_T,\mathrm{BdK}^*}$	bkg angles $B_d \to J/\psi\ K^{0*}$	0.22196
$p^0_{\theta_T,\mathrm{BdK}\pi}$	bkg angles $B_d \to J/\psi\ K\pi$	0.00915016
$p^1_{\theta_T,\mathrm{BdK}\pi}$	bkg angles $B_d \to J/\psi\ K\pi$	-0.00487563
$p^2_{\theta_T,\mathrm{BdK}\pi}$	bkg angles $B_d \to J/\psi\ K\pi$	-0.00427443
$p^0_{\psi_T,\mathrm{BdK}\pi}$	bkg angles $B_d \to J/\psi\ K\pi$	0.488972
$p^1_{\psi_T,\mathrm{BdK}\pi}$	bkg angles $B_d \to J/\psi\ K\pi$	0.0462224
$p^2_{\psi_T,\mathrm{BdK}\pi}$	bkg angles $B_d \to J/\psi\ K\pi$	0.0256144
$p^3_{\psi_T,\mathrm{BdK}\pi}$	bkg angles $B_d \to J/\psi\ K\pi$	0.0128224
$p^4_{\psi_T,\mathrm{BdK}\pi}$	bkg angles $B_d \to J/\psi\ K\pi$	0.0123103
$p^0_{\varphi_T,\mathrm{BdK}\pi}$	bkg angles $B_d \to J/\psi\ K\pi$	2.73329
$p^1_{\varphi_T,\mathrm{BdK}\pi}$	bkg angles $B_d \to J/\psi\ K\pi$	0.180232
$p^2_{\varphi_T,\mathrm{BdK}\pi}$	bkg angles $B_d \to J/\psi\ K\pi$	0.0185354
$p^1_{\theta_T,\mathrm{bck}}$	bkg angles for generic background	$-1.382\ \pm\ 0.055$
$p^2_{\theta_T,\mathrm{bck}}$	bkg angles for generic background	$-0.829\ \pm\ 0.059$
$p^1_{\psi_T,\mathrm{bck}}$	bkg angles for generic background	$-0.229\ \pm\ 0.013$
$p^0_{\varphi_T,\mathrm{bck}}$	bkg angles for generic background	$-3.131\ \pm\ 0.011$
$p^1_{\varphi_T,\mathrm{bck}}$	bkg angles for generic background	$0.3902\ \pm\ 0.0043$

Table 10.4: A table containing the fit parameters for the tagged fit of the 2011 ATLAS dataset

Correlations	$\|A_0(0)\|^2$	$\|A_{\|\|}(0)\|^2$	$\|A_S(0)\|^2$	Γ_s	$\Delta\Gamma_s$	ϕ_s	$\delta_{\|\|}$	$\delta_\perp$	$\delta_\perp - \delta_S$	m_{Bs}	SF m_{Bs}	SF τ_{Bs}	f_{sig}
	-0.316	1	0.077	-0.093	0.105	0.01	0.009	0.004	-0.009	-0.002	0.005	-0.001	0.007
$\|A_0(0)\|^2$	1	-0.316	0.284	-0.064	0.103	0.003	-0.003	-0.017	-0.024	0.002	-0.002	0.001	-0.016
$\|A_{\|\|}(0)\|^2$	-0.316	1	0.077	-0.093	0.105	0.01	0.009	0.004	-0.009	-0.002	0.005	-0.001	0.007
$\|A_S(0)\|^2$	0.284	0.077	1	0.033	0.071	0.032	-0.011	-0.055	-0.091	0.005	0.012	0.002	0.033
Γ_s	-0.064	-0.093	0.033	1	-0.619	0.015	-0.003	0.002	-0.009	-0.003	0.033	0.005	0.12
$\Delta\Gamma_s$	0.103	0.105	0.071	-0.619	1	0.114	0.006	-0.02	0.001	0	0.005	0	0.006
ϕ_s	0.003	0.01	0.032	0.015	0.114	1	0.021	-0.06	-0.002	-0.002	0.006	0	0.006
$\delta_{\|\|}$	-0.003	0.009	-0.011	-0.003	0.006	0.021	1	0.031	0.007	0	0	0	0
$\delta_\perp$	-0.017	0.004	-0.055	0.002	-0.02	-0.06	0.031	1	0.08	-0.002	-0.003	0.001	-0.004
$\delta_\perp - \delta_S$	-0.024	-0.009	-0.091	-0.009	0.001	-0.002	0.007	0.08	1	-0.006	-0.002	-0.001	-0.004
m_{Bs}	0.002	-0.002	0.005	-0.003	0	-0.002	0	-0.002	-0.006	1	-0.012	0	-0.014
SF m_{Bs}	-0.002	0.005	0.012	0.033	0.005	0.006	0	-0.003	-0.002	-0.012	1	0.002	0.188
SF τ_{Bs}	0.001	-0.001	0.002	0.005	0	0	0	0.001	-0.001	0	0.002	1	0.006
f_{sig}	-0.016	0.007	0.033	0.12	0.006	0.006	0	-0.004	-0.004	-0.014	0.188	0.006	1

Table 10.5: A table showing the correlation between key variables of the tagged ATLAS fit

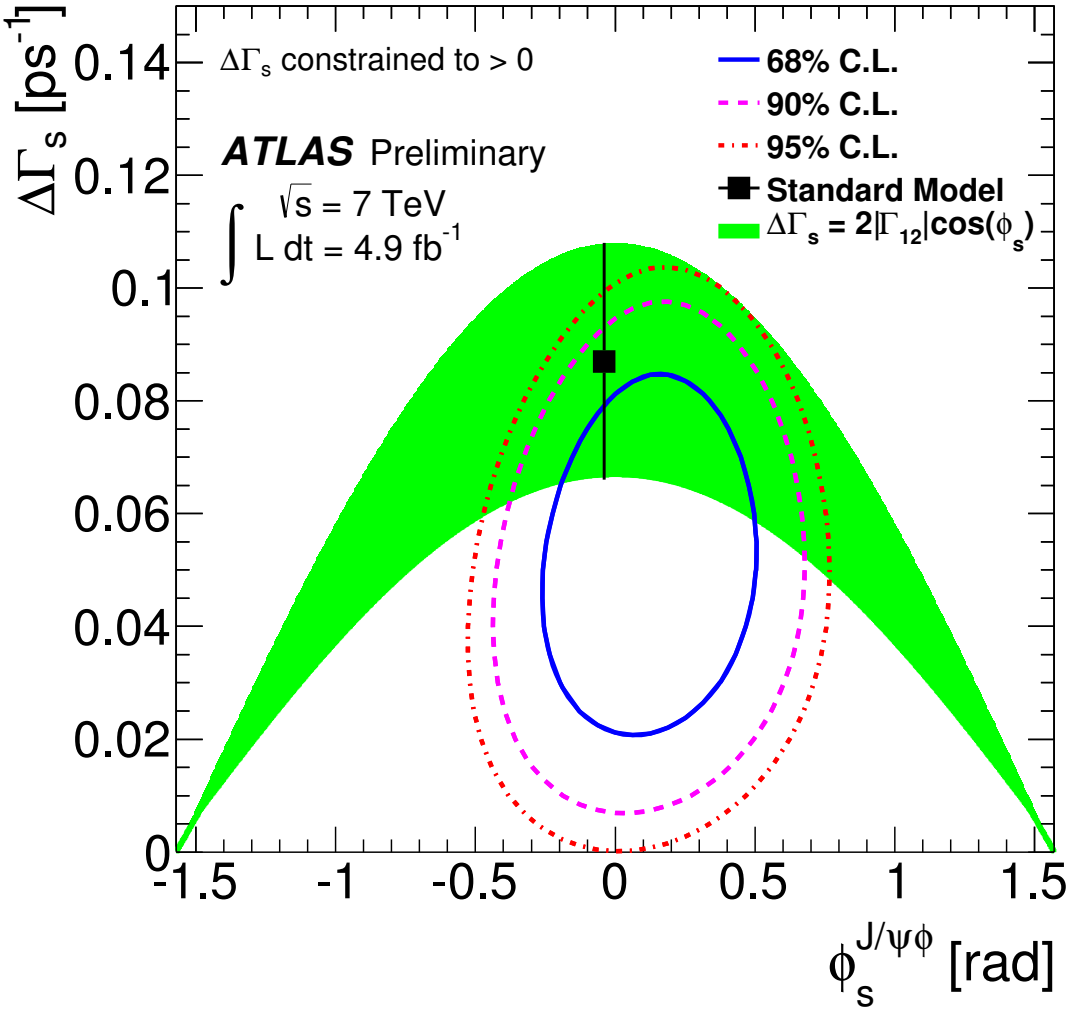

Figure 10.8: Likelihood contours in ϕ_s - $\Delta\Gamma_s$ plane. The blue and red contours show the 68% and 95% likelihood contours, respectively (statistical errors only). The green band is the theoretical prediction of mixing-induced CP violation. The PDF contains a twofold ambiguity, one minimum is excluded by applying information from LHCb measurements.

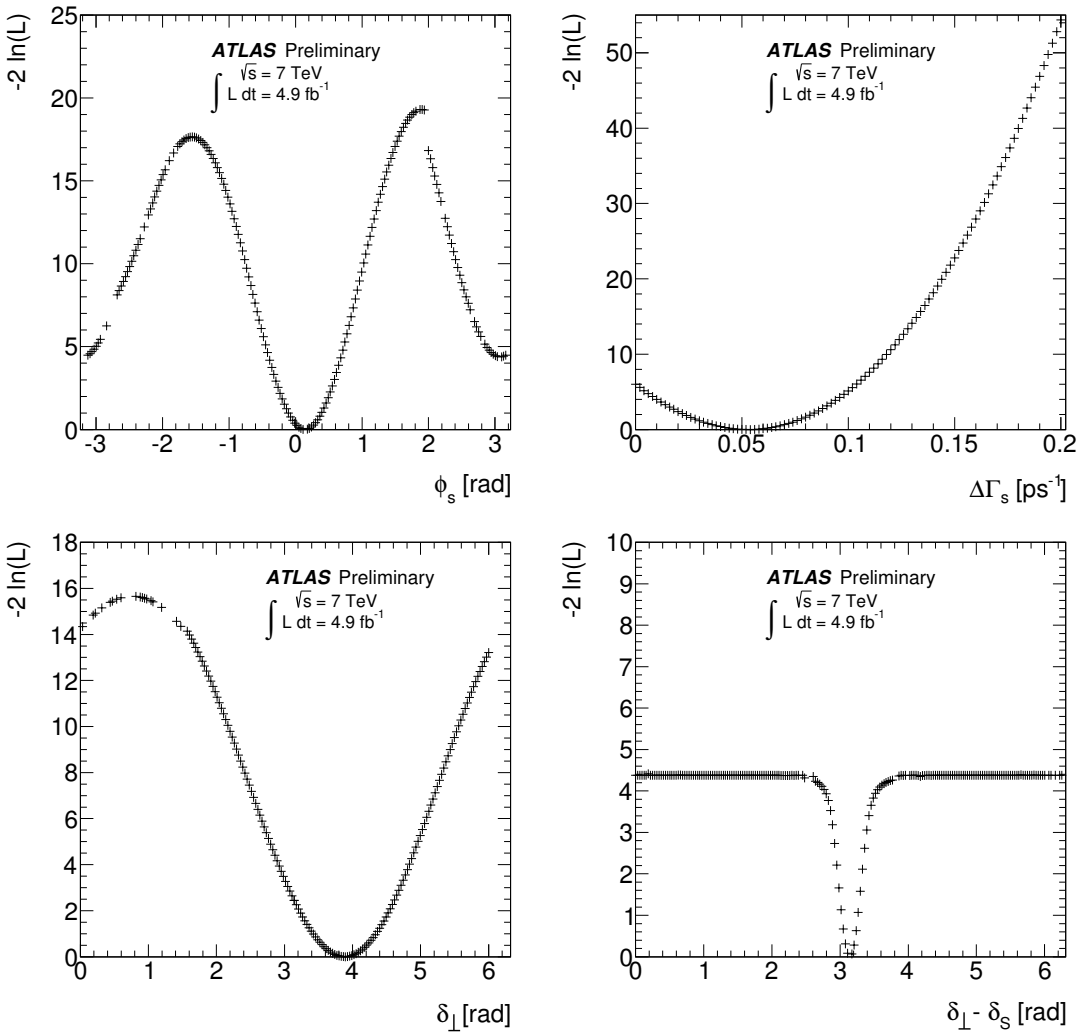

Figure 10.9: Plots showing 1 dimensional likelihood scan for ϕ_s, $\Delta\Gamma_s$, $\delta_{\parallel}$ and $\delta_{\perp}$ for the tagged likelihood fit using the ATLAS 2011 dataset

10.4 Limitations of the Analysis

This analysis provides a complete measurement for the key parameters of interest. The untagged version has passed ATLAS approval and is already published in the Journal of High Energy Physics [65]. The tagged version has passed ATLAS approval and been released as a public note[2] and will later be published in a journal. However, while it can exclude large violations of the standard model it is not accurate enough to exclude or confirm the Standard Model predictions. This can be understood better by looking at figures 10.8, 10.7 and 10.5. The primary source of the remaining uncertainty is statistical limitations arising from the low event statistics and the lifetime uncertainty of the detector. More events will be collected over the natural course of the ATLAS data program. As of writing the 2012 dataset is already recorded and almost ready for analysis. As the LHC increases the instantaneous luminosity of its runs, the B-physics trigger strategy will be revised to increase the average p_T of the muons selected which will provide marginally better lifetime resolution (see figure 6.3).

The ATLAS upgrade will provide significant improvements to the lifetime resolution as layers are added to the inner detector. The ATLAS insertable B-layer [81] is estimated to improve proper decay time resolution significantly, bringing it to similar levels obtained by the LHCb experiment (see section 10.5). ATLAS is also predicted to retain its accuracy in high luminosity environments permitting the analysis to benefit from the scalability of the LHC. This is described in more detail in section 10.5.

The assessment of the systematic uncertainty (summarised in table 9.7) shows the largest sources of uncertainty are focused on the tagging and the modelling of the background. Further development of the tagging techniques are possible. The improvements to the proper decay time resolutions provided by the upgrade should help reduce correlations which should also reduce the systematic uncertainty.

The systematics associated with the backgrounds can be addressed by exploring

[2] In ATLAS Terminology - CONF Note

alternative modelling techniques; some suggestions include:

- Exploring the results of switching to the helicity angular definitions for fitting. Preliminary consideration suggest that they can provide simpler acceptance and background angle functions.
- The background angles demonstrate a slight dependence on the $p_T(B_s)$; this could be investigated further.
- Smooth acceptance corrections could be produced by increasing Monte Carlo statistics or introducing a system where more bins are used in more heavily populated regions.
- The trigger weighting could be refined further to better emulate the trigger menu.
- The tagging system can improve further to fully exploit the tagging potential.

10.5 Potential measurements after ATLAS upgrades

In this section the potential of accuracy of this analysis after the planned upgrades for the LHC and the ATLAS detector is assessed. $B_s^0 \to J/\psi\phi$ MC signal was generated and reconstructed using the expected conditions for two additional periods of operation. The first operating period called "Run 2" or "ATLAS-IBL" is where the primary upgrade is the addition of an insertable B-layer [81]. The second set of conditions simulated are the conditions expected after "Phase-II" upgrade, the high luminosity LHC, referred to as "ATLAS-ITK" [82]. This analysis now makes up a public ATLAS note [83].

The ATLAS-IBL layout features a new Insertable B-Layer, which is a fourth layer added to the current Pixel Detector between a new beam pipe and the current inner pixel layer (B-layer). With this design the inner most silicon cylinder will

Year	LHC	ATLAS detector	Energy TeV	Pileup $< \mu >$	Luminosity fb^{-1}
2011	Run 1	current	7	6-12	5
2012			8	21	20
2013-2014	LS1 (long shutdown)	Phase-0	-	-	-
2015-2017	Run 2	IBL	14	60	100
2018-2019	LS2 (long shutdown)	Phase-I	-	-	-
2019-2021	Design luminosity	IBL	14	60	250
2022-2023	LS3 (long shutdown)	Phase-II	-	-	-
2023-2030+	HL-LHC (High luminosity)	ITK	14	200	3000

Table 10.6: Summary of predicted detector and luminosity conditions for considered LHC periods.

have an inner radius 32 mm from the beam line. This design will be implemented during the first long shutdown and will be active until the complete replacement of the ATLAS inner tracker during the third long shutdown which will begin a new phase referred to as High Luminosity LHC (HL-LHC). The design requirements for the ATLAS IBL have assumed an integrated luminosity of 550 fb^{-1} and a peak luminosity of 3×10^{34} cm^2s^{-1}.

The second upgrade of the ATLAS detector (ATLAS-ITK) will allow operation at five times the nominal LHC luminosity, 5×10^{34} cm^2s^{-1}, and the full exploitation of the physics accessible with a total integrated luminosity of up to 3000 fb^{-1}. To cope with the increased instantaneous luminosity the new inner detector will have increased pixel granularity and the inner most layers will be closer to the collision than the current design.

The specifications of the ATLAS triggers during this time are unknown but it is safe to predict that the muon p_T threshold will need to be higher accounting for the increase of luminosity. For this study the thresholds were set at 6 GeV and 11 GeV for each muon for the IBL sample and 11 GeV for the ITK sample.

Signal $B_s^0 \to J/\psi\phi$ events are generated using Pythia 8 [84] with a centre-of-mass energy of 14 TeV. Reflecting the expected trigger thresholds, two sets of events are produced: first requiring the p_T of both muons coming from the J/ψ are larger than 6 GeV and secondly the p_T of the muon larger than 11 GeV. Both generated samples are reconstructed with the expected conditions of ATLAS-IBL, and the 11

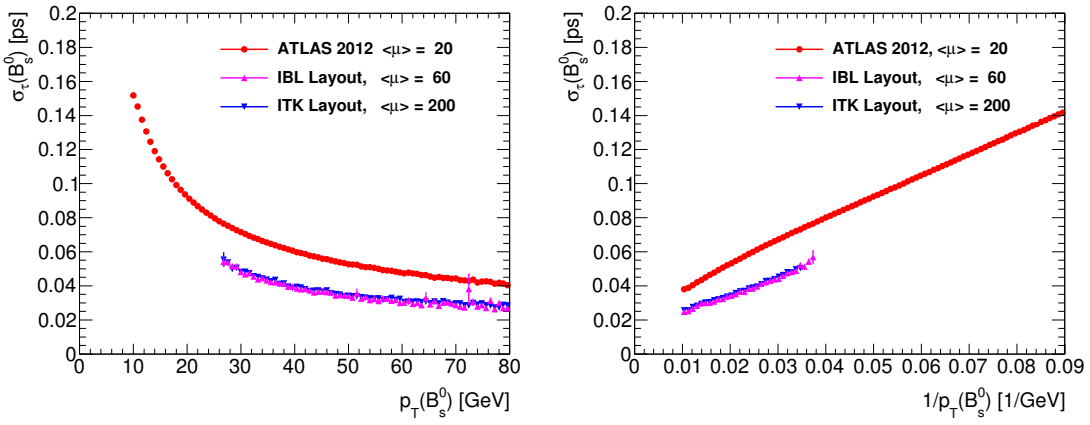

Figure 10.10: The per-candidate proper decay time resolution is plotted as a function of the p_T of the B_s^0 meson shown for the three detector layouts; the current ATLAS layout, IBL and ITK. The vertical axis gives the average value of per-candidates proper decay time errors for B_s^0 candidates within the p_T bin.

GeV sample is reconstructed with the ITK layout. During the simulation the data is mixed with simulated minimum bias events to replicate conditions of pile-up. The IBL samples are mixed with a Poisson average of 60 pile-up events, whereas the ITK samples are mixed with a Poisson average of 200 pile-up events. The reconstruction procedure is adapted to the appropriate levels of pile-up but the selection criteria remain identical to the previous 2011 analysis.

The per-candidate uncertainty for the proper decay time measurements are compared between the samples and their relationship with the p_T of the B meson and the number of reconstructed primary vertices in figures 10.10 and 10.11. It is apparent from these figures that the IBL upgrade will significantly increase the accuracy of the proper decay time measurements while the increasing pileup does not significantly hinder the same measurement. While the ITK upgrade does not significantly reduce the uncertainty of the proper decay time measurements beyond the benefit obtained by the IBL, it does improve the accuracy of the mass measurement as seen in figure 10.12. While the statistical uncertainty of the ϕ_s parameter is heavily influenced by the uncertainty on the proper decay time, a more accurate mass measurement can also help in reducing systematic error and reducing background contamination.

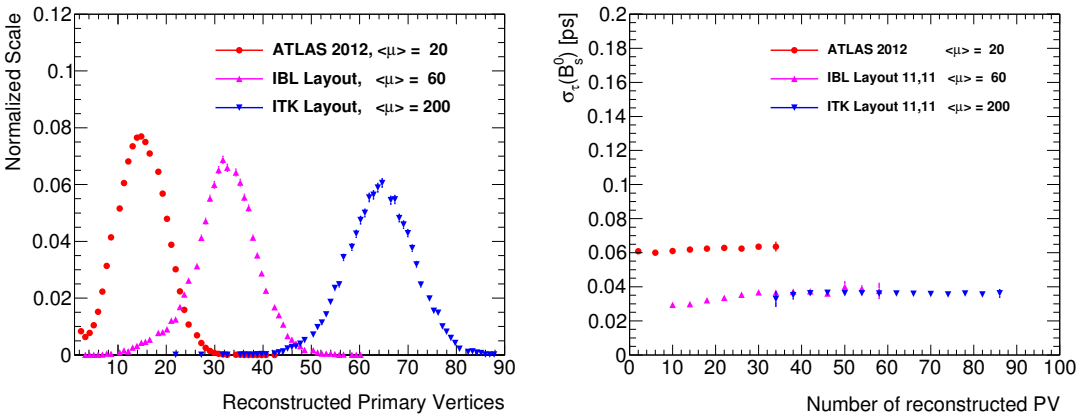

Figure 10.11: The plot on the left shows the number of primary vertices for each simulation layout. The plot on the right shows the average uncertainty of the proper decay time as a function of the number of primary vertices reconstructed.

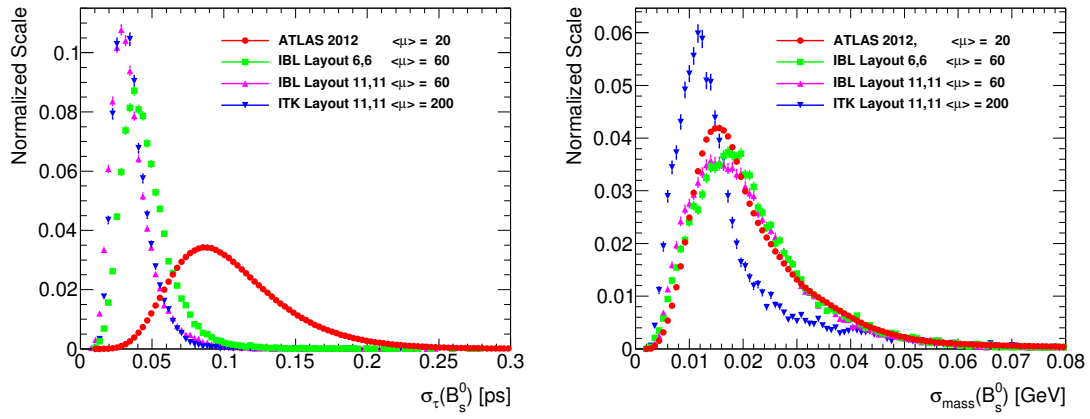

Figure 10.12: In the plot on the left the uncertainty of the proper decay time for each sample is presented. The plot on the right shows the uncertainty of the mass measurement

10.5.1 Estimation of signal statistics and background level

For the purposes of these estimations, the cross section of the process $b\bar{b} \to J/\psi\ X$ at 14 TeV is assumed to be twice as large as the same cross section at 7 TeV. The same factor is assumed for the direct J/ψ production cross section. It is also assumed the cross section ratios of the J/ψ produced from beauty decays and prompt production varies in the same way at 14 TeV as it does at 7 TeV. Note that a lifetime cut to exclude the direct production component is not applied, as with the presented analysis.

To estimate the signal statistics expected in these future periods of data taking three subsets of 2012 data are created: all selected B_s^0 candidates, candidates with both muons possessing a p_T larger than 6 GeV and finally candidates with the p_T of both muons being above 11 GeV. From each sample the number of signal candidates (N_{sig}) is extracted using a fit to the mass distributions. Each N_{sig} is corrected by a factor that takes into account signal efficiencies from MC simulated with the future layouts relative to the efficiencies in the 2012 MC simulation. Each N_{sig} is multiplied by 2 to account for the estimated difference in cross section at 14 TeV energies. The N_{sig} values extracted for each period is expressed as the number of signal events per fb^{-1}. The N_{sig} values are then calculated for the integrated luminosities expected to be recorded in each period. This is shown in table 10.7.

	2011	2012	2015-17		2019-21	2023-30+
Detector	current	current	IBL		IBL	ITK
$< \mu >$	6-12	21	60		60	200
Luminosity, fb^{-1}	4.9	20	100		250	3 000
μ p_T thresholds, GeV	4 - 4(6)	4 - 6	6 - 6	11 - 11	11 - 11	11 - 11
Signal events per fb^{-1}	4 400	4 320	3 280	460	460	330
Signal events	22 000	86 400	327 900	45 500	114 000	810 000
Total events in analysis	130 000	550 000	1 874 000	284 000	758 000	6 461 000
MC $\sigma(\phi_s)$ (stat.), rad	0.25	0.12	0.054	0.10	0.064	0.022

Table 10.7: Estimated ATLAS statistical precisions ϕ_s for considered LHC periods (considering only data in that period). Values for 2011 and 2012 in this table are derived using the same method as for future periods. The result for 2011 agrees with the analysis presented in this thesis. [83]

It is not feasible to simulate background events for these estimates as the background rejection is too high and the high computing resources needed were unavailable. There is a combinatorial background present in the signal event samples. The levels presented in the 2012 simulation are found to be consistent with those determined from 2012 data. To estimate the background in the desired periods the fraction of combinatorial background found in the reconstructed samples are scaled using the cross-sections for $pp \to J/\psi\ X$ and $b\bar{b} \to J/\psi\ X$. These estimates are used in Table 10.7.

In order to estimate the final precisions on a future analysis pseudo-experiments are constructed to generate and fit toy MC data. Events are generated with the following components:

The signal mass is generated from the average B_s^0 mass convoluted by Gaussian functions using per-candidate mass errors taken from data (or from fully simulated events for future layouts in the necessary cases). The background mass distribution is generated according to a first order polynomial function, using parameters obtained from data. In the case of future layouts the appropriate cuts are made to the p_T of the muons in the data sample.

The proper decay time and angular amplitudes are generated according to the probability density functions described in chapter 4. The physics parameters used are taken from the standard model values. The proper decay time distributions are convoluted with Gaussian functions with widths equal to the per-candidate errors from data (or from fully simulated events for future layouts in the necessary cases).

Combinatorial background lifetimes are constructed using three exponential functions and a Gaussian model similar to how they are fit in the analysis presented. The background angular distributions are generated using sidebands from 2012 data. Background shapes for future measurements are derived from the same 2012 data after applying p_T cuts of 6 and 11 GeV to the muons.

A **tag decision** for the signal is generated according to tag decision distributions

taken from the simulated MC samples for future conditions. For 2011 and 2012 the signal tag decisions are generated according to distributions extracted from fits to real events from a signal region after a sideband subtraction. The tag decision for the background is generated using events in the B_s^0 mass sidebands from 2012 data. For future periods the 2012 sidebands data are used as well, after applying the relevant cuts on p_T of the muons.

Table 10.7 summarises the estimated statistical precision on ϕ_s for the LHC periods under consideration. The model appears to be reliable since the 2011 estimation matches the full analysis of the 2011 data. It should be noted that the estimates presented can be considered conservative as they preclude potential improvements in the tagging systems and the inclusion of lower p_T thresholds that may be possible with ATLAS' delayed reconstruction methods.

10.6 Conclusions

This analysis of the 2011 ATLAS dataset (containing 4.9 fb^{-1} of pp collisions) demonstrates that ATLAS is capable of producing a measurement of parameters that could potentially falsify standard model predictions of ϕ_s and $\Delta\Gamma_s$ (see Table 4.5). The accuracy of the ATLAS $\Delta\Gamma_s$ measurement has already surpassed the pre-LHC experiments (see figure 10.5) and ϕ_s accuracy surpasses these experiments after including flavour tagging information. The accuracy of the $\Delta\Gamma_s$ and Γ_s measurements are already competitive with the equivalent LHCb dataset (see figure 10.5).

All measurements of physical parameters are consistent with standard model predictions within one standard deviation of their uncertainties but ϕ_s and $\Delta\Gamma_s$ are not yet accurate enough to exclude the standard model region of parameter space. Other parameters meausured include the transversity amplitudes $|A_0(0)|$ and $|A_\parallel(0)|$ which are consistent with the world averages. The fraction of the "S-wave" KK or f_0 contamination is found to be consistent with zero at 0.024 ± 0.014 in the tagged fit and 0.02 ± 0.02 in the untagged fit. The tagged and untagged fits

produce results that are very consistent with each other.

Measurement	ϕ_s [rad.]	$\Delta\Gamma_s$ [ps^{-1}]	Γ_s [ps^{-1}]
untagged [65]	$0.22 \pm 0.41 \pm 0.10$	$0.053 \pm 0.021 \pm 0.010$	$0.677 \pm 0.007 \pm 0.004$
tagged [61]	$0.12 \pm 0.25 \pm 0.11$	$0.053 \pm 0.021 \pm 0.009$	$0.677 \pm 0.007 \pm 0.003$

Table 10.8: A table comparing the key parameters of the tagged and untagged fit

Without tagging information there is the ambiguity in the equation described in equation 10.1. This is resolved by applying a Gaussian constraint in the untagged likelihood to the value $\delta_\perp = (2.95 \pm 0.39)$ rad, which was obtained from the LHCb measurement [74]. In the flavour tagged fit this ambiguity is not present. The addition of flavour tagging information also significantly reduces the uncertainty on the ϕ_s as illustrated in Table 10.8 and is also observed by the reduced size of likelihood contours when comparing figure 10.4 with figure 10.8 which shows the two dimensional contour scan for the $\phi_s - \Delta\Gamma_s$ plane.

$$\{\phi_s, \Delta\Gamma_s, \delta_\perp, \delta_\parallel, \delta_s\} \rightarrow \{-\phi_s, \Delta\Gamma_s, \pi - \delta_\perp, -\delta_\parallel, -\delta_s\} \tag{10.1}$$

$$\{\phi_s, \Delta\Gamma_s, \delta_\perp, \delta_\parallel, \delta_s\} \rightarrow \{\pi - \phi_s, -\Delta\Gamma_s, \pi - \delta_\perp, -\delta_\perp, -\delta_s\} \tag{10.2}$$

Even with tagging an ambiguity still exists for the transformation in equation 10.2. The analysis by LHCb is cited [31] as justification for disregarding the $\Delta\Gamma_s < 0$ solution allowing the fits to produce a unique solution. It would be valuable if ATLAS could independently verify this finding.

The associated uncertainty on the solutions of individual parameters have been studied in detail in likelihood scans. Figure 10.9 shows the one dimensional scan for ϕ_s, $\Delta\Gamma_s$, $\delta_\parallel$ and $\delta_\perp$.

From the conservative estimates of future periods described in section 10.5, it is apparent that the ATLAS sensitivity on ϕ_s will improve after the IBL upgrade becomes operational in the planned 2015 runs. This will be a result of the IBL significantly improving the proper decay time resolution. Subsequent improvements in sensitivity could also depend on changes to the trigger menu and tagging

mechanisms that are still being optimised.

This measurement does not provide evidence of new physics at this time but is not conclusively within the theoretical boundaries set by the Standard Model. With additional statistics this measurement can confirm the Standard Model prediction to a sufficient degree of accuracy. While the Standard Model has been successful in explaining the current experimental data, it is known to generate insufficient CP violation to explain the observed baryon asymmetry of the Universe. Therefore, additional sources of CP violation are still required to resolve this discrepancy. More accurate measurements of Γ_s and $\Delta\Gamma_s$ can also aid in constraining new physics in Γ_{12}^s [42].

Appendix A

Mass Lifetime Fit

During the course of the analysis a relatively simple mass lifetime was required to make early measurements and run tests on the data. A *roofit* macro for simultaneously fitting the mass and lifetime of the $B_s^0 \to J/\psi\phi$ and $B_d^0 \to J/\psi K^{0*}$ was developed and used in ATLAS conf notes [85] [86].

A.1 Mass fit

To extract the B mass and the number of signal events for early data publications and tests, an unbinned maximum likelihood fit to the invariant mass is used:

$$\mathcal{L} = \prod_{i=1}^{N} [f_{\text{sig}} \cdot \mathcal{M}_{\text{sig}}(m_i, \delta_{m_i}) + (1 - f_{\text{sig}})\mathcal{M}_{\text{bkg}}(m_i)] \tag{A.1}$$

where m_i and δ_{m_i} are the invariant mass and its uncertainty calculated using the covariance of the four tracks in the vertex fit. N is the number of candidates. The parameter f_{sig} represents the fraction of signal events. The probability density functions $\mathcal{M}_{\text{sig}}$ and $\mathcal{M}_{\text{bkg}}$ are used to model the signal and background shape of the mass distribution. The signal uses a poly-Gaussian function:

$$\mathcal{M}_{\text{sig}} = \frac{1}{\sqrt{2\pi} S_m \delta_m} \exp\left(\frac{-(m_i - m_B)^2}{2(S_m \cdot \delta_{m_i})^2}\right) \tag{A.2}$$

This per-candidate method accounts for varying mass resolution in different parts of

the detector using the track parameters provided by the reconstruction algorithms. Possible inaccuracy in the calculation of these errors is corrected by a scale factor S_m. The extracted B mass is represented by the fitted parameter m_B.

The background is modelled by a linear polynomial or in the case of $B_d^0 \to J/\psi K^{0*}$ a combination of constant and exponential functions approximating a flat mass spectrum:

$$\mathcal{M}_{\rm bkg}(m_i) = \frac{1 + d_{\rm exp} \cdot \exp\left(\frac{-(m_i - m_C)}{m_{\rm sl}}\right)}{\int_{m_{\rm min}}^{m_{\rm max}} \left(1 + d_{\rm exp} \cdot \exp\left(\frac{-(m_i - m_C)}{m_{\rm sl}}\right)\right) dm} \tag{A.3}$$

A.2 Mass Lifetime fit

The proper decay time of the fake B mesons constructed from prompt J/ψ and some other two hadronic tracks in the primary vertex is modelled by a delta function convoluted by a Gaussian:

$$\mathcal{T}_{\rm prompt}(\tau_i, \delta_{\tau_i}) \equiv R(\tau_i, \delta_{\tau_i}) = \frac{1}{\sqrt{2\pi} S_\tau \delta_{\tau_i}} \exp\left(\frac{-\tau_i^2}{2(S_\tau \cdot \delta_{\tau_i})^2}\right) \tag{A.4}$$

where τ_i and δ_{τ_i} are per-candidate proper decay times and their uncertainties - the data being entered from the sample. The scale factor (S_τ) is to account for possible differences between the measured δ_{τ_i} and the true resolution. The B candidates formed from the indirect J/ψ are represented by two exponentials convoluted with the resolution function:

$$\mathcal{T}_{\rm indirect}(\tau_i, \delta_{\tau_i}) = \left[\frac{b}{\tau_{eff1}} \exp\left(\frac{-\tau\prime}{\tau_{eff1}}\right) + \frac{1-b}{\tau_{eff2}} \exp\left(\frac{-\tau\prime}{\tau_{eff2}}\right)\right] \otimes R(\tau\prime - \tau_i, \delta_{\tau_i}) \tag{A.5}$$

These exponential models for two types of fake B candidates, a fast decaying component where J/ψ from a B-hadron decay is combined with two tracks from the primary vertex, and a slow decaying component of a partially reconstructed B-decay in the left mass sideband. τ_{eff1} and τ_{eff2} are fitted parameters as well as the relative fraction b of those two exponential PDFs. An additional double-

exponential term symmetric around zero is introduced to describe small negative tails in the data, corresponding to small fractions of bad measurements:

$$\mathcal{T}_{\text{tails}}(\tau_i, \delta_{\tau_i}) = \left[\frac{1}{2 \cdot \tau_{eff3}} \exp\left(\frac{-|\tau\prime|}{\tau_{eff3}}\right)\right] \otimes R(\tau\prime - \tau_i, \delta_{\tau_i}) \tag{A.6}$$

Combining the background time likelihoods gives:

$$\mathcal{T}_{\text{bkg}}(\tau_i, \delta_{\tau_i}) = b_2 \cdot [b_1 \cdot \mathcal{T}_{\text{prompt}}(\tau_i, \delta_{\tau_i}) + (1 - b_1) \cdot \mathcal{T}_{\text{tails}}(\tau_i, \delta_{T_i})] + (1 - b_2) \cdot \mathcal{T}_{\text{indirect}}(\tau_i, \delta_{\tau_i}) \tag{A.7}$$

The likelihood of the simultaneous mass-lifetime fit is:

$$\mathcal{L} = \prod_{i=1}^{N} [f_{\text{sig}} \cdot \mathcal{M}_{\text{sig}}(m_i, \delta_{m_i}) + (1 - f_{\text{sig}}) \cdot \mathcal{M}_{\text{bkg}}(m_i) \cdot \mathcal{T}_{\text{bkg}}(\tau_i, \delta_{\tau_i})] \tag{A.8}$$

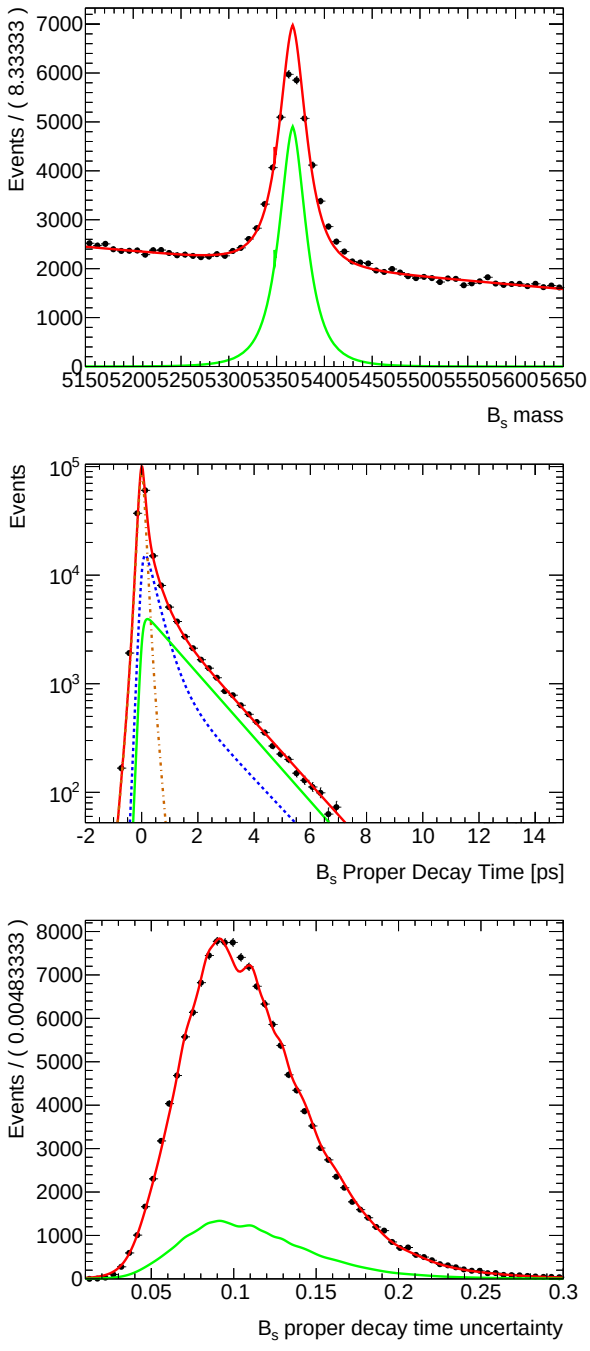

Figure A.1: Plots showing the mass lifetime fit on the 2011 data sample for $B_s^0 \to J/\psi\phi$. Red describes the sum of all functions, green describes the signal, blue is the non-prompt background and the brown is the prompt background.

Appendix B

ATLAS datasets and good run lists used

This appendix contains the datasets used for the various tasks in the analysis.

These datasets were used for the untagged analysis [65]:

data11_7TeV.periodB2.physics_Muons.PhysCont.DAOD_ONIAMUMU.repro09_v01/

data11_7TeV.periodD.physics_Muons.PhysCont.DAOD_ONIAMUMU.repro09_v01/

data11_7TeV.periodE.physics_Muons.PhysCont.DAOD_ONIAMUMU.repro09_v01/

data11_7TeV.periodF2.physics_Muons.PhysCont.DAOD_ONIAMUMU.repro09_v01/

data11_7TeV.periodF3.physics_Muons.PhysCont.DAOD_ONIAMUMU.repro09_v01/

data11_7TeV.periodG.physics_Muons.PhysCont.DAOD_ONIAMUMU.repro09_v01/

data11_7TeV.periodH.physics_Muons.PhysCont.DAOD_ONIAMUMU.repro09_v01/

data11_7TeV.periodI.physics_Muons.PhysCont.DAOD_ONIAMUMU.repro09_v01/

data11_7TeV.periodJ.physics_Muons.PhysCont.DAOD_ONIAMUMU.repro09_v01/

data11_7TeV.periodK1.physics_Muons.PhysCont.DAOD_ONIAMUMU.repro09_v01/

data11_7TeV.periodK2.physics_Muons.PhysCont.DAOD_ONIAMUMU.repro09_v01/

data11_7TeV.periodK3.physics_Muons.PhysCont.DAOD_ONIAMUMU.repro09_v01/

data11_7TeV.periodK4.physics_Muons.PhysCont.DAOD_ONIAMUMU.repro09_v01/

data11_7TeV.periodL.physics_Muons.PhysCont.DAOD_ONIAMUMU.t0pro09_v01/

data11_7TeV.periodM2.physics_Muons.PhysCont.DAOD_ONIAMUMU.t0pro09_v01/

data11_7TeV.periodM4.physics_Muons.PhysCont.DAOD_ONIAMUMU.t0pro09_v01/

data11_7TeV.periodM5.physics_Muons.PhysCont.AOD.t0pro09_v01/

data11_7TeV.periodM6.physics_Muons.PhysCont.DAOD_ONIAMUMU.t0pro09_v01/

data11_7TeV.periodM8.physics_Muons.PhysCont.AOD.t0pro09_v01/

data11_7TeV.periodM10.physics_Muons.PhysCont.AOD.t0pro09_v01/

In the tagged analysis the datasets used are:

data11_7TeV.periodB2.physics_Muons.PhysCont.DAOD_ONIAMUMU.pro10_v01/

data11_7TeV.periodD.physics_Muons.PhysCont.DAOD_ONIAMUMU.pro10_v01/

data11_7TeV.periodE.physics_Muons.PhysCont.DAOD_ONIAMUMU.pro10_v01/

data11_7TeV.periodF2.physics_Muons.PhysCont.DAOD_ONIAMUMU.pro10_v01/

data11_7TeV.periodF3.physics_Muons.PhysCont.DAOD_ONIAMUMU.pro10_v01/

data11_7TeV.periodG.physics_Muons.PhysCont.DAOD_ONIAMUMU.pro10_v01/

data11_7TeV.periodH.physics_Muons.PhysCont.DAOD_ONIAMUMU.pro10_v01/

data11_7TeV.periodI.physics_Muons.PhysCont.DAOD_ONIAMUMU.pro10_v01/

data11_7TeV.periodJ.physics_Muons.PhysCont.DAOD_ONIAMUMU.pro10_v01/

data11_7TeV.periodK1.physics_Muons.PhysCont.DAOD_ONIAMUMU.pro10_v01/

data11_7TeV.periodK2.physics_Muons.PhysCont.DAOD_ONIAMUMU.pro10_v01/

data11_7TeV.periodK3.physics_Muons.PhysCont.DAOD_ONIAMUMU.pro10_v01/

data11_7TeV.periodK4.physics_Muons.PhysCont.DAOD_ONIAMUMU.pro10_v01/

data11_7TeV.periodL.physics_Muons.PhysCont.DAOD_ONIAMUMU.pro10_v01/

data11_7TeV.periodM2.physics_Muons.PhysCont.DAOD_ONIAMUMU.pro10_v01/

data11_7TeV.periodM4.physics_Muons.PhysCont.DAOD_ONIAMUMU.pro10_v01/

data11_7TeV.periodM5.physics_Muons.PhysCont.DAOD_ONIAMUMU.pro10_v01/

data11_7TeV.periodM6.physics_Muons.PhysCont.DAOD_ONIAMUMU.pro10_v01/

data11_7TeV.periodM8.physics_Muons.PhysCont.DAOD_ONIAMUMU.pro10_v01/

data11_7TeV.periodM10.physics_Muons.PhysCont.DAOD_ONIAMUMU.pro10_v01/

The following Monte Carlo data samples used were also used:

mc11_7TeV.108523.PythiaB_bb_Jpsimu2p5mu2p5X.e835_s1310_s1300_r2728_r2780

mc11_7TeV.108543.PythiaB_Bs_Jpsi_mu0mu0_phi_KKe923_a131_s1353_a133_r2780

mc11_7TeV.108543.PythiaB_Bs_Jpsi_mu0mu0_phi_KK.e923_s1310_s1300_r2920_r2900

mc11_7TeV.108411.PythiaB_bb_Jpsimu4mu4X.AOD.e835_a131_s1353_a133_r2780

mc11_7TeV.108411.PythiaB_bb_Jpsimu4mu4X.e974_a131_s1353_a140_r2900

mc11_7TeV.108494.Pythia_directJpsimu2p5mu2p5.e835_a131_s1353_a140_r2900

mc11_7TeV.108523.PythiaB_bb_Jpsimu2p5mu2p5X.e835_s1310_s1300_r2728_r2780

mc11_7TeV.108536.Pythia_directJpsimu4mu4.e835_s1310_s1300_r2927_r2900

mc11_7TeV.108543.PythiaB_Bs_Jpsi_mu0mu0_phi_KKe923_a131_s1353_a133_r2780

mc11_7TeV.108543.PythiaB_Bs_Jpsi_mu0mu0_phi_KK.e923_s1310_s1300_r2920_r2900

mc11_7TeV.108547.PythiaB_Bs_Jpsi_mu4mu4_phi_KK_cutsFlat.e923_a131_s1353_a133_r2780

mc11_7TeV.108566.PythiaBs_Jpsi_mu1mu1_phi_KK.e1106_a131_s1353_a146_r2993

Appendix C

Fit Consistency Checks

This section contains consistency checks for the maximum likelihood fit. Most of the comparisons were done on an untagged sample but are not expected to change significantly for a tagged sample. Those checks ran on the simple mass-lifetime fits will remain completely unaffected by tagging.

C.1 Fit stability with PV multiplicity

The number of reconstructed primary vertices per event increases with the LHC instantaneous luminosity. Since the B_s pseudo-proper decay time depends on a correct choice of primary vertex, a fit stability was tested through the 2011 data periods as the luminosity was increasing. An unbinned simultaneous mass-lifetime likelihood fit was performed for each period separately, for joined periods B-K and L-M (because of the big differences in luminosity and primary vertex multiplicity between the two sets), and for all 2011 data together. Standard $B_s \to J/\psi\phi$ selection cuts were used. A summary of the fit results is shown in the Tab. C.1. It is clear that the lifetime determination is stable over all periods.

Period	PV mult. (mean)	m [MeV]	τ [ps]
B	4.746	5360 ± 4	1.6 ± 0.2
D	4.441	5367.1 ± 0.6	1.47 ± 0.05
E	4.775	5367 ± 1	1.6 ± 0.1
F	4.652	5366.0 ± 0.8	1.38 ± 0.05
G	4.565	5366.7 ± 0.4	1.50 ± 0.03
H	4.147	5366.6 ± 0.6	1.45 ± 0.04
I	4.578	5366.1 ± 0.5	1.47 ± 0.04
J	5.235	5366.8 ± 0.7	1.45 ± 0.05
K	5.297	5366.5 ± 0.4	1.51 ± 0.03
L	7.394	5367.0 ± 0.3	1.48 ± 0.02
M	7.628	5366.4 ± 0.5	1.47 ± 0.04
B-K	4.728	5366.5 ± 0.2	1.48 ± 0.02
L-M	7.459	5366.8 ± 0.3	1.48 ± 0.02
ALL	5.757	5366.7 ± 0.2	1.48 ± 0.01

Table C.1: Primary vertex multiplicities (mean value) and fit results for selected $B_s \to J/\psi\phi$ candidates.

C.1.1 Cross check of background angles in ϕ meson mass side bands

To check whether the fit could be strongly affected by the choice of ϕ meson mass window, the background angular distributions are compared in three ϕ meson mass ranges.

- $0.99 < m(\phi) < 1.0$ GeV/c
- $1.008 < m(\phi) < 1.028$ GeV/c
- $1.040 < m(\phi) < 1.100$ GeV/c

Consistency across these ranges implies that the fit will not be adversely affected by variations in the background angular distributions with ϕ meson mass.

The distributions in Figure C.1 show that the background angular distributions are consistent in different ϕ meson mass windows.

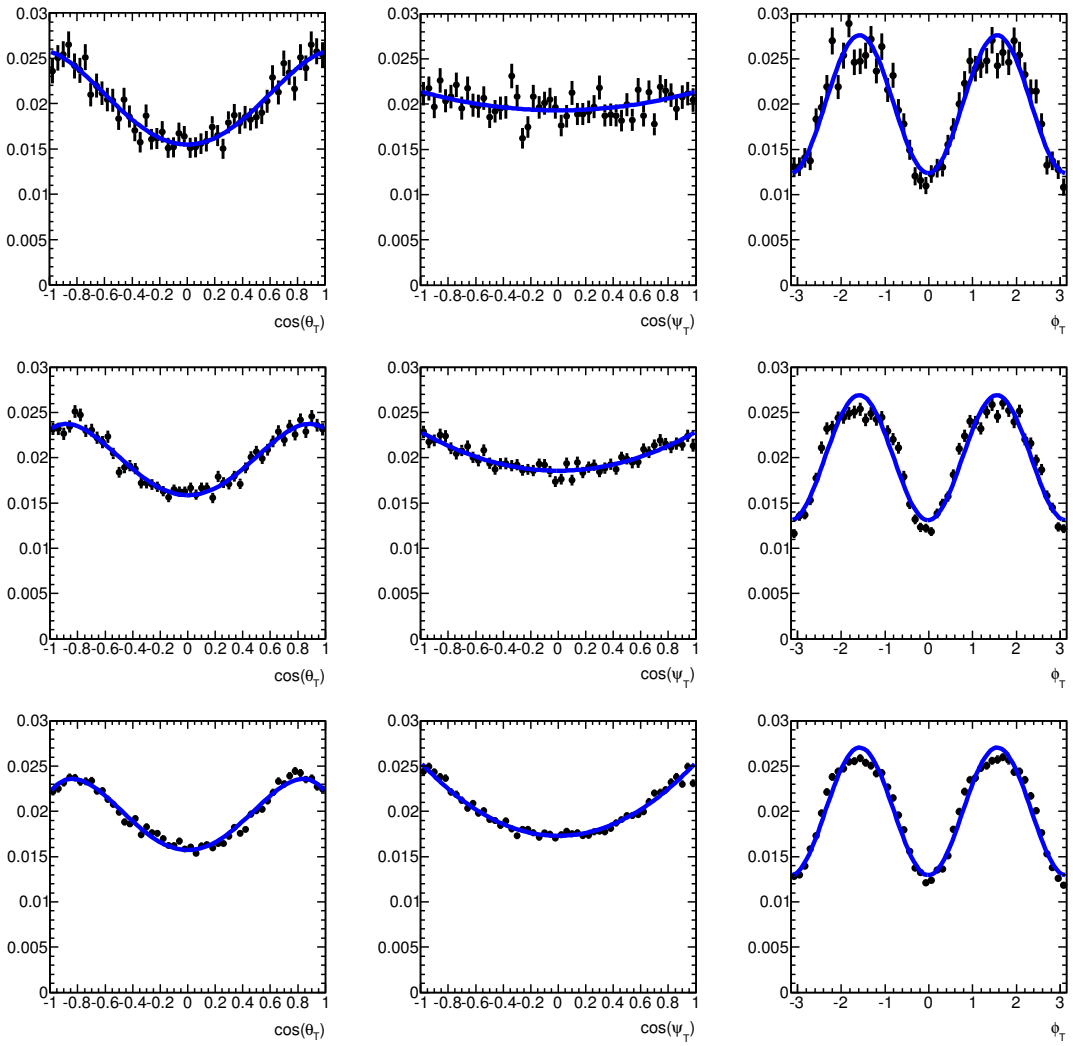

Figure C.1: Background treansversity angles in 3ϕ meson mass ranges (top) low ϕ mass sideband (centre) signal ϕ mass region and (bottom) high ϕ mass sideband

C.2 Checking the stability of the fit with different mass windows

Since ATLAS has a large background compared with other experiments it would be particularly sensitive to the mass windows chosen for the B_s mass spectrum. So these were changed and the fit rerun. The results of key parameters can be seen in figure C.2.

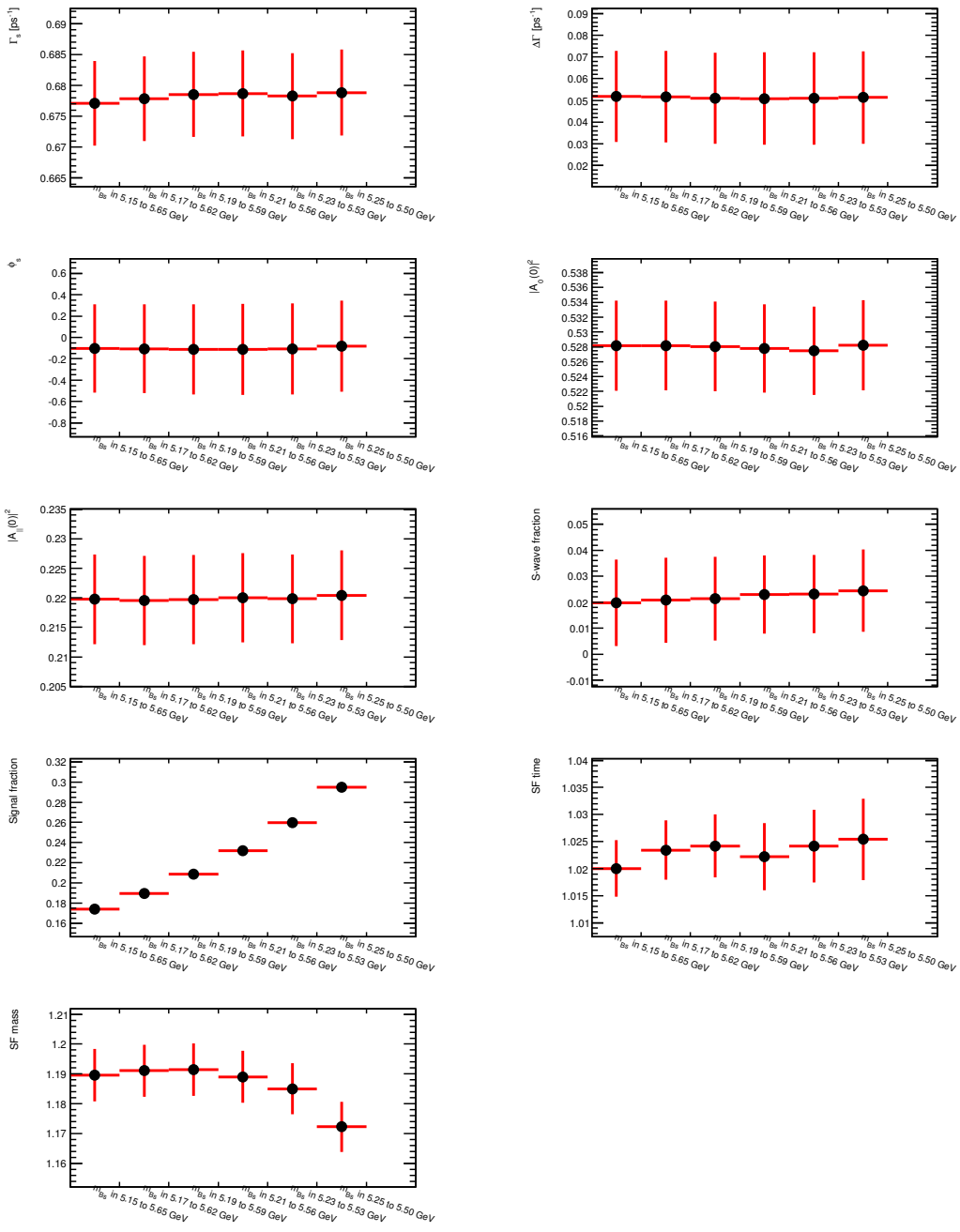

Figure C.2: Figure showing how the key fit parameters change as the mass window the fit is performed in changes

C.3 Stability of fit due to Selections

In order to exclude any systematic effects in lifetime determination, a test of stability is carried out using high statistics MC data. A sample of 16 million signal events generated with flat angles and with a single lifetime $\tau = 1/0.652$ ps was used to test a stability of lifetime determination for various intervals of transverse momentum p_T of B_s meson and various stages of event selection. The events were simulated and reconstructed with MC11B. The goal was to test potential sources of instability in determination of lifetime that could arise from detector performance, reconstruction or event selection of the signal. The test was performed by dividing the reconstruction and selection processes into individual steps and important combinations of these steps were formed. The results of fit after applying the most important combinations are summarised in Figures C.3. The upper figure shows four combinations all using the standard analysis code JpsiFinder that provides vertexing and selection of J/ψ particle. The first case (black points) is when this code was applied to true signal particle tracks parameters. The other three cases in the same figure show results when JpsiFinder was applied to reconstructed tracks after which some selection cuts were applied. The blue points show no other selection cuts applied, red - with selection requesting maximal value of $\chi^2 < 3$, and green, in addition a selection of ψ mass in interval as used for real data, (1008.5 - 1030.5) MeV. The bottom figure shows analogous cases, but JpsiFinder was replaced by a code directly calling vertexing tools. This test was done to exclude any possible bias from the JpsiFinder code.

The fit used was a non-bin likelihood fit to B_s mass and lifetime using per-candidate errors. The results of fits to Γ_s applied to evens from 6 p_T intervals, Figure C.3, demonstrate a consistency with a generated value (0.652 ps^{-1}) as well as between each of the p_T bins, within statistical errors of this test. These results allowed to prove that there are no effects on lifetime measurement coming from reconstruction of signal track, from vertexing nor from any of the cuts used to select the signal. Very important is to stress that any bias possibly coming from

a calculation of proper decay time, using primary and secondary vertex is also excluded with this test. A small increase (over 1 standard deviation of this test) is seen in the highest p_T interval (45-50 GeV) after applying a selection cut on ϕ mass window, (1008.5 - 1030.5) MeV. However with the statistical precision of real data in this p_T interval, such a deviation is negligibly small.

An additional fit stability test on data is carried out by dividing the sample randomly into four data sets. This consistency check shows that the fit is not underestimating the statistical errors. The results for the main parameters of interest are shown in Figure C.4.

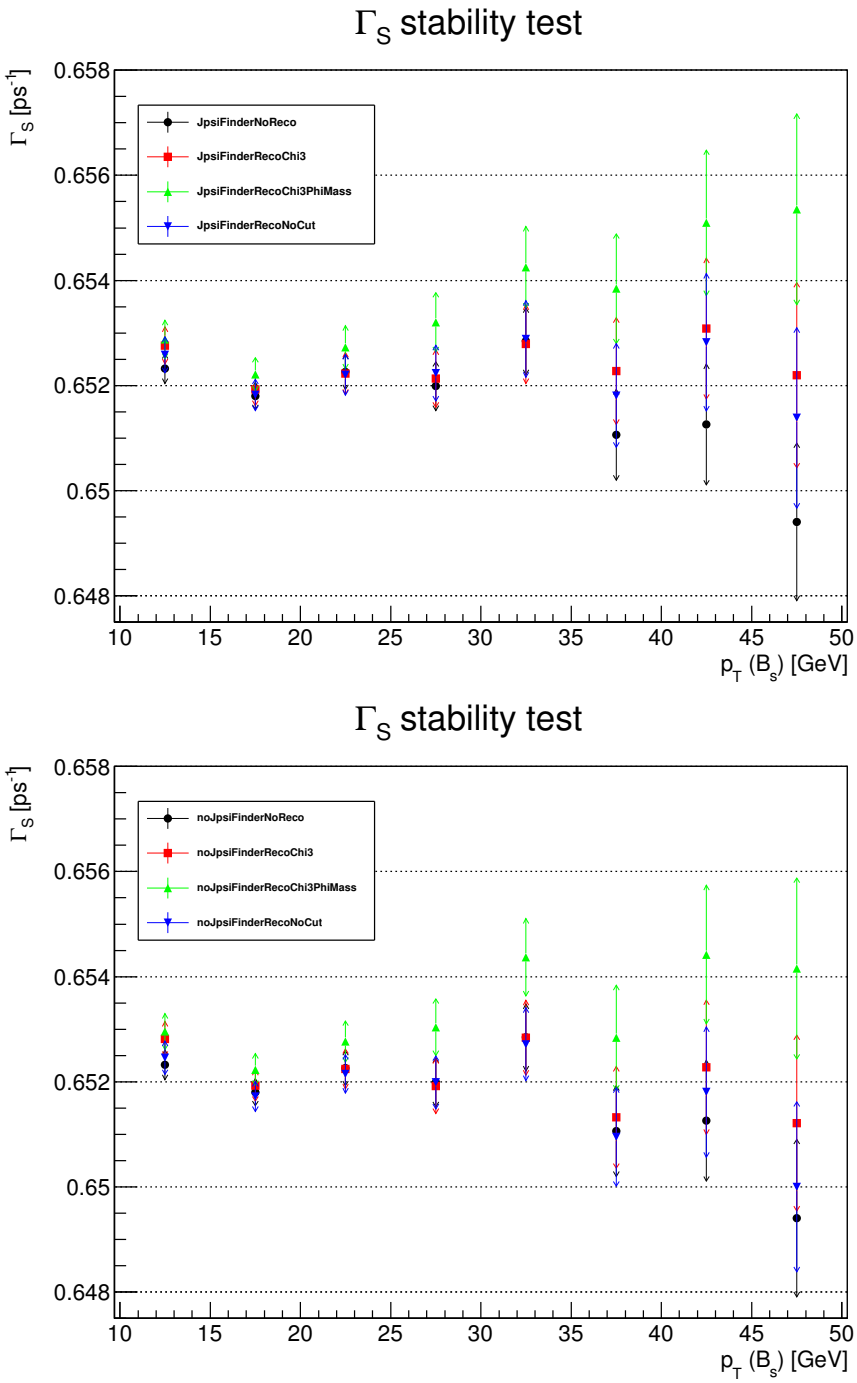

Figure C.3: Fit results to B_s lifetime in eight p_T bins using 16M of MC B_s signal events simulated with flat angles and with a single lifetime.Top figure shows combinations of selection criteria using standard JpsiFinder code, bottom figure shows same combinations when JpsiFinder was not used. More details in the text.

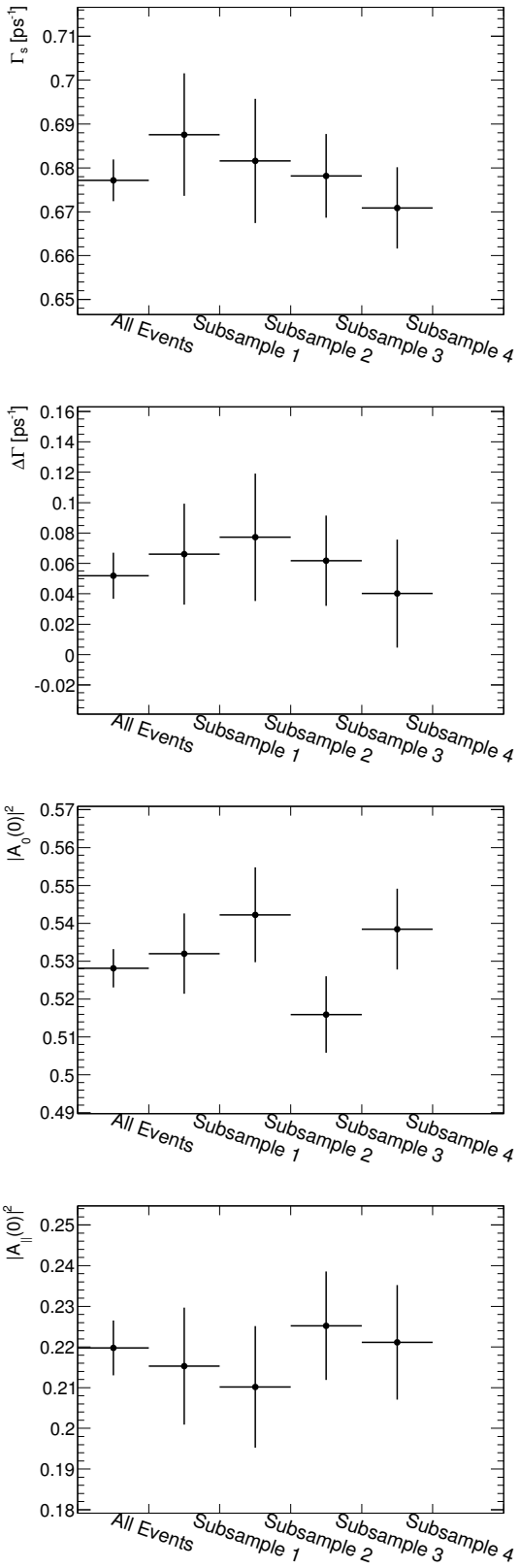

Figure C.4: Stability of key fit parameters in four non-overlapping sub-samples of randomly selected events. First point in each Figure showing fit result using all events.

Bibliography

[1] A.D. Sakharov. "Violation of CP Invariance, c Asymmetry, and Baryon Asymmetry of the Universe". *Pisma Zh.Eksp.Teor.Fiz.* 5 (1967), pp. 32–35. DOI: 10.1070/PU1991v034n05ABEH002497.

[2] J. H. Christenson et al. "Evidence for the 2π Decay of the K_2^0 Meson". *Phys. Rev. Lett.* 13 (4 June 1964), pp. 138–140. DOI: 10.1103/PhysRevLett.13.138. URL: http://link.aps.org/doi/10.1103/PhysRevLett.13.138.

[3] J R Fry. "CP violation and the standard model". *Reports on Progress in Physics* 63.2 (2000), p. 117. URL: http://stacks.iop.org/0034-4885/63/i=2/a=202.

[4] Thomas Sven Pettersson and P Lefevre. *The Large Hadron Collider: conceptual design. oai:cds.cern.ch:291782*. Tech. rep. CERN-AC-95-05 LHC. Geneva: CERN, Oct. 1995.

[5] *How the LHC works*. 2012. URL: http://public.web.cern.ch/public/en/lhc/howlhc-en.html.

[6] L. Rossi. "The LHC superconducting magnets". *Particle Accelerator Conference, 2003. PAC 2003. Proceedings of the* 1 (2003), pp. 141–145.

[7] Christiane Lefevre. "The CERN accelerator complex. Complexe des accelerateurs du CERN". Dec. 2008.

[8] S et al. Catani. "QCD; rev. version". hep-ph/0005025. CERN-TH-2000-131 (May 2000), 115 p.

[9] *ATLAS Collaboration ATLAS public standalone plots*. URL: http://www.atlas.ch/photos/index.html.

[10] "The ATLAS Experiment at the CERN Large Hadron Collider". *JINST* 3 (2008), S08003. DOI: 10.1088/1748-0221/3/08/S08003.

[11] *ATLAS detector and physics performance: Technical Design Report, 1*. Technical Design Report ATLAS. Geneva: CERN, 1999.

[12] "ATLAS inner detector: Technical design report. Vol. 1" (1997).

[13] ATLAS Collaboration. *Expected performance of the ATLAS experiment: detector, trigger and physics*. Geneva: CERN, 2009.

[14] Ph. Schwemling. "The ATLAS Liquid Argon Calorimeters : Construction, Integration, Commissionning". *Nuclear Physics B - Proceedings Supplements* 172 (2007). Proceedings of the 10th Topical Seminar on Innovative Particle and Radiation Detectors, Proceedings of the 10th Topical Seminar on Innovative Particle and Radiation Detectors, pp. 104 –107. ISSN: 0920-5632. DOI: DOI:10.1016/j.nuclphysbps.2007.07.032. URL: http://www.sciencedirect.com/science/article/B6TVD-4PYS2WC-13/2/04d15412506c02369ad670d30d130b52.

[15] "ATLAS muon spectrometer: Technical design report" (1997).

[16] Trigger Operation. *Public Results*. URL: https://twiki.cern.ch/twiki/bin/view/AtlasPublic/TriggerOperationPublicResults.

[17] R. Hauser. "The ATLAS trigger system". *Eur.Phys.J.* C34 (2004), S173–S183. DOI: 10.1140/epjcd/s2004-04-018-6.

[18] E. Rutherford. "LXXIX. The scattering of α and β particles by matter and the structure of the atom". *Philosophical Magazine Series 6* 21.125 (1911), pp. 669–688. DOI: 10.1080/14786440508637080. eprint: http://www.tandfonline.com/doi/pdf/10.1080/14786440508637080.

[19] Sheldon L. Glashow. "Partial-symmetries of weak interactions". *Nuclear Physics* 22.4 (1961), pp. 579 –588. ISSN: 0029-5582. DOI: http://dx.doi.org/10.1016/0029-5582(61)90469-2. URL: http://www.sciencedirect.com/science/article/pii/0029558261904692.

[20] K. Nakamura et al. "Review of particle physics". *J.Phys.G* G37 (2010). (And 2011 partial update for the 2012 edition), p. 075021. DOI: 10.1088/0954-3899/37/7A/075021.

[21] J.J. Thomson. "Cathode Rays". *Philosophical Magazine* 44 (1897), p. 295.

[22] A.I. Sanda I.I Bigi. *CP Violation*. Cambridge University Press, 2000.

[23] Murray Gell-Mann. "Symmetries of baryons and mesons". *Phys. Rev.* 125.3 (1962), pp. 1067–1084.

[24] J. E. et al. Augustin. "Discovery of a Narrow Resonance in e^+e^- Annihilation". *Phys. Rev. Lett.* 33 (23 Dec. 1974), pp. 1406–1408. DOI: 10.1103/PhysRevLett.33.1406. URL: http://link.aps.org/doi/10.1103/PhysRevLett.33.1406.

[25] J. J. et al. Aubert. "Experimental Observation of a Heavy Particle J". *Phys. Rev. Lett.* 33 (23 Dec. 1974), pp. 1404–1406. DOI: 10.1103/PhysRevLett.33.1404. URL: http://link.aps.org/doi/10.1103/PhysRevLett.33.1404.

[26] Makoto Kobayashi and Toshihide Maskawa. "CP-Violation in the Renormalizable Theory of Weak Interaction". *Progress of Theoretical Physics* 49.2 (1973), pp. 652–657. DOI: 10.1143/PTP.49.652. URL: http://ptp.ipap.jp/link?PTP/49/652/.

[27] S. W. et. al. Herb. "Observation of a Dimuon Resonance at 9.5 GeV in 400-GeV Proton-Nucleus Collisions". *Phys. Rev. Lett.* 39 (5 Aug. 1977), pp. 252–255. DOI: 10.1103/PhysRevLett.39.252. URL: http://link.aps.org/doi/10.1103/PhysRevLett.39.252.

[28] F. et. al. Abe. "Observation of Top Quark Production in $\overline{p}p$ Collisions with the Collider Detector at Fermilab". *Phys. Rev. Lett.* 74 (14 Apr. 1995), pp. 2626–2631. DOI: 10.1103/PhysRevLett.74.2626. URL: http://link.aps.org/doi/10.1103/PhysRevLett.74.2626.

[29] T. D. Lee and C. N. Yang. "Question of Parity Conservation in Weak Interactions". *Phys. Rev.* 104 (1 Oct. 1956), pp. 254–258. DOI: 10.1103/PhysRev.104.254. URL: http://link.aps.org/doi/10.1103/PhysRev.104.254.

[30] Y. Nir et al (Particle data group) D. Kirby. "CP VIOLATION IN MESON DECAYS". *Phys. Rev. D* 86.1 (2012), p. 010001.

[31] R. Aaij et al. "Determination of the sign of the decay width difference in the B_s^0 system". *Phys.Rev.Lett.* 108 (2012), p. 241801. DOI: 10.1103/PhysRevLett.108.241801. arXiv:1202.4717 [hep-ex].

[32] Isard Dunietz, Robert Fleischer, and Ulrich Nierste. "In pursuit of new physics with B_s decays". *Phys. Rev. D* 63 (11 May 2001), p. 114015. DOI: 10.1103/PhysRevD.63.114015. URL: http://link.aps.org/doi/10.1103/PhysRevD.63.114015.

[33] Alexander Lenz and Ulrich Nierste. "Theoretical update of $B_s^0 - \bar{B}_s^0$ mixing". *JHEP* 0706 (2007), p. 072. DOI: 10.1088/1126-6708/2007/06/072. arXiv:hep-ph/0612167 [hep-ph].

[34] Michael Gronau and Jonathan L. Rosner. "Flavor symmetry for strong phases and determination of β_s, $\Delta\Gamma$ in $B_s \to J/\psi\phi$". *Phys.Lett.* B669 (2008), pp. 321–326. DOI: 10.1016/j.physletb.2008.09.062. arXiv:0808.3761 [hep-ph].

[35] R. Aaij et al. "Measurement of the CP-violating phase ϕ_s in the decay $B_s \to J/\psi\phi$". *Phys.Rev.Lett.* 108 (2012), p. 101803. DOI: 10.1103/PhysRevLett.108.101803. arXiv:1112.3183 [hep-ex].

[36] Bernard Aubert et al. "Amplitude analysis of the decay $D^0 \to K^-K^+\pi^0$". *Phys.Rev.* D76 (2007), p. 011102. DOI: 10.1103/PhysRevD.76.011102. arXiv:0704.3593 [hep-ex].

[37] Bernard Aubert et al. "Measurement of CP-Violating Asymmetries in the $B^0 \to K^+K^-K^0_s$ Dalitz Plot" (2008). arXiv:0808.0700 [hep-ex].

[38] Yuehong Xie et al. "Determination of $2\beta_s$ in $B^0_s \to J/\psi K^+K^-$ Decays in the Presence of a K^+K^- S-Wave Contribution". *JHEP* 0909 (2009), p. 074. DOI: 10.1088/1126-6708/2009/09/074. arXiv:0908.3627 [hep-ph].

[39] Isard Dunietz, Robert Fleischer, and Ulrich Nierste. "In pursuit of new physics with B_s decays". *Phys.Rev.* D63 (2001), p. 114015. DOI: 10.1103/PhysRevD.63.114015. arXiv:hep-ph/0012219 [hep-ph].

[40] Cheng-Wei Chiang et al. "New Physics in $B^0_s \to J/\psi\phi$: A General Analysis". *JHEP* 1004 (2010), p. 031. DOI: 10.1007/JHEP04(2010)031. arXiv:0910.2929 [hep-ph].

[41] Alakabha Datta and Shaaban Khalil. "Supersymmetry and CP violation in B0(s) - anti-B0(s) mixing and B0(s) to J/psi phi decay". *Phys.Rev.* D80 (2009), p. 075006. DOI: 10.1103/PhysRevD.80.075006. arXiv:0905.2105 [hep-ph].

[42] R Aaij et al. "Implications of LHCb measurements and future prospects". *Eur.Phys.J.* C73 (2013), p. 2373. DOI: 10.1140/epjc/s10052-013-2373-2. arXiv:1208.3355 [hep-ex].

[43] J. Charles et al. "Predictions of selected flavour observables within the Standard Model". *Phys.Rev.* D84 (2011), p. 033005. DOI: 10.1103/PhysRevD.84.033005. arXiv:1106.4041 [hep-ph].

[44] Christoph Bobeth and Ulrich Haisch. "New Physics in Γ_{12^s}: $(\bar{s}b)(\bar{\tau}\tau)$ Operators". *Acta Phys.Polon.* B44 (2013), pp. 127–176. DOI: 10.5506/APhysPolB.44.127. arXiv:1109.1826 [hep-ph].

[45] Alexander J. Lenz. "A simple relation for B_s mixing". *Phys.Rev.* D84 (2011), p. 031501. DOI: 10.1103/PhysRevD.84.031501. arXiv:1106.3200 [hep-ph].

[46] *Atlas Computing: technical design report.* Geneva: CERN, 2005.

[47] A Valassi et al. *LCG Persistency Framework (CORAL, COOL, POOL): Status and Outlook*. Tech. rep. CERN-IT-2011-008. Submitted for publication in the Proceedings of CHEP 2010, Taipei. Geneva: CERN, Feb. 2011.

[48] Torbjorn Sjostrand et al. "High-energy physics event generation with PYTHIA 6.1". *Comput.Phys.Commun.* 135 (2001), pp. 238–259. DOI: 10.1016/S0010-4655(00)00236-8. arXiv:hep-ph/0010017 [hep-ph].

[49] G. Corcella et al. "HERWIG 6.5 release note" (2002). arXiv:hep-ph/0210213 [hep-ph].

[50] Elisabetta Barberio, Bob van Eijk, and Zbigniew Was. "PHOTOS: A Universal Monte Carlo for QED radiative corrections in decays". *Comput.Phys.Commun.* 66 (1991), pp. 115–128. DOI: 10.1016/0010-4655(91)90012-A.

[51] P. Golonka et al. "The Tauola photos F environment for the TAUOLA and PHOTOS packages: Release. 2." *Comput.Phys.Commun.* 174 (2006), pp. 818–835. DOI: 10.1016/j.cpc.2005.12.018. arXiv:hep-ph/0312240 [hep-ph].

[52] D.J. Lange. "The EvtGen particle decay simulation package". *Nucl.Instrum.Meth.* A462 (2001), pp. 152–155. DOI: 10.1016/S0168-9002(01)00089-4.

[53] Miklos Gyulassy and Xin-Nian Wang. "HIJING 1.0: A Monte Carlo program for parton and particle production in high-energy hadronic and nuclear collisions". *Comput.Phys.Commun.* 83 (1994), p. 307. DOI: 10.1016/0010-4655(94)90057-4. arXiv:nucl-th/9502021 [nucl-th].

[54] M Smizanska. *PythiaB an interface to Pythia6 dedicated to simulation of beauty events*. Tech. rep. ATL-COM-PHYS-2003-038. Geneva: CERN, 2003.

[55] James Richard Catmore. "$B_s \to J/\psi\phi$ with LHC-ATLAS simulations and sensitivity studies". PhD thesis. Lancaster University, June 2007.

[56] "The ATLAS Simulation Infrastructure". *Eur.Phys.J.* C70 (2010), pp. 823–874. DOI: 10.1140/epjc/s10052-010-1429-9. arXiv:1005.4568 [physics.ins-det].

[57] V Kostyukhin. *VKalVrt - package for vertex reconstruction in ATLAS.* Tech. rep. ATL-PHYS-2003-031. revised version number 1 submitted on 2003-09-24 11:10:53. Geneva: CERN, Aug. 2003.

[58] J. Beringer. "Review of Particle Physics". *Phys. Rev. D* 86 (1 July 2012), p. 010001. DOI: 10.1103/PhysRevD.86.010001. URL: http://link.aps.org/doi/10.1103/PhysRevD.86.010001.

[59] ATLAS BPhysics Group. *Public Results.* URL: https://twiki.cern.ch/twiki/bin/view/AtlasPublic/BPhysPublicResults.

[60] Fons Rademakers et al. *Roofit.* http://root.cern.ch/drupal/content/roofit.

[61] *Flavour tagged time dependent angular analysis of the $B_s \to J/\psi\phi$ decay and extraction of $\Delta\Gamma$ and the weak phase ϕ_s in ATLAS.* Tech. rep. ATLAS-CONF-2013-039. Geneva: CERN, Apr. 2013.

[62] *Commissioning of the ATLAS high-performance b-tagging algorithms in the 7 TeV collision data.* Tech. rep. ATLAS-CONF-2011-102. Geneva: CERN, July 2011.

[63] "Measurement of the Λ_b lifetime and mass in the ATLAS experiment" (2012). Submitted to Phys.Rev. **D**. arXiv:1207.2284 [hep-ex].

[64] O Igonkina and B Petersen. *Proposal and Motivations for 2011 Trigger Menu.* Tech. rep. ATL-COM-DAQ-2011-007. Geneva: CERN, Jan. 2011.

[65] Georges Aad et al. "Time-dependent angular analysis of the decay $B_s \to J/\psi\phi$ and extraction of $\Delta\Gamma_s$ and the CP-violating weak phase ϕ_s by ATLAS". *JHEP* 1212 (2012), p. 072. DOI: 10.1007/JHEP12(2012)072. arXiv:1208.0572 [hep-ex].

[66] F. James and M. Roos. "Minuit: A System for Function Minimization and Analysis of the Parameter Errors and Correlations". *Comput.Phys.Commun.* 10 (1975), pp. 343–367. DOI: 10.1016/0010-4655(75)90039-9.

[67] S Wandernoth. "Precision measurement of the oscillation frequency in the $B_s^0 - \bar{B}_s^0$ system" (Mar. 2013). Linked to LHCb-PAPER-2013-006.

[68] A. Abulencia et al. "Observation of $B_s^0 - \bar{B}_s^0$ Oscillations". *Phys.Rev.Lett.* 97 (2006), p. 242003. DOI: 10.1103/PhysRevLett.97.242003. arXiv:hep-ex/0609040 [hep-ex].

[69] V.M. Abazov et al. "First direct two-sided bound on the B_s^0 oscillation frequency". *Phys.Rev.Lett.* 97 (2006), p. 021802. DOI: 10.1103/PhysRevLett.97.021802. arXiv:hep-ex/0603029 [hep-ex].

[70] J. Abdallah et al. "Search for B0(s) - anti-B0(s) oscillations in DELPHI using high-p(t) leptons". *Eur.Phys.J.* C35 (2004), pp. 35–52. DOI: 10.1140/epjc/s2004-01827-0. arXiv:hep-ex/0404013 [hep-ex].

[71] A. Heister et al. "Improved search for B(0)S anti-B(0)S oscillations". *Eur.Phys.J.* C29 (2003), pp. 143–170. DOI: 10.1140/epjc/s2003-01230-5.

[72] K. Ackerstaff et al. "A Study of B meson oscillations using hadronic Z^0 decays containing leptons". *Z.Phys.* C76 (1997), pp. 401–415. DOI: 10.1007/s002880050564. arXiv:hep-ex/9707009 [hep-ex].

[73] Koya Abe et al. "Search for time dependent B0(s) - anti-B0(s) oscillations using a vertex charge dipole technique". *Phys.Rev.* D67 (2003), p. 012006. DOI: 10.1103/PhysRevD.67.012006. arXiv:hep-ex/0209002 [hep-ex].

[74] Victor Mukhamedovich Abazov et al. "Measurement of the CP-violating phase $\phi_s^{J/\psi\phi}$ using the flavor-tagged decay $B_s^0 \to J/\psi\phi$ in 8 fb^{-1} of $p\bar{p}$ collisions". *Phys.Rev.* D85 (2012), p. 032006. DOI: 10.1103/PhysRevD.85.032006. arXiv:1109.3166 [hep-ex].

[75] The Ludwig Maximilian University of Munich ATLAS group. Collegues in ATLAS.

[76] T. Agatonovic-Jovin University of Belgrade. Collegue in ATLAS.

[77] "Alignment of the ATLAS Inner Detector Tracking System with 2010 LHC p-p collisions at $\sqrt{s} = 7$ TeV". *ATLAS-CONF-2011-012,* *http://cdsweb.cern.ch/record/1334582* ().

[78] *Study of alignment-related systematic effects on the ATLAS Inner Detector tracking*. Tech. rep. ATLAS-CONF-2012-141. Geneva: CERN, Oct. 2012.

[79] T. Aaltonen et al. "Measurement of the CP-Violating Phase $\beta_s^{J/\psi\phi}$ in $B_s^0 \to J/\psi\phi$ Decays with the CDF II Detector". *Phys.Rev.* D85 (2012), p. 072002. DOI: 10.1103/PhysRevD.85.072002. arXiv:1112.1726 [hep-ex].

[80] R et al. Aaij. *Measurement of CP violation and the B_s^0 meson decay width difference with $B_s^0 \to J/\psi K^+K^-$ and $B_s^0 \to J/\psi\pi^+\pi^-$ decays*. Tech. rep. arXiv:1304.2600. CERN-PH-EP-2013-055. LHCB-PAPER-2013-002. Comments: 33 pages, 16 figures. Geneva: CERN, Apr. 2013.

[81] M Capeans et al. *ATLAS Insertable B-Layer Technical Design Report*. Tech. rep. CERN-LHCC-2010-013. ATLAS-TDR-19. Geneva: CERN, Sept. 2010.

[82] Collaboration ATLAS. *Letter of Intent for the Phase-II Upgrade of the ATLAS Experiment*. Tech. rep. CERN-LHCC-2012-022. LHCC-I-023. Draft version for comments. Geneva: CERN, Dec. 2012.

[83] *ATLAS B-physics studies at increased LHC luminosity, potential for CP-violation measurement in the $B_s \to J/\psi\phi$ decay*. Tech. rep. ATL-PHYS-PUB-2013-010. Geneva: CERN, Sept. 2013.

[84] Torbjorn Sjostrand, Stephen Mrenna, and Peter Skands. "A Brief Introduction to PYTHIA 8.1". *Comput. Phys. Commun.* 178.arXiv:0710.3820. CERN-LCGAPP-2007-04. LU TP 07-28. FERMILAB-PUB-07-512-CD-T (Oct. 2007), 852âĂŞ867. 27 p.

[85] *Measurement of the B_d and B_s lifetimes in the decay modes $B_d^0 \to J/\psi K^{0*}$ and $B_s^0 \to J/\psi\phi$ in ATLAS*. Tech. rep. ATLAS-CONF-2011-092. Geneva: CERN, Aug. 2011.

[86] *Observation of the B0d and B0s mesons in the decays $B_d^0 \to J/\psi K^{0*}$ and $B_s^0 \to J/\psi\phi$ in ATLAS*. Tech. rep. ATLAS-CONF-2011-050. Geneva: CERN, Apr. 2011.